PSL UNIVERSITÉ PARIS

THÈSE DE DOCTORAT
DE L'UNIVERSITÉ PSL

Préparée à MINES ParisTech

Recrystallization of 6016 aluminum alloy during and after hot rolling

Soutenue par

Saoussen OUHIBA

22/02/2022

Ecole doctorale n° 364

Sciences fondamentales et appliquées

Spécialité

Mécanique numérique et matériaux

Composition du jury :

Knut, MARTHINSEN Professeur, NTNU	*Rapporteur*
Myriam, DUMONT Maître de conférences, ENSAM Lille	*Rapporteur*
Frank, MONTHEILLET Professeur émérite, MINES Saint-Étienne	*Examinateur*
Nathalie, BOZZOLO Professeur, CEMEF-Mines Paristech	*Examinateur*
Marc, BERNACKI Professeur, CEMEF-Mines Paristech	*Examinateur*
Laurent, BOISSONNET Ingénieur de recherche, CTEC	*Invité*

MINES ParisTech | PSL

CONFIDENTIEL

jusqu'au 22/02/2027

ACKNOWLEDGEMENT

I would like to express my gratitude to my academic supervisors **Prof. Nathalie Bozzolo** and **Prof. Marc Bernacki** for their invaluable supervision and support during my PhD. Without their motivation, this research would not have been successfully completed.

Besides, I would like to thank **C-TEC Constellium Technology Center** for providing me with the financial means to complete this project. I am very grateful for the time spent at the beginning of my PhD at C-TEC Constellium Technology Center, Voreppe. This experience allowed me to familiarize with the PhD research topic and to understand the industrial challenges of the project. I would like to thank especially **Dr. Laurent Boissonnet**, **Dr. Louis-Marie Rabbe** and **Dr. Juliette Chevy** for the constructive discussions that I had with them about the progress of the project and for their insightful suggestions. I am also indebted to **Alain Legendre** for conducting hot compression tests, **Eric Janot** and **Bruno Nicolas** for helping me with sample preparation, semi-quantitative and quantitative analysis of precipitates at C-TEC Constellium Technology Center, Voreppe.

In addition, my sincere thanks must go to the **MSR** (Métallurgie, Structure, Rhéologie) team at **CEMEF** (Centre de mise en forme des matériaux), especially, to **Dr. Alexis Nicolay** for performing sequential annealing experiments on my samples in the SEM chamber and FIB cross sectioning, to **Suzanne Jacomet** for helping me with EBSD acquisitions, to **Cyrille Colin** for helping me with sample preparation and metallography, to **Gilbert Fiorucci** for performing torsion tests, to **Karen Alvarado** for helping me with DIGIMU simulations, and to **Juhi Sharma** for being such a nice office mate. Acknowledgments should also be given to the **DIGIMU consortium partners** for fruitful discussions.

Last but not the least, I would like to thank **my family** for believing in me and for their continued guidance and support despite the physical distance between us. I wish to extend my profound sense of gratitude to **my fiancé** for his love, kindness and patience to help me get through difficult times.

TABLE OF CONTENTS

LIST OF FIGURES

Introduction

Contents

1.1 Industrial process and context

1.1.1 Thesis context

In the last years, the increasing need for weight reduction in automotive applications has led to an increasing attention for aluminum alloys, especially for age-hardenable 6xxx (Al-Mg-Si) alloys. The 6xxx alloys reach their final strength through age hardening during the final paint baking steps. They are known for their good formability, good corrosion resistance and sufficient strengthening potential, making them the preferred alloys for autobody sheets. However, they are prone to the appearance of surface defects such as roping on the sheet surface.

The roping phenomenon is represented by a series of macroscopic ridges and valleys (see figure 1.1) that form on the sheet in the T4 state (defined in section 1.1.2) after being stretched in the transverse direction (TD) for car body applications. This leads to a wavy surface profile that cannot be covered by painting and that is unacceptable for aesthetical reasons [1–6].

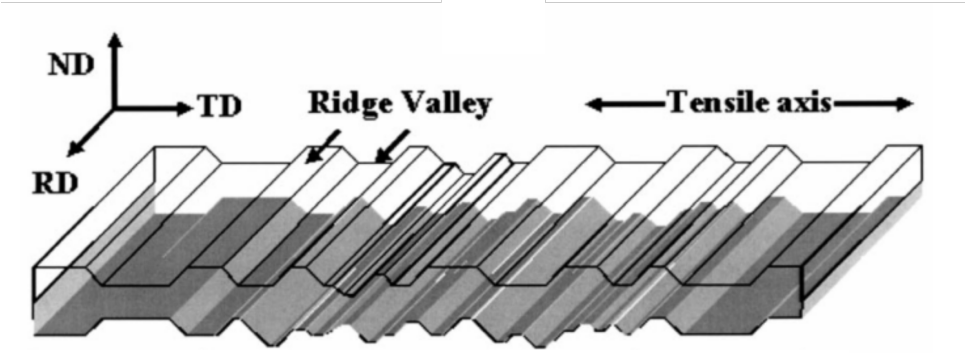

Fig. 1.1 Schematic representation of roping observed in 6xxx aluminum alloys after stretching in the transverse direction (TD) [3]. RD and ND correspond to the rolling direction and the normal direction, respectively.

The roping phenomenon has been attributed to the presence of bands of similar crystallographic orientation in the AA6xxx sheet in the T4 state [1–6]. For instance, Qin et al. [6] reported that, for AA6016, the roping susceptible sample has a stronger global texture than the roping resistant one in the T4 state. Particularly, the volume fractions of Goss and Cube rotated of 27° about RD texture components in the roping susceptible sample are higher than in the roping resistant sample (refer to Chapter 2, section 2.4 for more details about texture components). Additionally, Goss and Cube rotated of 27° about RD tend to form grain clusters in the roping susceptible sample compared to the roping resistant sample (see figure 1.2). These grain clusters will promote the formation of ridges and valleys on the stretched sheet surface. Indeed, different texture components respond differently to the applied tensile test in the TD depending their Lankford coefficient (i.e. frequently referred to as the r-value and defined as the ratio of the true width strain to the true thickness strain at a particular value of length strain). The Lankford coefficient allows to characterize the resistance to thinning during stretching. It has been found in [6] that the r-values of the Goss and Cube rotated of 27° about RD texture components in the transverse direction are higher than the r-value of a random texture, while the r-values of S and Cube rotated of 27° about ND are lower than the r-value of a random texture. Therefore, Goss and Cube rotated of 27° about RD are the most resistant texture components under straining in the TD and form hence ridges on the stretched sheet surface. On the other hand, the S and Cube rotated of 27° about ND form valleys on the stretched sheet surface [6].

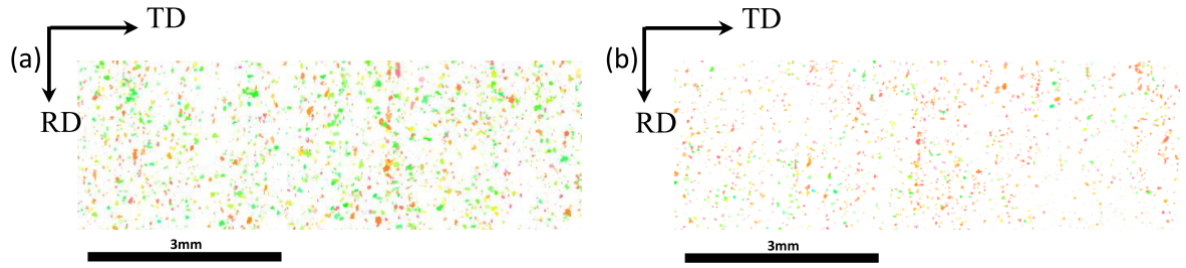

Fig. 1.2 Electron Backscatter Diffraction (EBSD) orientation maps showing grains that are within 16.5° of exact Goss and Cube rotated of 27° about RD texture components (a) for the roping susceptible AA6016 T4 sample and (b) for the roping resistant AA6016 T4 sample [6].

Besides, roping has been attributed to the formation of coarse grains at the exit of the reversible hot rolling mill (see figure 1.3 (a)). These coarse grains are then drawn out into fibers during cold rolling, which will subsequently recrystallize into a finer grain structure. The grains originating from the same fiber tend to deform collectively resulting in the band like microstructure at the T4 state (see figure 1.3 (c)). On the other hand, when the microstructure at the exit of the reversible hot rolling mill is fine-grained (see figure 1.3 (b)), the roping on the surface of the T4 sheet becomes less relevant (see figure 1.3 (d)).

In short, roping is linked to the formation of coarse recrystallized grains of particular crystallographic orientations during hot rolling or intermediate annealing. Therefore, it is important to control the evolution of the microstructure during the thermomechanical process, especially during hot rolling, in order to avoid the occurrence of this surface defect [1–6].

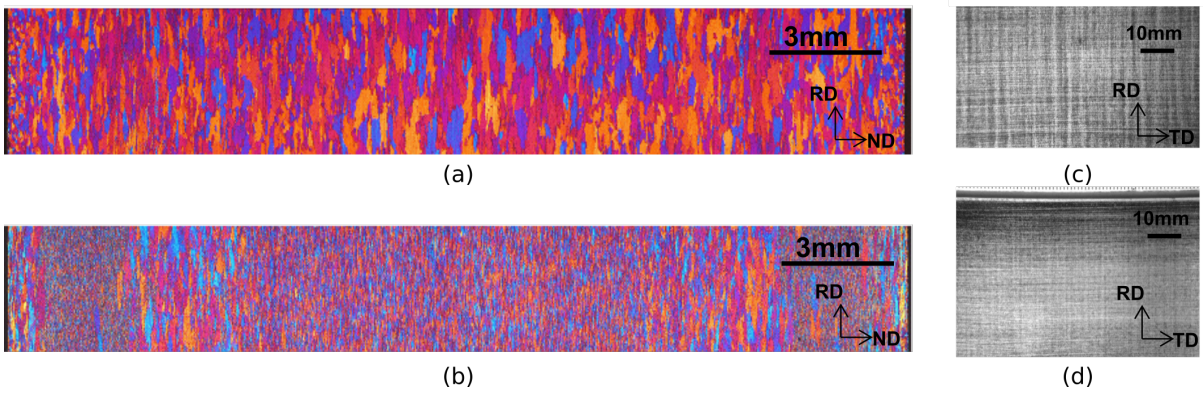

Fig. 1.3 (a,b) Optical micrographs showing AA6016 typical microstructures that can be obtained at the exit of reversible hot rolling mill (specimens have been anodized with Barker's reagent and have been observed through Polarized light in the optical microscope), (c,d) Photographs showing the surface appearance of the sheet at the T4 state (after stretching 15% along the TD and stoning), corresponding to the microstructures shown in (a) and (b), respectively.

1.1.2 Industrial processing route

Generally, the 6xxx aluminum alloy sheet goes through the thermomechanical process illustrated schematically by figure 1.4. The aluminum alloys are direct chill (DC) cast as ingots with dimensions up to 600 mm thick, 2m wide and 4 to 9 m in length (figure 1.4 (a)). The ingots are initially preheated up to 600°C for about 48h in order to homogenize the material (i.e. dissolve soluble phases, spheroidize the constituent phases and reduce short-range segregation) (figure 1.4 (b)). The preheated ingots are subsequently cooled down to the hot rolling temperature (maximum temperature is 500°C) and transferred to the hot rolling line, which is composed of a reversible breakdown mill (figure 1.4 (c)) and a multi-stand tandem mill (figure 1.4 (d)). The hot rolling is therefore performed in multiple passes. The temperature decreases from one pass to the next one. Inversely, the strain rate increases from pass to pass and may reach 100 s^{-1} at the last step in the tandem mill. During the breakdown mill, the thickness is reduced to 25-40 mm, whereas, during the tandem mill, the thickness is reduced to 3-6 mm. The hot rolled sheet is later coiled and cooled down before cold rolling. During cooling of the coiled hot rolled sheet, recrystallization occurs. The sheet is later cold rolled to a final thickness of 0.8-1.2 mm (figure 1.4 (e)). Finally, the cold-rolled sheet is solution treated at a temperature between 500 and 570°C to dissolve hardening phases and then quenched to retain alloying elements in solid solution. The solution-treated and quenched sheet is subsequently artificially aged (i.e. at a low temperature between 100 and 200°C) for about 20-30 min until reaching a full hardening potential. This state is called T4 temper condition [1, 2, 7]. The industrial processing route for aluminum alloy sheets involves therefore a number of steps where complex evolutions of microstructure can take place.

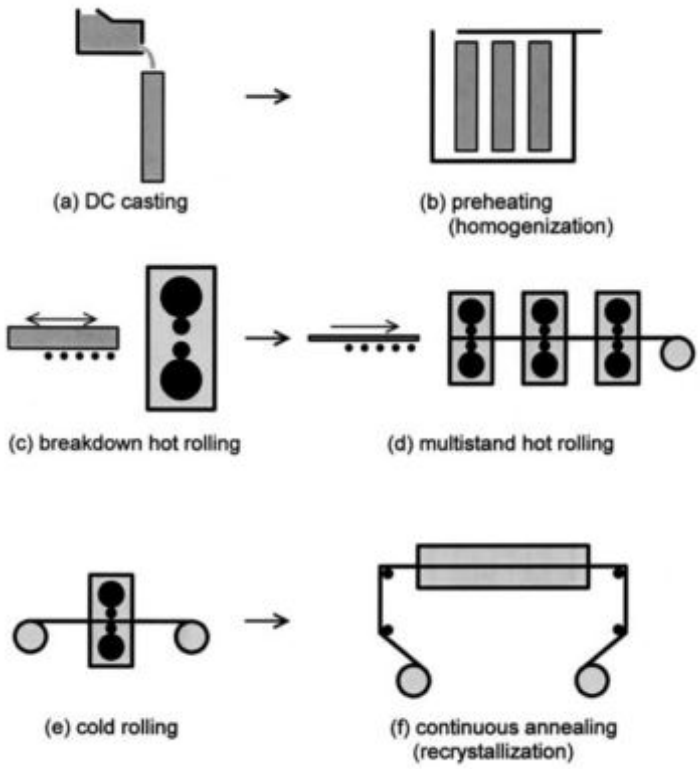

Fig. 1.4 Schematic diagram illustrating the typical steps during the thermomechanical processing of aluminum alloy sheets [2].

As mentioned above, the hot rolling process is a very complex process where the rolling parameters including temperature, strain and strain rate change from one pass to another and where simultaneous precipitation can occur. The rolling temperature decreases, while the strain and strain rate increase from one pass to another. These varying parameters will affect the deformed microstructure and therefore the recovery (i.e. annihilation of redundant dislocations and rearrangement of others into low angle boundaries [8]) and recrystallization (i.e. formation of new strain free grains and their subsequent growth at the expense of deformed or recovered microstructure [9]) processes. Meanwhile, the second phase particles may strongly interfere with the deformed and recrystallized structures. First, they can modify the deformation structure by increasing the overall dislocation density, inducing large scale microstructural heterogeneities such as shear bands and large orientation gradients around them. In return, deformation may lead to the evolution of second-phase particles such as fragmentation of coarse particles or dynamic precipitation. These different aspects may have significant influence on the subsequent recrystallization process. Second, second-phase particles may interact with recrystallized structure by accelerating the nucleation of recrystallization (i.e., particle simulated nucleation), pinning the boundaries of recrystallized grains or becoming unstable during recrystallization due to particle coarsening, dissolving and re-precipitation. Furthermore, solute elements are almost always present in particle-containing alloys such as 6xxx aluminum al-

loys and can interact with dislocations by reducing the grain boundary mobility [10]. All these phenomena taking place at the same time make the contribution of second-phase particles and solutes on recrystallization quite complex. Therefore, there is a strong scientific and industrial interest in better understanding the effect of precipitates and solutes on the progress of recrystallization during and after hot rolling. Thus, based on the previous observations, the objectives of this thesis are to understand the formation mechanisms of overgrown grains and to determine the effect of precipitates and solutes on recrystallization during and after hot rolling in our studied material.

1.2 Preliminary study

In order to choose the material of best interest for this work, five different compositions of 6xxx aluminum alloys were provided by C-TEC (Constellium Technology Center, Voreppe) and tested. The main difference between the different compositions is the concentration of Si, Mg and Mn leading to different amounts of Mg_2Si and Si precipitates and Mn dispersoids and therefore to different recrystallization behaviors. Hot compression specimens of 56 mm (in the rolling direction RD), 50 mm (in the transverse direction TD) and 9 mm (in the normal direction ND) were machined from $\frac{1}{4}$ thickness of as-cast ingot of each composition. Prior to hot compression, the specimens were subjected to homogenization followed by two different thermal treatments that aim at generating two extreme initial precipitations of soluble phases (i.e. high and low initial amounts of precipitation). It is possible that the initial amounts of precipitates change during the subsequent hot compression tests. However, this aspect will not be verified in this preliminary study, but will be studied in more details in Chapter 4.

The heat treated specimens from each composition were subsequently tested using hot compression and the resulting microstructures after holding for the same amount of time ($1200\,\mathrm{s}$) were compared to determine which composition and initial amount of precipitation have the most interesting behavior after recrystallization.

More precisely, hot compression tests were performed in the temperature range of $400\,^{\circ}\mathrm{C}$ to $435\,^{\circ}\mathrm{C}$ and in the strain rate range of $1\,\mathrm{s}^{-1}$ to $50\,\mathrm{s}^{-1}$. The applied strain was 1.4. After hot deformation, the samples were held for $1200\,\mathrm{s}$ in the working furnace before water quench in order to allow recrystallization to occur. The samples were later prepared metallographically, electro-etched using Barker's solution and observed under optical microscope to determine whether the microstructure is recrystallized or not.

Figure 1.5 illustrates the effect of strain rate and temperature on the resulting microstructure for both initial precipitate contents in the case of a particular 6016 alloy composition. It is clear from Figure 1.5 (a) that the transition from non-recrystallized microstructure to recrystallized one at about $430\,^{\circ}\mathrm{C}$ is very rapid in terms of strain rate. In addition, it is important to note that the resulting recrystallized microstructure after deformation at about $435\,^{\circ}\mathrm{C}$ and $3\,\mathrm{s}^{-1}$ and holding for $1200\,\mathrm{s}$ (as seen in 1.5 (c)) exhibits coarse recrystallized grains with a mean length

higher than 1 mm. This type of microstructure is actually the one described as detrimental for surface aspect properties in section 1.1.1. Due to this interesting recrystallization behavior, the focus in this study was placed on this 6016 alloy composition.

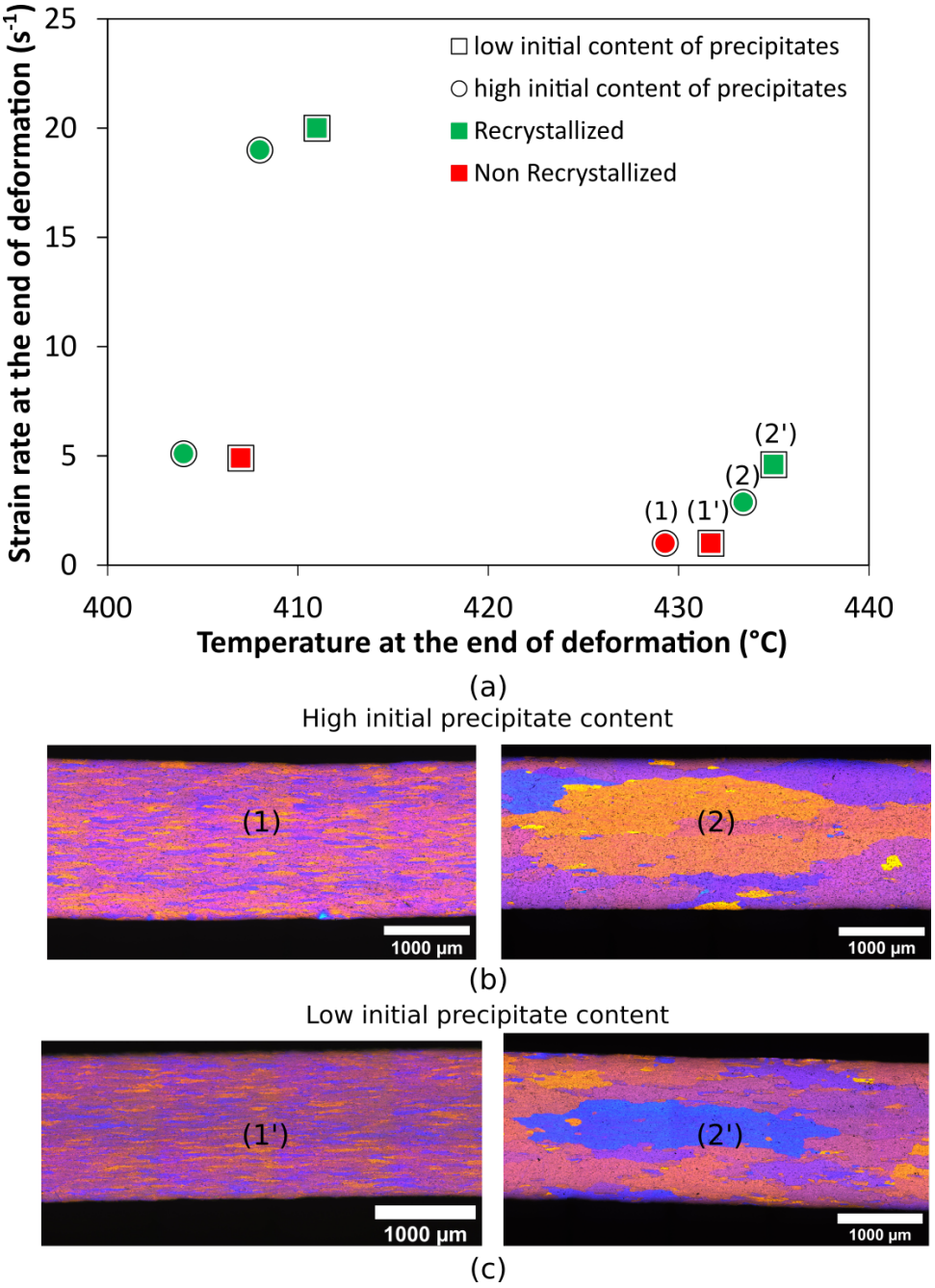

Fig. 1.5 (a) Influence of temperature and strain rate on the recrystallization behavior of 6016 alloy at a strain of 1.4. The microstructure was observed after holding for 1200s before water quench. (b,c) Optical micrographs showing the microstructures corresponding to states 1, 2, 1' and 2' in (a) after anodic oxidation.

1.3 Material of interest

The 6016 alloy studied in this work was supplied as a direct chill (DC) cast ingot by C-TEC. The dimensions of the ingot where the hot compression samples were cut are shown in figure 1.6. The standard chemical composition for AA6016 is given by table 1.1. The main alloying elements are Si, Mg, Cu, and Mn. The studied material also contains unavoidable Fe traces that form large Fe rich intermetallic phases during casting that are difficult to dissolve even after homogenization. Due to their large size (usually higher than $1\,\mu\mathrm{m}$), these particles are known to promote recrystallization by particle simulated nucleation (PSN) [2, 11, 12]. Mn is added to form dispersoids during homogenization. Because of their high melting point, these dispersoids remain stable during subsequent thermomechanical processing steps and therefore are generally used to control grain growth during thermomechanical processing. In addition to Mn, the elements Mg and Si are added to promote the formation of metastable $\beta^{"}$ (Mg_5Si_6) precipitates during artifical ageing. These $\beta^{"}$ precipitates are semi-coherent with the matrix and responsible for maximum age-hardening effect in AA6016. They are 10-15 nm in length [13, 14]. Furthermore, the addition of Cu to AA6016 results in the formation of Cu containing metastable precipitates (L, C, S and $Q^{'}$) during artificial ageing. These precipitates improve the mechanical properties of the alloy, particularly the ductility [14]. However, Mg_2Si, Si and Q phase precipitates can form at earlier stages during the thermomechanical process (e.g. during hot rolling, coiling or cold rolling) and may strongly impede the progress of recrystallization through Smith-Zener pinning [2, 11, 12]. In the current study, the focus will be put on the precipitates that form during hot rolling as well as during annealing after hot rolling, more specifically on Mg_2Si, Si and Q phase precipitates.

Alloy	Mg	Si	Cu	Fe	Mn	Zn	Ti
AA6016	0.25-0.6	1.0-1.5	<0.2	<0.5	<0.2	<0.2	<0.15

Table 1.1 Chemical composition (wt.%) for 6016 aluminum alloy [2].

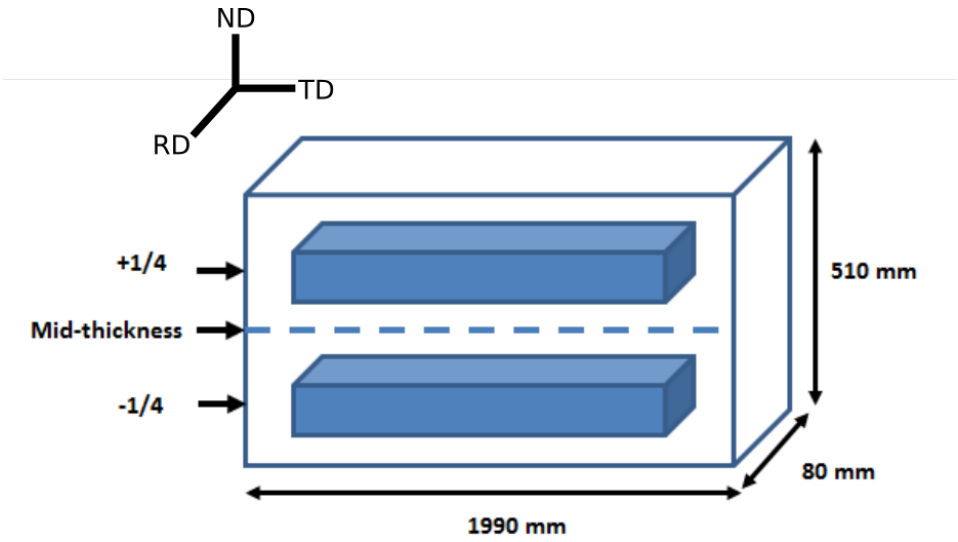

Fig. 1.6 Dimensions of the ingot and positions (in blue) where hot compression samples are machined.

1.4 Thesis objectives and outline

The objectives of this PhD work are to:

1. understand the formation of the coarse recrystallized grains formed during annealing right after hot deformation in 6xxx aluminum alloys.
2. understand how precipitates that are formed before or during hot deformation or during annealing after hot deformation interact with recrystallization.
3. use DIGIMU, which is a full-field (FF) simulation software dedicated to grain growth and recrystallization modeling, to numerically model the development of coarse recrystallized grains by taking into account Smith-Zener pinning, stored energy, capillarity effect and the anisotropic behavior of grain boundaries.

The manuscript is organized in eight main chapters. Chapter 1 was an introduction of the thesis context, industrial processing route, results of the preliminary study and thesis objectives. Chapter 2 summarizes the literature review about recrystallization in aluminum alloys during hot deformation. It introduces firstly the concept of dynamic and post-dynamic recrystallization. Secondly, phenomena where coarse recrystallized grains form during annealing after hot deformation are presented in both aluminum alloys and other materials. Finally, the role of second phase particles on grain boundary migration is reviewed. Chapter 3 presents the experimental methods employed in this work. Chapters 4, 5, 6 and 7 present and discuss the results of the performed experiments and simulations. More specifically, Chapter 4 describes the evolution of the microstructure during and after hot deformation for 3 different initial microstructures with different precipitate contents. Chapter 5 studies in depth the origin of coarse recrystallized grains formed after hot deformation. In Chapter 6, results of experimental work

designed to get closer to the industrial process conditions are presented. During industrial processing, hot deformation is applied in multiple passes separated by an interpass time. Therefore, a comparison between single and multipass tests is conducted. In chapter 7, the possible factors that may promote the anisotropic development of the coarse recrystallized grains identified in Chapter 5 are tested using a full field model based on a level-set approach. Chapter 8 of the thesis outlines the main conclusions drawn from this work and open perspectives.

Literature review

Contents

2.1 Mechanisms controlling grain boundary motion

The migration of grain boundaries is crucial for the occurrence of recovery, recrystallization and grain growth. Actually, grain boundaries are often classified into low angle grain boundaries (LAGBs) and high angle grain boundaries (HAGBs). The misorientation angle at which the transition from a LAGB to a HAGB occurs is typically between 10° and 15° [8]. Winning et al. [15] provided a quantitative analysis of the transition misorientation angle from LAGB to HAGB. The tested materials were high purity aluminium bicrystals and the investigated grain boundaries were planar, symmetric tilt grain boundaries having different tilt axes. The transition from LAGB to HAGB was found to be characterized by a sharp change in the activation enthalpy of grain boundary mobility and to occur at different misorientation angles for different misorientation axes [15].

The migration of LAGBs takes place through the movement of the dislocations which compose them and thus contributes to the occurrence of recovery, while the migration of HAGBs occurs by the jump of atoms across the boundary and contributes to the occurrence of recrystallization and grain growth [8].

In general, the LAGBs are generally composed of arrays of dislocations and their properties are dependent on misorientation. Meanwhile, the properties of HAGBs are generally not dependent on misorientation except in the case of special HAGBs [8].

At the mesoscopic scale, the velocity norm of a high angle grain boundary is generally given by [8]:

$$V = M\,|P| = M\,|\,P_{SE} + P_Z + P_C\,| \tag{2.1}$$

where:

M = boundary mobility [$\mathrm{m}^4/J.s$]
P = net driving pressure [Pa] i.e. [$\mathrm{J/m}^3$]
P_{SE} = difference in stored energy between the matrix and the considered grain per unit grain boundary area
P_C = pressure due to capillarity
P_Z = Smith-Zener pinning pressure

Therefore, a higher grain boundary velocity is caused by a higher boundary mobility and/or a higher net driving pressure.

In hot metal forming, the mobility is usually well described by an Arrhenius law [8]:

$$M = M_0\, e^{\frac{-Q}{RT}} \tag{2.2}$$

where:

M_0 = generally considered as a constant [$\mathrm{m}^4/J.s$]
T = absolute temperature [K]
Q = activation energy for boundary migration [J/mol]
R = gas constant [J/mol.K]

Huang et al. [16] determined the mobility of HAGBs in a deformed single-phase Al-Si aluminum alloy using a combination of in situ annealing and EBSD. They found that high angle tilt boundaries having approximately a misorientation of 40° $\langle 111 \rangle \pm 10°$ have a higher mobility than general and twist boundaries [16]. Similarly, the mobility of LAGBs in a similar material was determined by the same authors [17]. It was found that during annealing, non uniform subgrain growth (i.e. a few subgrains grew much more rapidly than others) occurs due to the strong dependence of LAGB mobility on misorientation. Indeed, the LAGB mobilities were found to increase significantly with increasing misorientation. An increase of 3° in the

misorientation angle of a LAGB leads to an increase in the mobility of a factor of 50. The variation of M_0 with misorientation for LAGBs was described by the following empirical power law [17]:

$$M_0 = k\,\theta^C \text{ with } k = 3 \times 10^{-6}\,m^4/Js \text{ and } C = 5.18 \tag{2.3}$$

However, it is important to keep in mind that the mobilities of LAGBs are 10-500 times lower than the mobilities of random HAGBs and 100-5000 times lower than 40° $\langle 111 \rangle$ tilt HAGBs [17].

The stored energy P_{SE} after deformation provides the driving force for recrystallization and can be approximated by [8]:

$$P_{SE} = \alpha\,\rho\,G\,b^2 \tag{2.4}$$

where:

ρ = dislocation density [m^{-2}]
α = a constant of the order of 0.5
b = norm of Burgers vector [m]
G = shear modulus [N/m^2]

The capillarity pressure P_C is a retarding pressure in the early stages of recrystallization. Indeed, a newly formed recrystallized grain growing into the deformed microstructure tends to shrink in order to reduce its grain boundary area and thus its grain boundary energy. P_C is often expressed as follows [8]:

$$P_C = \frac{-\,2\,\gamma_b}{R} \tag{2.5}$$

where:

γ_b = grain boundary energy [J/m^2]
R = recrystallized grain radius [m]

During grain growth following recrystallization (i.e. in the absence of stored energy), P_C becomes the main driving pressure for the biggest grains to the detriment of small ones.

The Smith-Zener pinning pressure P_Z is a retarding pressure exerted by second-phase particles on the moving grain boundary and can be approximated by [8]:

$$P_C = \frac{-\,3\,F_V\,\gamma_b}{d} \tag{2.6}$$

where:

F_V = volume fraction of a random distribution of particles
d = mean equivalent diameter of particles [m]

Globally, a higher net driving pressure for recrystallization means therefore higher gradients of stored energy and a lower Smith-Zener pinning. The influence of these different contributions to the formation of coarse recrystallized grains will be presented in details in section 2.3.

2.2 Recrystallization in aluminum alloys during hot deformation

During thermal processing operations such as hot rolling, extrusion or forging, the majority of metallic materials undergo dynamic recovery (DRV) and/or dynamic recrystallization (DRX). DRV occurs by dislocation migration, annihilation and rearrangement into LAGBs during hot working [18, 19]. DRX is the formation of strain free grains during hot working. Since DRX occurs during deformation, the dislocation density of new recrystallized grains will increase. Recrystallized grains that are formed dynamically are thus characterized by a higher dislocation density than post-dynamically recrystallized grains (i.e. recrystallized grains that form right after deformation while the material is still hot).

In this section, the focus will be put on DRX occurring in aluminum alloys during hot deformation. Three types of DRX should be considered:

- Discontinuous dynamic recrystallization (DDRX);
- Continuous dynamic recrystallization (CDRX);
- Geometric dynamic recrystallization (GDRX).

The occurrence of one mechanism or another depends on many factors including stacking fault energy (SFE), thermomechanical processing conditions, initial grain size, second phase particles and solutes [20]. The difference between these three types of DRX will be reviewed in the next section.

2.2.1 Discontinuous dynamic recrystallization

DDRX is mostly observed in low SFE materials and is therefore rarely observed in aluminum alloys. Table 2.1 shows the stacking fault energies of different materials. In fact, SFE (i.e. γ_{SFE}) controls the distance between partial dislocations. The lower SFE is, the larger the distance between partial dislocations (separated by a stacking fault) is. It will be therefore more difficult for dislocations to climb or cross-slip and to form subgrain structures [20–22]. In this case, the dislocation density will increase until reaching a critical value necessary for the nucleation of new grains. Hence, during DDRX, nucleation and growth of a recrystallized grain are distinct stages [8, 20].

Material	γ_{SFE} (mJ/m^2)
Aluminum	166
Nickel	128
Copper	78
Silver	22
Gold	45
Magnesium	125
304 stainless steel	21

Table 2.1 Stacking fault energies of common metals and alloys measured at room temperature [20].

Nevertheless, DDRX may occur in high purity (at least 99.99 mass %) aluminum [23–25]. DDRX in high purity aluminum has indeed been reported by Yamagata et al. [23, 24], who found that, at low strains, recrystallized grains nucleate in deformation bands and that the increase in the strain leads to the growth of these grains between the deformation bands with further nucleation of new grains. A substructure was observed within these grains [23, 24], confirming the occurrence of DRX. The occurrence of DDRX in high purity aluminum can be explained by the high mobility of grain boundaries due to the absence of solutes [26].

DDRX has been also observed in aluminum alloys containing large particles [27]. Castro-Fernandez [27] reported that the presence of large particles (typically $>$ 1 μm in size) in aluminum alloys promotes the occurrence of particle stimulated dynamic recrystallization (PSDRX), which has been subsequently confirmed by more recent studies [28–31]. In order for PSDRX to happen, it is necessary that dislocations accumulate at or near the particles during deformation. However, at high temperatures and low strain rates, dynamic recovery retards the formation of deformation zones and hence prevents the occurrence of PSDRX. Humphreys and Kalu [32] investigated dislocation-particle interactions in binary Al-Si alloys for a wide range of particle sizes and deformation conditions and concluded that dislocation structures that are necessary for PSDRX to occur only form at particles of sizes higher than $\eta_c = K(TZ)^{\frac{-1}{3}}$, where K is a constant, T is the temperature and Z is the Zener-Hollomon parameter.

Figure 2.1 shows an example of recrystallized grains formed in the deformation zone surrounding a large particle during the early stages of annealing at a temperature of 350°C in a cold rolled Al-Mn alloy. The deformation zone is caused by the strain incompatibility between the deformed matrix and non-deformable large particles and characterized by rotated zones to the left and right of the particle and distorted zones below and above it. As can be seen from figure 2.1, the deformation zone around the large particle corresponds to a particle and solute depleted zone. Therefore, it recrystallizes easily due to the lower Smith-Zener drag, while the growth of recrystallized grains beyond this zone is hindered due to the high solute and Smith-Zener drag effect [28].

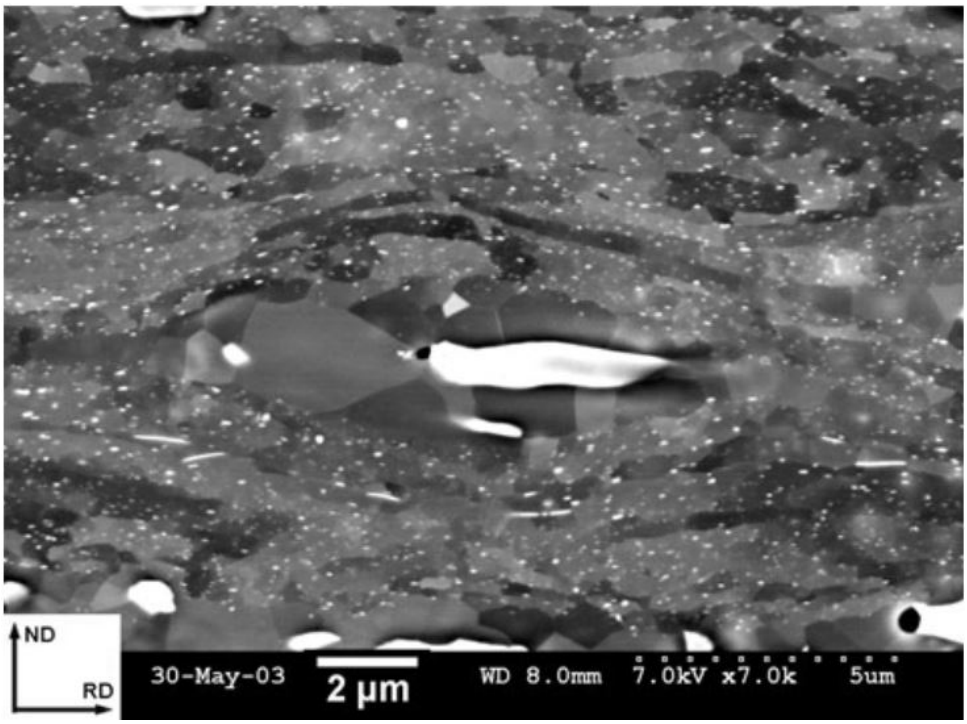

Fig. 2.1 Micrograph showing nucleation of recrystallized grains in a deformation zone surrounding a large particle during annealing of a cold rolled Al-Mn alloy [28].

In addition to nucleation around second-phase particles, pre-existing grain boundaries represent favorable nucleation sites in hot deformed aluminum alloys. Nucleation at pre-existing grain boundaries occurs by strain induced boundary migration (SIBM) (i.e. a grain boundary bulging mechanism where the grain boundary migrates towards the side with higher stored energy). This mechanism leads to the formation of grains with orientations similar to the deformation texture [20]. Examples of DDRX at pre-existing grain boundaries have been reported in the following studies [33–35].

Specifically, Shi et al. [33] studied the microstructure evolution of 7150 (Al-Zn-Mg-Cu) aluminum alloy during hot compression at different temperatures between 300°C and 450°C and strain rates between $10^{-3}\mathrm{s}^{-1}$ and $10\,\mathrm{s}^{-1}$. They found that the level of DRV increases with increasing temperature and with decreasing strain rate and that, at a high deformation temperature of 450°C with strain rates between $10^{-3}\mathrm{s}^{-1}$ and $10^{-1}\mathrm{s}^{-1}$, DRX occurs. Indeed, DDRX dominates at higher strain rates between $10^{-2}\mathrm{s}^{-1}$ and $10^{-1}\mathrm{s}^{-1}$, while CDRX dominates at lower strain rates between $10^{-3}\mathrm{s}^{-1}$ and $10^{-2}\mathrm{s}^{-1}$ [33]. Figure 2.2 taken from their study [33] shows an example of a dynamically recrystallized grain before pinching off from the original grain. The boundaries of the recrystallized grain indicated by C (see figure 2.2 (a)) are composed of a partially bulged original grain boundary having a misorientation angle higher than 30° with grain A and a low angle boundary having a misorientation angle between 3 and 5° with grain B. This implies that grain C is formed by bulging of original grain boundary into grain A and therefore by SIBM. Moreover, figures 2.2 (d-e) show that grain C contains substructures, suggesting that grain C is formed dynamically during hot deformation.

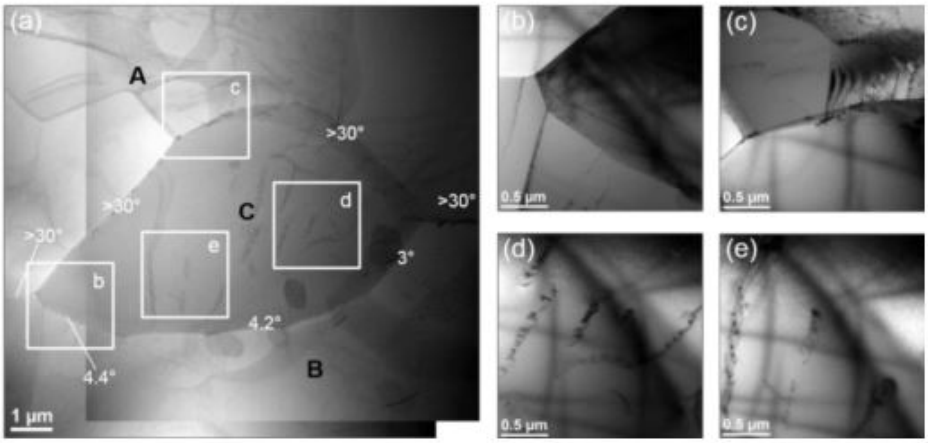

Fig. 2.2 Transmission electron microscope (TEM) image of an Al-Zn-Mg-Cu alloy compressed at 450°C and $0.01\,\mathrm{s}^{-1}$ to a strain of 0.8: (a) scanning transmission electon microscope (STEM) image showing one dynamically recrystallized grain and its surroundings and (b-e) bright-field TEM images showing the enlarged views of four locations in (a) [33].

Similar observations were made by Li [34] and Yang [35] , who investigated the dynamic recrystallization behavior of an AA7085 aluminum alloy during hot compression at different temperatures and strain rates. The authors observed the formation of small recrystallized grains of similar orientation as the deformed grain near the original grain boundary, which led to the conclusion that SIBM is the most likely recrystallization mechanism.

Finally, nucleation of recrystallized grains from cube bands in hot deformed aluminum alloys has been reported in a considerable number of studies [36–41]. In these studies, it has been shown that the cube oriented grains survive after hot deformation and are therefore flattened into bands. Subgrains within these cube bands possess a size advantage compared to subgrains of other orientations due to their enhanced recovery rate. This makes cube oriented subgrains very potent nucleation sites for recrystallized grains by SIBM. Moreover, it has been found that the nucleation from cube bands is enhanced when they are surrounded by an S texture component. In fact, a cube grain when surrounded by an S neighbor makes a $40°\langle 111\rangle$ boundary that is reported in the literature to have a high mobility. In addition to a high mobility, S oriented subgrains have a slightly higher stored energy than average. This leads to the preferential nucleation of cube oriented recrystallized grains at Cube-S boundaries, inducing a strong cube texture in hot deformed aluminum alloys [37–39, 41]. The strength of this cube texture increases with increasing the initial cube fraction, increasing strain and decreasing Zener-Hollomon parameter [38].

The appearance of new grains from cube bands is not the only cause of cube recrystallization texture in hot deformed Al-Mg-Si alloy according to De La Chapelle [40]. Cube recrystallized grains can also arise from cube subgrains in non-cube grains exhibiting a wide spread of orientations [40].

2.2.2 Continuous dynamic recrystallization

2.2.2.1 CDRX by homogeneous and progressive misorientation increase

As mentioned previously, aluminum alloys have high SFE. Thus, the dissociation of dislocations into partials is inhibited. Dynamic recovery is therefore the main softening mechanism occurring in aluminum alloys during deformation at elevated temperatures or at low strain rates. Indeed, elevated temperatures lead to an increased mobility of LAGBs and low strain rates give enough time for dislocations to move. As a result, a well-developed subgrain structure with almost no dislocations inside the subgrains will be formed. The stored energy is therefore lowered and is not high enough to initiate DDRX. Therefore, CDRX is promoted instead of DDRX at high temperature or low strain rate [20].

CDRX occurs by progressive accumulation of dislocations in LAGBs, resulting in an increase in their misorientation and hence to the formation of HAGBs when the misorientation reaches the critial value considered to separate both types of boundaries [20]. This mechanism has been confirmed by Gourdet et al. [26]. The transformation of LAGBs into HAGBs was clearly demonstrated for the two aluminum single crystal orientations $\langle 001 \rangle$ and $\langle 111 \rangle$ as well as for the polycrystalline specimens from different grades (i.e. 1199, 1200 and 5052). The evolution of the misorientation distribution of the 1199 aluminum alloy with increasing strain is shown in figure 2.3. It is clear that there is a progressive shift of the small misorientations towards the larger ones between $\epsilon = 0.3$ and $\epsilon = 1.5$. The LAGBs with $\theta < 6°$ are continuously transformed into medium angle boundaries ($6° < \theta < 15°$), which in turn transform into HAGBs ($\theta > 15°$) [26].

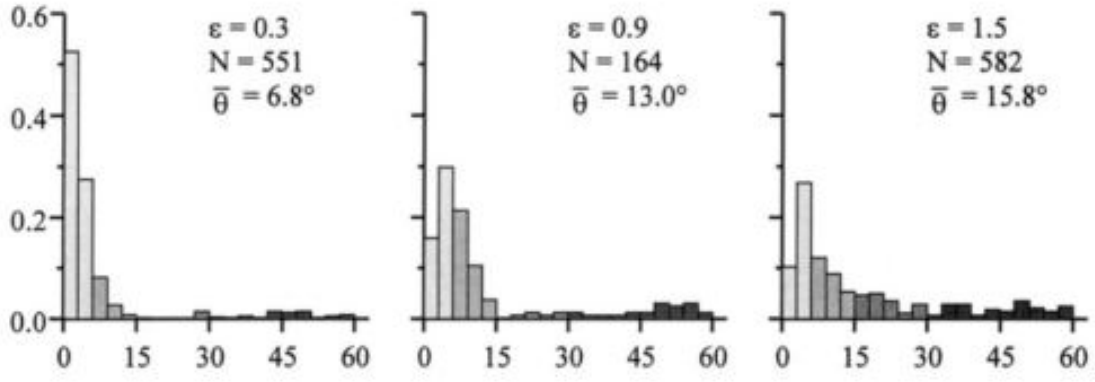

Fig. 2.3 Evolution of the misorientation distribution for the 1199 grade with increasing strain. Specimens were water quenched within 1 s after hot compression at $\dot{\epsilon} = 10^{-2}\,\mathrm{s}^{-1}$ and 380°C [26].

CDRX by homogeneous and progressive misorientation increase has been reported in numerous studies [26, 29, 33, 42–46]. Figure 2.4 shows an example of the microstructure of an AA7150 alloy that was hot compressed at 450°C and $10^{-3}\,\mathrm{s}^{-1}$ to a strain of 0.8. The black thick

lines represent HAGBs while the white and blue lines represent boundaries with misorientation angles in 1°-5° and 5°-15° ranges respectively (see figure 2.4 (b)). It is evident from figure 2.4 (b) that the microstructure contains elongated original grains with a large number of subgrains inside as well as some newly formed grains with HAGBs. The misorientation profile along vector V3 (see figure 2.4 (c)) demonstrates that the recrystallized grain consists of partially the original grain boundary (30° - 60°) and the newly formed high angle boundary (15° - 30°). Similarly, the misorientation profile along vector V4 (see figure 2.4 (d)) shows that a subgrain is progressively increasing its misorientation and being transformed into a dynamically recrystallized grain. Therefore, CDRX is involved at these deformation conditions, which makes sense. Actually, during slow straining at $10^{-3}\,\mathrm{s}^{-1}$ and at a high temperature 450°C, dynamic recovery is enhanced, leading to a considerable decrease in the accumulation rate of dislocations. The resulting driving force is not sufficient for nucleation and growth by DDRX [33].

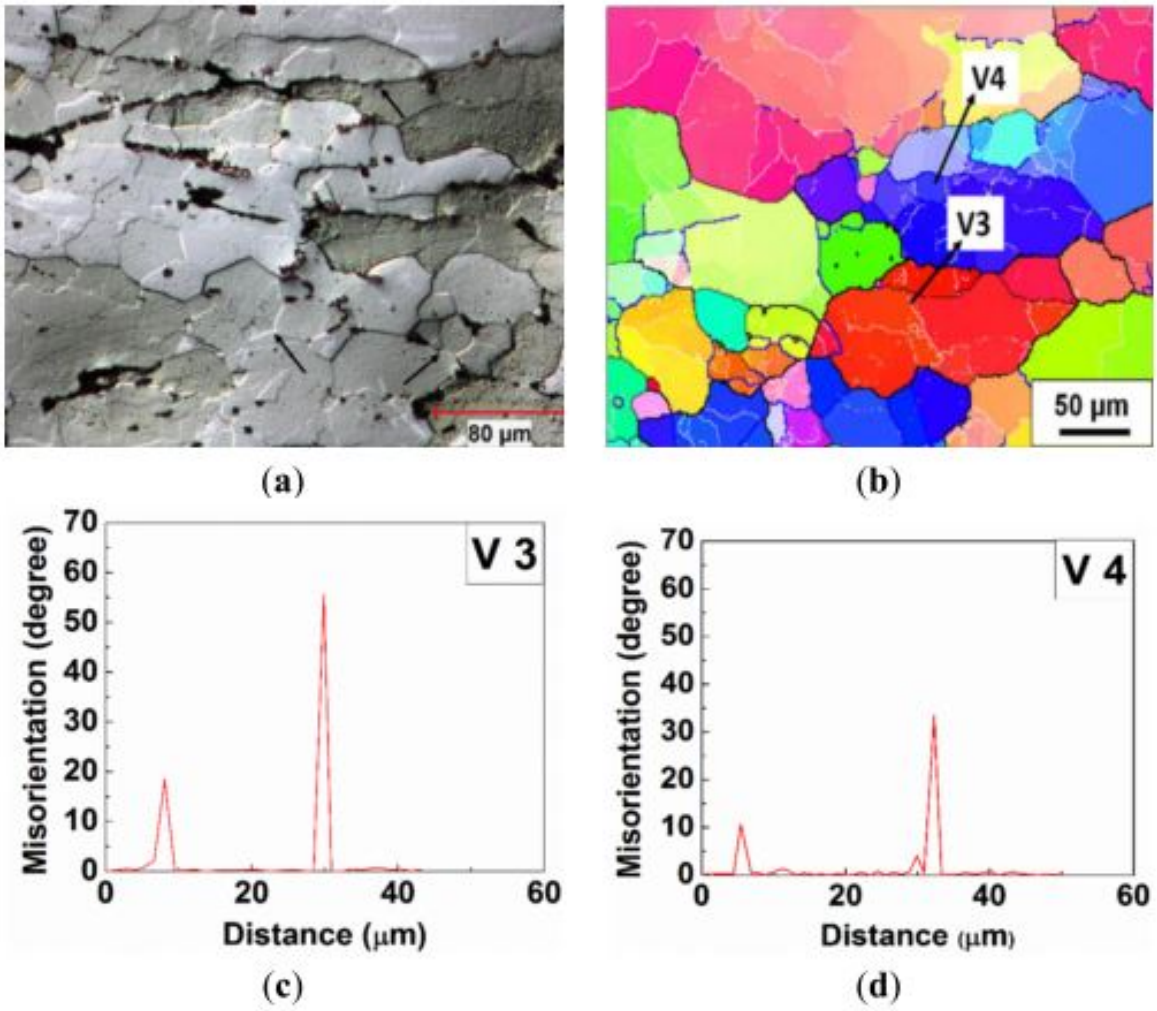

Fig. 2.4 Microstructure of an AA7150 alloy hot compressed at 450°C and $10^{-3}\,\mathrm{s}^{-1}$ up to a strain of 0.8: (a) optical micrograph, (b) EBSD orientation map, (c) misorientation profile along vector V3 and (d) misorientation profile along vector V4 [33].

Nevertheless, it is worth noting from figures 2.2 and 2.4 that there are similarities between

CDRX by homogeneous misorientation increase and DDRX at original grain boundaries. In both cases, the recrystallized grains are formed near original grain boundaries and their orientation is close to their parent grain orientation. The only difference between these two mechanisms is the bulging out of the pre-existing grain boundaries during DDRX. Therefore, it is actually difficult to distinguish between the two mechanisms.

2.2.2.2 Evolution of cells/subgrains with deformation conditions

In this section, the evolution of cells/subgrains with deformation conditions are summarized.

The evolution of misorientation of subgrain boundaries in 1199 aluminium alloy with increasing strain has been studied by Gourdet et al. [26] and is shown by figure 2.3. With increasing strain, the fraction of subgrain boundaries with small misorientation ($<6°$) is reduced whereas the number of subgrain boundaries with larger misorientations increases due to the accumulation of dislocations at subgrain boundaries. It has been reported also that the average subgrain size decreases with increasing strain until reaching a steady state value. This has been achieved at $\epsilon = 0.3$ in hot deformed 1199 and 1200 grades [26].

Wang et al. [47] investigated the influence of deformation temperature on the subgrain evolution of commercial purity aluminum (AA1050) during hot extrusion. It was found that increasing the deformation temperature from 298 K to 523 K leads to an increase in the subgrain size due to the enhancement in the mobility of LAGBs. However, average subgrain boundary misorientation decreases when the deformation temperature decreases. Indeed, the evolution of LAGBs to HAGBs is attributed to the absorption of moving dislocations by LAGBs, leading to an increase in the subgrain boundary misorientation. With increasing temperature, the annihilation of dislocations by cross slip and climb is enhanced within subgrain interiors. As a result, the absorption of dislocations into a LAGB is less frequent and the subgrain misorientation decreases with increasing deforming temperature [47].

Finally, it has been found by Deng et al. [48] that, with decreasing Z parameter (i.e. decreasing strain rate or increasing temperature), the size of subgrains increases due to the fact that dislocations have enough time or mobility to reorganize into more widely spaced and less dense tangles. Regarding the misorientation evolution, decreasing Z values results in a decrease in the number of LAGBs having a misorientation between 2° and 5° associated with an increase in the number of HAGBs [48].

2.2.3 Geometric dynamic recrystallization

The concept of geometric dynamic recrystallization (GDRX) was firstly introduced in 1980s by McQueen and co-authors, who worked on hot deformation of aluminum to large strains [49, 50]. It has been later observed in different aluminum alloys [51–55]. The following is a brief review of the general concept of GDRX.

During hot deformation and due to the efficiency of dynamic recovery in aluminum alloys,

subgrains are formed and original grain boundaries develop serrations due to the tension of the connecting LAGBs (see figure 2.5 (a)). The wavelength of these serrations is similar to the subgrain size. After a small deformation, the subgrain size reaches a steady state value and does not change with further increase in the strain. Therefore, with increasing strains, the original grains are significantly flattened to about twice the subgrain diameter as shown in figure 2.5 (b). Eventually, inward serrations on opposite grain boundaries may touch, leading to the "pinching off" of the subgrains and formation of small equiaxed grains with a size similar to the subgrain size as illustrated in figure 2.5 (b). This recrystallization process is often termed geometric dynamic recrystallization because it involves a change in grain geometry during deformation [8, 20, 52, 56–58].

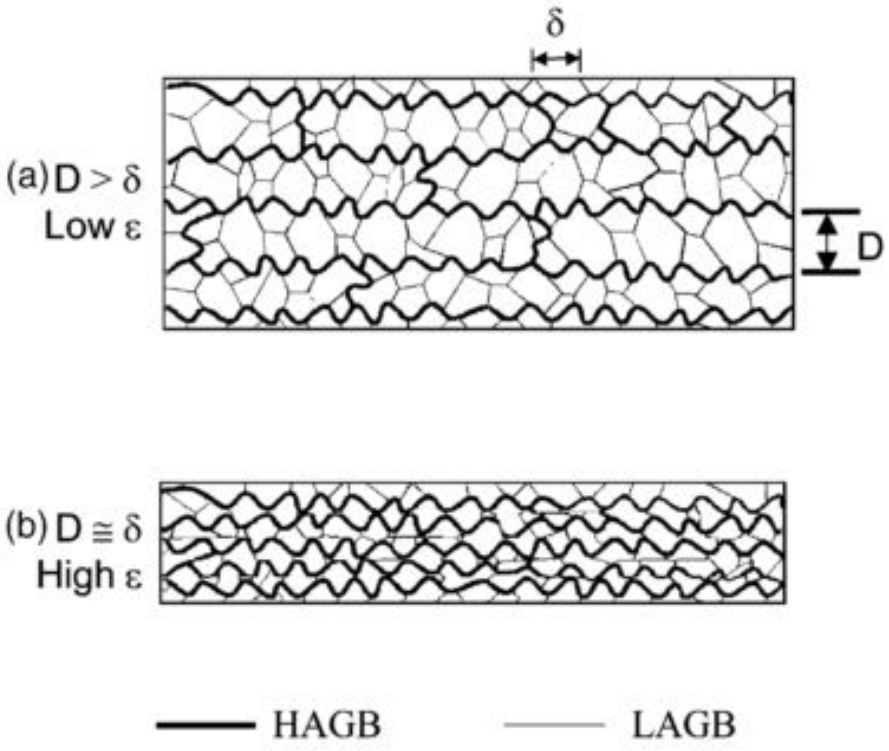

Fig. 2.5 Schematic illustration of effect of increasing strain on grain thickness D and subgrain size δ. HAGBs and LAGBs are represented by dark and light lines respectively [52].

As mentioned above, GDRX has been reported in many studies on aluminum alloys [29, 51–56]. For example, figure 2.6 shows the evolution of the microstructure of a AA6061 alloy deformed at 500°C and at a strain of 1.2 with increasing strain rate. Elongated and pinched off original grains with equiaxed subgrains are clearly revealed when the strain rate is increased to $1\,s^{-1}$. With increasing strain rate, the subgrains become finer and small equiaxed grains aligned along the original grains having a size similar to that of the subgrains start to develop (example shown by a black box in figure 2.6 (c)). This is the typical indication that GDRX is occurring [54].

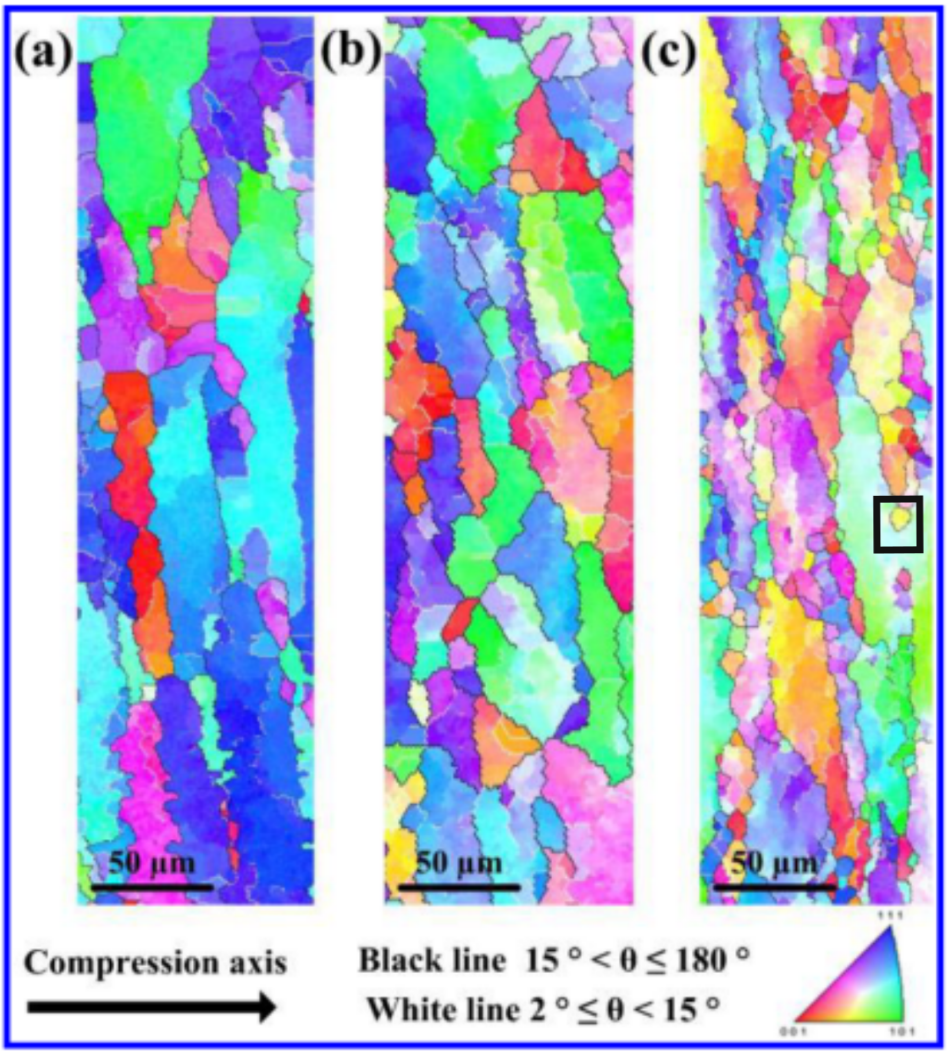

Fig. 2.6 EBSD orientation maps showing the evolution of the microstructure of 6061 aluminum alloy deformed at 500°C and a strain of 1.2 with increasing strain rate: (a) $\dot{\epsilon} = 10^{-2}\,\mathrm{s}^{-1}$, (b) $\dot{\epsilon} = 10^{-1}\,\mathrm{s}^{-1}$ and (c) $\dot{\epsilon} = 1\,\mathrm{s}^{-1}$ [54].

2.3 Formation of coarse recrystallized grains after hot deformation

The term "recrystallized grain overgrowth" has been chosen in this work because we are interested in the abnormally large grains that are formed during annealing after hot deformation, meaning in the presence of a stored energy [59]. Since grain overgrowth shares common characteristics with abnormal grain growth (AGG) which is driven only by capillarity and since most of the studies found in the literature focus on AGG rather than grain overgrowth, AGG will be introduced at first. Second, the factors leading to AGG will be listed. Finally, some examples of AGG and recrystallized grain overgrowth taking place in aluminum alloys and in other materials will be presented.

2.3.1 Abnormal grain growth phenomenon

Abnormal grain growth (AGG) phenomenon consists of the growth of a small number of grains at the expense of their neighbors driven by capillarity forces. For AGG to occur, abnormally growing grains need to possess a growth advantage over neighboring grains [8]. It has been found that a simple size advantage is not sufficient for persistent AGG [8, 60, 61]. Indeed, small grains grow at a faster rate than surrounding large grains, so that large grains return to the normal grain size distribution [60, 61]. Therefore, AGG cannot take place in an "ideal grain assembly" (i.e. a grain structure without impurities and with constant and isotropic grain boundary properties) [8]. The advantage that is necessary for presistent AGG is mostly related to:

- Non-uniform boundary mobility: Decost et al. [62] have confirmed recently this result by using Monte Carlo Potts model simulations, where AGG was observed in systems containing at least 20% of fast boundaries. AGG in these systems takes place by a series of rapid and localized growth jumps as the abnormally growing grains encounter clusters of grains with which they form high mobility boundaries, which leads to irregular morphology for abnormally growing grains in addition to island and peninsular grains [62]. One example of this is highly textured materials. When a grain belonging to the dominant texture components grows, the neighboring grains encountered are likely to be similarly oriented, forming therefore LAGBs. Its growth will be then stopped due to the low mobility of LAGBs. In contrast, when a growing grain belongs to a minority texture component, it has a higher chance of having HAGBs characterized by high mobility. Thus, grains belonging to minority texture components can grow more easily and reach abnormal grain sizes [63–66].
- Non-uniform boundary energy: It has been shown that grains having a high percentage of low-energy boundaries with other grains have a growth advantage by solid-state wetting [67, 68]. Figure 2.7 illustrates the sub-boundary-enhanced solid-state wetting phenomenon by a simple 2D phase field model simulation. In figure 2.7 (a), grain A and grain A* share a low-energy sub-boundary ($E_{AA^\star}$=0.1) and are both in contact with grain B. The energy of the boundary between grain A and grain B (E_{AB}) is 2.2, while the energy of the boundary between grain A* and grain B ($E_{BA^\star}$) is 2.0. The solid-state wetting condition is therefore satisfied (i.e. $E_{AA^\star} + E_{BA^\star} < E_{AB}$). Grain A* will grow by penetrating the highest energy boundary which is the boundary between grain A and grain B, in order to decrease the energy of the system.

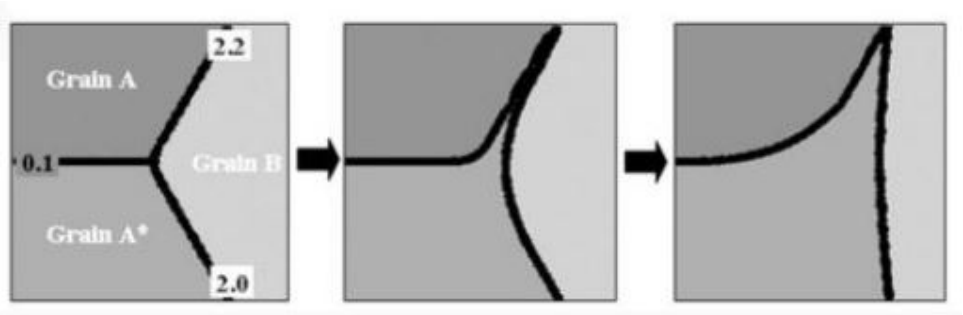

Fig. 2.7 Simple 2D Phase field model simulations showing that a low-energy sub-boundary shared by grain A and grain A* can wet high-energy boundaries. The numbers represent the energy values for different sub-boundaries and boundaries. The units are arbitrary [68].

- Second-phase particles: It is known that second-phase particles exert a so called Smith-Zener pinning force on boundaries and therefore are often used to control grain size during grain growth [8]. However, it was found that AGG can take place in microstructures containing pinning second-phase particles. For instance, in a study conducted by Fjeldberg [69], the influence of particles on mobility-driven AGG has been investigated using a Potts Monte Carlo model. AGG has been observed even in the presence of particles and the abnormal grains grow to a size larger than the Zener limit. Holm et al. [70] conducted mesoscale simulations in 3D polycrystals having uniform and isotropic grain boundary properties. In the absence of particles, only normal grain growth took place. However, in the presence of static particles, AGG occurred after a long incubation time. This AGG phenomenon has be explained by the thermal fluctuation of a grain boundary away from its particle cloud and has been therefore named "particle-assisted AGG" [70]. Finally, in a more recent study conducted by Lu et al. [71], it was found that a non-random distribution of particles is responsible for AGG in Al-Cu alloy. Abnormally large grains were found in regions with a low local density of precipitates, where the Smith-Zener pinning force is insufficient to prevent AGG [71].
- Surface effects in the case of thin films: Grain growth in thin films is strongly influenced by the properties of the top and bottom surfaces of the film. Figure 2.8 gives a schematic illustration of AGG occurring in thin films. As can be seen from figure 2.8 (a), when a columnar structure develops where all grain boundaries intersect the top and bottom surfaces of the film, the free surface contribution to the total energy of any grain becomes significant. The grains with favorable orientations leading to low surface energies will have an energetic advantage and start to grow abnormally as seen in figure 2.8 (b). Therefore, normal grain growth stops and abnormal grain growth proceeds until reaching a microstructure of abnormally large grains as shown in figure 2.8 (c) [72].

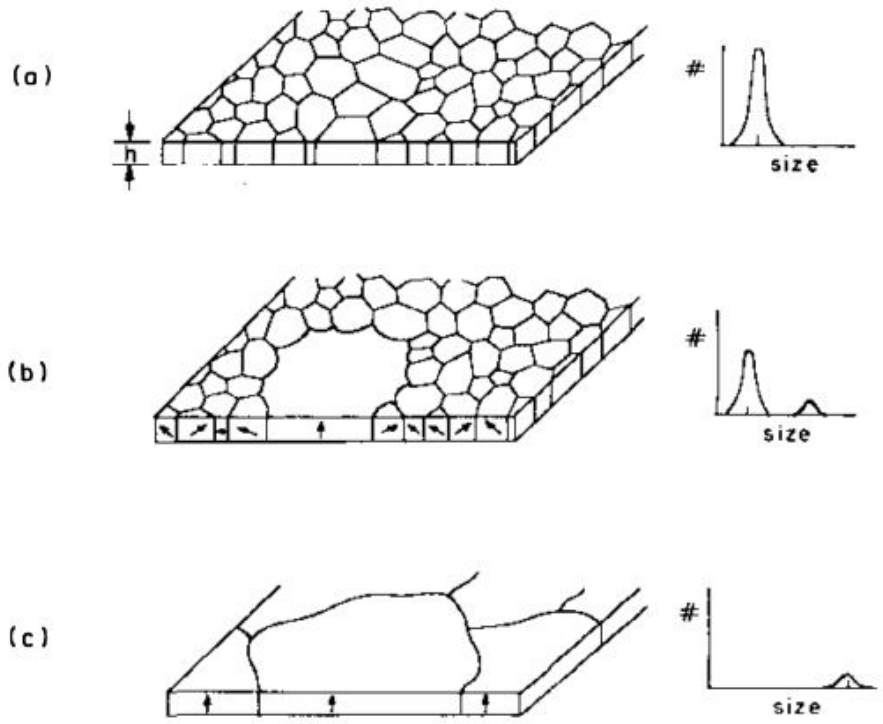

Fig. 2.8 Schematic microstructures and grain size distributions for a thin film undergoing abnormal grain growth [72].

- Solutes: Kim et al. [73] examined the role of solute drag in the occurrence of AGG. For this purpose, grain growth in presence of grain boundary segregation in 2D polycrystalline systems was simulated by a phase-field model. It was shown that the solute drag effect induces AGG under the specific circumstance where a portion of the grain boundaries in a material breaks away from the solute atmosphere. Indeed, a portion of a grain boundary is able to break away from the solute atmosphere when a critical driving force for grain growth is reached. At such critical value, the velocity of the grain boundary makes a discontinous jump and a transition from a low velocity regime (i.e. where migration kinetics are governed by the solute diffusion near the grain boundary) to a high velocity regime (i.e. where migration kinetics are goverened by the atomic jump across the grain boundary) occurs. Therefore, AGG takes place when few portions of grain boundaries are subjected to a supercritical driving force. In the case of a capillarity driven grain growth (i.e. without stored energy), the driving force for growth of a grain i with radius r_i is approximated by $\frac{1}{r_{neighbor}} - \frac{1}{r_i}$ where $r_{neighbor}$ is the average radius of its neighboring grains. It can be deduced from the expression of the driving force that large grains surrounded by small grains will be subjected to a supercritical driving force and will hence grow freely despite the solute atoms. The AGG phenomenon takes place hence even in homogeneous systems without any texture, anisotropic grain boundary properties, second phase particles and grain size advantage [73].

2.3.2 Examples of AGG in aluminum alloys

Abnormal grain growth has been observed in different aluminum alloys, for example, in AA2xxx (Al-Cu alloys) [71, 74], AA5052 (Al-Mg alloy) [66], AA5182 (Al-Mg alloy) [75], AA3102 (Al-Mn alloy) [76] and AA5052 (Al-Mg-Cr alloy) [77].

Dennis et al. [74] reported that the lower fraction of pinning particles at abnormal grain boundaries than at boundaries between small grains is responsible for the occurrence of abnormal grain growth. Therefore, a lower Smith-Zener pinning force due to a lower local density of precipitates may be responsible for this AGG. This has been confirmed later by Lu et al. [71]. The interactions between grain boundaries and particles have been studied in Al-Cu alloy using integrated three-dimensional X-ray imaging and it is found that the larger grains are generated in regions of a lower density of particles. Once the abnormal grain has reached its size advantage, a capillarity-driven grain growth will proceed until the sample volume is consumed. An analytical model considering both capillarity and Smith-Zener pinning pressures has been used in order to predict the critical grain size above which AGG occurs. It has been found that the critical grain size for which a grain will grow abnormally is $\frac{R_{ab}}{R_n} > \frac{2(1-\delta^2)}{(1+\delta^2)}$ where R_n is the mean normal grain size, R_{ab} is the abnormal grain size and $\delta = \frac{\Delta R_n}{R_n}$. In case of a random distribution of particles, $\delta = 0$ and hence $\frac{R_{ab}}{R_n} > 2$ so that abnormal grain growth persists. In case of a non random distribution of particles, an abnormal grain does not need to have a size double the normal grain size to persist in its growth. For example, when $\delta = 0.15$, the critical grain size to induce AGG occurs at $\frac{R_{ab}}{R_n} > 1.9$ [71].

Kim et al. [66] investigated the effect of primary recrystallization texture on grain growth in a fully recrystallized 5052 aluminum alloy. For this purpose, two samples with different primary recrystallization textures were studied. One sample had an initial pronounced cube texture and another one had an initial random texture. The sample with an initial pronounced cube texture underwent AGG upon annealing at 500°C unlike the sample with an initial random texture. The difference in grain growth behavior between the two samples can be explained by the difference in the distribution of high and low angle grain boundaries. In fact, detailed EBSD examination of the sample with an initial pronounced cube texture shows that the cube-oriented grains are clustered together in the microstructure. Therefore, a grain in the cube oriented clusters will be separated from its neighbors by a low angle boundary. Due to the low mobility of LAGBs, grains in cube-oriented clusters will grow more slowly than randomly-oriented grains. Conversely, the boundaries of randomly (i.e. non Cube) oriented grains will be HAGBs allowing randomly oriented grains to grow abnormally and eventually consume the stagnating cube-oriented grains. In contrast, in the sample with an initial random texture, the spatial distribution of individual orientations is homogeneous. Most of grain boundaries are therefore HAGBs and all the grains have the same growth conditions, which leads to normal grain growth [66].

The evolution of the microstructure of a AA5052 alloy during sequential annealing at 500°C

was studied by Park et al. [77], who found that AGG occurs by repeated events of triple-junction wetting. They also found that abnormally growing grains contain sub-boundaries, confirming that AGG in this alloy happens by sub-boundary enhanced solid-state wetting [77].

All the studies mentioned above were conducted on fully recrystallized microstructures, meaning that AGG is occurring in the absence of stored energy. The studies that will be mentioned in the next paragraphs will relate to grain overgrowth (i.e. development of abnormally large grains in the presence of stored energy).

2.3.3 Grain overgrowth with stored energy in aluminum alloys

Abnormally large grains have been observed in 5182 aluminum alloy (AA5182) during annealing or air cooling following hot deformation [75]. It was found that, due to the low number of available nuclei formed during hot deformation, each nucleus will be surrounded by a large volume of deformed grains. These nuclei will therefore be able to grow into abnormally large grains by consuming the surrounding deformed grains until mutual impingement. According to this article, the mechanism that allows these nuclei to grow abnormally is called static AGG. Since stored energy is involved in the growth of these nuclei, it would be more reasonable to consider the development of these abnormally large grains as a case of grain overgrowth [75].

Finally, grain overgrowth took also place during annealing at 600°C of prestrained multiport extrusion tubes [76]. Microstructural evolutions during annealing were characterized using EBSD. Nucleation of recrystallized grains by SIBM occurs at the hardened zones near grain boundaries or triple junctions during annealing. An incubation time is needed for nucleation and the duration of this incubation time is inversely proportional to the amount of applied strain (very typical of static recrystallization). The formed recrystallized grains can grow subsequently rapidly into abnormally large grains. The driving force for the grain growth in this case arises from the residual strain in the grains ahead the growth front. The grain growth stops when a growing grain impinges on grains with similar low stored energy. During overgrowth of abnormally large grains, some grains are not consumed and left behind the growth front, forming then island grains inside the abnormally large grains. The special boundary relationships between island grains and the coarse recrystallized grains where they reside (e.g. coincidence site lattice boundaries (CSL)) seem to be responsible for their formation [76]. Indeed, CSL or any other reason for the low energy and/ or low mobility of some boundaries would lead to island grains.

2.4 Typical texture components in aluminum alloys

The Euler angles of possible texture components observed in aluminum and aluminum alloys during hot rolling and recrystallization are listed by table 2.2 [1]. During hot rolling or plane strain compression, the texture of deformed grains is transformed into β-fiber rolling ori-

entations (Brass, Copper and S) [1]. The distribution of orientation intensities along the β-fiber is affected by the rolling parameters. At elevated rolling temperatures, the Brass component becomes stronger in the deformed microstructure because initial orientations are more easily rotated to the Brass component. However, at room temperature, initial orientations are more easily rotated to the S component than to the Brass and Copper components [78]. During annealing after hot rolling, the texture of recrystallized grains is dominated by a Cube orientation (developed from remaining Cube bands after deformation) with a strong scattering about the rolling direction (RD) and the normal direction (ND). The volume fraction of recrystallized grains belonging to Cube component increases with decreasing Zener-Hollomon parameter Z (i.e. $Z = \dot{\epsilon}\exp\{\frac{Q}{RT}\}$, where Q = 156 kJ/mol, R = 8.31 J/K mol, T is the temperature and $\dot{\epsilon}$ is the strain rate) [38, 78].

Designation	$\phi 1$ (°)	Φ (°)	$\phi 2$ (°)	
Copper	90	35	45	rolling
Brass	35	45	0	rolling
S	53	35	63	rolling
Goss	0	45	0	recrystallization
Cube	0	0	0	recrystallization
CubeND45	45	0	0	recrystallization
CubeRD20	0	22	0	recrystallization
CubeND18	18	0	0	recrystallization
R	53	36	60	recrystallization
P	65	45	0	recrystallization

Table 2.2 Euler angles of typical texture components in aluminum alloys following Bunge's convention [1]. The sample reference frame is {RD,TD,ND}.

2.5 Role of second-phase particles on recrystallization in aluminum alloys

2.5.1 Influence of stable second-phase particles

The interaction between second-phase particles and recrystallization process is quite complex. Second-phase particles can be classified according to their size: large particles of size typically > 1 µm and fine particles. As a usual trend, large particles are formed during solidification and small particles are formed in the subsequent thermomechanical processing steps. These two categories of particles interact differently with the recrystallization process. Large particles can promote recrystallization by particle stimulated nucleation (PSN), where as fine particles may strongly impede the progress of recrystallization through Smith-Zener pinning

[10].

The influence of stable particles (i.e precipitates that precede deformation and that do not change with the subsequent thermomechanical process) on the evolution of microstructure during deformation has been extensively studied [10]. For instance, the effect of stable precipitation on texture evolution of a rolled 3105 aluminum alloy has been studied by Liu et al. [79]. It has been found that large particles generally promote recrystallization by PSN and tend to randomize the recrystallized texture, while small particles tend to enhance the formation of a Cube recrystallized texture. In fact, small particles are found to selectively inhibit nucleation by PSN. However, nucleation at the Cube bands is hardly affected by these fine particles since the subgrains within Cube bands easily recover and exceed the critical nucleus size for recrystallization [1, 79]. It has been also found that these fine particles impede the evolution of texture from initial Cube texture to β fiber rolling texture, leading thus to an increase in the amount of remaining Cube bands in the deformed microstructure and consequently to a preferential nucleation of Cube-oriented grains [79].

This has been confirmed in [80] where it has been shown that the texture evolution during cold rolling in an AA3105 is affected by the precipitation state. Initial orientations are gradually rotated to β fiber components. An increase in the amount of small precipitates and a decrease in their size leads to an increase in the volume fractions of the Cube texture component and to a decrease in the volume fractions of the β fiber components. Thus, the retarding effect of the small precipitates on the texture evolution is related to the amount and size of these precipitates [80].

The influence of amount, size and coherency of precipitates on the development of rolling texture in AA8090 (Al-Li alloy) has been investigated by Engler et al. [81]. It has been found that, in homogeneous supersaturated material, the deformation proceeds homogeneously. However, in peak-aged microstructures where there is a large amount of fine and coherent δ' precipitates, precipitates can be cut by dislocations, leading thus to slip localization and subsequent extensive shear band formation. A weakening of the rolling texture occurs due to the non-crystallographic deformation induced by shear bands. In overaged state where the precipitates are larger in size and semicoherent or incoherent, precipitates cannot be cut by dislocations. The dislocation movement is restricted therefore to the small interparticle spaces, which impedes planar slip and causes a homogenization of deformation. The strength of the rolling texture is thus similar to that in the supersaturated material [81].

Adam [30] studied the effect of stable large and small second-phase particles on the recrystallized microstructure of a hot rolled AA7050. It was found that recrystallization occurs by PSN at large particles located along the grain boundaries. Particle free zones (PFZ) exist at the vicinity of constituent large particles and coincide hence with the localized deformation zones around particles. The dislocations present in the PFZ can easily recover and form subgrains. The subgrains with at least partial high-angle grain boundaries may act as nuclei

during recrystallization. The growth of recrystallized grains in a longitudinal pattern is due to the overlapping of particle deformation zones. This explains what can be seen on figure 2.1.

2.5.2 Influence of unstable second-phase particles

Little work about the effect of unstable particles is found in the literature due to the complexity of the dynamic interactions between precipitates and deformation or recrystallization [10]. The unstable precipitates are formed or dissolved simultaneously with the deformation or after deformation, varying therefore the solute level. All these aspects make the analysis of the interactions between precipitates and deformation or recrystallization quite complex. In the next section, First, the interaction between concurrent precipitation and deformed structure will be reviewed. Second, the interaction between concurrent precipitation and recrystallization will be summarized.

During deformation, many processes can act simultaneously such as:

- acceleration of precipitate nucleation due to the presence of dislocations;
- acceleration of precipitate growth or coarsening due to pipe diffusion and solute transport by dislocation sweeping;
- acceleration of precipitate nucleation, growth or coarsening due to non equilibrium vacancies produced by plastic straining;
- partial or complete dissolution of precipitate due to shearing by dislocations [82].

Due to these complex interactions, the coupling between precipitation and plastic straining was characterized in an Al-Zn-Mg-Cu (AA7449) alloy by Deschamps et al. [82] using in situ small angle X ray scattering measurements during thermomechanical tests at 160°C. It was reported that coarsening of particles is induced dynamically by plastic straining and that the coarsening rate increases linearly with strain and reaches a maximum at the end of the straining stage. Non-equilibrium vacancies that are formed during deformation accelerate the kinetics of solute diffusion. The effect of different initial precipitation states on the deformed microstructure of a commercial 6082 aluminum alloy processed by equal channel angular pressing (ECAP) was also investigated by Gutierrez-Urrutia et al. [83]. Different initial heat treatments were applied to produce different states of solutionized or aged samples. Samples were subsequently processed at room temperature to a maximum of 6 passes, corresponding to a total strain of 4.2. The authors found that coarse precipitates and dispersoids are unaffected by the severe deformation and allow the stabilization of a finer deformation microstructure. On the other hand, very fine precipitates are sheared by the severe deformation and are redissolved in the matrix. They reported also that the extent of recovery depends more on the solute content rather than precipitates since coarse precipitates are present in small volume fraction and widely dispersed [83]. Therefore, depending on different parameters (e.g deformation temperature, strain, strain rate, supersaturation, precipitate morphology and size), precipitates may nucleate, grow, coarsen or dissolve [10, 82]. These evolved precipitates may

affect not only the deformed structure, but also the microstructure evolution right after deformation [10]. The effect of concurrent precipitation on recrystallization during annealing after deformation is reviewed below.

The effect of concurrent precipitation on recrystallization of a cold-rolled 6000 aluminum alloy during annealing at 300°C is investigated by Lillywhite et al. [12]. Three different initial heat treatments were applied on the material before deformation in order to generate three precipitate contents: solution treated and water quenched, solution treated and furnace cooled, and solution treated and pre-aged samples. The fastest recrystallization is observed in the solution treated and furnace cooled sample due to its highest density of coarse β-(Mg_2Si) particles. These coarse particles (i.e. $>$ 1 µm) promote recrystallization by PSN. In both water quenched and pre-aged samples, recrystallization is hindered because of the pinning effects of fine precipitates. In solution treated and water quenched sample, fine β' rods (i.e. $<$ 200 nm) precipitate heterogeneously on the subgrain boundaries during and after deformation, whereas, in the pre-aged sample, fine β' precipitates are sheared during deformation, lose their coherency and transform rapidly into equilibrium β phase, forming a very high density of stable fine β precipitates. In both cases (i.e. water quenched and pre-aged), particle free zones (PFZ), surrounding Al(FeSi) insoluble particles on which β phase nucleates, promote PSN. New grains formed at PFZ by PSN could therefore grow only when the pinning pressure due to pinning precipitates and boundary curvature is lower than the driving pressure due to the stored energy. In water quenched sample, boundary migration rate is found to be controlled by the transformation of metastable β' phase to equilibrium β phase and the subsequent coarsening of equilibrium β phase at the recrystallization front. In pre-aged sample, boundary migration is found to be controlled by coarsening of equilibrium β phase at the recrystallization front. Twinning is finally reported to take place when recrystallization is strongly hindered by a fine particle dispersion due to the lower interfacial energy of twin boundaries, reducing therefore the Smith-Zener pinning [12].

The influence of concurrent precipitation on recrystallization is also analyzed in a cold rolled and annealed Al-Mn-Fe-Si alloy [84]. In the absence of precipitation (e.g commercially pure aluminum), all nucleation sites including grain boundaries and constituent particles are activated. Cube and ND-rotated Cube recrystallized grains have a growth advantage compared to P and other oriented grains, leading to a Cube dominant recrystallization texture. However, when precipitation occurs concurrently with precipitation, P and ND-rotated Cube become the dominant texture components. The nucleation by PSN at constituent particles is less affected by concurrent precipitation than nucleation at grain boundaries. Additionally, P and ND-rotated Cube oriented nuclei have a growth advantage due to a 40°$\{111\}$ misorientation with the surrounding deformed matrix. This leads to a strong P and ND-rotated Cube recrystallization texture. Finally, the effect of Mn additions on recrystallization resistance of 6082 aluminum alloys is investigated in [85]. The microstructure evolution during annealing at 500°C after hot

deformation is studied. A large amount of dispersoids is introduced due to the Mn additions, which retards recrystallization and abnormal grain growth during post-deformation annealing. During annealing at 500°C for 4 hours, gradual coarsening and dissolution of dispersoids occur in the dispersoid rich zones, while, dispersoid free zones (DFZ) remain unchanged. Static recrystallization takes place in the dispersoid free zones and the recrystallization resistance is mainly controlled by the dispersoid free zones fraction. An increase in the DFZ fraction leads to an increase in the recrystallization fraction [85]. Therefore, the interaction between concurrent precipitation and microstructure evolution during annealing after deformation is quite complex and depends on many parameters such as the deformed structure, supersaturation, annealing temperature and time and initial precipitate size and morphology.

Experimental procedure and data processing methods

Contents

3.1 Hot compression tests

3.1.1 Experimental setup

Hot plane strain compression tests were conducted using a Servotest thermo-mechanical treatment simulator (TMTS) equipment installed at C-TEC (Constellium Technology Center,

Voreppe). This equipment is capable of simulating complex industrial multi-step thermomechanical process, including different post-deformation annealing times and also to achieve relatively high strain rates $\dot{\epsilon}$. It is composed of:

- a preheat furnace which allows to preheat the sample to the desired test temperature. The maximum temperature that can be reached by the preheat furnace is 1200°C. The temperature is usually set at a temperature higher than the testing temperature in order to reach more rapidly the testing temperature. For example, for a deformation temperature range between 360°C-430°C, the preheat furnace temperature is set at a high temperature (>560°C), allowing to reach the testing temperature in 2-3 minutes;
- a test furnace where the preheated sample is transferred and deformed;
- a manipulator composed of a robot arm allowing the transfer of the sample between the preheat furnace and test furnace;
- a quench tank located in front of the test furnace above which the sample is transferred by the manipulator and water quenched. The time that it takes to transfer the tested sample from the test furnace to above the quench tank is about 2s, leading therefore to a quench delay of about 2s;
- upper and lower tools whose temperatures are controlled separately from the furnace temperature. To limit self heating during testing, the tool temperatures are 10°C lower than the testing temperature.

3.1.2 Specimens prior to hot compression

Figure 3.1 shows a schematic drawing of a hot compression sample. Hot compression specimens of $46\,\mathrm{mm}$ (in the rolling direction RD), $50\,\mathrm{mm}$ (in the transverse direction TD) and $15\,\mathrm{mm}$ (in the normal direction ND) were machined from $\frac{1}{4}$ thickness of an as-cast ingot as mentioned in figure 1.6. Prior to hot compression, the specimens are separated into two batches. One batch is subjected to homogenization followed by a particular subsolvus thermal process aiming at generating a significant precipitation of soluble phases (see figure 3.2 (a)). Another batch is subjected to homogenization followed by a different subsolvus thermal process aiming at generating a less significant precipitation of soluble phases (see figure 3.2 (b)). These two different initial precipitation states will be presented in chapter 4.

Two thermocouples are attached to each sample in order to follow the evolution of the temperature during the whole thermomechanical process as shown by figure 3.1. Both thermocouples are placed at the mid-thickness of the sample. One thermocouple is placed at the central part of the sample to measure the temperature of the deformed part. The other thermocouple is positioned in the non-compressed part. During hot compression, the force, displacement, velocity, temperature and time are measured and stored. An Excel macro that has been developed at C-TEC is used to process the stored parameters and thus to provide stress, strain and strain

rate evolution during testing time.

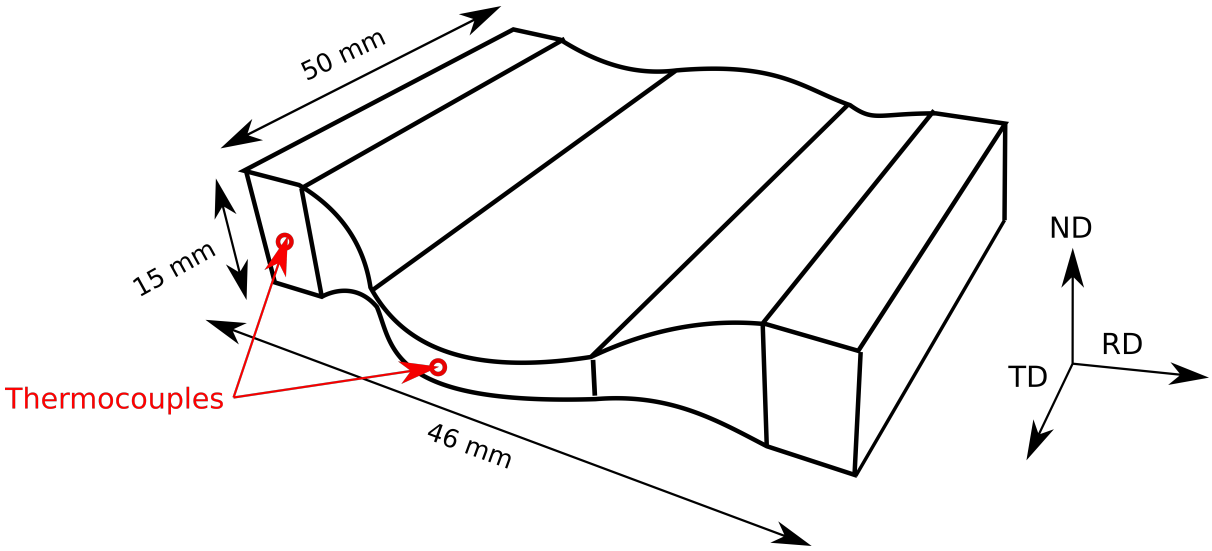

Fig. 3.1 Schematic drawing showing the dimensions of a hot compression sample and the positions of thermocouples attached to the sample to measure the temperature during testing.

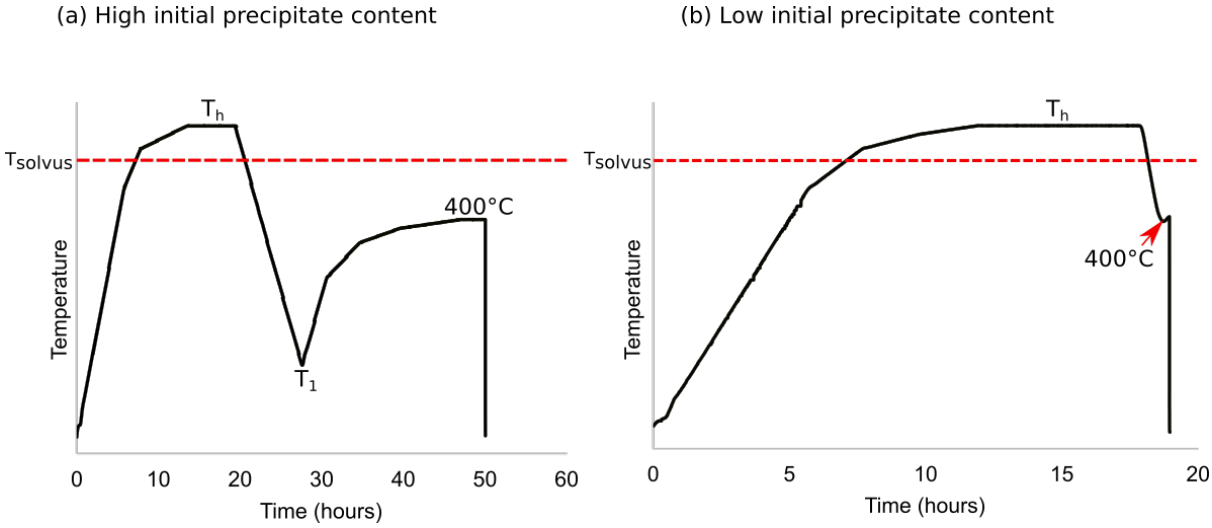

Fig. 3.2 Heat treatments on the specimens prior to hot compression in order to generate two different initial precipitate states. T_{solvus} is the solvus temperature for soluble phases including Mg_2Si, Si and Q phase. T_h is the homogenization temperature.

3.1.3 Thermomechanical paths

The samples were hot compressed according to two different thermomechanical paths as shown by figure 3.3 in order to get different precipitation states to be deformed. The objective of the thermomechanical path illustrated on figure 3.3 (a) is to examine the interaction between precipitates formed prior to deformation and recrystallization, while the objective of thermomechanical path illustrated by figure 3.3 (b) is to study the interaction between elements in solid solution and recrystallization.

One set of samples were subjected to the thermomechanical path illustrated by figure 3.3 (a): (A) the sample is preheated in the preheat furnace (set at 700°C) from the room temperature to the testing temperature (e.g 430°C), (B) the sample is transferred to the test furnace and deformed at the testing temperature and a given strain rate up to a given strain level, (C) after deformation, the sample is taken out immediately from the test furnace and water quenched with the smallest possible quench delay ($\approx$ 2s) to freeze the deformed microstructure. The holding time after deformation is varied from 2s to 1200s depending on the testing temperature to follow the post-dynamic evolution of the microstructure.

Another set of samples were subjected to another thermomechanical path illustrated by figure 3.3 (b): (A) the sample is preheated in the preheat furnace from the room temperature to 560°C and kept for 15 minutes at this temperature for dissolution of precipitates that may form during preheat, (A') the sample is air cooled (air cooling rate is about 0.7°C/s) down to a temperature lower or equal to the deformation temperature depending on the testing conditions (eg. 360°C and 400°C if the deformation is performed at 360°C and 430°C respectively, 400°C was selected in case of a deforming temperature of 430°C in order to get close to the temperature at the slab mid-thickness prior to hot rolling), (B) and (C) are similar to the steps (B) and (C) presented in figure 3.3 (a).

The preheat from the room temperature to the testing temperature during the thermomechanical path illustrated by figure 3.3 (a) may generate additional precipitation. On the other hand, the homogenization step introduced by the thermomechanical path illustrated by figure 3.3 (b) allows to dissolve the soluble precipitates consisting of Mg_2Si, Si and Q phase and therefore to generate a rich solid solution.

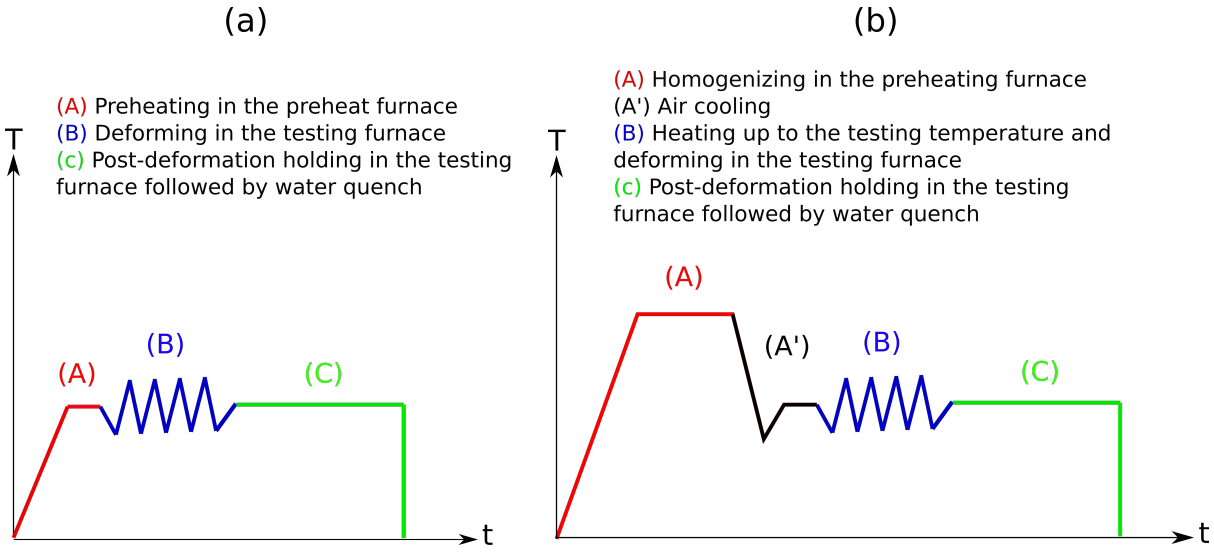

Fig. 3.3 (a,b): Schematic graphs showing the two thermomechanical paths applied to simulate the hot rolling process.

Different deformation temperatures, strain rates, strains and post-deformation holding times are tested to investigate the influence of these parameters on the microstructure evolution. The

temperature, strain rate and strain ranges are 360°C to 430°C, 1 to $100\,s^{-1}$, and 0.5 to 2.4 respectively. The tool width for plane strain compression is 28 mm. The samples are coated with graphite and wrapped in Teflon tape to reduce friction effects during deformation.

3.1.4 Example of temperature evolution during a thermomechanical process

Figure 3.4 (a) shows the actual evolution of the temperature during the thermomechanical path illustrated by figure 3.3 (a) whereas figure 3.4 (b) shows a part of the actual evolution of temperature during the thermomecanical path illustrated by figure 3.3 (b). The first steps of homogenization and beginning of air cooling are not shown by figure 3.4 (b). Both temperatures measured at the central part (blue lines) and non compressed part (red lines) of the hot compressed specimen are shown by figures 3.4 (a) and (b). In both figures 3.4 (a) and (b), the nominal deformation temperature is 430°C while the nominal strain rate and strain are $3\,s^{-1}$ and 2.4 respectively. It is clear that the temperature at the deformed zone (i.e. central part of the sample) increases to 450°C from the nominal temperature of 430°C due to self-heating associated with plastic deformation (which cannot be avoided when the strain rates are higher than about $0.1\,s^{-1}$ [86]).

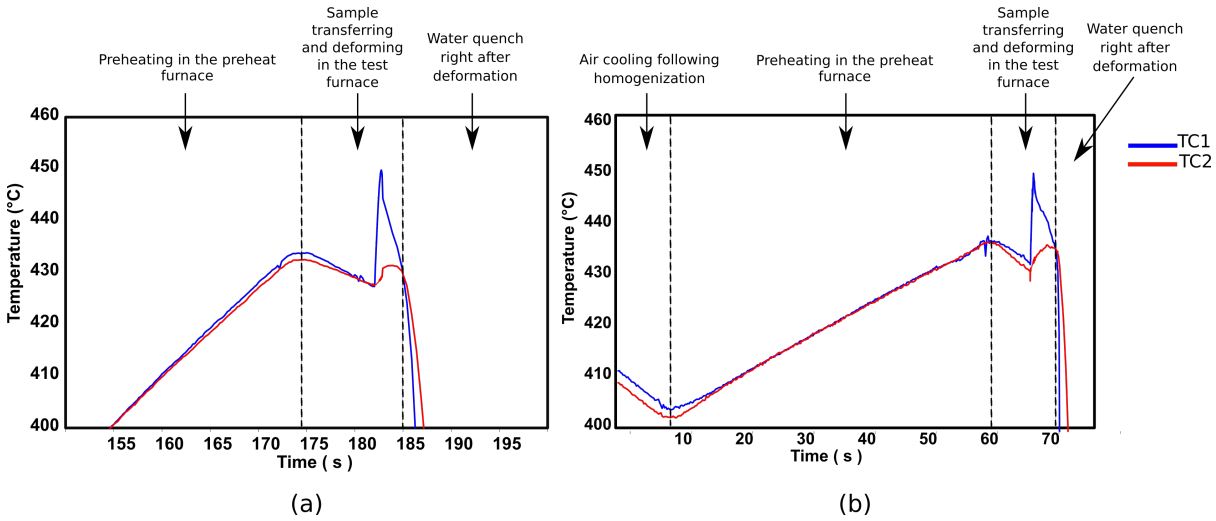

Fig. 3.4 (a,b) Actual evolution of the temperature during the thermomechanical paths shown by figure 3.3 (a) and (b) respectively. In (b), the first steps corresponding to homogenization and beginning of air cooling are not shown. In (a) and (b), the nominal deformation temperature is 430°C, the nominal strain rate is $3\,s^{-1}$ and the applied strain is 2.4 (performed in a single pass). TC1 is the actual temperature measured at the central part of the hot compression specimen while TC2 is the actual temperature measured at the non-compressed part of the hot compression specimen.

3.2 Microstructure characterization

3.2.1 Sampling zone

In order to characterize the evolved microstructure and precipitation after hot compression, the hot compression samples are cut according to figure 3.5. Sections cut along the RD-ND plane are subsequently polished. The preparation method depending on the type of the required analysis will be presented below.

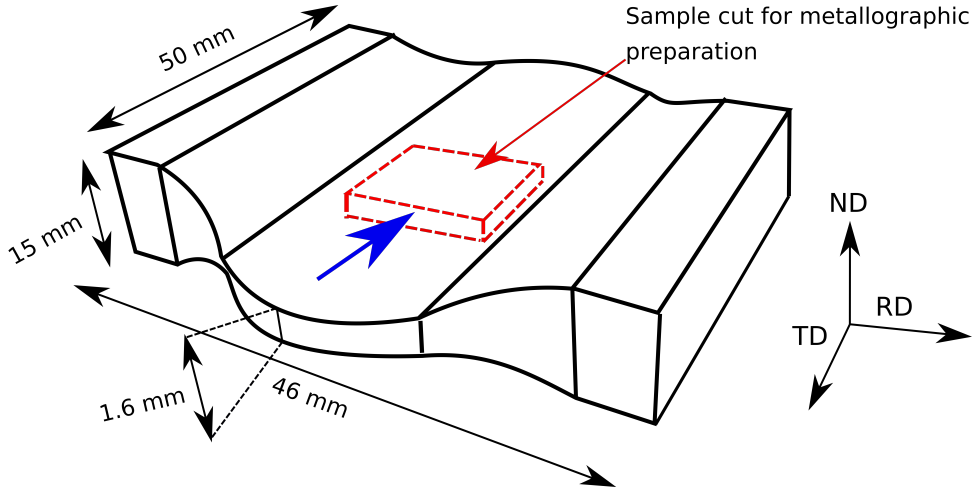

Fig. 3.5 Schematic drawing showing where hot compression samples for precipitation and EBSD characterization are cut.

3.2.2 Precipitation analysis

Semi-quantitative and quantitative analyses of precipitates evolution during recrystallization are performed using SEM in order to study the interaction between precipitates and recrystallized grains.

3.2.2.1 Semi-quantitative analysis

For semi-quantitative analysis, the samples are sequentially ground with P320, P600, P1200 SiC papers and polished with 6 µm, 3 µm and 1 µm diamond suspensions. Samples are finally electropolished in 30% nitric acid in methanol. Individual SEM SE images at different magnifications are acquired.

Additionally, for deformed samples, a larger area of 440 µm (RD) x 330 µm (ND) at mid-thickness is analyzed by acquiring automatically multiple SEM SE images and stitching them together by using SmartStitch software as shown by figures 3.6 (a) and (b). Figure 3.6 (a) shows an example of a SEM SE image composed of 121 stitched SEM SE images taken on a sample that has been heat treated according to figure 3.5 (a) prior to hot compression (i.e. to generate a high initial precipitate content) and that has been subsequently deformed at 430°C, $3\,s^{-1}$ and a strain of 2.4 and water quenched. A single SEM SE image acquired among the 121 stitched SEM SE images is shown by figure 3.6 (b). Such SEM SE image shows soluble phases including Mg_2Si, Si and Q precipitates as well as Fe containing particles popping out of the

sample surface thanks to the electropolishing. Unfortunately, dispersoids are not revealed with this preparation method.

For non-deformed samples, a larger total area of 1200 µm (RD) x 900 µm (ND) at mid-thickness is analyzed in order to obtain more representative statistics (consistently with the larger size of initial grains ($>$ 100 µm) prior to deformation) as can be seen on figure 3.6 (c). For this purpose, 900 SEM SE images of 40 µm (RD) x 30 µm (ND) each (see figure 3.6 (d)) are acquired automatically and stitched.

The stitched SEM SE images are subsequently processed using the ImageJ software in order to quantify soluble phases. The analysis of soluble phases using this method is referred to as semi-quantitative because Mg_2Si, Si, Q phase precipitates and Fe rich intermetallic particles are popping out of the prepared sample's surface. The area fraction and size of precipitates are therefore overestimated.

In ImageJ, for the detection of second-phase particles, the stitched SEM SE image is converted from RGB to 8-bit grayscale and both contrast and brightness of the image are adjusted. A threshold is set manually in order to separate particles from matrix. A binary image showing particles in black and matrix in white is generated and analyzed afterwards. The area and equivalent circle diameter of each detected particle is determined using the function $Analyze\ Particles$ of ImageJ. The results are therefore very sensitive to the choice of threshold, which can alter the interpretation of the data. The equivalent diameter of the smallest detected particle with ImageJ is 0.05 μm.

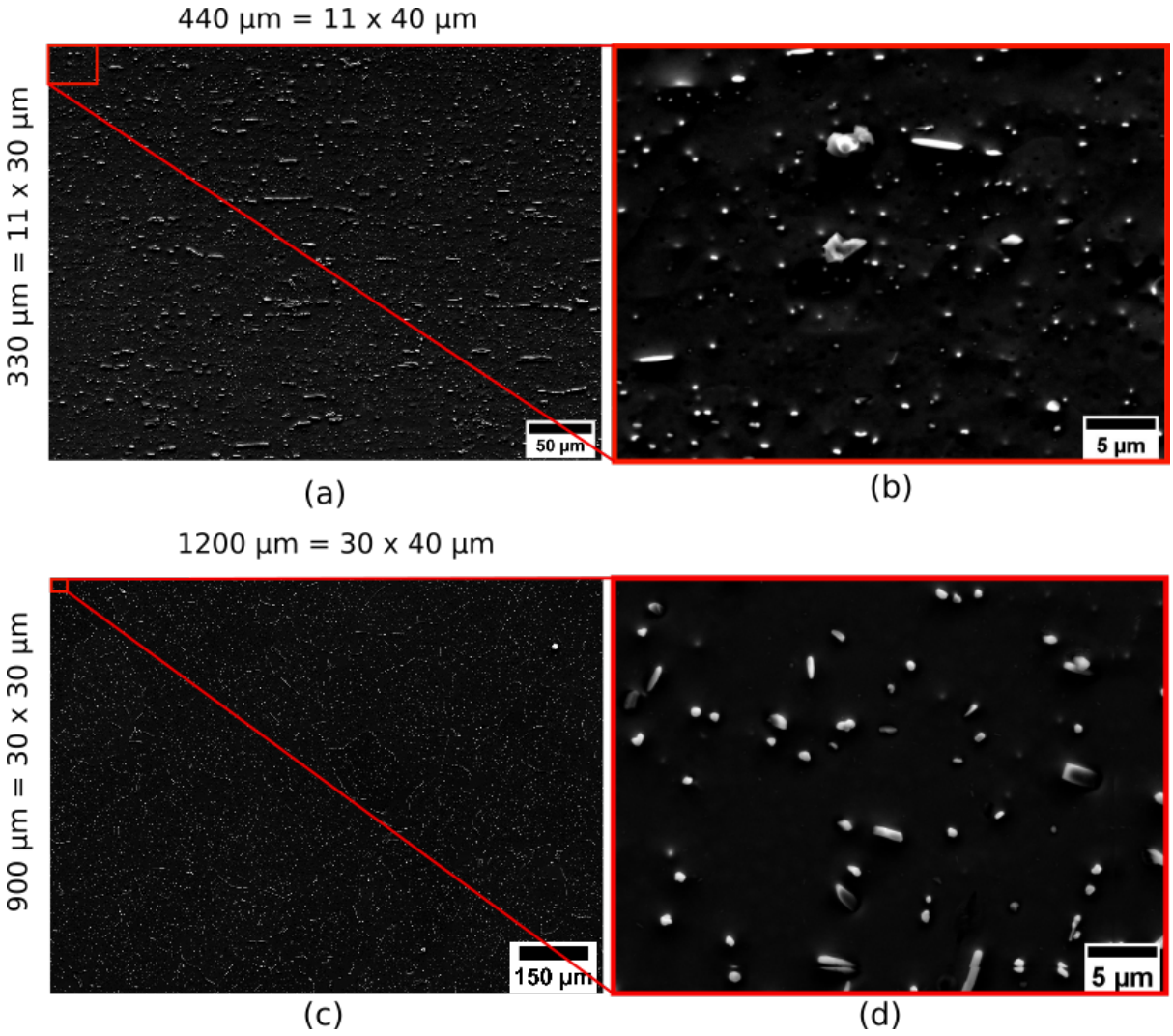

Fig. 3.6 (a) SEM SE images stitched for analysis of soluble phases in a deformed sample, (b) An individual SEM SE image among the stitched images shown in (a), (c) SEM SE images stitched for analysis of soluble phases in a non deformed sample, (d) An individual SEM SE image among the stitched images shown in (c). The size of a pixel in the images shown in (a-d) is 0.039 μm x 0.039 μm.

3.2.2.2 Quantitative analysis

For quantitative analysis, the samples are mechanically polished using a following specific internal procedure, and then ion milled by argon-ion beam using the Gatan Ilion II device. Afterward, SEM in lens SE and BSE images of 40 µm (RD) x 30 µm (ND) each (see figure 3.7) are acquired using SmartStitch software, allowing automatic acquisition and stitching of multiple images. A total area of 1600 µm (RD) x 600 µm (ND) is analyzed to obtain representative statistics. The size of a pixel in the stitched SEM in lens SE and BSE images is 0.039 μm x 0.039 μm. The advantage of such a method is that it distinguishes clearly between the different types of precipitates and the matrix and therefore quantifies with more accuracy the mean size and area fraction of particles as a whole.

The stitched SE and BSE images are subsequently processed using MATLAB R2018a.

More specifically, for quantification of Mg_2Si and Si particles, the stitched in-lens SE image was analyzed as shown in figure 3.8 (a). Mg_2Si and Si particles appear gray and black in the stitched in-lens SE image, respectively. For quantification of dispersoids and Fe containing particles, the stitched BSE image was analyzed as shown in figure 3.8 (b). Both fine dispersoids and large Fe containing particles appear white in the stitched BSE image. The stitched BSE image was chosen instead of the stitched in-lens SE image for determination of dispersoids and Fe containing particles because of the better contrast between these particles and the dark background. For processing both stitched in-lens SE and BSE images, the contrast was adjusted and the noise was reduced by adding a salt and pepper noise followed by a median filter (i.e. replacing each pixel by the median value of a 3 by 3 neighborhood around the corresponding pixel). The particles were subsequently identified based on their gray level as can be seen in figure 3.8. The particle size was determined as the equivalent circle diameter. The equivalent diameter of the smallest detected particle is 0.06 μm. The area fraction of all particles without any distinction was calculated by adding their areas and dividing by the total analyzed area.

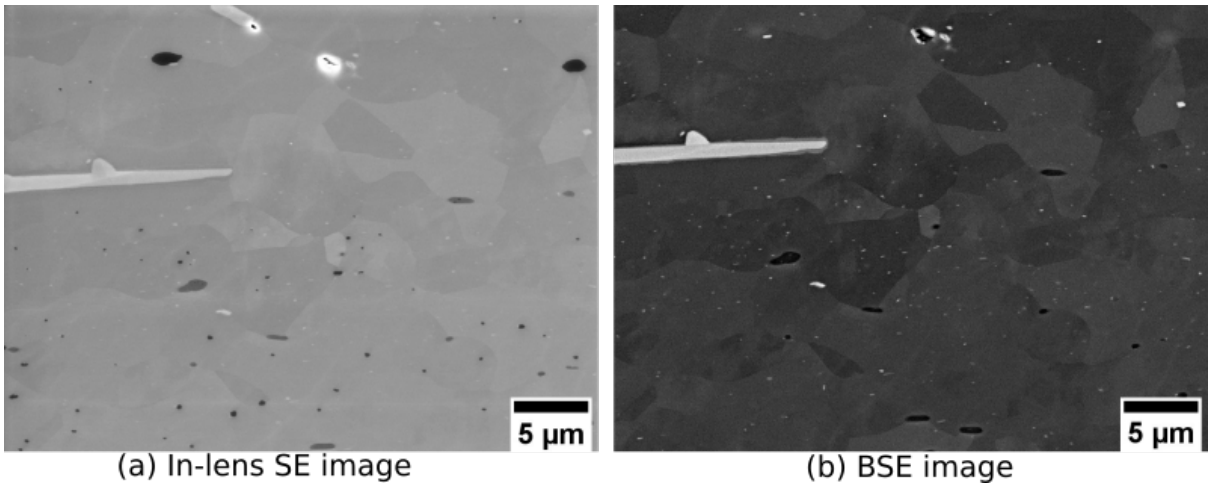

Fig. 3.7 (a) SEM in lens SE image among the stitched SEM in lens SE images, (b) Corresponding BSE image.

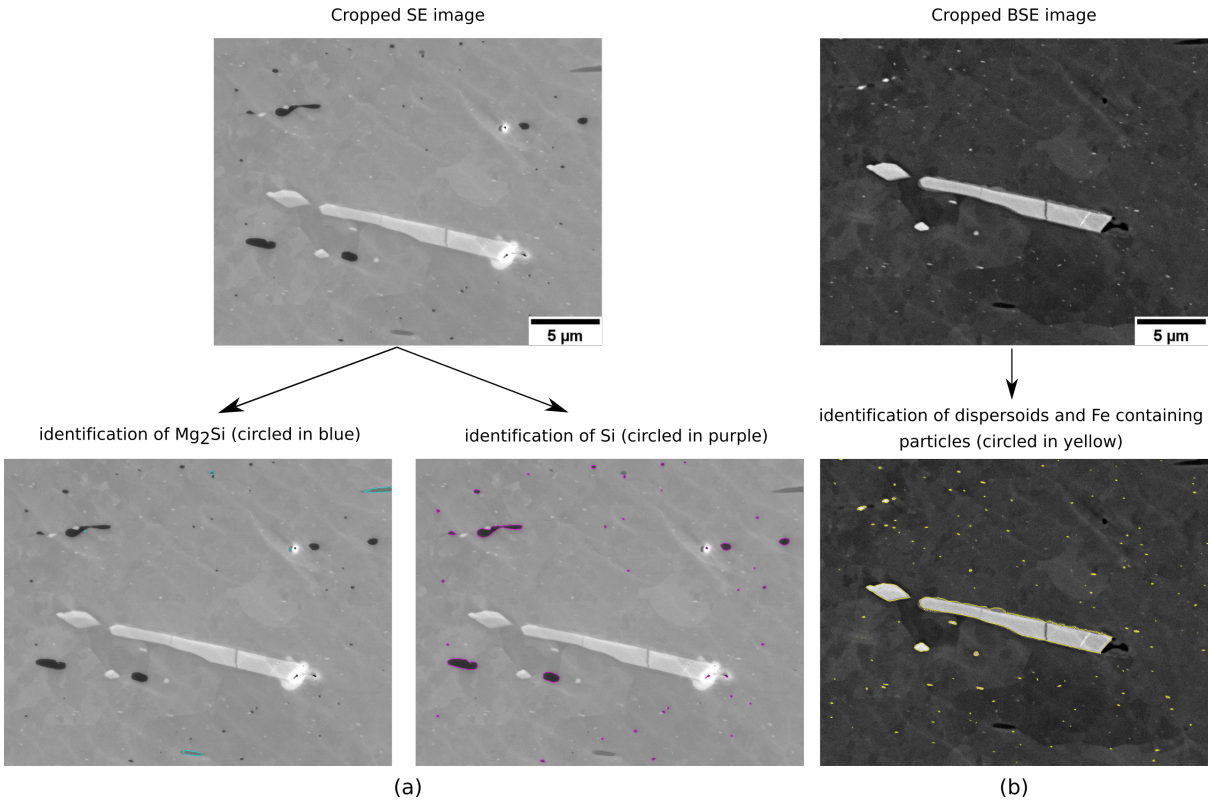

Fig. 3.8 Identification of precipitates for quantification: (a) a cropped area from the stitched in lens SE image showing how Mg_2Si and Si phases are identified and (b) the same cropped area from stitched BSE image showing how fine dispersoids and large Fe containing particles are identified.

3.2.3 Study of grain evolution during and after deformation

3.2.3.1 Optical microscopy

Samples are sequentially ground with P320, P600, P1200 SiC papers and polished with 6 µm, 3 µm and 1 µm diamond suspensions and 0.05 colloidal silica suspension. Samples are finally anodized using Barker's reagent (2% HBF4) for 60 s at 20 V at room temperature. Optical micrographs are acquired automatically under polarized light to reveal grains in different colors and are subsequently stitched to form a mosaic. This method is a fast way to qualitatively determine whether the microstructure is completely recrystallized or not.

3.2.3.2 Electron BackScatter Diffraction (EBSD)

For EBSD characterization, samples are first ground and polished as for optical microscopy. The samples are then electropolished using the electrolytic solution A2 provided by Struers at $48\,\mathrm{V}$ and at $0\,^{\circ}\mathrm{C}$ for $10\,\mathrm{s}$. A Zeiss Supra40 scanning electron microscope (SEM) was used for running EBSD analyses with a Bruker system. At least five EBSD orientation maps, with a size of 1200 µm (RD) x 800 µm (ND) each and a measurement step size of 3 µm, are taken at the mid thickness of the samples and stitched together to study texture. Higher magnification EBSD orientation maps are also acquired when needed to study recrystallization mechanisms in

details. EBSD analyses have been performed in the RD-ND plane where the elongated shape of deformed grains can be clearly seen. MTEX Toolbox [87] is finally used for EBSD data processing and analysis as detailed in section 3.4.1.

3.3 Sequential annealing using a fast heating stage coupled to SEM

3.3.1 Experimental setup

A 6 mm (RD) x 4.5 mm (TD) sample is cut at mid-thickness of the previously deformed and water quenched hot compression sample, parallel to the RD-TD plane. The sample is polished on both sides to avoid recrystallization to be initiated from the backside. The sample is subsequently mounted and mechanically polished down to a thickness of $300\,\mu\mathrm{m}$. The polishing process includes polishing using diamond suspensions followed by vibratory polishing in a 0.05 µm colloidal silica suspension for 3 hours to achieve an excellent surface quality required for EBSD measurements. Electropolishing is avoided for preparing this sample because it reveals precipitates on top of the prepared surface, causing therefore, a lower Smith-Zener pinning force for migrating boundaries intersecting the sample surface, compared to the case where the sample surface is flat and the precipitates are at the same level as the matrix.

A fast heating stage is mounted inside the chamber attached to that of a Tescan FERA3 FIB-SEM equipped with EBSD. The working principle of the heating stage is described in [88, 89] for more details. The sample surface is point-welded on the heating device, consisting of a thin tantalum foil and temperature measured with two thermocouples welded on the top surface of the sample, as shown in figure 3.9 (a). The tantalum foil is heated by Joule effect. The small dimensions of both tantalum foil and sample ensure low thermal inertia and therefore allow high heating and cooling rates ($\approx 100°\mathrm{C/s}$). The observed zone is chosen at a certain distance from the welding points to avoid the impact of welding on the microstructure.

A series of nine successive thermal cycles with intermediate EBSD measurements are performed, as shown in figure 3.9 (b). After each annealing step, EBSD orientation maps with a step size of 3 µm are acquired next to each other and stitched together to cover a wide total area of 4 mm (RD) x 2 mm (TD). Such large analyzed area allows to follow the growth of a significant number of recrystallized grains (i.e. 494 recrystallized grains analyzed at the final step of sequential annealing).

The advantage of the sequential annealing coupled to EBSD is the possibility of keeping the same area of observation and therefore following the evolution of individual overgrown grains in time. However, it is important to keep in mind that results may be influenced by artifacts due to free surface effects.

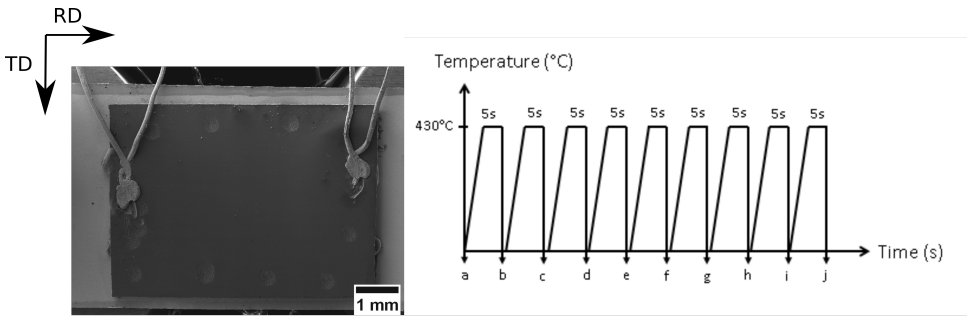

Fig. 3.9 (a) Thermocouples welded on the sample intended for sequential annealing, (b) Schematic representation of the sequential annealing applied using the fast heating stage coupled to SEM.

3.3.2 Possible artifacts due to surface effects

The presence of a free surface during sequential annealing coupled to a fast heating stage in the SEM chamber may result in a recrystallization behavior different than that occurring in bulk samples. The free surface may induce the following artifacts:

- Temperature gradients could be generated through the sample thickness leading to a lower temperature at the surface than in the interior [90].
- The migration of boundaries intersecting the free surface may be affected by the high energy of the free surface as mentioned in section 2.3.1. Indeed, the grains with low surface energy will tend to grow abnormally to lower the free surface energy [90].
- Due to the high energy of the free surface, boundaries intersecting the surface tend to become perpendicular to the free surface, and they tend to groove in order to reach an energetic equilibrium between the grain boundary and free surface tensions. Thermal grooving may therefore pin the movement of grain boundaries on the surface [89, 90].

A comparison of the kinetics of recrystallization during sequential annealing using a fast heating stage and during post-deformation annealing in the hot compression test furnace is thus required in order to determine whether the EBSD observations made on the sequentially annealed surface are representative of the bulk recrystallization process [90].

3.3.3 Evolution of actual temperature during sequential annealing

Figure 3.10 shows an example of the evolution of a real measured temperature during a sequential annealing step. As mentioned in section 3.3.1, two thermocouples are welded on the sample surface in order to measure the output temperature. It is clear from figure 3.10 that the two measured temperatures are very similar (see red and green curves which are so close to each other than they appear as one single curve). The output temperatures are also very close to the input one, especially, during the heating and holding stages.

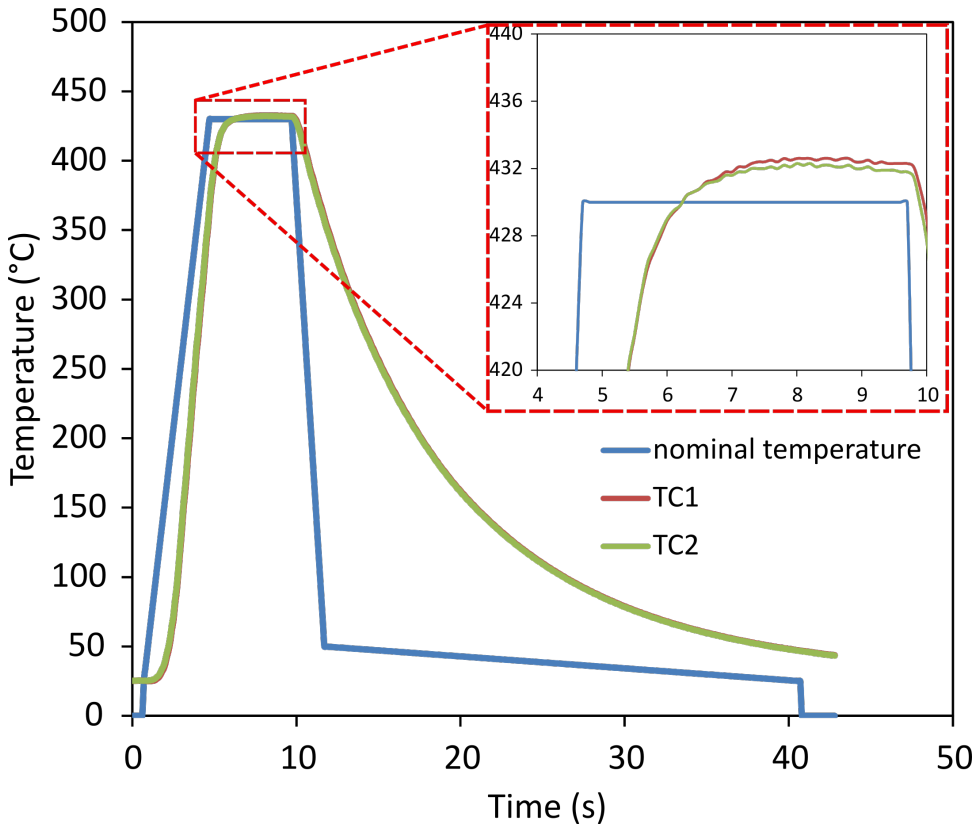

Fig. 3.10 An example of a real measured temperature during a sequential annealing step. The nominal input temperature is given by the blue curve. The ouput temperatures measured by the two thermocouples welded on the sample surface (i.e. named by TC1 and TC2) are given by the red and green curves respectively. A zoom of the three curves is shown on the top right corner.

3.4 EBSD data analysis

3.4.1 Determination of recrystallized grains

The raw EBSD data sets were at first filtered using the local linear adaptation of smoothing splines (LLASS) filter [91], which is implemented within the MTEX toolbox [87]. This filter allows decreasing the orientation noise and improving the angular resolution of intragranular misorientations [91, 92].

Individual grains were identified from the EBSD data as having a minimum size of 12 pixels (i.e. a minimum equivalent circle diameter of 12 µm when using a step size of 3 µm, 4 µm with a step size of 1 µm and 1.5 µm with a step size of 0.4 µm). Throughout this work, the pixels assigned to the same grain have a point to point misorientation lower than 10°.

The grain average misorientation (GAM), defined as the average of the misorientation angle between each pair of neighboring pixels within a grain, is used in order to separate recrystallized grains from deformed ones. First, for the determination of the GAM value of each grain, the Kernel average misorientation (KAM) of each pixel in the grain is calculated and the av-

erage of all these calculated KAM values gives the GAM value of the considered grain. A threshold and a kernel size are required for the calculation of KAM values. In this case, the threshold is set to 10° to exclude grain boundaries from contributing to the KAM calculation and a 2^{nd} order kernel is used (i.e. both first and second nearest neighbors are considered). Second, the threshold value of GAM used to distinguish between recrystallized and deformed grains is adjusted according to the EBSD measurement step. Here, for a measurement step size of 0.4 µm, a GAM value lower than 0.4° was considered in order to determine recrystallized grains. For a measurement step size of 1 µm, a GAM value lower than 0.8° was considered. And finally, for a measurement step size of 3 µm, a GAM value lower than 1.2° was considered. The grain size is determined as the equivalent circle diameter (i.e., the diameter of a disk having the same area as the grain). The average grain size is therefore the arithmetic average value of equivalent circle diameters calculated for all the considered grains.

3.4.2 Determination of texture of recrystallized grains

The area fractions of recrystallized grains belonging to the typical texture components (mentioned by table 2.2) are calculated at different holding times after deformation based on EBSD data. A grain is classified as belonging to a specific texture component if its orientation is within a 10° deviation disregarding the rotation axis from the ideal texture component. The area fraction of a texture component within the recrystallized grains is calculated as the area of grains belonging to a specific texture component divided by the area of all recrystallized grains. The same approach is followed for the calculation of area fractions of deformed grains belonging to the main texture components.

3.5 Estimation of driving pressures acting on grain boundaries

At the mesoscopic scale, the grain boundary velocity (V) is generally assumed to be well approximated by the equation $V = MP$ with M the grain boundary mobility and P the net driving pressure. A higher boundary migration rate can be then related either to a higher mobility (M) or to a higher net driving pressure (P). A brief description of how to roughly estimate the net driving pressure is summarized below. The net driving pressure P in the early stage of recrystallization can be expressed as follows [8]:

$$P = P_{SE} + P_Z + P_C \tag{3.1}$$

where P_{SE} is the driving pressure due to stored energy, P_Z is the Smith-Zener pinning pressure due to second-phase particles and P_C is the capillarity pressure due to boundary curvature.

Grain growth is a 3D phenomenon. However, the grain size distribution is determined from a 2D EBSD map. Similarly, the second-phase particle distribution is determined from

2D SEM micrographs. Saltykov method [93] is thus used in order to convert statistically these distributions from 2D to 3D.

The driving pressure due to the difference in stored energy between a grain g_i and a grain g_j can be expressed using the following formula [8]:

$$P_{SE} = E_j - E_i \text{ with } E_{i,j} = 0.5\,\rho_{i,j}\,G\,b^2 \tag{3.2}$$

where $E_{i,j}$ is the averaged stored energy of grain $g_{i,j}$ (per unit volume), $\rho_{i,j}$ is the average total dislocation density in grain $g_{i,j}$, b is the norm of Burgers vector (= 0.286 nm for pure aluminum [8]) and G is the shear modulus (estimated here as 26.1 GPa [76])

Assuming that the statistically stored dislocations (SSD) are negligible compared to geometrically necessary dislocations (GND), $\rho_{i,j}$ can be approximated as the GND density ($\rho_{GND_{i,j}}$), which in turn can be approximated from intergranular misorientation by using the following expression [94]:

$$\rho_{i,j} = \rho_{GND_{i,j}} = \frac{K\,\theta_{i,j}}{b\,x} \tag{3.3}$$

where K is a parameter depending on the assumed type of dislocation structures (= 3 in case of parallel edge dislocations according to [94]), $\theta_{i,j}$ is the misorientation angle between two pixels separated by a distance x and x is the distance over which the misorientation angle is calculated.

By taking into account equations 3.2 and 3.3, the driving pressure due to the difference in stored energy between grain g_i and grain g_j can be approximated as follows:

$$\begin{aligned} P_{SE} &= 0.5\,(\,\rho_{GND_j} - \rho_{GND_i}\,)\,G\,b^2 \\ &= 0.5\,\frac{K\,(\,\theta_j - \theta_i\,)\,G\,b}{x} \\ &= \frac{3\,(\,\theta_j - \theta_i\,)\,G\,b}{2\,x} \end{aligned} \tag{3.4}$$

In the present study, the driving pressure for the migration of recrystallized grain boundaries is estimated in order to determine whether stored energy contributes to the overgrowth of recrystallized grains. For this purpose, the difference in stored energy between each recrystallized grain and its neighborhood is calculated as follows:

$$P_{SE} = \frac{3\,(\,\theta_{neighbor} - \theta_{rex}\,)\,G\,b}{2\,x} \tag{3.5}$$

The GAM, equivalent to the average of KAM values in a grain and already introduced in section 3.4.1, is chosen in order to estimate the average θ_{rex} value at the recrystallized grain scale (see figure 3.11 (a)). However, because of the strong heterogeneity of the strain field at the intra- and intergranular scales (see figure 3.11 (b)), the neighborhood of each recrystallized grain is set to a three pixels width for the estimation of $\theta_{neighbor}$ as can be

shown in figure 3.11 (a). The average of the KAM values of all the pixels included in the neighborhood ($\overline{KAM}_{neighborhood}$) is calculated. $\theta_{neighbor} - \theta_{rex}$ can therefore be replaced by $\overline{KAM}_{neighborhood} - GAM_{rex}$ in equation 3.5. In this case, a threshold of 10° and a 1^{st} order kernel where only the first neighbors are considered are used to calculate KAM values and therefore $\overline{KAM}_{neighborhood}$ and GAM_{rex}. Finally, the x value in equation 3.5 must be taken as equal to the EBSD measurement step size.

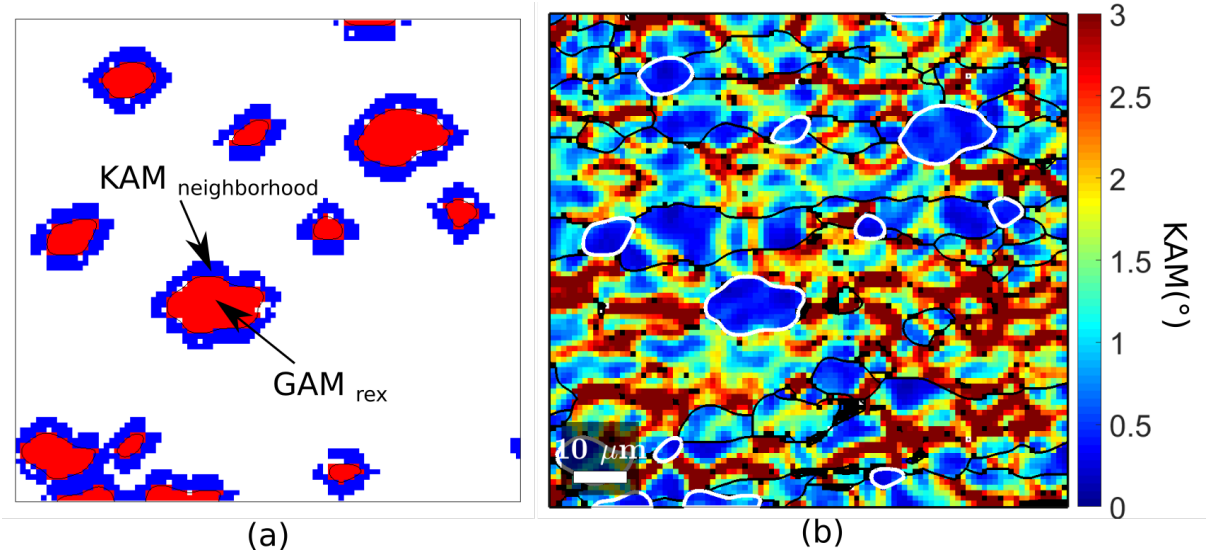

Fig. 3.11 (a) Schematic image showing the 3 pixel thick deformed neighborhood (blue) around each recrystallized grain (red), as considered for estimating the local driving force associated with stored energy. (b) Corresponding KAM map showing recrystallized grain boundaries in white lines and deformed grain boundaries in black lines.

The Smith-Zener pinning pressure can be approximated by the following expression [8]:

$$P_Z = \frac{-3\,\gamma\,f_{3D}}{d_{3D}} \tag{3.6}$$

where f_{3D} is the precipitate volume fraction (equal to the area fraction f_{2D}), d_{3D} is the precipitate average equivalent diameter (extrapolated from d_{2D} using the Saltykov method [93]) and γ is the grain boundary energy ($0.324\,\mathrm{J}\,/\mathrm{m}^2$ for pure aluminum [95]).

Finally, the pressure due to the curvature of recrystallized grain boundaries can be estimated by:

$$P_C = \frac{-2\,\gamma}{R_{3D}} \tag{3.7}$$

where R_{3D} is the mean recrystallized grain radius in 3D (extrapolated from R_{2D} using the Saltykov method [93]).

Microstructure evolution during and after hot deformation

Contents

4.1 Initial microstructure prior to hot compression

4.1.1 Semi-quantitative analysis of initial precipitation

Two initial microstructures are investigated in this work as shown by figure 4.1. These initial microstructures have been obtained through the specific heat treatments shown on figure 3.2 with the aim of generating two initial precipitation states. More specifically, the high initial precipitate content is obtained by the thermal path shown by figure 3.2 (a) while the low initial precipitate content is obtained by the thermal path shown by figure 3.2 (b). Since the homogenization step applied during both these two initial heat treatments is the same, the content of Fe rich intermetallic particles and dispersoids is expected to be similar between the two initial

microstructures with low and high precipitate contents. Thus, the only difference between the two initial heat treated samples is the content of soluble phases. The amount of soluble phases such as Mg_2Si, Si particles and Q phase is expected to be higher in the material with high initial precipitate content than in that with low initial precipitate content. This will be verified qualitatively in this section.

The SEM SE images have been acquired on initially heat treated samples that have been prepared according to the method described by section 3.2.2.1. This preparation method allows soluble phases and Fe rich intermetallic particles to pop out of the sample surface, while dispersoids are on the same level as the matrix. Since the only difference between the two initial heat treated samples is the content of soluble phases, it is appropriate to use such a preparation method in the first instance in order to qualitatively compare the two initial precipitate contents in terms of number, size and morphology of soluble phase precipitates.

Figures 4.1 (a) and (b) show qualitatively that the number of intragranular soluble phases is indeed higher in the so called high initial precipitate content material than in the low initial precipitate content material. This is confirmed by the semi-quantitative analysis shown by figure 4.1 (c). The particle size distribution clearly shows that the number of soluble phases (having an equivalent diameter lower than 1 µm) per unit area is higher for the high initial precipitate content than for the low initial precipitate content.

The morphology of intragranular soluble phases seems to be different between the two initial microstructures. From magnified SEM SE images, intragranular soluble phases appear to be more globular in the high initial precipitate content state that in the low initial precipitate content one. This implies the existence of different types of intragranular soluble phases between the two initial precipitate contents, which will be discussed quantitatively in section 4.1.2.

The low magnification SEM SE images show also that large and elongated particles are decorating grain boundaries. Based on their shape and size, these particles may only be Fe rich intermetallic particles.

Finally, it is evident from the zooms around Fe rich intermetallic particles (shown at the top left and top right corners of figures 4.1 (a) and (b) respectively) that depletion zones exist around Fe rich intermetallic particles and hence around grain boundaries. This depletion zone is larger in the case of the low initial precipitate content microstructure than in the case of the high initial precipitate content one.

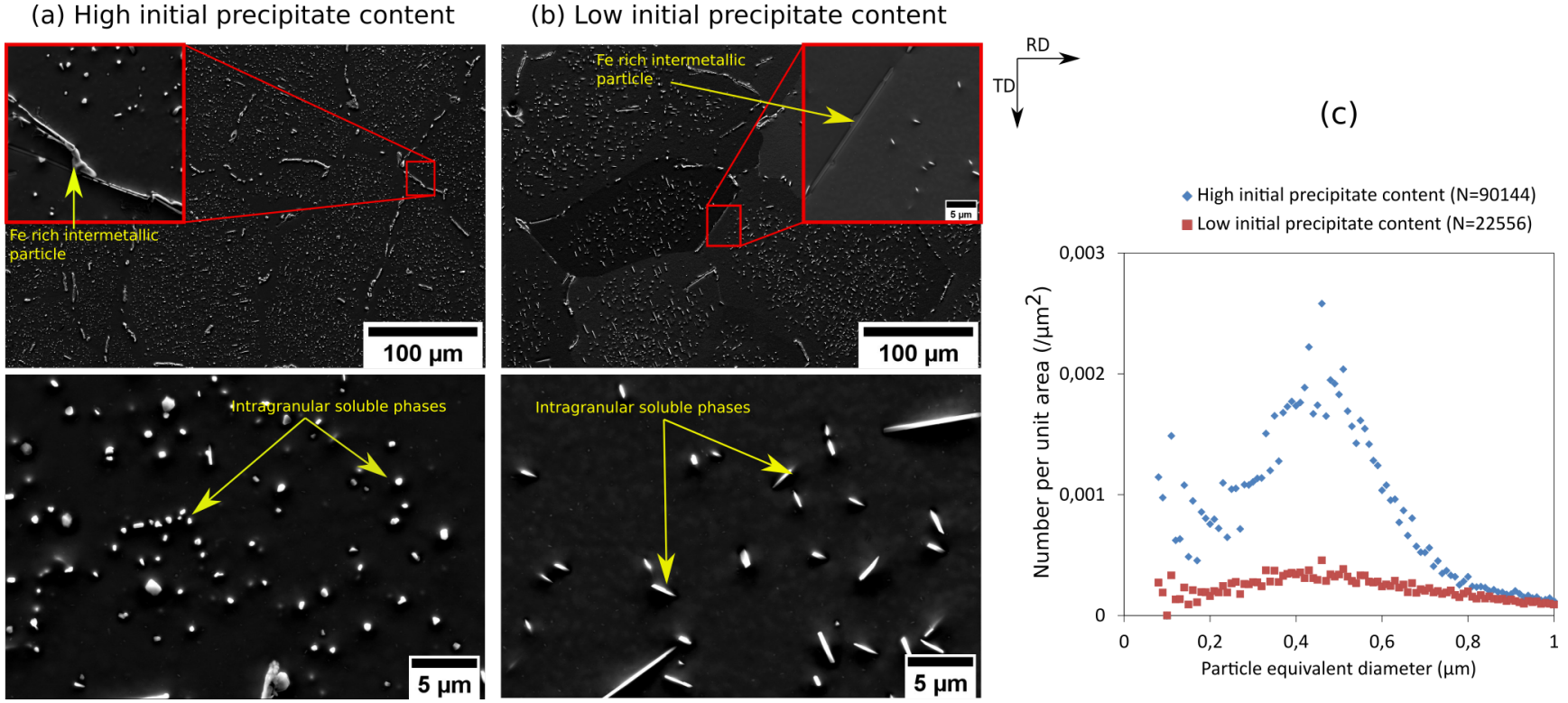

Fig. 4.1 (a,b) SEM SE images showing high and low initial precipitate contents respectively. The samples have been electropolished using 30% nitric acid in methanol (see section 3.2.2.1). Only soluble phases and Fe containing particles are revealed in these images owing to the preparation method. (c) Particle size distribution considering only soluble phases (having an equivalent diameter lower than 1 µm). N indicates the number of analyzed particles in each sample.

4.1.2 Identification of the initial precipitate types

As explained in section 3.2.2.2, the different types of intragranular soluble phases have been identified thanks to the specific preparation method combining mechanical polishing followed by ion milling and acquisition of SEM in-lens SE and BSE images. In these images, precipitates appear under different grey levels depending on their chemical composition (details described by section 3.2.2.2). Energy-dispersive X ray (EDX) analysis in the SEM has also been used in order to confirm the different types of particles observed in these two initial precipitate content states.

Examples of single in-lens SE images taken on high and low initial precipitate contents are shown in figures 4.2 (a) and (c), respectively. BSE images corresponding to these in-lens SE images are shown on figures 4.2 (b) and (d).

The comparison between figures 4.2 (a) and (c) confirms that, in the microstructure with high initial precipitate content, the intragranular soluble phases are more globular and higher in number. Figure 4.2 (a) shows the presence of both Si (i.e. black particles in in-lens SE image) and Mg_2Si (i.e. gray particles in in-lens SE image) particles in the state with high initial precipitate content. The comparison between figures 4.2 (a) and (b) shows that a number of intragranular soluble particles visible on the in-lens SE image do not appear in the corresponding BSE image, confirming the presence of Si particles.

For the low initial precipitate content, it is quite difficult to determine from figure 4.2 (c) whether the intragranular soluble phases are Si and/or Mg_2Si due to their smaller size. Indeed, it is hard to say whether the dark particles that appear on figure 4.2 (c) are gray or black. Higher magnification and therefore better resolution in-lens SE images are required in order to make the distinction between Si and Mg_2Si particles. On the other hand, the comparison between figures 4.2 (c) and (d) shows that most of the dark particles in the in-lens SE image (see figure 4.2 (c)) do not appear in the corresponding BSE image (see figure 4.2 (d)). This confirms that these dark particles are mostly Si particles rather than Mg_2Si particles. Some of these dark particles in the in-lens SE image (shown by figure 4.2 (c)) appear as dull white particles in the corresponding BSE image (shown by figure 4.2 (d)). The EDX analysis shows qualitatively that these fine needle shaped precipitates are enriched with Al, Mg, Si and Cu, suggesting that these precipitates are Q phase particles.

Higher magnification in-lens SE and BSE images are also taken around an Fe rich intermetallic particle as shown by figures 4.2 (e) and (f). It is clear that the Fe rich intermetallic particle is surrounded a dull white colored layer. The EDX analysis (see figure 4.2 (g)) shows that this layer is enriched with Al, Mg, Si and Cu, suggesting that Q phase may be precipitating on top of Fe rich intermetallic particles during subsolvus cooling following homogenization. The Cu enriched layer appears in light gray color (i.e. similar to the matrix) in the in-lens SE image (see figure 4.2 (e)) unlike the Q phase that is detected in figure 4.2 (c) and that appears in dark gray or black. This difference implies that this Cu enriched layer is another form of Q

phase. Different values of the stoichiometric composition of the Q phase have been reported in the literature [96]. This hypothesis requires additional characterization using Transmission Electron Microscopy (TEM) or Atom Probe Tomography (APT) analyses in order to prove it. It is important to notice also that some Si (black colored in (e)) and Mg_2Si (dark gray colored in (e)) particles are precipitating on top of the Fe rich intermetallic particle.

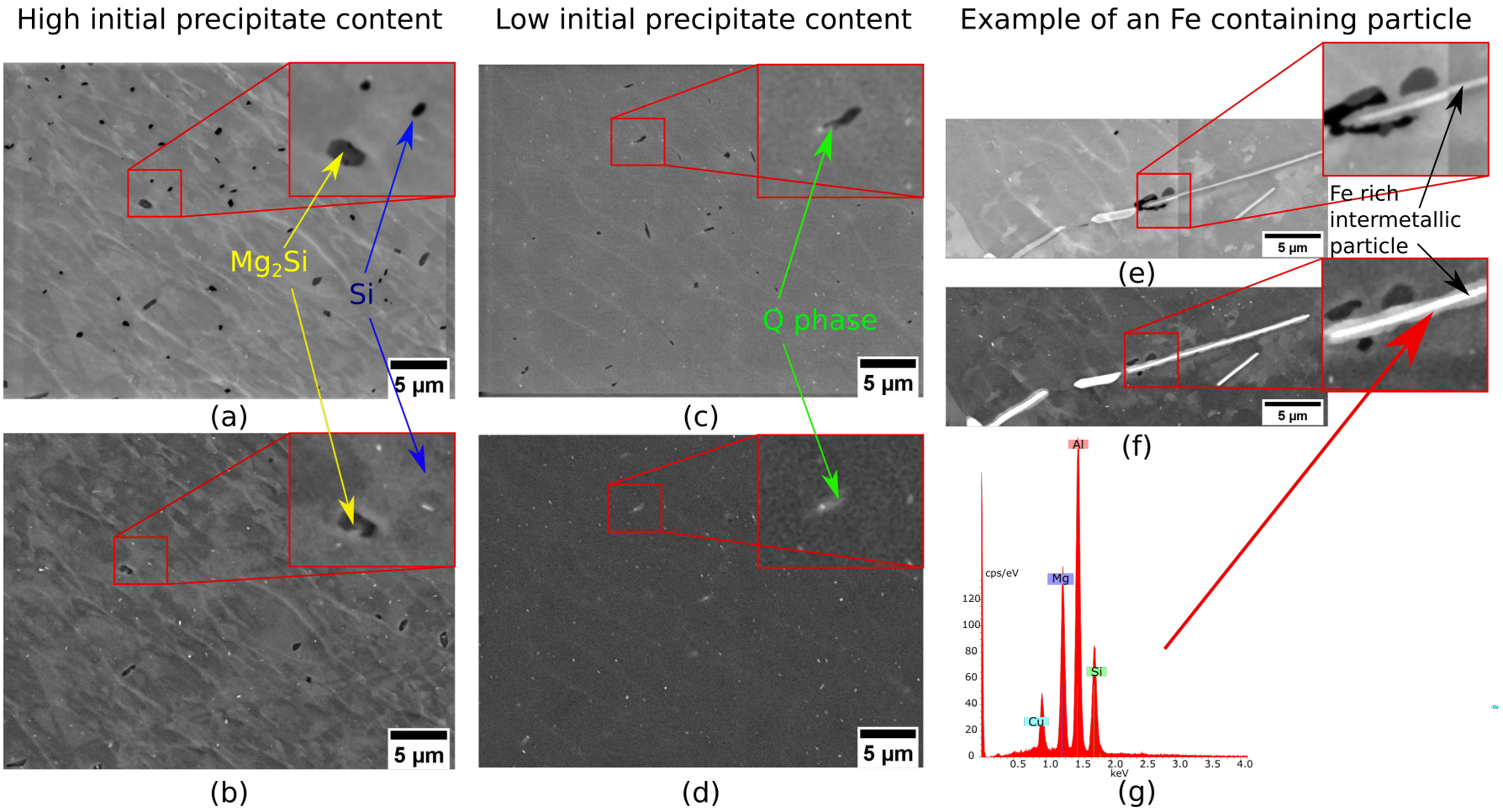

Fig. 4.2 (a) An example of SEM in-lens SE image taken from high initial precipitate content and showing Mg_2Si particles in gray and Si particles in black , (b) SEM BSE image corresponding to (a) showing Mg_2Si particles in black and dispersoids in white, (c) An example of SEM in-lens SE image taken from low initial precipitate content and showing Q phase and Si particles in black, (d) SEM BSE image corresponding to (c) showing Q phase particles and dispersoids in white, (e,f) SEM in-lens SE and BSE images taken around an Fe rich intermetallic particle showing the presence of a Cu enriched layer (dull white colored in (f)) around it as well as large Si and $Mg2Si$ particles precipitating on top of it.

4.1.3 Characterization of initial grain structure

Figure 4.3 illustrates the initial grain structure for the two initial precipitation states. Regardless of the amount of precipitates, the initial microstructures are homogeneous with equiaxed grains. For the high initial precipitate content, the average equivalent diameter is about 135 µm with a standard deviation of 66 µm. For the low initial precipitate content, the average equivalent diameter is about 133 µm with a standard deviation of 64 µm. {111} pole figures of both initial microstructures show that there is no preferential orientation for the initial grains.

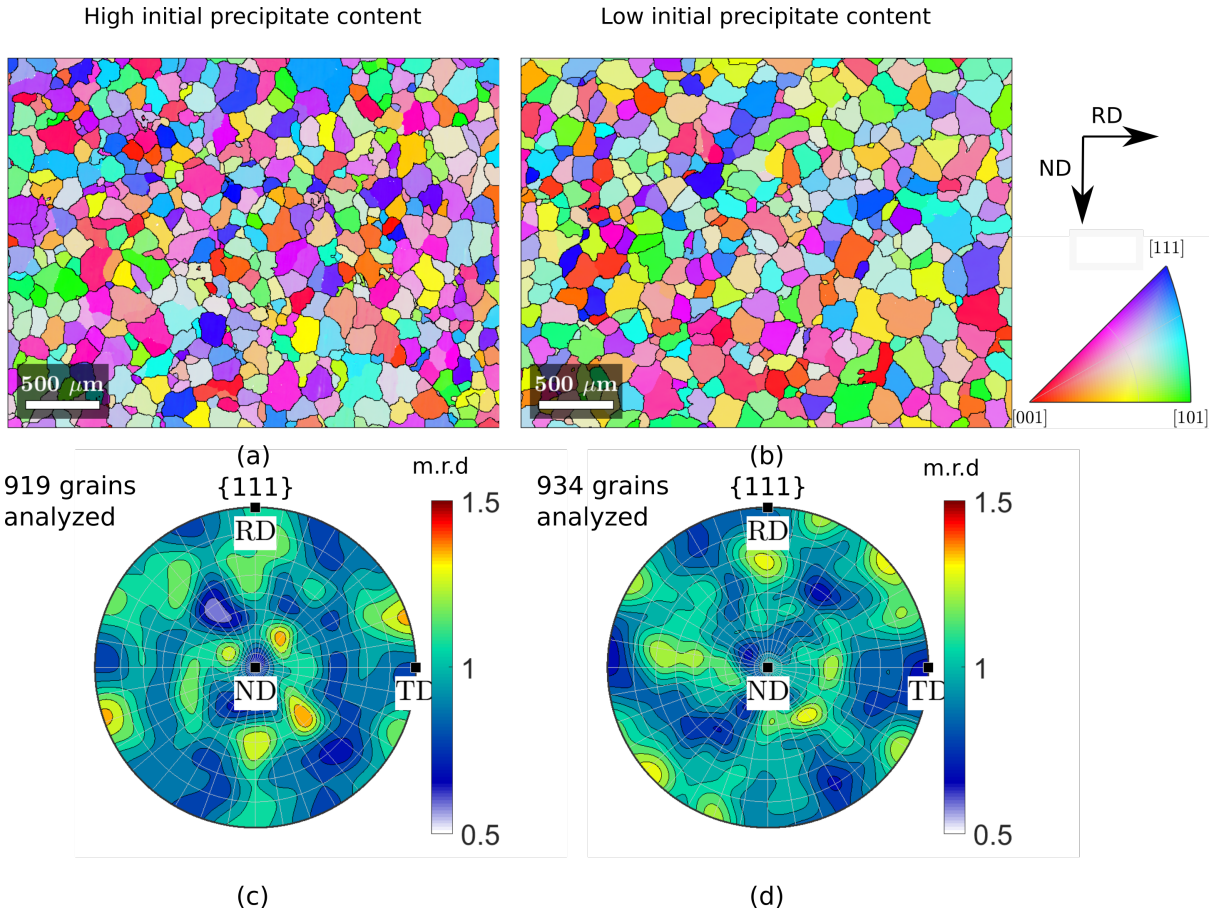

Fig. 4.3 (a,b) EBSD orientation maps showing the two initial microstructures. The grain boundaries ($\theta \geq 10°$) are plotted in black.The color code defined on the standard triangle refers to the normal direction. The measurement step size is 5 µm. (c,d) The corresponding {111} pole figures. The texture intensity is expressed in multiple of random distribution (m.r.d.).

4.2 Generation of three different precipitate contents right before deformation

In order to understand the influence of precipitates and solutes on the evolution of recrystallization during and after hot rolling, the two initial microstructures described in section 4.1 have undergone the thermomechanical schedules named by TMTa, TMTb and TMTc in figure

4.4. The difference between the three thermomechanical schedules is the amount of solutes and precipitates at the state right before deformation (identified by state 1a, 1b and 1c) as can be seen qualitatively by the high magnification SEM SE images shown in figure 4.4. In fact, TMTa aims at generating a microstructure enriched with elements in solid solution (i.e. state 1a), while TMTb and TMTc aim at generating a microstructure enriched with precipitates (i.e. state 1b and 1c). The difference between TMTb and TMTc is the density and the size of precipitates. The thermomechanical tests have been interrupted by water quenching at different stages to study the evolution of the precipitation state and its influence on the microstructure evolution.

For this purpose, the samples have been water quenched during each thermomechanical path at the different states identified by 1a, 2a, 3a, 1b, 2b, 3b, 1c, 2c and 3c (see figure 4.4) and the precipitation content at these different positions has been semi-quantified as explained in section 3.2.2.1. For this purpose, the samples have been electropolished to reveal soluble phases and SEM SE images have been taken.

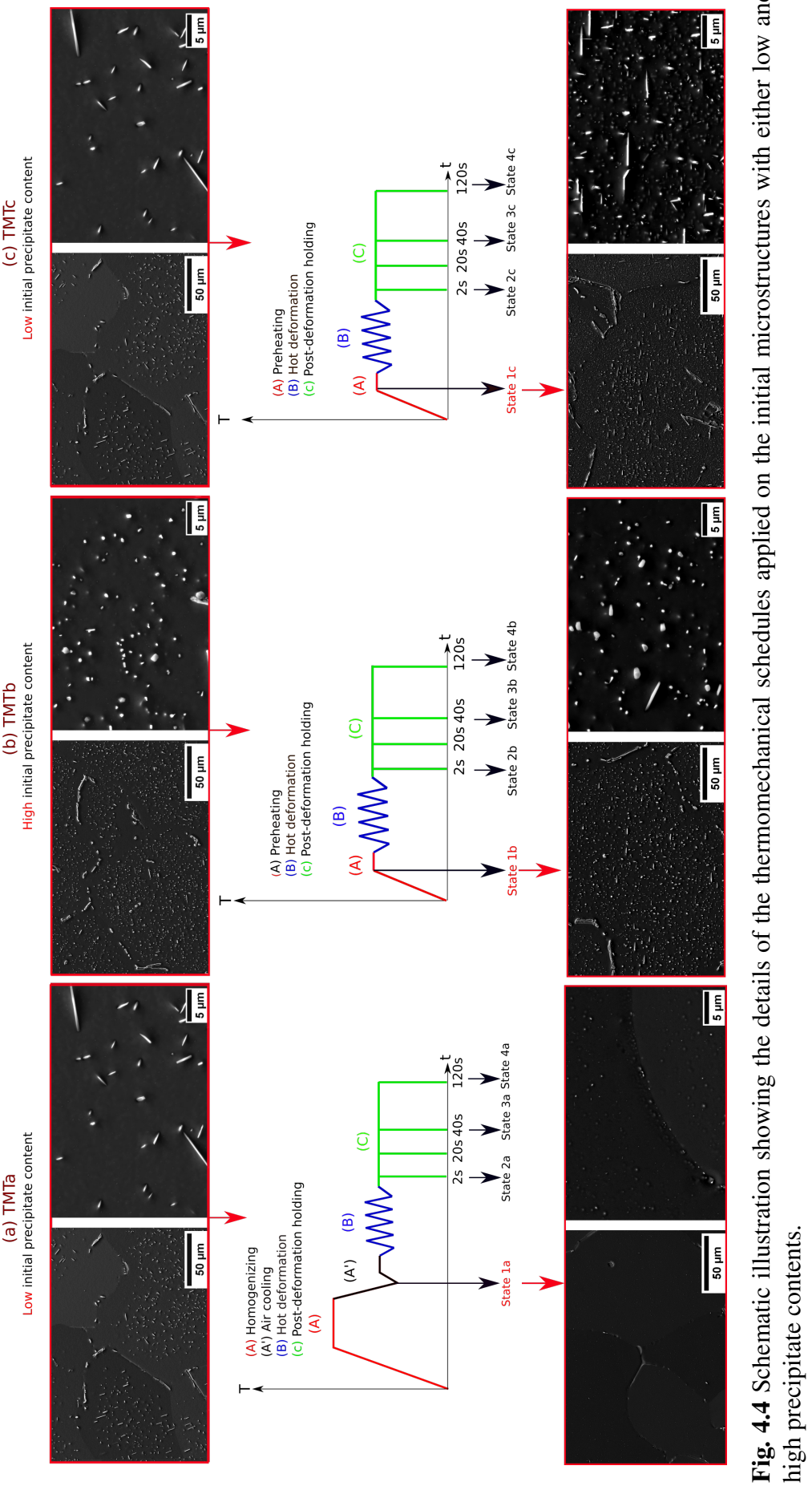

Fig. 4.4 Schematic illustration showing the details of the thermomechanical schedules applied on the initial microstructures with either low and high precipitate contents.

In order to distinguish between the three thermomechanical schedules TMTa, TMTb and TMTc, the area fraction f_{spp} and the mean equivalent radius r_{spp} of soluble phases have been measured. The ratio $\frac{f_{spp}}{r_{spp}}$ has also been calculated at the states 1a, 1b and 1c since it is related to the Smith-Zener pinning force exerted by these particles as seen in section 2.1 ($P_{SZ} = \frac{3\gamma f_{spp}}{2 r_{spp}}$). The area fraction f_{spp} is calculated as the sum of areas of soluble phases detected on the acquired SEM SE images divided by the total analyzed area. r_{spp} is calculated as the mean value of equivalent radii of all detected soluble phases considered together.

The estimated values are summarized by table 4.1. The microstructures obtained at the different states 1a, 1b and 1c can hence be classified by the ratio $\frac{f_{spp}}{r_{spp}}$. The lowest value of $\frac{f_{spp}}{r_{spp}}$ suggests that recrystallization is less affected by the Smith-Zener pinning force due to precipitates that are formed prior to deformation. However, it is important to keep in mind the possible drag effect of solutes or pinning effect of precipitates that may form during deformation or during post-deformation holding. The recrystallization behavior during deformation or post-deformation holding will therefore be analyzed and discussed based on the value of $\frac{f_{spp}}{r_{spp}}$ right before deformation. For simplicity, state 1a, state 1b and state 1c will be identified by "low $\frac{f_{spp}}{r_{spp}}$", "medium $\frac{f_{spp}}{r_{spp}}$" and "high $\frac{f_{spp}}{r_{spp}}$" respectively hereafter.

States	1a	1b	1c
$f_{spp}(\%)$	0.45	2.8	3.6
$r_{spp}(\mu m)$	0.115	0.278	0.138
$\frac{f_{spp}}{r_{spp}}(\mu m^{-1})$	0.039	0.1	0.26

Table 4.1 Estimated values useful for Smith-Zener pinning force calculation right before deformation.

4.3 Evolution of precipitation during deformation and post-deformation holding

The evolution of precipitates during deformation and post-deformation holding has been studied qualitatively as can be seen on figure 4.5. For this purpose, SEM SE images at high magnification are taken on the samples that have been water quenched right before deformation, right after deformation and after post-deformation holding for 40 s (i.e. at positions identified by states 1a, 1b, 1c, 2a, 2b, 2c, 3a, 3b and 3c in figure 4.4). The values of f_{spp}, r_{spp} and $\frac{f_{spp}}{r_{spp}}$ have been also determined at each state (see section 3.2.2.1) and plotted in figure 4.6.

For the lowest $\frac{f_{spp}}{r_{spp}}$, it is clear that, right before deformation (see figure 4.5, state 1a), the intragranular precipitates are so small in size that it is difficult to distinguish them from the matrix. The precipitates located at the grain boundaries seem to be bigger in size, which makes sense. Indeed, during air cooling (i.e the step following homogenization represented by (A') in figure 4.4), precipitates tend to nucleate and grow preferentially along grain boundaries

since they are sinks for vacancies. During deformation (see figure 4.5, state 2a), both the number and the size of precipitates increase, which is confirmed by figures 4.6 (b) and (c). This suggests that, during deformation, nucleation and coarsening of precipitates occur. During post-deformation holding, the number of finer precipitates seems to increase at first glance by looking at state 3a, figure 4.5. This is confirmed semi-quantitatively. In fact, the formation of additional finer precipitates will lower the mean equivalent radius of precipitates (see figure 4.6 (c)), while the area fraction of precipitates will increase (see figure 4.6 (b)).

For the medium $\frac{f_{spp}}{r_{spp}}$, the precipitates examined right before deformation (see figure 4.5, state 1b) are the largest in size compared to the precipitates present in the other two samples (see figure 4.5, states 1a and 1c). During deformation (see figure 4.5, state 2b), the precipitates seem to get smaller in size, but higher in number. Figures 4.7 (a) and (c) show magnified SEM SE images of the precipitates examined right before deformation and right after deformation in the sample having a medium $\frac{f_{spp}}{r_{spp}}$, respectively. These SEM SE images suggest that fragmentation of precipitates or formation of additional finer precipitates occur during deformation. Figures 4.6 (b) and (c) show clearly that the area fraction of precipitates remains almost constant and that the mean equivalent radius of precipitates decreases significantly during deformation, respectively. This implies that fragmentation of precipitates occurs during deformation rather than additional precipitation in the case of medium $\frac{f_{spp}}{r_{spp}}$. After holding for 40 s, the size and number of precipitates do not seem to change (see figure 4.5, state 3b). This is confirmed quantitatively from the measured values of area fraction and mean equivalent radius of precipitates right after deformation and after holding for 40 s (see figures 4.6 (b) and (c)).

Finally, for the highest $\frac{f_{spp}}{r_{spp}}$, the precipitates examined right after deformation (see figure 4.5, state 2c) seem to be smaller in size and higher in number than before deformation, suggesting the precipitation of additional finer precipitates or the fragmentation of precipitates present before deformation. The area fraction of precipitates measured right after deformation is lower than the one measured right before deformation, suggesting therefore the dissolution of some precipitates during deformation. This is consistent with the literature presented in section 2.5.2. It has been reported that precipitates can be dissolved due to shearing by dislocations during deformation [82]. In order to confirm the occurrence of dissolution, magnified SEM SE images have been taken on the samples having the highest $\frac{f_{spp}}{r_{spp}}$ and water quenched just before deformation (see figure 4.7 (b)) and right after deformation (see figure 4.7 (d)). It is clear from these two SEM SE images that the shape of fine precipitates is different between the two states. Fine precipitates are more needle-shaped before deformation than right after deformation. These observations (i.e. decrease in the area fraction, decrease in the mean equivalent radius and spheroidization of precipitates during deformation) suggest that some of the precipitates that are formed during preheat (i.e. step represented by (A) in the thermomechanical path TMTc shown by figure 4.4) could be metastable due to the high preheating rate (2.25°C/s), leading thereby to their dissolution and the repecipitation of more stable precipitates having a globular

shape during deformation. The fragmentation of some stable precipitates that are present in the initial state (i.e. low initial state) before preheating may also takes place during deformation, resulting therefore in the decrease in the mean equivalent radius. All these assumptions need to be validated by performing a quantitative analysis by the method described in section 3.2.2.2 instead of a semi-quantitative analysis at both states before deformation and right after deformation. The type of the different precipitates would need to be determined more accurately (eg. by using TEM or Electron Energy Loss Spectroscopy (EELS)), which could not be done in this work. However, after holding for 40 s, precipitates do not seem to evolve (see figure 4.5, state 3c), which is confirmed semi-quantitatively. Both the area fraction and mean equivalent radius of precipitates remain almost constant during holding in the case of highest $\frac{f_{spp}}{r_{spp}}$ (see figures 4.6 (b) and (c)).

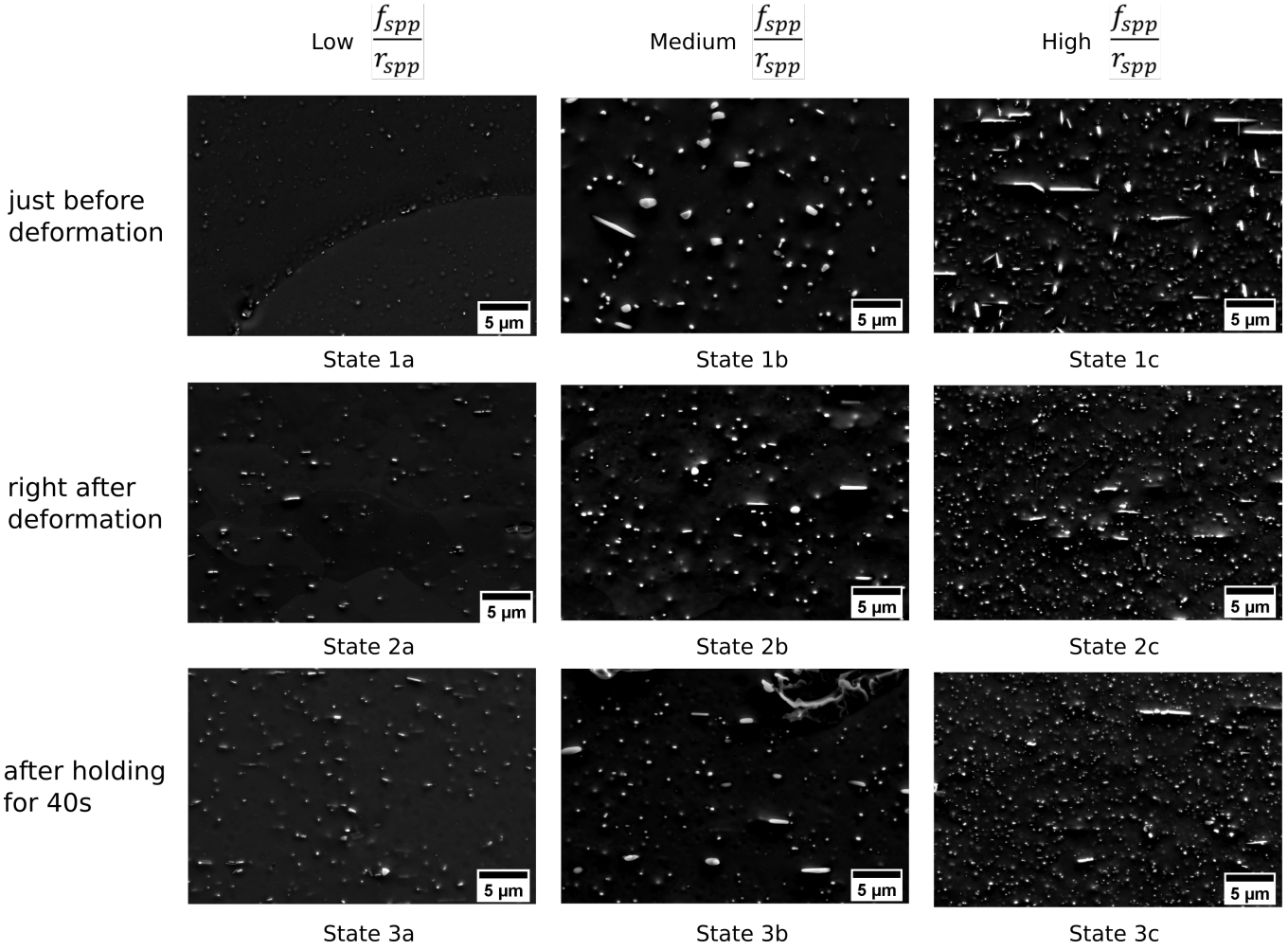

Fig. 4.5 Evolution of precipitation for the three different values of $\frac{f_{spp}}{r_{spp}}$ measured before deformation during the thermomechanical test. The states from 1a to 3c are defined in figure 4.4. The SEM SE images have been taken on samples that have been prepared by mechanical polishing followed by electropolishing with 30% nitric acid in methanol.

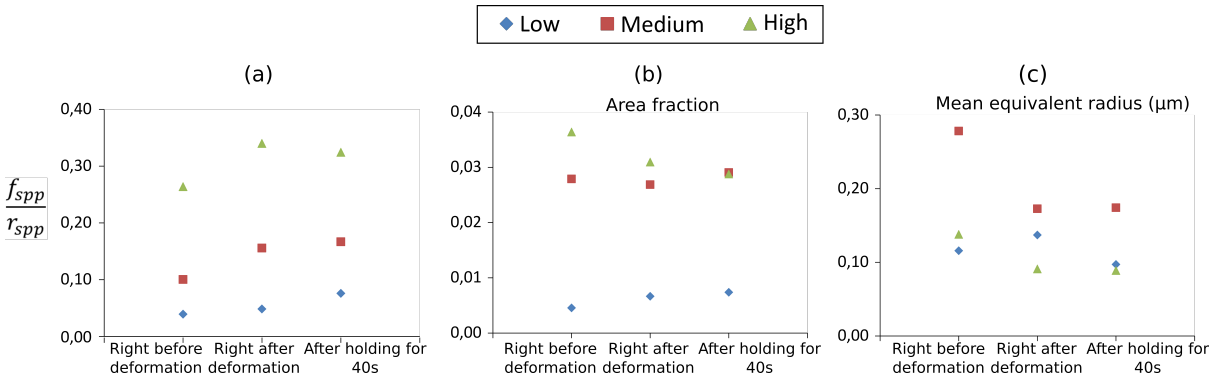

Fig. 4.6 Evolution of (a) $\frac{f_{spp}}{r_{spp}}$, (b) f_{spp} and (c) r_{spp} with hot deformation for the three initial precipitation states.

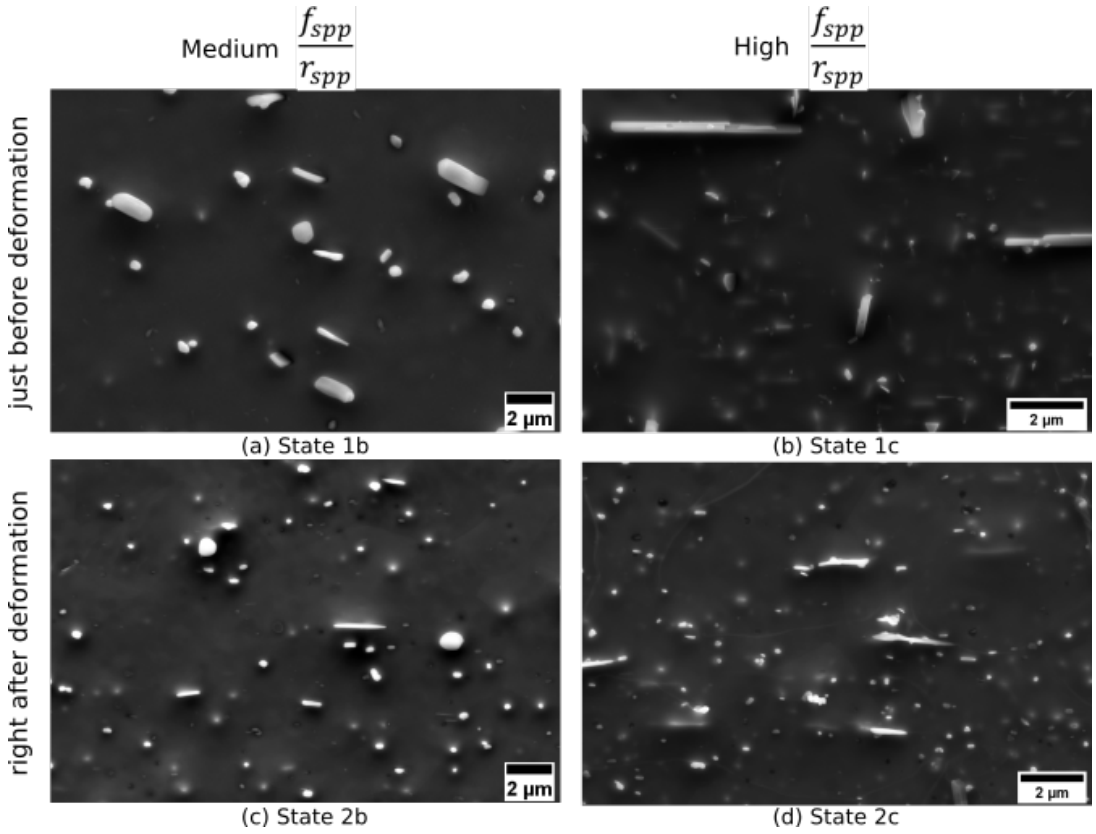

Fig. 4.7 (a,b) Magnified SEM SE images showing the shape of precipitates in medium and high $\frac{f_{spp}}{r_{spp}}$ right before deformation, respectively. (c,d) Magnified SEM SE images showing the shape of precipitates in medium and high $\frac{f_{spp}}{r_{spp}}$ right after deformation, respectively.

The evolution of the size distribution of precipitates during and after hot deformation is shown in figure 4.8 for each $\frac{f_{spp}}{r_{spp}}$. Figure 4.8 (a) shows that, in the case of lowest $\frac{f_{spp}}{r_{spp}}$, the number of precipitates increases during both deformation and holding after deformation, confirming therefore the occurrence of precipitation during deformation and holding. Both precipitate nucleation and coarsening seem to occur during deformation, which may be accelerated by the presence of dislocations, solute transport by dislocation sweeping and/or non equilibrium va-

cancies related to plastic deformation as explained in the section 2.5.2. Precipitates continue to form during post-deformation holding.

Figures 4.8 (b) and (c) show that, in the case of medium and highest $\frac{f_{spp}}{r_{spp}}$, no evolution of precipitates occurs during holding after deformation. However, it is clear from figures 4.8 (b) and (c) that precipitates evolve during deformation.

For medium $\frac{f_{spp}}{r_{spp}}$ (see figure 4.8 (b)), the number of particles having an equivalent diameter between 0.5 and 0.8 µm decreases, while the number of particles having an equivalent diameter between 0.5 and 0.1 µm increases during deformation. This confirms the occurrence of fragmentation of precipitates that are present just before deformation. A similar observation has been made by Munoz-Morris et al. [97], who observed the refinement of particle size after hot rolling of an Al-Cu-Li alloy. This particle size reduction may be caused by two processes: a fine precipitation induced by the high density of dislocations produced by deformation or the breakage of initial precipitates by heavy deformation.

For the highest $\frac{f_{spp}}{r_{spp}}$ (see figure 4.8 (c)), the number of fine precipitates having an equivalent diameter between 0.3 and 0.1 µm increases during deformation. There is still a doubt regarding the origin of finer precipitates observed right after deformation. They may be formed due to fragmentation of initially present precipitates, dissolution of some less stable precipitates and reprecipitation of more stable ones and/or nucleation of additional finer precipitates.

Besides, it is important to keep in mind that, in the analysis of precipitates using ImageJ, the determination of area and equivalent radius of particles can be altered due to the choice of the applied threshold as mentioned in section 3.2.2.1. Quantitative analyses of precipitates examined right before deformation and of those right after deformation would be required in order to determine exactly how these precipitates are evolving during deformation in the case of highest $\frac{f_{spp}}{r_{spp}}$.

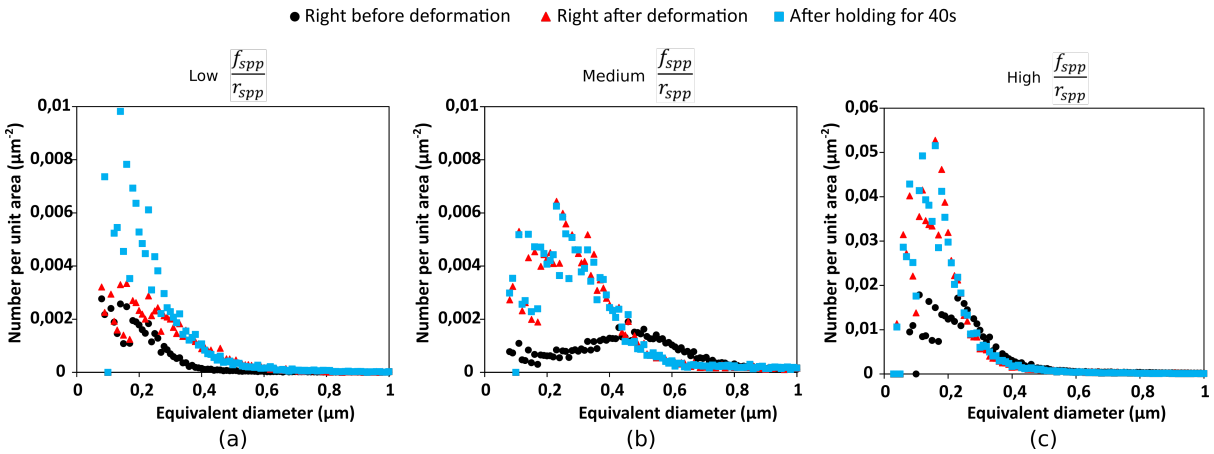

Fig. 4.8 Evolution of particle size distribution for the three different initial microstructures during deformation and post-deformation holding.

The influence of the above mentioned precipitates on recrystallization during deformation and post-deformation holding will be investigated in sections 4.4 and 4.5 respectively.

4.4 Microstructure right after deformation

4.4.1 Characterization of recrystallized grains

The quenched microstructures obtained right after hot deforming the three states with different values of $\frac{f_{spp}}{r_{spp}}$ are shown by figure 4.9, where low and high magnification EBSD orientation maps at different $\frac{f_{spp}}{r_{spp}}$ are illustrated. The comparison between the different low magnification EBSD orientation maps (see figure 4.9 (a-c)) shows that few recrystallized grains are larger in size in low $\frac{f_{spp}}{r_{spp}}$ and that the number of recrystallized grains seems to be higher in medium $\frac{f_{spp}}{r_{spp}}$. These observations will be confirmed quantitatively in the next paragraph. The high magnification EBSD orientation maps (see figure 4.9 (d-f)) show also the presence of a higher number of high angle grain boundaries in the sample with medium $\frac{f_{spp}}{r_{spp}}$, which could be due to grain subdivision in addition to the presence of a higher number of recrystallized grains in this sample compared to the other two samples. The possibility of grain subdivision occurring during deforming metals from medium to high strains has been reported by Hughes et al. [98]. The high angle grain boundaries due to grain subdivision form as a result of both microstructural and textural evolutions. The microstructural evolution consists of cell block formation where grains start to subdivide into crystallites surrounded by dislocation boundaries (i.e. dense dislocation walls/microbands) whose misorientations increase steadily with increasing strain. The textural evolution consists of the rotation of individual crystallites forming a subdivided grain to preferred orientations during deformation. Since the end orientations are far apart, large misorientations within the original subdivided grain can build up during deformation, producing thereby high angle boundaries [98]. Based on the high magnification EBSD orientation maps shown by figure 4.9 (d-f), grain subdivision is more likely to occur in medium $\frac{f_{spp}}{r_{spp}}$ than in the other two samples. Since subgrain formation is a precursor to the subdivision of original grains [98], the difference in the grain subdivision behavior between the three microstructures may be due to a difference in the subgrain formation behavior. This will be discussed in more details in section 4.4.3.

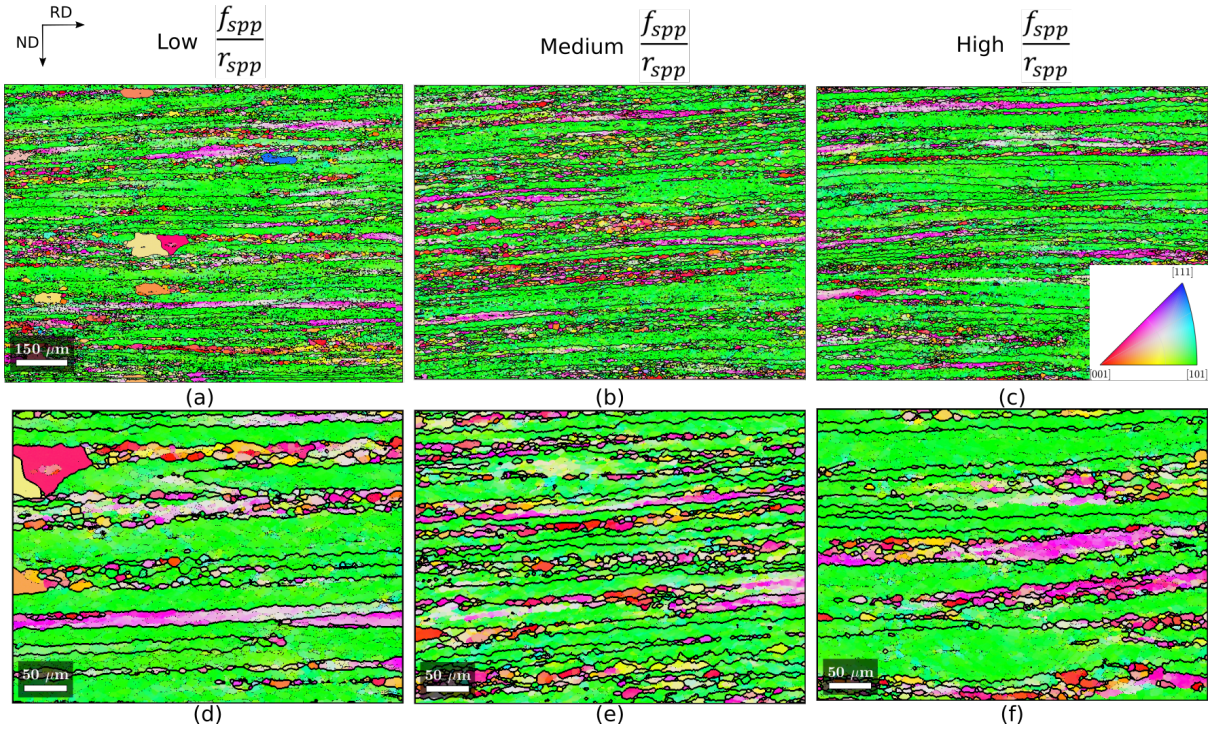

Fig. 4.9 Microstructure right after deformation for the three different values of $\frac{f_{spp}}{r_{spp}}$: (a-c) Low magnification EBSD orientation maps with a measurement step size of 1 µm. (d-f) High magnification EBSD orientation maps with a measurement step size of 0.4 µm. The color code defined on the standard triangle refers to the normal direction. High angle grain boundaries ($\theta \geq 10°$) are represented by black lines.

The recrystallized grains are determined (according to section 3.4.1) in all EBSD orientation maps shown by figure 4.9 (a-c) and are shown by figure 4.10 (a-c). Nucleation of recrystallized grains occurs regardless of the initial precipitate content. However, the size and density of recrystallized grains differ from one sample to another.

In low $\frac{f_{spp}}{r_{spp}}$, few recrystallized grains have a larger size than other recrystallized grains (see figure 4.10 (a)), leading therefore to a higher standard deviation from the mean equivalent diameter of recrystallized grains (see figure 4.10 (d)) and to a higher recrystallization area fraction (see figure 4.10 (e)). Nevertheless, the density of recrystallized grains per unit area is lower than the one in the case of medium $\frac{f_{spp}}{r_{spp}}$ (see figure 4.10 (f)). This lower density value may be due to two factors: nucleation rate is lower in the case of low $\frac{f_{spp}}{r_{spp}}$ than medium $\frac{f_{spp}}{r_{spp}}$ and/or some small recrystallized grains are consumed by the large recrystallized grains.

For medium and high $\frac{f_{spp}}{r_{spp}}$, the mean equivalent diameter of recrystallized grains is quite similar (see figure 4.10 (d)). However, the main difference between these two samples is the density of recrystallized grains per unit area (see figure 4.10 (f)). It is much higher in medium $\frac{f_{spp}}{r_{spp}}$ than in high $\frac{f_{spp}}{r_{spp}}$, resulting then in a higher recrystallization area fraction in medium $\frac{f_{spp}}{r_{spp}}$ than in high $\frac{f_{spp}}{r_{spp}}$ right after deformation (see figure 4.10 (e)). Thus, the nucleation rate is lower in the case of high $\frac{f_{spp}}{r_{spp}}$ than in the case of medium $\frac{f_{spp}}{r_{spp}}$.

Different factors including second-phase particles, solutes, stored energy, substructure and

self-heating may have an influence on the recrystallization behavior of each microstructure right after deformation. In addition to that, at high deformation temperature, dynamic recovery is promoted in aluminum alloys and recrystallization is more likely to originate from pre-existing subgrains in the deformed microstructure. It is therefore important to study the subgrain structure and the interaction between the above mentioned factors and the developed substructure in the three deformed and quenched microstructures (i.e. low, medium and high $\frac{f_{spp}}{r_{spp}}$) before making any conclusions regarding the reasons behind the differences in the nucleation behavior (will be discussed in sections 4.4.2 and 4.4.3)

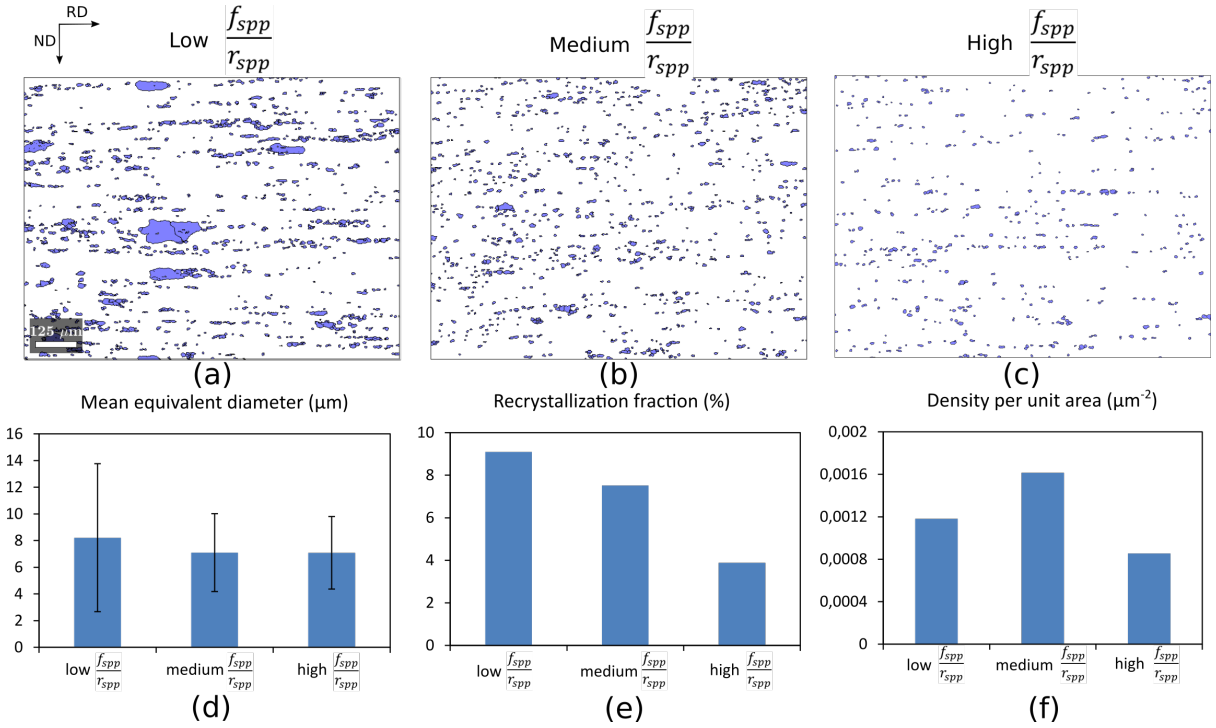

Fig. 4.10 (a-c) Determination of recrystallized grains in the three microstructures shown by figure 4.9 (a-c), (d-e) Mean equivalent diameter of recrystallized grains, recrystallization area fraction and density of recrystallized grains per unit area for each precipitation state.

Figure 4.11 (a) shows the $\{111\}$ pole figures for the deformed and recrystallized grains right after deformation. The recrystallized grains do not seem to exhibit any strong preferred orientation unlike the deformed grains which seem to be highly textured. This is confirmed by figure 4.11 (b) which shows the area fraction of recrystallized grains and deformed grains belonging to the typical texture components present in aluminum and aluminum alloys respectively. The recrystallized grains do not show clearly any preferred orientation. However, the deformed grains are mainly Goss and Brass oriented. It is important to note that the texture of deformed and recrystallized grains is quite similar between the three states with different values of $\frac{f_{spp}}{r_{spp}}$.

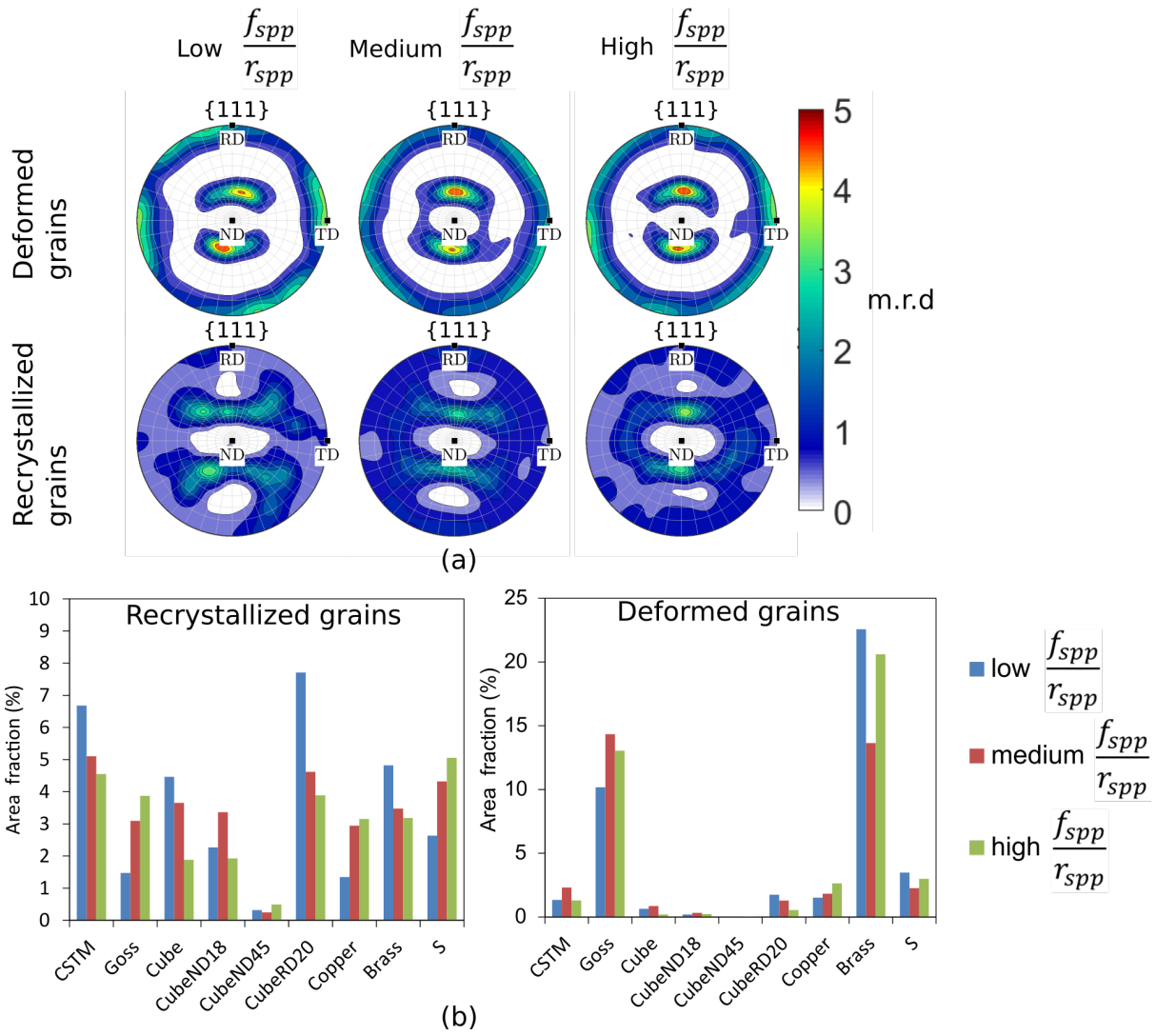

Fig. 4.11 Texture of recrystallized and deformed grains right after deformation.

4.4.2 Spatial distribution of precipitates with respect to subgrains/grains right after deformation

Figure 4.12 shows low and high magnification BSE images taken right after deformation on the three states with different initial values of $\frac{f_{spp}}{r_{spp}}$ right after deformation. The low magnification BSE images show that a substructure is developed in all samples regardless of their precipitate content. The high magnification BSE images show that the subgrain size seems to be larger in the case of the deformed and quenched state with low $\frac{f_{spp}}{r_{spp}}$.

Subgrain coarsening is generally assumed to be controlled by the migration of low angle grain boundaries and both solutes and precipitates have a strong influence on the recovery process by slowing down the movement of dislocations and migration of low angle boundaries [8].

Particularly, solutes may lower the stacking fault energy γ_{SFE}, pin movement of dislocations and affect the concentration and mobility of vacancies, resulting thereby to inhibition of

dynamic recovery. This inhibition of dynamic recovery may result in a retention of a higher dislocation density than in a solute-free material, promoting thus subgrain formation and coarsening on subsequent annealing. These subgrains may serve as potential nuclei for recrystallization if they grow large enough and if they are surrounded by sufficient stored energy and high misorientation angles (between 10° and 15°) [8]. The interaction between solutes and subgrains can be therefore quite complex. In one hand, solutes inhibit movement of LAGBs during dynamic recovery resulting therefore to an increase in the driving force for recrystallization. In the other hand, they can promote recovery occurring during subsequent annealing and therefore nucleation resulting from subgrain growth. Taking into account that there is 2 seconds of quench delay, the substructures observed in deformed and quenched states (see figure 4.12) may have developed during deformation or during the quench delay. This experimental constraint adds another difficulty about the interpretation of the net effect of solutes on subgrain formation and coarsening.

Regarding second-phase particles, the effect of stable second-phase particles (not evolving after their appearance) has been extensively studied as seen in Chapter 2, section 2.5 and is quite understood. Indeed, stable second-phase particles pin the movement of high and low angle boundaries. They retard hence subgrain growth (due to a higher retarding force from precipitates on subgrain boundaries) and therefore nucleation (because of the smaller subgrain size which is not sufficient to initiate nucleation), in addition to retarding grain growth owing to the well-known Smith-Zener pinning effect. However, in some circumstances, they can promote recrystallization through abnormal subgrain growth. Abnormal subgrain growth can take place in regions with less precipitates (if precipitates are not homogeneously distributed) or when the subgrain size is much lower than the spacing between particles. These larger subgrains may therefore serve as nuclei for recrystallization [10]. The difficulty in the three states shown by figure 4.12 comes from the evolution of precipitates (including newly formed, dissolving and coarsening precipitates), leading simultaneously to an evolution of solute drag. In addition to that, formation of new precipitates occurs preferentially along subgrain and grain boundaries. Besides, the boundary migration may lead to the dissolution, re-precipitation, coarsening and/or loss of coherency of precipitates. The study of these complex interactions between precipitates and migrating boundaries (including LAGBs and HAGBs) will be discussed in section 4.4.3. In addition to the effects of solutes and precipitates, the effects of self-heating and flow stress on the developed substructures need to be taken into account in the analysis. All these aspects will be discussed in section 4.4.3. Only a description of the spatial distribution of precipitates with respect to subgrain/ grain boundaries will be given in this section.

High magnification BSE images shown by figure 4.12 (d-f) show qualitatively that fine precipitates (probably consisting of soluble phases and dispersoids) are randomly located inside the subgrains/grains as well as at the boundaries. It is important to note that the interparticle spacing is much lower than the subgrain/grain size, meaning therefore that the recovery process

is greatly affected by the pinning effect of fine precipitates, but to different extents depending on the value of $\frac{f_{spp}}{r_{spp}}$.

Zooms into Fe rich intermetallic particles present in the three deformed and quenched states with different values of $\frac{f_{spp}}{r_{spp}}$ (see figure 4.12 (a-c)) show the existence of a particle free zone around these large particles. The particle free zone seems to be larger in the states with low and medium $\frac{f_{spp}}{r_{spp}}$ than in the state with a high $\frac{f_{spp}}{r_{spp}}$, resulting therefore in the development of larger subgrains in the vicinity of these Fe rich intermetallic particles. Thus, formation of recrystallized grains by PSN is expected to be more frequent in the case of low and medium $\frac{f_{spp}}{r_{spp}}$ than in the case of high $\frac{f_{spp}}{r_{spp}}$. This may explain, in part, the higher density of recrystallized grains per unit area observed in these states than in the states with a high $\frac{f_{spp}}{r_{spp}}$.

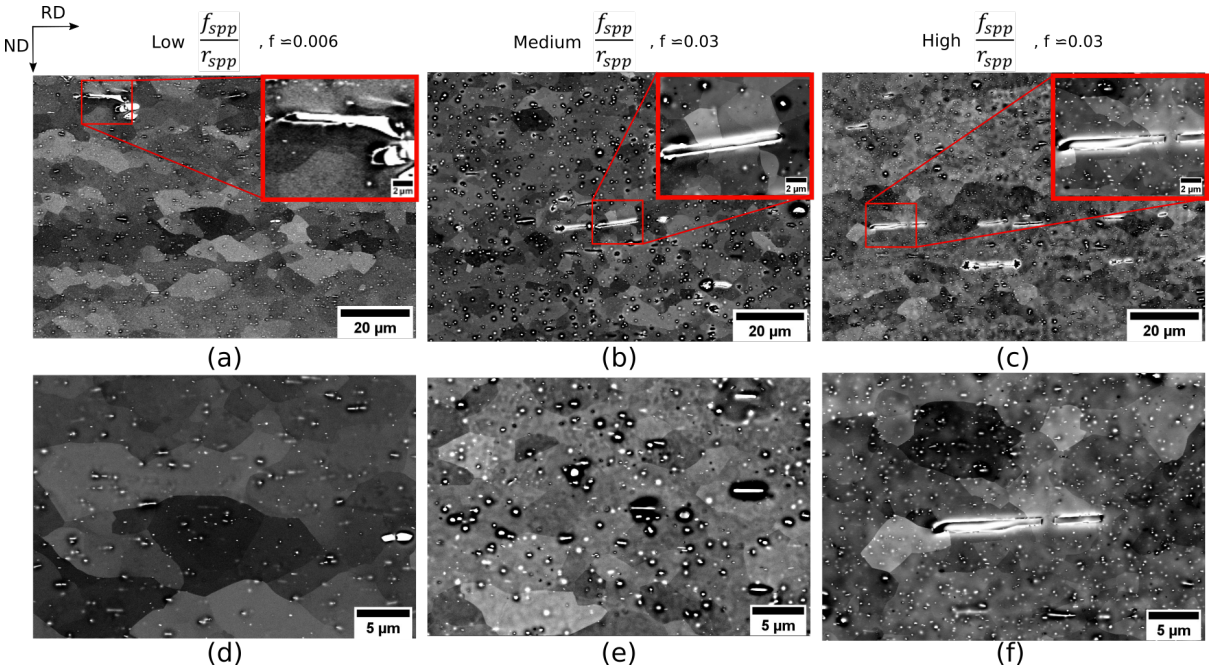

Fig. 4.12 (a-c) Low magnification BSE images showing the microstructure right after deformation for different values of $\frac{f_{spp}}{r_{spp}}$ respectively. Zooms onto Fe rich intermetallic particles are shown on the top right corner of each BSE image. (d-f) Higher magnification BSE images showing the distribution of precipitates with respect to the substructure. The total area fraction of precipitates is indicated above each microstructure.

4.4.3 Characterization of the substructure

4.4.3.1 Description of the developed substructures

Figures 4.13 (a-c) show the KAM maps corresponding to EBSD orientation maps of figures 4.9 (d-f), respectively. The boundaries of deformed grains are plotted in black lines, whereas the boundaries of recrystallized grains are plotted in red lines. The comparison between figures 4.13 (a-c) show that the fraction of high angle boundaries (i.e. including red and black lines) is higher in the case of medium $\frac{f_{spp}}{r_{spp}}$.

Zooms into the KAM maps shown by figures 4.13 (a-c) are illustrated by figures 4.13 (d-f). It is evident from the magnified KAM maps that a subgrain structure is developed in the three states, suggesting therefore the occurrence of dynamic recovery. The fraction of low angle boundaries seems to be higher in medium $\frac{f_{spp}}{r_{spp}}$ than in the other two states with low and high $\frac{f_{spp}}{r_{spp}}$. The total lengths of LAGBs and HAGBs per unit area have been calculated respectively in each state (based on the KAM maps shown by figure 4.13 (a-c)) and have been summarized by table 4.2. The total length per unit area measurements confirm that the deformed and quenched state with medium $\frac{f_{spp}}{r_{spp}}$ possesses the highest fraction of both LAGBs and HAGBs, suggesting therefore that dynamic recovery is promoting the occurrence of dynamic and post-dynamic recrystallization in this case. This has been demonstrated in [99, 100]. It is generally assumed that recovery reduces the driving force available for recrystallization and that recovery and recrystallization are therefore competing processes. However, it has been found that, under some circumstances (e.g. in high stacking fault energy materials [99] or in hot rolled steels where strain induced boundary migration is the main recrystallization mechanism [100]), pre-recovery may accelerate recrystallization by reducing the time needed for polygonization prior to recrystallization.

The KAM values at LAGBs in medium $\frac{f_{spp}}{r_{spp}}$ are higher than than the KAM values at LAGBs in low and high $\frac{f_{spp}}{r_{spp}}$, suggesting a higher density of geometrically necessary dislocations accumulated at subgrain boundaries in the deformed and quenched state with medium $\frac{f_{spp}}{r_{spp}}$. The subgrain size seems to be also finer in the case of medium $\frac{f_{spp}}{r_{spp}}$ than in the case of low and high $\frac{f_{spp}}{r_{spp}}$. These variations are probably due to the differences in precipitate and solute contents between the three states, resulting therefore in different interactions between precipitates/solutes and dislocations/subgrain boundaries. The influence of these interactions between precipitates/solutes and dislocations/subgrains will be studied in more details in sections 4.4.3.2 and 4.4.3.3.

Figures 4.13 (d-f) show evidence of dynamically and post-dynamically recrystallized grains (shown by red lines) in the three deformed and quenched microstructures. The dynamically recrystallized grains are the ones containing substructure. It is difficult to determine exactly the recrystallization mechanism by which these dynamically recrystallized grains are formed. Nevertheless, CDRX seems to be the most probable dynamic recrystallization mechanism occurring in hot deformed aluminum alloys (read section 2.2.2 for more details) and thus in the three hot deformed and quenched microstructures in this study. GDRX could be also taking place in the deformed and quenched states due to the smaller thickness of some deformed grains (i.e. the thickness of some deformed grains has the same order of magnitude as the subgrain size as shown by figure 4.13 (d-f)). Finally, some recrystallized grains are surrounded by Fe rich intermetallic particles, suggesting the occurrence of PSN (see figure 4.12).

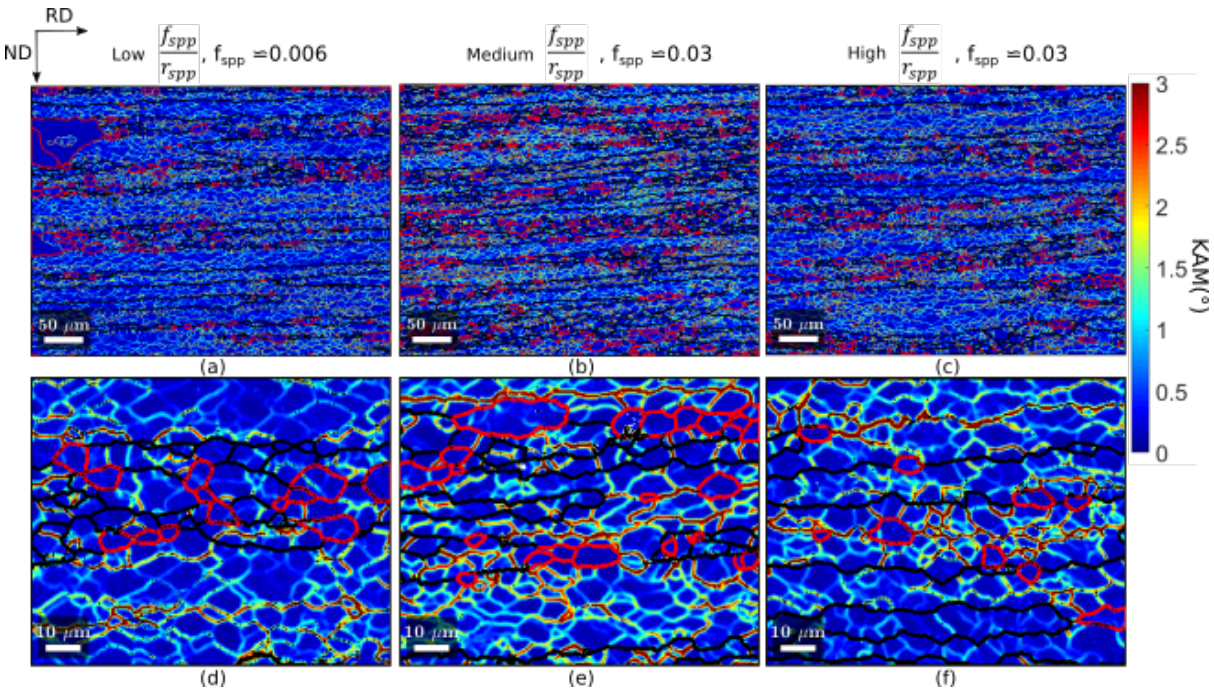

Fig. 4.13 (a-c) KAM maps corresponding to EBSD orientation maps shown by figure 4.9 (d-f). (d-f) Zooms into KAM maps shown by (a-c), respectively. Boundaries of recrystallized grains are plotted in red lines. Boundaries of deformed grains are plotted in black lines. The area fraction of precipitates f_{spp} is indicated above the KAM maps.

Total length per unit area (μm^{-1})	low $\frac{f_{spp}}{r_{spp}}$	medium $\frac{f_{spp}}{r_{spp}}$	high $\frac{f_{spp}}{r_{spp}}$
$LAGBs$ $(1° \leq \theta < 10°)$	0.38	0.58	0.47
$HAGBs$ $(\theta \geq 10°)$	0.08	0.15	0.10

Table 4.2 Total length of low angle grain boundaries (LAGBs) and high angle grain boundaries (HAGBs) per unit area in deformed and quenched states with different $\frac{f_{spp}}{r_{spp}}$.

Figures 4.14 (a-c) show the HAGBs and LAGBs plotted in black and in blue lines respectively on magnified EBSD orientation maps corresponding to each deformed and quenched state. Zooms into each EBSD orientation map are shown on the top right corner of each of these maps. The comparison between the three deformed and quenched microstructures shows that dynamic recovery occurs whatever the precipitate state right before deformation. However, the rate of dynamic recovery seems to depend on the precipitate and solute contents during deformation. The highest rate of dynamic recovery is observed for medium $\frac{f_{spp}}{r_{spp}}$ (confirmed by the highest total length of LAGBs per unit area as shown by table 4.2). Figures 4.14 (d-f) show the distributions of misorientation angles for the three microstructures illustrated by figures 4.14 (a-c). The mean misorientation angles corresponding to LAGBs and HAGBs are shown on the top of each misorientation angle distribution. It is clear that the misorientation angle values are quite similar between the three deformed and quenched microstructures. The only visible difference between the three deformed and quenched microstructures is that the state

with medium $\frac{f_{spp}}{r_{spp}}$ has a higher number of LAGBs having a misorientation angle between 1° and 3° (see histograms shown in figures 4.14 (d-f)). This increase may be simply due to an increase in the overall number of LAGBs in this sample.

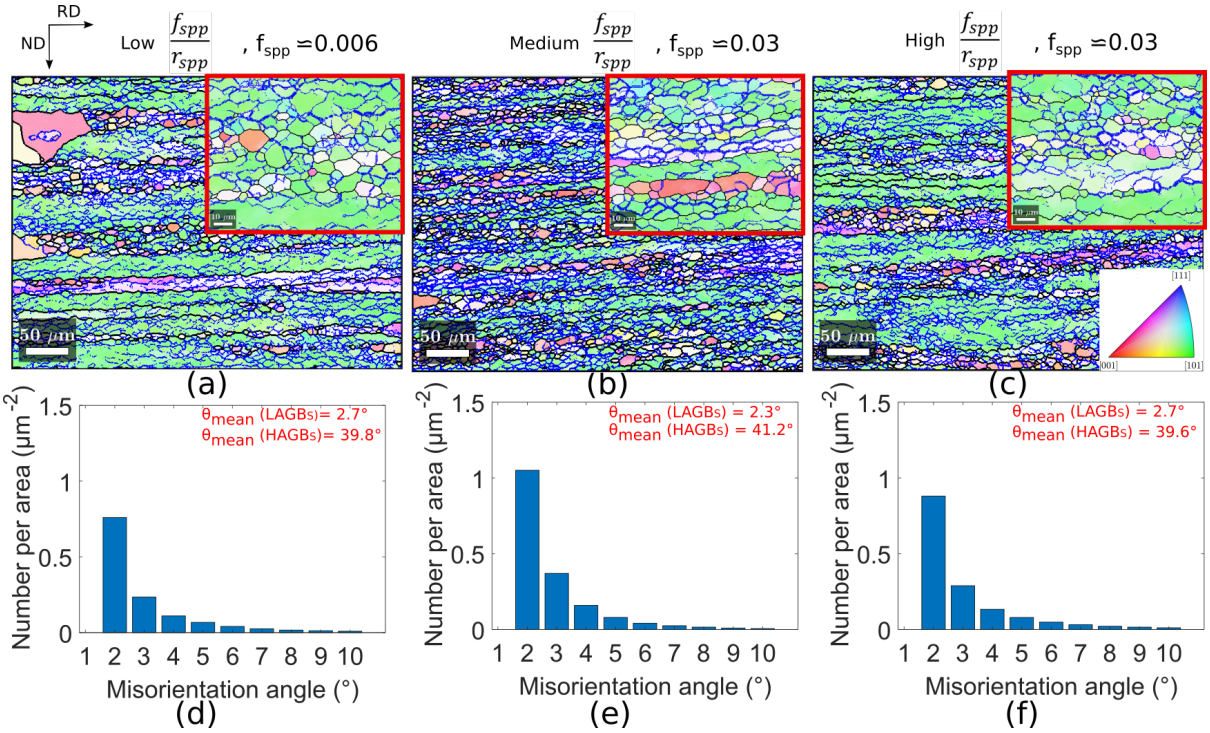

Fig. 4.14 (a-c) EBSD orientation maps showing high angle grain boundaries ($\geq$ 10°) in black lines and low angle boundaries (1°-10°) in blue lines. The color code defined on the standard triangle refers to the normal direction. The measurement step size is 0.4 μm. The area fraction of precipitates f_{spp} is indicated above each EBSD orientation map. (d-f) Histograms showing the misorientation angle distribution in (a-c) respectively. The mean misorientation angles corresponding to LAGBs and HAGBs are shown on each histogram.

4.4.3.2 Effect of solutes/precipitates on the flow stress and dynamic recovery

The differences in the developed substructures right after deformation between the three deformed and quenched states may be due to differences in the flow stress values (related to work hardening) or in the evolution of temperature during deformation. Therefore, the effects of flow stress and temperature are examined in this section.

Figure 4.15 shows the true stress-true strain curves as well as the temperature-true strain curves recorded during hot deformation. For the three deformed and quenched microstructures, the true stress increases quickly to reach a maximum value at a small strain. This means that work hardening plays an important role during the early stages of deformation. After reaching a maximum, the true stress decreases, suggesting the occurrence of dynamic softening through dynamic recovery or dynamic recrystallization. This is confirmed by the substructures shown by figures 4.14 and 4.13, which show evidence of both dynamic recovery and dynamic recrystallization. The main difference between the true stress-true strain curves obtained for the

three different deformed and quenched microstructures is the yield stress value. The sample having a medium value of $\frac{f_{spp}}{r_{spp}}$ has the lowest yield stress value, suggesting therefore a lower work hardening rate and a higher dynamic recovery rate compared to the other two states. This is consistent with the observations made in figures 4.14 and 4.13.

The increase in the yield stress for the state with a low $\frac{f_{spp}}{r_{spp}}$ (see figure 4.15 (a)) is probably due to the enhanced interactions between solutes and dislocations/subgrains during deformation. Indeed, the state with a low $\frac{f_{spp}}{r_{spp}}$ has the lowest area fraction of precipitates right after deformation (see figure 4.6 (b)) and therefore the highest amount of solutes. It has been found in [100, 101] that a higher amount of solutes leads to a higher amount of forest dislocations (i.e. often referred to as redundant or statistically stored dislocations), which will act in return as obstacles for movement of other dislocations. Both solutes and generated dislocations act therefore as obstacles for the movement of dislocations/subgrains during deformation [100, 101], resulting therefore in an increase of the work hardening rate. Solutes may also lower the stacking fault energy, lowering hence the degree of recovery of the substructure [102]. The temperatures at the end of deformation in the samples with low and medium $\frac{f_{spp}}{r_{spp}}$ are almost similar, confirming thus that the differences in the examined substructures and in the flow stress values is not due to a difference in the sample temperatures.

The increase in the yield stress for the state with a high $\frac{f_{spp}}{r_{spp}}$ (see figure 4.15 (c)) is probably due to the enhanced interactions between precipitates and dislocations/subgrains rather than to the interactions between solutes and dislocations/subgrains because the amount of solutes right after deformation is almost similar between the two states with medium and high $\frac{f_{spp}}{r_{spp}}$ (see figure 4.6 (b)). Finer stable precipitates have been reported as effective pinning sites for the movement of dislocations/subgrains [52, 101, 102], leading therefore to an increase in the work hardening rate and a decrease in the dynamic recovery rate in the state with high $\frac{f_{spp}}{r_{spp}}$. The comparison of the temperatures at the end of deformation between the states with high and low $\frac{f_{spp}}{r_{spp}}$ shows that the deforming temperature in case of high $\frac{f_{spp}}{r_{spp}}$ is higher. An increase in the temperature is expected to promote dynamic recovery due to the enhanced dislocations/subgrains motion. However, it is not the case in this sample, confirming thus that the difference in dynamic recovery behaviors between the two states with medium and high $\frac{f_{spp}}{r_{spp}}$ is attributed to the difference in precipitates content.

In addition to this, the additional fine precipitates that form during deformation and that have been observed in both samples with low and high $\frac{f_{spp}}{r_{spp}}$ will cause a delay in the substructure formation because they will tend to form at vacancies, dislocations and subgrains. Another mechanism responsible for the retardation of dynamic recovery has been discussed by Radetic et al. [103]. According to these authors, when Cu is added to an AA5182 alloy, a larger number of lattice defects and therefore a larger number of potential nucleation sites of fine stable S precipitates are introduced during hot deformation. This fine dispersion of S precipitates retards the formation of deformation bands because of the slip homogenization and more deformation

passes are hence needed for deformation bands to form. Slip homogenization due to the generation of finer precipitates in the case of low or high $\frac{f_{spp}}{r_{spp}}$ may be therefore an explanation for the delay in dynamic recovery in these two states.

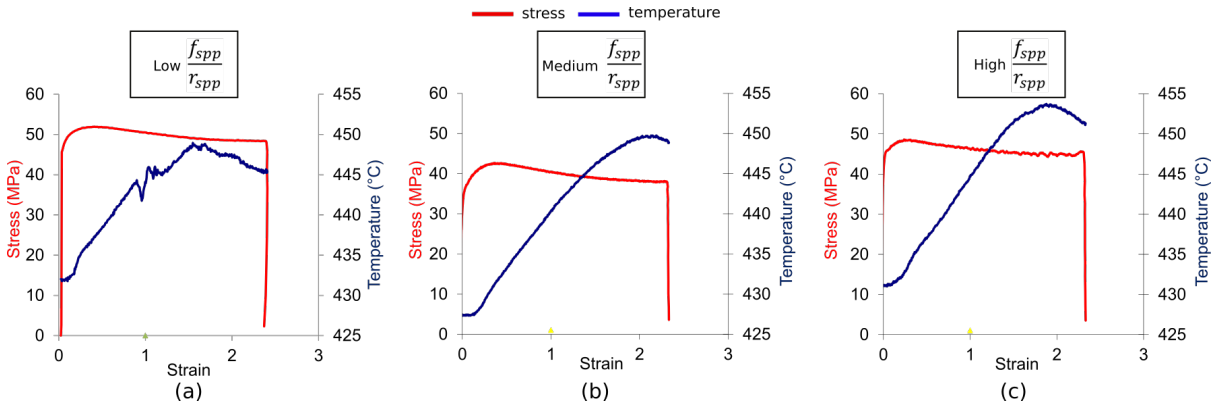

Fig. 4.15 True stress-true strain curves and Temperature-true strain curves during hot deformation for the three states with different values of $\frac{f_{spp}}{r_{spp}}$.

This work allows us therefore to determine whether solutes or precipitates are more effective at inhibiting dynamic recovery, which is a controversial topic in the literature [83, 104]. Gutierrez-Urrutia et al. [83] investigated the substructure developed during severe plastic deformation by ECAP in various solutionized and precipitated states of a 6082 aluminum alloy. They found that the final deformation structure is more dependent on the amount of solutes rather than the presence of precipitates. This may be due to the small volume fraction (less than 1%) of the present particles [83]. However, in another study [104] where the influence of vanadium addition on the hot deformation behavior of 7150 aluminum alloy was studied, Shi et al. [104] reported that both dispersoids and solutes contribute to the retardation of dynamic recovery and dynamic recrystallization. Vanadium solutes could segregate at subgrain boundaries during hot deformation, acting as barriers to dislocation movement. Dynamic recovery is therefore restrained, leading to the formation of a very fine substructure. At higher levels of vanadium, the precipitation of dispersoids takes place during homogenization, leading to a stronger pinning effect on substructures and therefore to a delay in dynamic recovery and dynamic recrystallization [104]. Based on our observations, a high amount of solutes and/or a high value of $\frac{f_{spp}}{r_{spp}}$ (i.e. a very high number of very fine precipitates) can effectively retard subgrain development.

4.4.3.3 Effect of solutes/precipitates on the initiation of dynamic and post-dynamic recrystallization

As mentioned previously in section 4.4.3.1, the subgrain development is very important for the onset of both dynamic and post-dynamic recrystallization. Due to the delay in subgrain formation, the number of subgrains that can be transformed into viable nuclei is smaller in the case of low $\frac{f_{spp}}{r_{spp}}$ than in the case of medium $\frac{f_{spp}}{r_{spp}}$, resulting therefore in a lower rate of nucleation

in the case of low $\frac{f_{spp}}{r_{spp}}$ (see figure 4.10 (f)). However, as soon as a nucleus is formed, it grows rapidly due to a combined effect of a lower Smith-Zener pinning pressure and a higher density of dislocations in its neighborhood (because of a higher work hardening rate) compared to the state with a medium $\frac{f_{spp}}{r_{spp}}$ (see figure 4.10 (a)).

Due to the very fine and dense dispersion of precipitates, the number of subgrains that can be transformed into viable nuclei is smaller in the case of high $\frac{f_{spp}}{r_{spp}}$ than in the case of medium $\frac{f_{spp}}{r_{spp}}$, explaining thereby the lower number of recrystallized grains examined in the deformed and quenched state with a high $\frac{f_{spp}}{r_{spp}}$ (see figure 4.10 (f)). The growth of these nuclei is subsequently inhibited due to the higher Smith-Zener pinning pressure compared to the state with a medium $\frac{f_{spp}}{r_{spp}}$ (see figure 4.10 (c)).

4.5 Evolution of microstructure during post-deformation holding

The evolution of the deformed microstructure during post-deformation holding is shown by figure 4.16 for the three different initial precipitate states (i.e. values of $\frac{f_{spp}}{r_{spp}}$ right before deformation). It is clear from figure 4.16 that the recrystallization kinetics during post-deformation holding are influenced by the precipitation state right after deformation.

The recrystallization behavior seems to be the slowest for the case of high $\frac{f_{spp}}{r_{spp}}$. Large recrystallized grains start to appear only after holding for 120 s after deformation in this case unlike in the case of medium and low values of $\frac{f_{spp}}{r_{spp}}$ where large recrystallized grains start to appear after holding for 20 s. This delay in the formation of large recrystallized grains may be due to the very fine and dense precipitation state that is generated both before deformation and during deformation (see figure 4.5, states 2c and 3c and figure 4.8 (c)). Therefore, precipitates that are formed right before deformation as well as during deformation seem to retard the development of large recrystallized grains during post-deformation holding.

In the case of low $\frac{f_{spp}}{r_{spp}}$, the recrystallization kinetics seem to vary with holding time. The development of large recrystallized grains is very rapid in the first 20 seconds of post-deformation holding. The number of large recrystallized grains does not seem to change when the holding time is increased to 40 s or 120 s, suggesting that the recrystallization kinetics are slowing down with post-deformation holding time. This slowdown may be due to the additional precipitation occurring during post-deformation holding (see figure 4.5, state 3a and figure 4.8 (a)) and/or to recovery of the deformed grains and/or to the fact that high stored energy areas are consumed first.

Grain boundaries in the case of low $\frac{f_{spp}}{r_{spp}}$ may provide favorable sites for nucleation of precipitates. Therefore, SEM BSE images (see figure 4.17) are taken around boundaries of large recrystallized grains to verify whether the precipitates that form during post-deformation holding are located preferentially at grain boundaries. For this purpose, the sample has been prepared for semi-quantitative analysis (according to the protocol of section 3.2.2.1). Figure 4.17

(b) shows the distribution of precipitates after holding for 40 s in the case of a low initial $\frac{f_{spp}}{r_{spp}}$. It is clear from this SEM BSE image that the precipitates that are formed prior to and/or during deformation seem to be distributed homogeneously through the microstructure.

Quantitative analyses (based on the method described in section 3.2.2.2) of the precipitation states right after deformation and after holding for 40 s would be required in order to confirm whether the precipitate distribution is homogeneous or heterogeneous with grain boundaries enriched with precipitates. Higher magnification SEM BSE images or TEM analysis could also help determining if there are finer precipitates that form preferentially at grain boundaries and that cannot be seen at such magnification.

For the medium value of $\frac{f_{spp}}{r_{spp}}$, the microstructure is almost completely recrystallized after holding for 120 s, suggesting that the precipitates that are formed prior to deformation and during deformation are not sufficient to hinder the development of large recrystallized grains. This is probably due to the fact that the driving pressure for development of large recrystallized grains is higher than the Smith-Zener pinning pressure. A more in depth study of the reasons behind the development of these large recrystallized grains will be presented in Chapter 5.

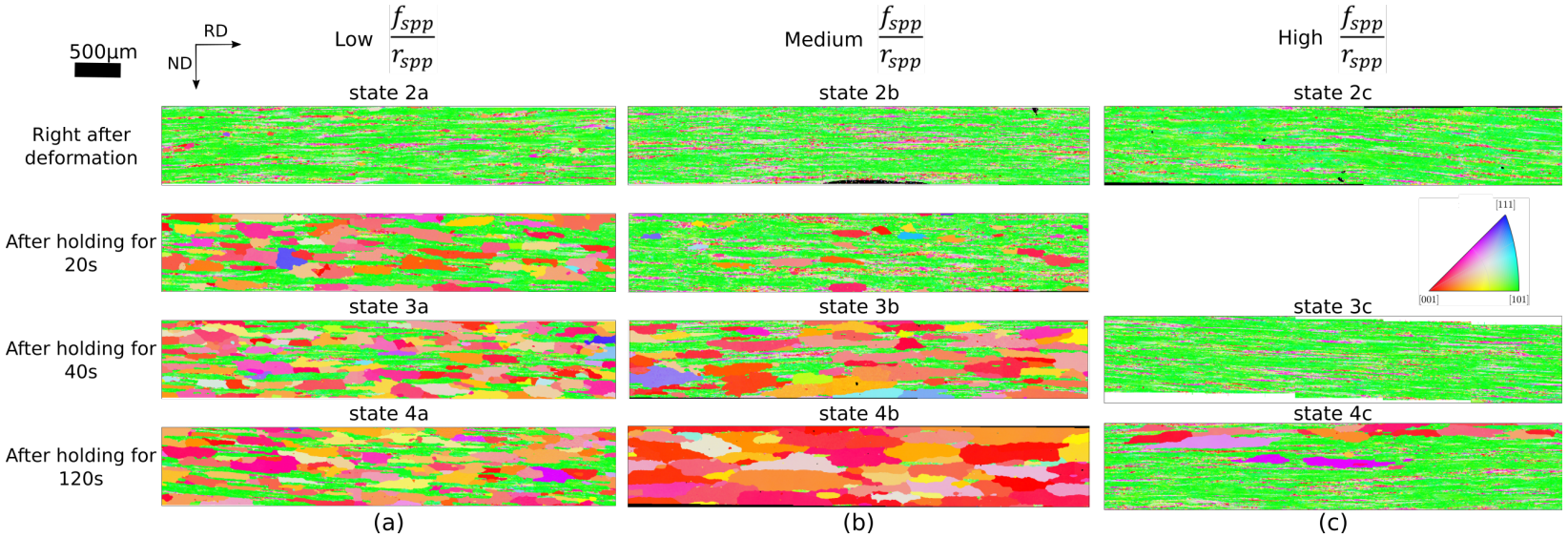

Fig. 4.16 EBSD orientation maps showing the evolution of microstructure during post-deformation holding for the three different values of $\frac{f_{spp}}{r_{spp}}$. The color code defined on the standard triangle refers to the normal direction. The measurement step size is 3 μm.

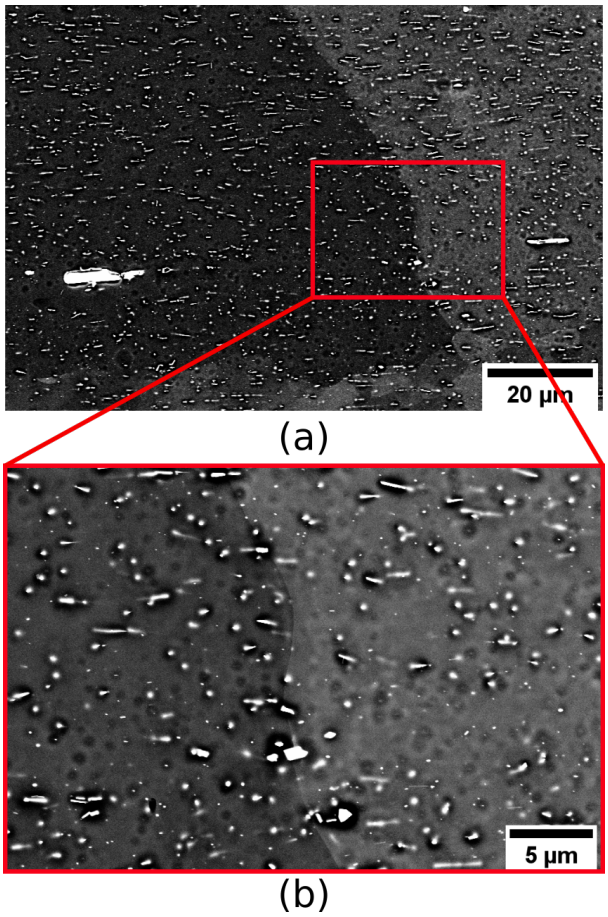

Fig. 4.17 SEM BSE low (a) and high (b) magnification images showing the spatial distribution of precipitates after holding for 40 s in the case of low value of $\frac{f_{spp}}{r_{spp}}$.

4.6 Summary

Three states with different values of $\frac{f_{spp}}{r_{spp}}$ right before deformation are generated and subsequently deformed at the same testing conditions. Only soluble phases have been considered for the calculation of f_{spp} and r_{spp}. In the case of low $\frac{f_{spp}}{r_{spp}}$, it has been shown that additional fine precipitation occurs during hot deformation and holding after deformation. In the case of medium $\frac{f_{spp}}{r_{spp}}$, the area fraction of precipitates does not change during deformation, whereas the size of precipitates decreases, suggesting thereby the breakage of precipitates during deformation. However, during holding, precipitates do not evolve in this state. In the case of high $\frac{f_{spp}}{r_{spp}}$, it is more difficult to conclude about the evolution of precipitates during deformation. The decrease in the total area fraction of precipitates, the decrease in the mean size of precipitates and the increase in the number of finer precipitates (i.e. having an equivalent diameter ≤ 0.4 µm) suggest the occurrence of dissolution of metastable particles and re-precipitation of finer precipitates during deformation. The formed precipitates do not evolve afterwards during holding in this sample.

Regarding the evolution of microstructure during deformation, it has been found that dy-

namic recovery and dynamic and post-dynamic recrystallization take place in all states regardless of their initial values of $\frac{f_{spp}}{r_{spp}}$. Nevertheless, the rate of dynamic recovery depends on both the values of $\frac{f_{spp}}{r_{spp}}$ (proportional to Smith-Zener pinning) and f_{spp} (inversely proportional to solute drag) during deformation. The lowest work hardening rate and the highest dynamic recovery rate are observed for the state with medium $\frac{f_{spp}}{r_{spp}}$. This has been explained in details in this chapter. It has been also found that a high amount of solutes and/or a high number of very fine precipitates during deformation can effectively retard subgrain development.

It has been demonstrated in this chapter that the subgrain development is very important for the initiation of dynamic and post-dynamic recrystallization. The influence of subgrain development on the nucleation is discussed in detail. Both the Smith-Zener pinning pressure and the surrounding dislocation density are found to control the subsequent growth of these nuclei.

Finally, the evolution of microstructure during post-deformation holding is studied in the three states with different values of $\frac{f_{spp}}{r_{spp}}$. It has been found that the growth kinetics are very dependent on the precipitation state right after deformation. The state with a medium initial value of $\frac{f_{spp}}{r_{spp}}$ recrystallized more easily than the two other states, leading to the formation of coarse recrystallized grains. The reasons behind the development of such coarse recrystallized grains will be studied in more details in chapter 5. The state with the highest initial value of $\frac{f_{spp}}{r_{spp}}$ shows the slowest growth kinetics due to the highest Smith-Zener pinning effect compared to the other two states. In the state with medium $\frac{f_{spp}}{r_{spp}}$, the growth kinetics seem to vary with holding time, being first fast and then slow. This could be due to the precipitation that occurs during holding. Additional quantitative analyses would be needed in order to confirm whether the additional precipitates form preferentially at migrating grain boundaries.

In-depth study of coarse recrystallized grains formed after deformation

Contents

In chapter 4, the study of the microstructure evolution during post-deformation holding shows the formation of coarse recrystallized grains in all three microstructures (figure 4.16), but coarser in those defined by medium and high initial $\frac{f_{spp}}{r_{spp}}$. As mentioned in chapter 2, the factors behind the formation of these grains are numerous and it is quite challenging to determine precisely the main factors contributing to this phenomenon. Therefore, the objective of this

chapter is to determine the possible factors leading to the growth of a few recrystallized grains at the expense of others.

First of all, the chapter begins with a description of the coarse recrystallized grains observed in the sample with a medium initial $\frac{f_{spp}}{r_{spp}}$. Second, the reasons behind the appearance and evolution of these grains are investigated.

5.1 Characteristics of coarse recrystallized grains developed during post-deformation holding

Figure 5.1 (a) shows the evolution of the microstructure during post-deformation holding in the case of medium $\frac{f_{spp}}{r_{spp}}$. It is evident that coarse recrystallized grains develop during post-deformation holding. Figure 5.1 (b) shows the evolution of the number of recrystallized grains per unit area during post-deformation holding. The number of recrystallized grains per unit area increases during the first 20s of holding after deformation, confirming the occurrence of post-dynamic recrystallization. The number of recrystallized grains per unit area decreases subsequently, suggesting that some recrystallized grains grow at the expense of both deformed matrix and other recrystallized grains. Figure 5.1 (a) shows also that coarse recrystallized grains possess an elongated shape when they are observed in the RD-ND plane, showing that the coarse recrystallized grains develop more in the RD than in the ND.

The possible factors behind the overgrowth of some recrystallized grains and their anisotropic behavior will be investigated in section 5.2.

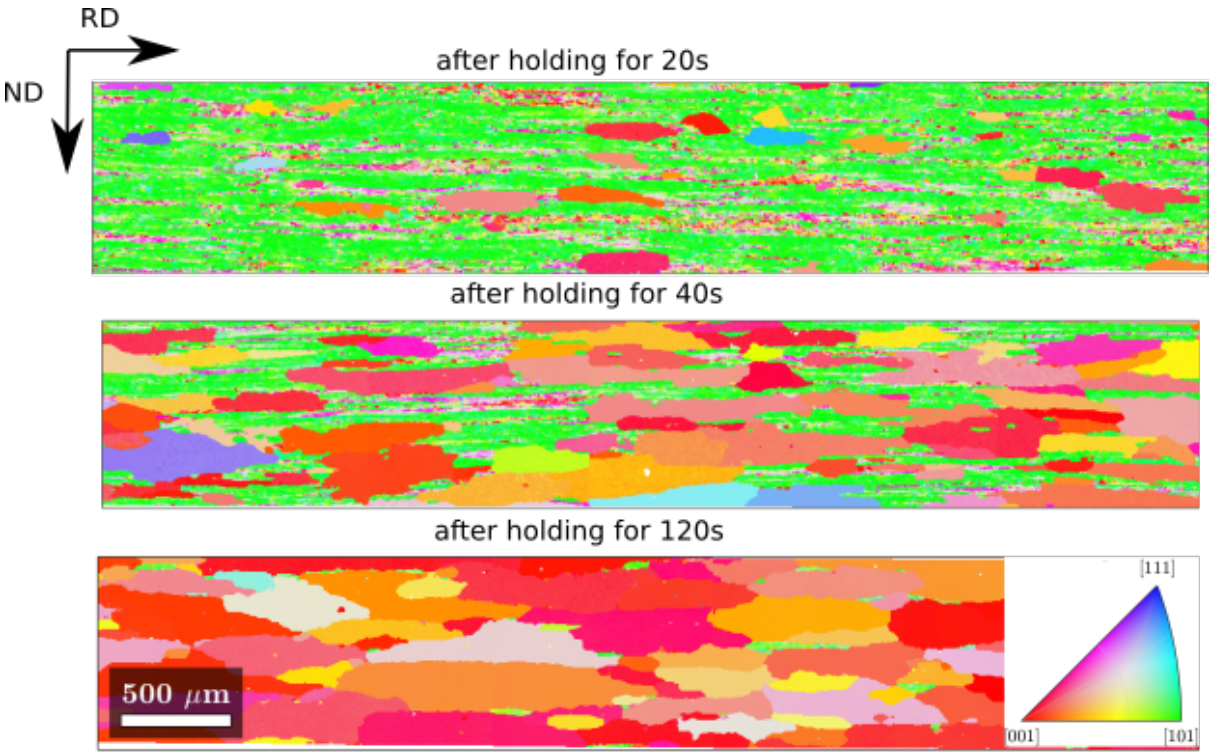

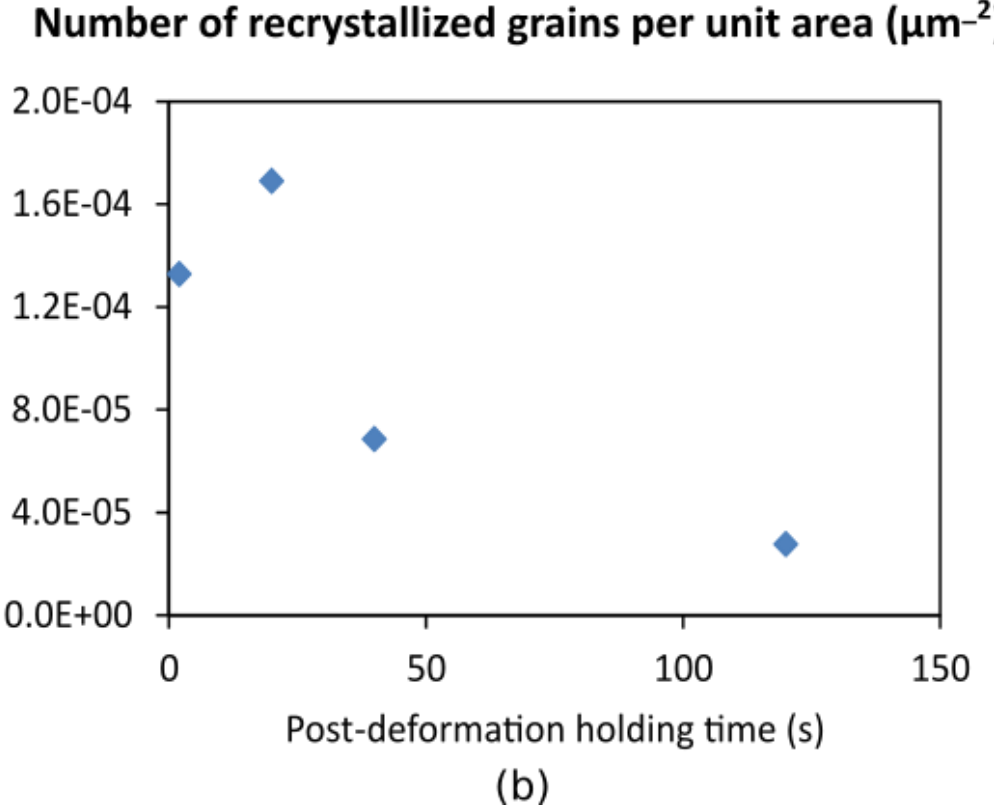

Fig. 5.1 (a) Stitched EBSD orientation maps showing the development of coarse recrystallized grains in the state with initially a medium $\frac{f_{spp}}{r_{spp}}$ that has been deformed at a nominal temperature of 430 °C, a strain rate of 3 s^{-1} and a strain of 2.4 and held for different holding times before quenching. The color code defined on the standard triangle refers to the normal direction. The measurement step size is 3 μm. (b) Evolution of the number of recrystallized grains per unit area during post-deformation holding.

5.1.1 Distribution of stored energy across coarse recrystallized grain boundaries

Figure 5.2 (a) shows a magnified EBSD map acquired on the sample deformed and quenched after holding for 20s. Small recrystallized grains can be detected in this region in addition to the presence of two coarse recrystallized grains (see figure 5.2 (b) where only recrystallized grains are plotted).

The KAM of each pixel in the EBSD orientation map is calculated to estimate the density of geometrically necessary dislocations and therefore the corresponding stored energy as can be shown by figure 5.2 (c). It is evident from figure 5.2 (c) that coarse recrystallized grains have a low stored energy compared to the surrounding deformed grains, which confirms that grain overgrowth is a stored energy driven phenomenon unlike abnormal grain growth.

The GAM values are subsequently calculated as the average of KAM values within each grain and plotted in figure 5.2 (d). The GAM map shows clearly that some small recrystallized grains exhibit low GAM values similar to those of coarse recrystallized grains. The difference in stored energy between recrystallized grains and deformed ones has been reported as a key factor leading to the formation of coarse recrystallized grains [59, 105]. Therefore, the ΔGAM values at grain boundaries are determined from figure 5.2 (d) and both distributions of ΔGAM values at the boundaries between coarse recrystallized grains and their neighboring grains and those between small recrystallized grains and their neighboring grains are shown by figure 5.2 (e). Some boundaries between small recrystallized grains and their neighborhood present similar ΔGAM values as the boundaries between coarse recrystallized grains and their neighborhood, suggesting that grain overgrowth cannot be explained only by the difference in stored energy between coarse recrystallized grains and their neighborhood. There may be another factor that is promoting the preferential growth of some recrystallized grains over others and/or preventing small recrystallized grains from overgrowth. This will be investigated in more details in section 5.2.

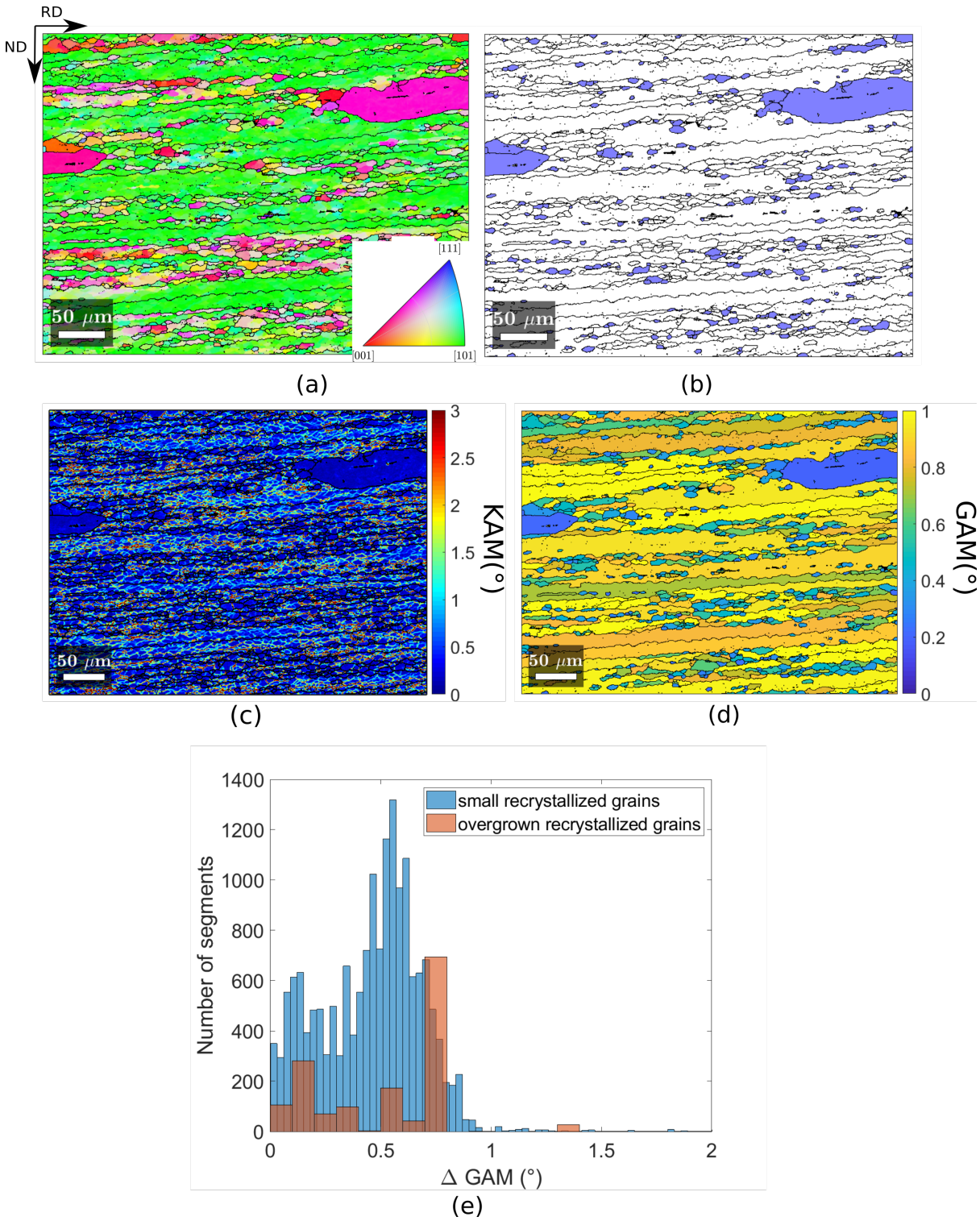

Fig. 5.2 (a) Higher magnification EBSD orientation map with a smaller measurement step size (0.4 µm) showing grain boundaries in black lines. The color code defined on the standard triangle refers to the normal direction. (b) Grain boundary map showing recrystallized grains in blue and grain boundaries in black lines. (c) Corresponding KAM map. (d) Corresponding GAM map. (e) Histograms showing both distributions of ΔGAM for the boundaries between coarse recrystallized grains and first neighbor deformed ones and for the boundaries between small recrystallized grains and first neighbor deformed ones.

5.1.2 Texture of coarse and small recrystallized grains

The evolution of texture of different types of grains (i.e. deformed, large and small recrystallized grains) is shown in figure 5.3 (a-c). The $\{111\}$ pole figures of main ideal orientations in FCC materials are represented on figure 5.4. By comparing the $\{111\}$ pole figures shown in figure 5.3 with figure 5.4, deformed grains seem to be mostly Brass oriented. The intensity of Brass texture component seems to be increasing with holding time for deformed grains, which means that deformed grains with other orientations are consumed first.

The texture of coarse recrystallized grains seems to be mostly Cube oriented with a wide scatter around the ideal Cube orientation. The Cube texture of coarse recrystallized grains gets stronger with increasing holding time. This is confirmed quantitatively by figure 5.3 (d), which shows clearly that the dominant texture components measured for coarse recrystallized grains are Cube, Cube rotated about 18° around ND and Cube rotated about 20° around RD (i.e. abbreviated in the following by "near Cube" including these three components).

It is important to note that the coarse recrystallized grains, observed after holding for 120 s and having a "near Cube" orientation, represent only $40\,\%$ of the surface covered by all large recrystallized grains (see figure 5.3 (d)), meaning that "near Cube" oriented recrystallized grains are not the only grains that can overgrow. Other oriented recrystallized grains can also overgrow to reach abnormally large sizes.

For small recrystallized grains (see figures 5.3 (c) and (e)), the texture seems to be quite random after holding for 20s after deformation. As holding time increases to 120s, the Cube texture component becomes the strongest with again wide scattering, suggesting that the remaining small recrystallized grains that are not consumed by coarse recrystallized grains are mostly "near Cube" oriented. This makes sense because similarly oriented grains are usually separated by a boundary of a low angle misorientation and hence of a low mobility. Orientation pinning seems to play therefore a role in the migration of boundaries of coarse recrystallized grains. This will be confirmed later in section 5.2.

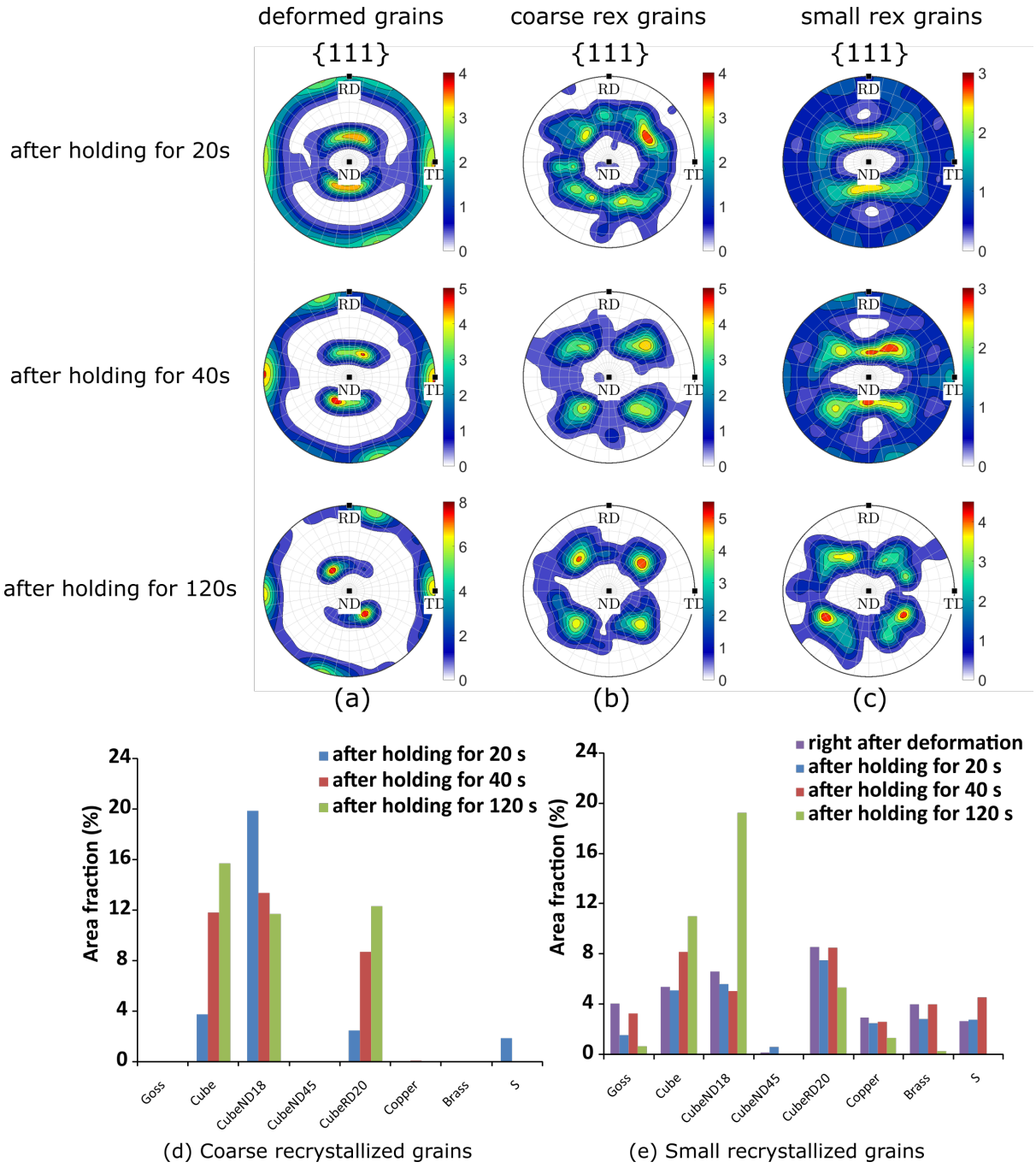

Fig. 5.3 {111} pole figure corresponding to (a) deformed, (b) large and (c) small recrystallized grains (determined from stitched EBSD orientation maps shown by figure 5.1). The texture intensity is expressed in multiple of random distribution (m.r.d). (d) Evolution of area fraction of coarse recrystallized grains belonging to main texture components during post-deformation holding. (e) Evolution of area fraction of small recrystallized grains belonging to main texture components during post-deformation holding.

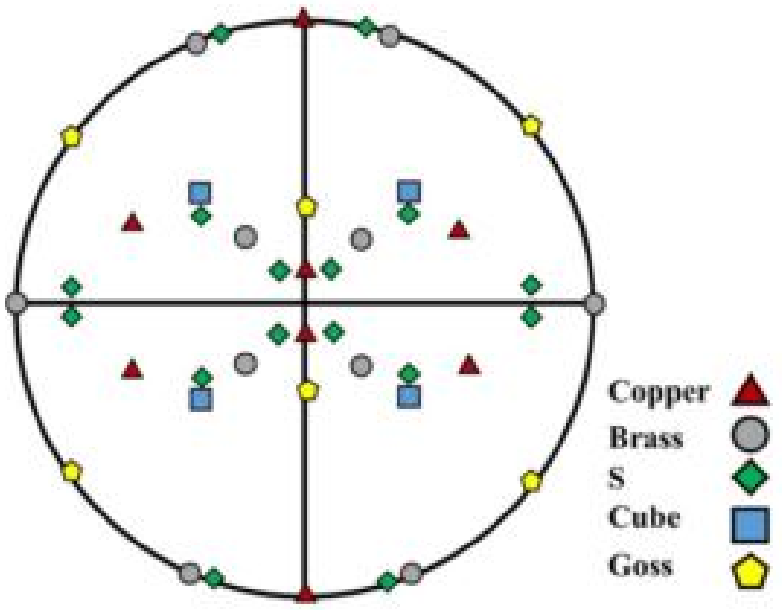

Fig. 5.4 {111} pole figure showing the main ideal crystal orientations of an FCC material [106].

5.1.3 Distribution of precipitates inside and around coarse recrystallized grains

The interaction between recrystallized grains and second phase particles is studied by taking BSE images around the boundaries of coarse recrystallized grains as well as in regions where no coarse recrystallized grains are observed, as can be seen in figure 5.5.

The zoom into the recrystallization front of a coarse recrystallized grain (see figure 5.5 (b)) shows that precipitates are also located inside the coarse recrystallized grain, suggesting that the coarse recrystallized grain boundaries have been able to overcome the Smith-Zener pinning pressure exerted by these precipitates and break away from them. The spatial distribution of precipitates in the coarse recrystallized grain seems to be qualitatively similar to that in the region where no coarse recrystallized grains are present.

Figure 5.5 (b) shows also an Fe containing particle that is aligned with the RD and that is located at the boundary of the coarse recrystallized grain. This observation suggests that the Fe containing particles aligned with the RD may slow down the migration of boundaries in the ND, which will be studied in more details in section 5.2.

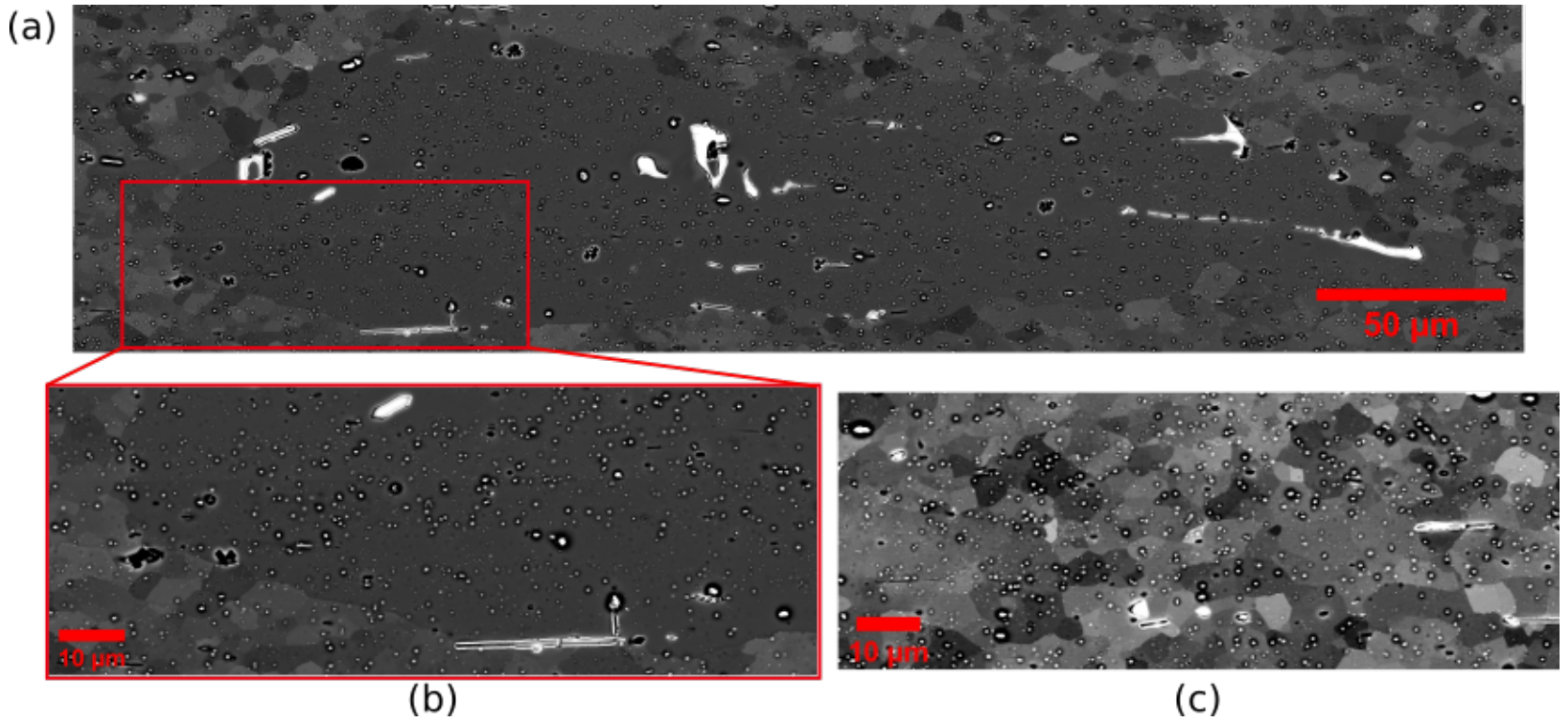

Fig. 5.5 (a) Stitched BSE images showing the distribution of second-phase particles inside and around a coarse recrystallized grain, (b) A zoom on the region marked by a red box in (a), (c) BSE image showing the distribution of second-phase particles in the region that is free from coarse recrystallized grains. The examined sample corresponds to the sample that is water quenched after holding for 20 s after hot deformation. The sample is electropolished using electrolytic solution A2 provided by Struers before BSE examination.

To summarize, the characteristics of coarse recrystallized grains including stored energy, crystallographic texture and spatial distribution of precipitates seem to be quite similar to the ones of small recrystallized grains at first glance. Therefore, a detailed investigation of the reasons behind the overgrowth of some recrystallized grains over others is required. For this purpose, in addition to the hot compression tests followed by different holding times, several annealing steps are performed on the same deformed and water quenched sample in order to sequentially describe the appearance and evolution of these coarse recrystallized grains. The results are analyzed and discussed in the light of the possible causes for grain overgrowth detailed in the literature review part.

5.2 Development of coarse recrystallized grains followed by sequential annealing in the SEM chamber

5.2.1 Initial microstructure used for sequential annealing

As explained in the experimental part, the initial microstructure is taken from the state with a medium $\frac{f_{spp}}{r_{spp}}$ that has been water quenched right after deformation at a temperature of 430 °C, a strain rate of 3 s^{-1} and a strain of 2.4. The RD-TD plane is examined during sequential annealing due to sample preparation constraints as explained again in the experimental part.

The region of interest that is studied by sequential annealing coupled to EBSD is shown by figure 5.6 (a). The deformed grains are less elongated in the RD-TD plane than in the RD-ND (see figure 4.9 in section 4.4 for comparison).

A zoom into a selected area in this EBSD orientation map (see figure 5.6 (b)) shows that the microstructure right after deformation contains already small recrystallized grains (their boundaries being plotted in red), which is consistent with section 4.4. Figure 5.6 (c) shows that dynamically recrystallized (DRX) and post-dynamically recrystallized (PDRX) grains coexist. Unlike the PDRX grains, the DRX grains are the ones that have inhomogeneous orientation, thus that contain substructures (indicated by blue lines).

The average equivalent diameter of recrystallized grains including both DRX and PDRX ones is about 7.7 µm with a standard deviation of 3.5 µm in the RD-TD plane, which is almost similar to that determined in the RD-ND plane (i.e. about 7.0 µm with a standard deviation of 2.8 µm, see figure 4.9 (b) in section 4.4).

The texture of recrystallized grains as well as that of deformed matrix measured in the RD-TD plane are shown in figure 5.6 (d). Both textures are consistent with those measured in the RD-ND plane right after deformation (see figure 4.11 in section 4.4 for comparison). The recrystallized grains do not exhibit therefore any strong preferred orientation while the deformed grains are mostly Brass and Goss oriented.

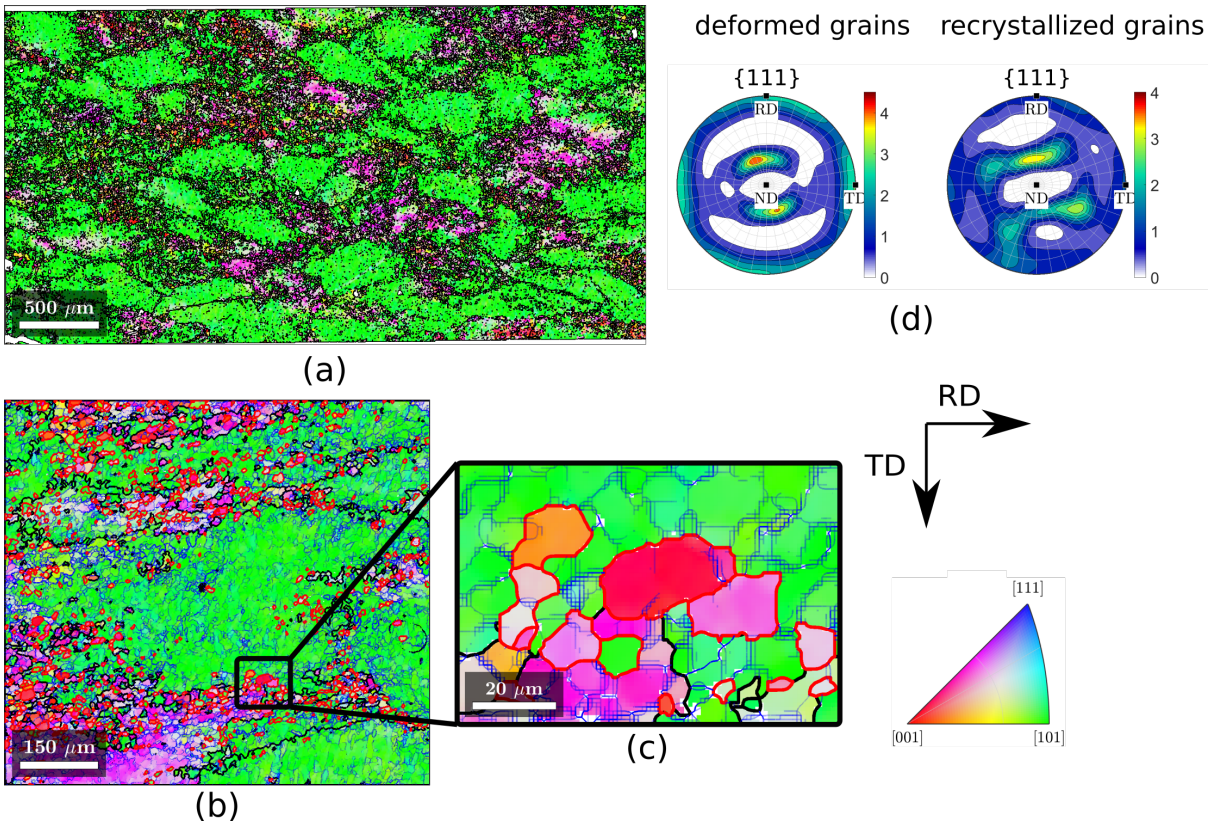

Fig. 5.6 Microstructure quenched right after deformation: (a) EBSD orientation map in the RD-TD plane. Measurement step size is 3 µm. Grain boundaries (θ higher than 10°) are plotted in black lines. (b) A magnified EBSD orientation map showing recrystallized grain boundaries in red, deformed grain boundaries in black and sub-boundaries (θ between 1 and 10°) in blue. A smaller measurement step size (1 µm) is used. (c) A zoom into (b) showing recrystallized grains containing substructure with same measurement step size as in (b). The color code defined on the standard triangle refers to the normal direction. (d) $\{111\}$ pole figures corresponding to deformed and recrystallized grains respectively (determined from EBSD orientation map in (a)). The texture intensity is expressed in multiple of random distribution (m.r.d).

5.2.2 Post-dynamic appearance of coarse recrystallized grains during sequential annealing

The evolution of the region of interest (ROI) detailed in figure 5.6 during sequential annealing using a heating stage in the SEM chamber is shown in figure 5.7. Grain overgrowth occurs also during sequential annealing. A comparison between the recrystallization fractions obtained during both types of experiments (see figure 5.8) shows a lookalike behavior, confirming that surface effects possibly biasing sequential annealing are negligible in the presence of stored energy.

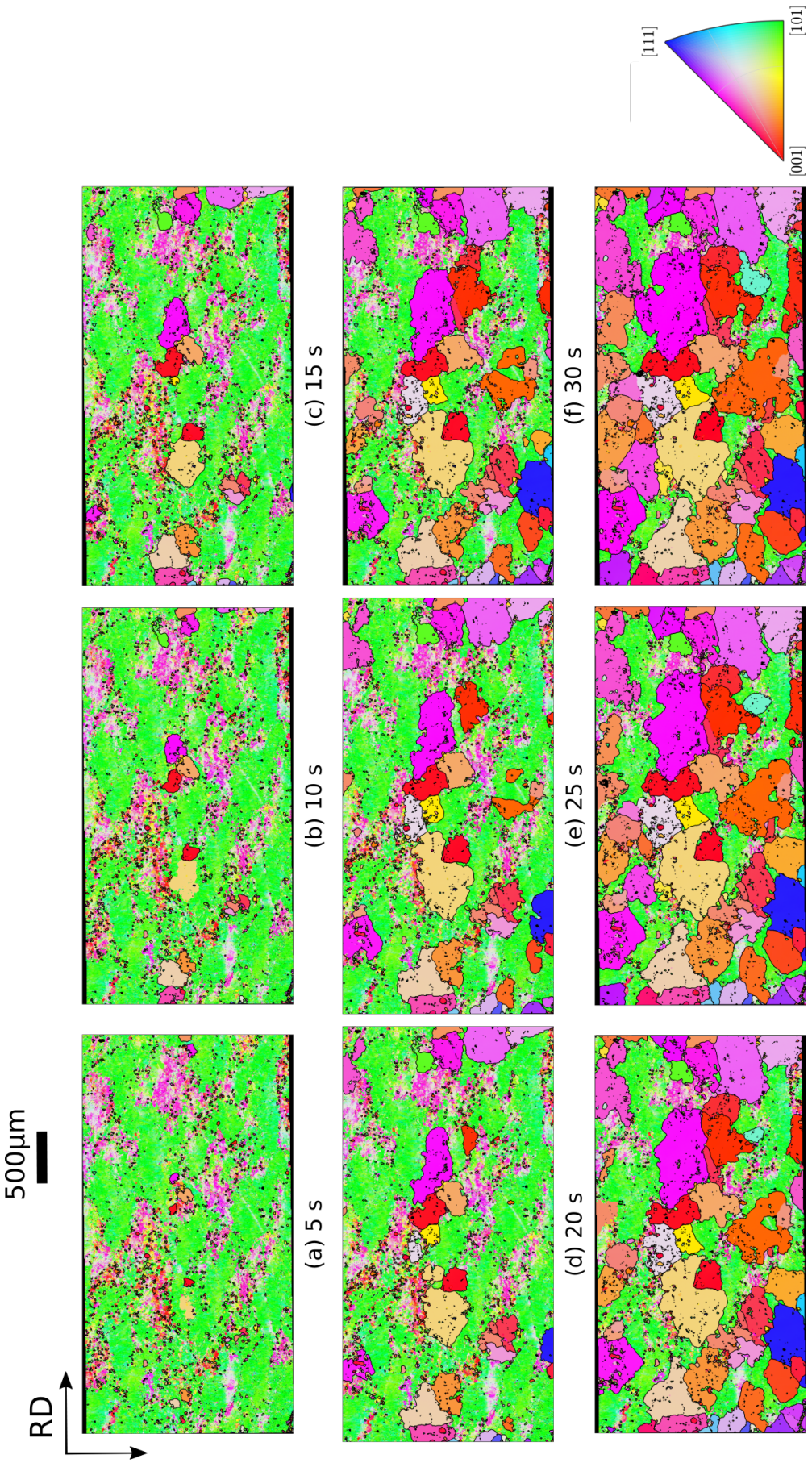

Fig. 5.7 (a-i) EBSD orientation maps showing microstructure evolution during successive annealing steps using a fast heating stage coupled to SEM. The boundaries of recrystallized grains are plotted in black. The color coding defined in the standard triangle refers to ND. The measurement step size is 3 µm.

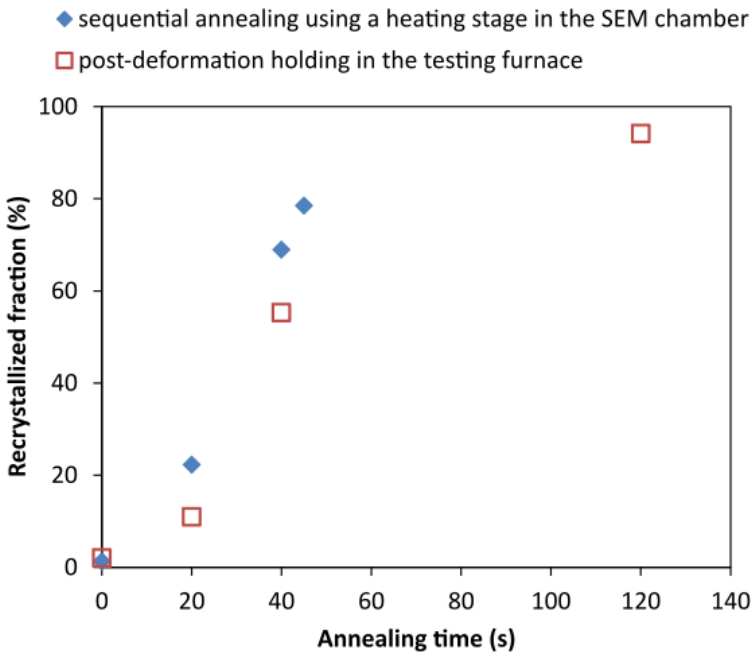

Fig. 5.8 Comparison of recrystallization kinetics between post-deformation holding in the testing furnace and sequential annealing of a deformed and quenched sample using a heating stage in the SEM chamber.

As mentioned in section 5.1, the coarse recrystallized grains possess an elongated shape when they are observed in the RD-ND plane. However, when they are examined in the RD-TD plane, they appear less elongated (see figure 5.7 (j)), showing that the coarse recrystallized grains develop more in the RD and TD than in the ND. The characteristics of these coarse recrystallized grains are further detailed in the following sub-sections.

5.2.2.1 Stored energy

Figure 5.9 shows the KAM maps corresponding to the EBSD orientation maps shown in figure 5.7. It evident from figures 5.9 (b) and (c) that the coarse recrystallized grains develop in regions with high KAM values (i.e. high stored energy), suggesting that the development of coarse recrystallized grains is driven mostly by stored energy differences.

It is important to note also the presence of small recrystallized grains (i.e. indicated by white arrows in figure 5.9 (i)) which have not grown much although their stored energy seems to be very low. This suggests that stored energy is not the only factor governing the migration of boundaries. This will be confirmed in section 5.3.

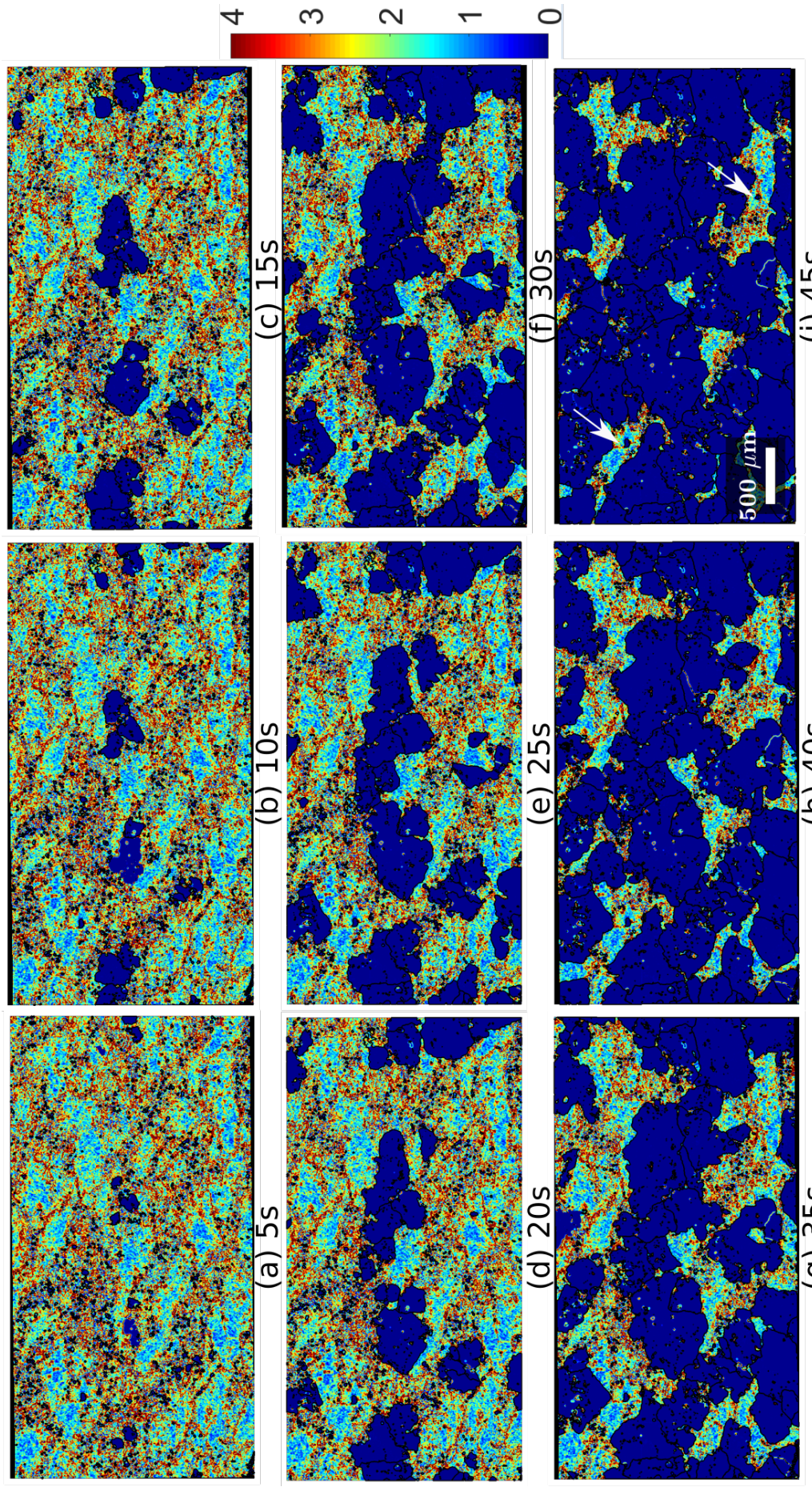

Fig. 5.9 Evolution of KAM values (°) during different sequential annealing steps. The boundaries of recrystallized grains are plotted in black lines.

5.2.2.2 Crystallographic texture of coarse and small recrystallized grains

The crystallographic texture of large and small recrystallized grains is studied in this paragraph. For this purpose, $\{111\}$ pole figures of small and coarse recrystallized grains are plotted at different sequential annealing steps in figures 5.10 (a) and (b) respectively. The evolution of both textures of small and coarse recrystallized grains in the RD-TD plane is consistent with that measured in the RD-ND plane (shown in figure 5.3). Small recrystallized grains do not show any particular orientation at the beginning, but as sequential annealing time increases, a Cube texture with a wide scattering becomes more prominent, confirming that the small "near Cube" oriented recrystallized grains are less likely to be consumed by coarse recrystallized grains, themselves being also "near Cube" oriented.

These observations are confirmed by figures 5.10 (c) and (d), where the area fractions of small and coarse recrystallized grains belonging to main texture components are calculated after different sequential annealing steps and shown respectively. It is evident that small recrystallized grains show a random texture, with a slight increase in the area fractions of "near Cube" oriented grains at the last sequential annealing steps (i.e., Cube, Cube rotated about 18° around ND and Cube rotated about 20° around RD), while, coarse recrystallized grains have mostly a "near Cube" orientation throughout the whole sequential annealing experiment. This confirms therefore that "near Cube" oriented grains develop preferentially compared to other oriented grains.

In order to double-check for the absence of any significant artifact associated with these observations of the microstructure evolution at a free surface, the texture of coarse recrystallized grains obtained after 40 s of sequential annealing is compared with the one obtained after 40 s of post-deformation holding (see figure 5.11). A weaker "near Cube" texture is found for coarse recrystallized grains during sequential annealing. This could possibly be a statistical effect associated with the lower number of grains included in the region of interest of the sequential annealing experiment.

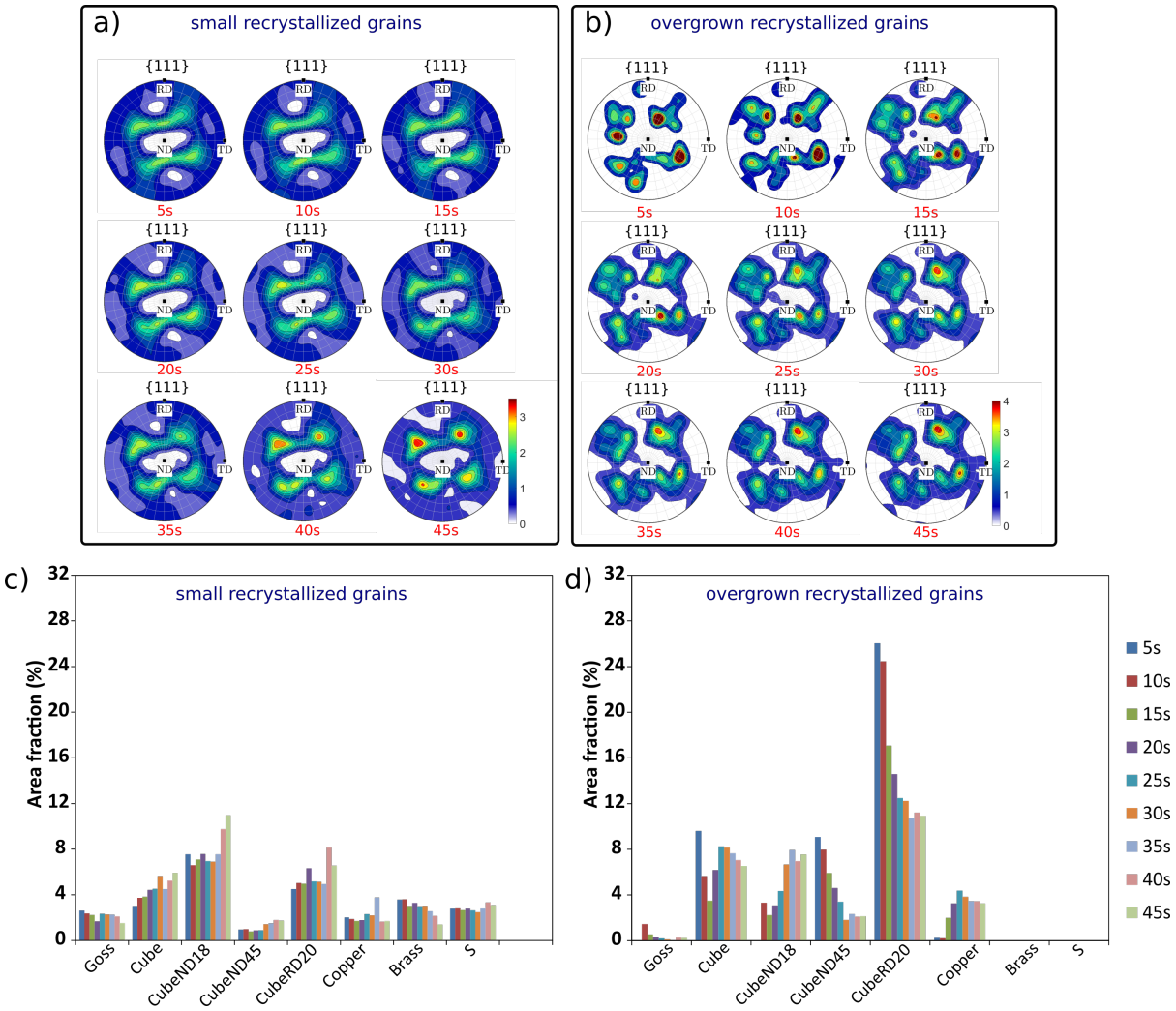

Fig. 5.10 (a,b) {111} pole figures corresponding to small and coarse recrystallized grains at different sequential annealing steps respectively (determined from EBSD orientation maps shown in figure 5.7). The texture intensity is expressed in multiple of random distribution (m.r.d). (c,d) Evolution of area fraction of small and coarse recrystallized grains belonging to typical texture components respectively.

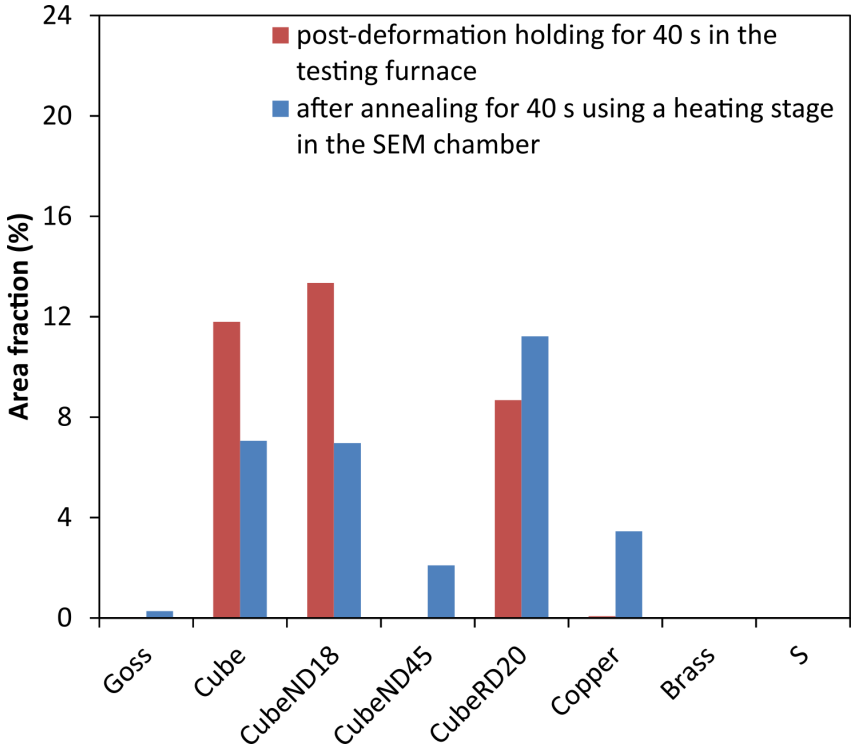

Fig. 5.11 Comparison of orientation of coarse recrystallized grains observed after 40 s between post-deformation holding in the testing furnace and sequential annealing in the SEM chamber.

5.2.2.3 Distribution of precipitates

In order to study the effect of precipitates on the stagnation of few small recrstallized grains, BSE images were taken around both coarse recrystallized grains and small recrystallized grains located in the region of interest of the sequential annealing experiment and compared as shown by figure 5.12.

Figure 5.12 shows the spatial distribution of precipitates around large and small recrystallized grains. Figure 5.12 (a) shows some coarse recrystallized grains. The low magnification BSE images taken around both a fast moving boundary (i.e. boundary between a coarse recrystallized grain and a deformed one, see figure 5.12 (b)) and a non-moving boundary (i.e. boundary between a small recrystallized grain and a deformed one, see figure 5.12 (d)) do not show any visible difference between the two spatial distribution of precipitates at first sight. High magnification BSE images are taken around these two boundaries as shown by figures 5.12 (c) and (e). It is clear that precipitates are located at and around these boundaries regardless their type (i.e. moving or non-moving).

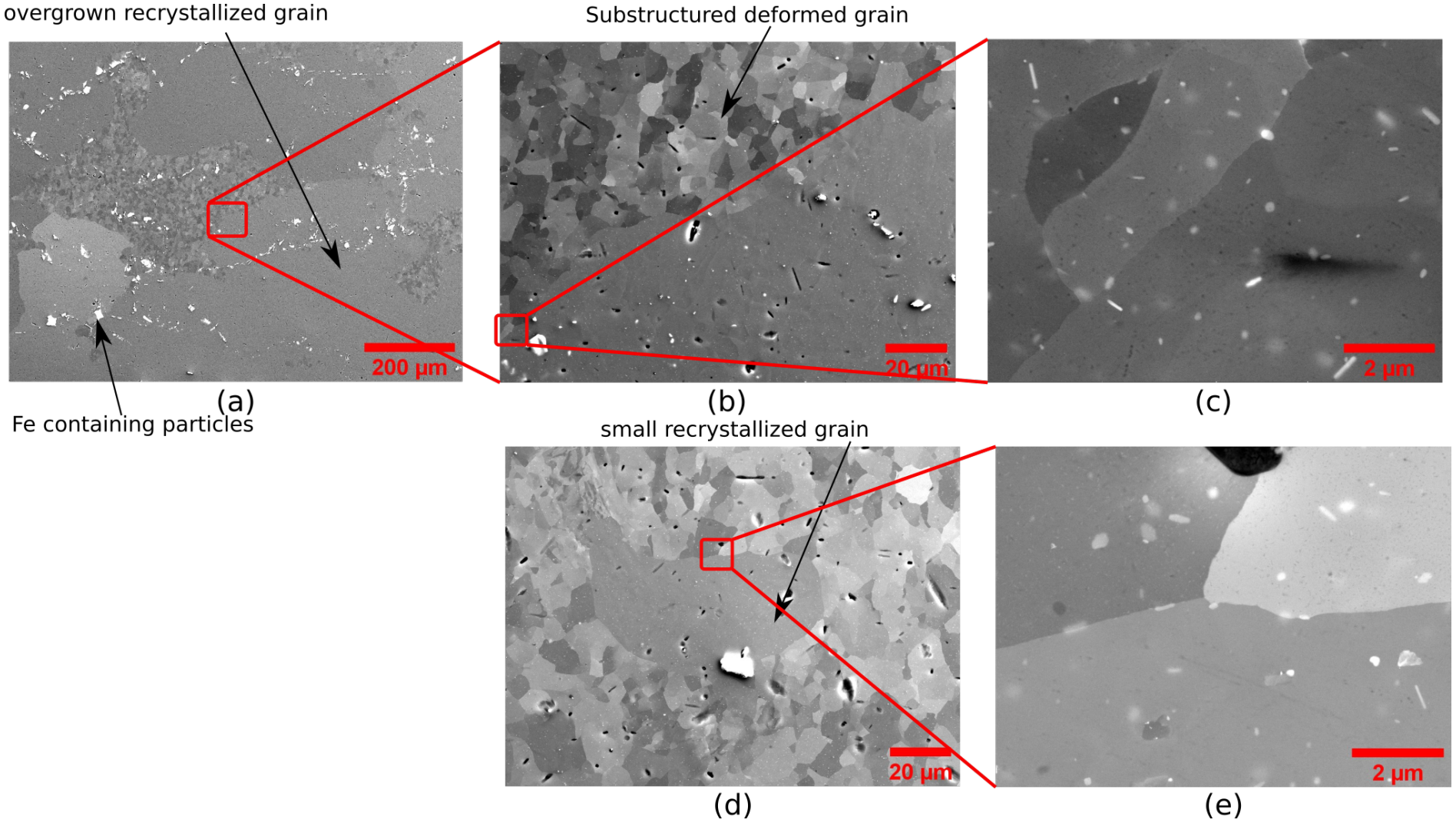

Fig. 5.12 BSE images showing the precipitate content around boundaries of large (a-c) and small (d-e) recrystallized grains respectively. The sample has been prepared according to section 3.3.1. The BSE images are taken on the sample that is annealed sequentially for 45 s in the SEM chamber.

To summarize, the characteristics of coarse recrystallized grains (i.e. stored energy, crystallographic texture and precipitates in the neighborhood) examined in the RD-TD plane during sequential annealing are similar to these examined in the RD-ND plane during post-deformation holding. The only visible difference is the shape of coarse recrystallized grains. They are less elongated in the RD-TD plane (observed during sequential annealing) than in the RD-ND plane (observed after post-deformation holding), which shows that they develop more in the RD and TD than in the ND. The reasons behind the anisotropic growth of these grains will be explored in section 5.3.4.

5.3 Exploring possible factors leading to grain overgrowth

The origin of Cube orientation has been extensively studied in the past in different materials including copper [107], Al-Mn-Mg alloys [38, 39] and commercial purity aluminum [36, 41]. However, there is still debate about it [108]. This section aims to discuss the factors possibly leading to the overgrowth of "near Cube" oriented grains in the studied alloy.

5.3.1 Initial size advantage of "near Cube" oriented recrystallized grains

One possible explanation of "near Cube" oriented grain overgrowth is that "near Cube" oriented subgrains dynamically recover more rapidly than other orientations, achieving therefore a low stored energy configuration that allows them to bulge out as DRX or PDRX "near Cube" nuclei from the very beginning of recrystallization. Such faster dynamic recovery would give rise to a size advantage for the "near Cube" recrystallized grains present at the end of deformation (i.e. after deformation and quenching). The size distribution of both "near Cube" and other-oriented recrystallized grains examined right after deformation before holding is displayed on figure 5.13. The mean size for "near Cube" oriented recrystallized grains ($\approx$ 9 µm) is indeed slightly higher than for other oriented recrystallized grains ($\approx$ 7 µm). The size distribution of "near Cube" oriented recrystallized grains is ranging from 5 µm to 25 µm, while the size distribution of other oriented recrystallized grains is ranging from 4 µm to 30 µm.

This means that the largest recrystallized grain obtained right after deformation does not necessarily have a "near Cube" orientation. Therefore, initial size advantage is unlikely to be sufficient to explain the growth advantage of "near Cube" oriented recrystallized grains.

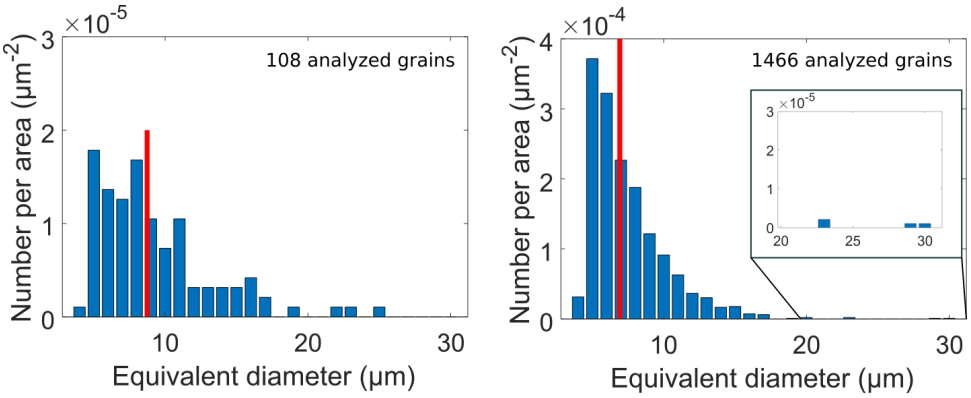

Fig. 5.13 Size distribution for (a) “near Cube” and (b) other oriented recrystallized grains examined right after deformation in the RD-ND plane. The number per area is calculated as the number of recrystallized grains divided by the EBSD orientation map area. Red lines show the average value of the distributions. The analyzed EBSD image is shown in figure 4.9 and its area is 1.127 mm x 0.844 mm.

5.3.2 Contribution of stored energy in the development of coarse “near Cube” recrystallized grains

The local variations in stored energy are estimated through $\left|\overline{KAM}_{neighborhood} - GAM_{rex}\right|$ values as mentioned in section 3.5 and their contribution in the preferential growth of “near Cube” oriented grains is investigated as shown in figure 5.14.

The mean $\left|\overline{KAM}_{neighborhood} - GAM_{rex}\right|$ values for both “near Cube” and other orientations (shown by the red lines) are almost similar in the microstructure right after deformation, meaning that the accumulation of stored energy is almost similar for the close neighborhood of “near Cube” and other oriented recrystallized grains. This suggests that particular local stored energy gradients do not seem to promote the preferential growth of “near Cube” oriented grains in the early stages of recrystallization. This is consistent with the poor size advantage shown in figure 5.13.

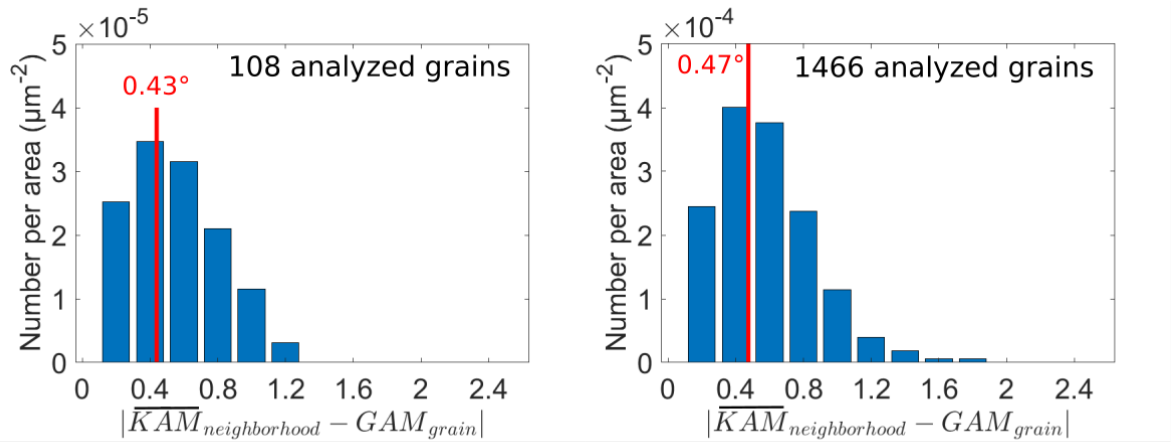

(a) "near" Cube oriented recrystallized grains (b) other oriented recrystallized grains

Fig. 5.14 $\left|\overline{KAM}_{neighborhood} - GAM_{rex}\right|$ distribution for (a) "near Cube" and (b) other oriented recrystallized grains examined right after deformation in the RD-ND plane. The number per area is calculated as the number of recrystallized grains divided by the EBSD orientation map area. The red lines and values represent the average values of the distributions. The analyzed area is 1.127 mm x 0.844 mm. The EBSD measurement step size is 1 μm.

The role of stored energy in boundary migration during post-deformation annealing could be further investigated thanks to the sequential annealing experiments. It is clear that grain overgrowth is stopped when coarse recrystallized grains impinge on each other and that coarse recrystallized grains contain some stable island grains (see figure 5.15). Therefore, grain boundaries can be classified into two types: moving and non-moving boundaries. The moving boundaries consist of the boundaries between coarse recrystallized grains and deformed ones (blue colored in figure 5.15). In contrast, the non-moving boundaries are composed of boundaries between impinged coarse recrystallized grains (brown-colored in figure 5.15), boundaries between island grains and coarse recrystallized ones (green colored in figure 5.15), and boundaries between small recrystallized grains and deformed ones (black colored in figure 5.15).

In this way, moving and non-moving boundaries are determined in each EBSD orientation map (shown in figure 5.15), and the local variations in stored energy are estimated by calculating the $\overline{KAM}_{neighborhood} - GAM_{rex}$ values across these boundaries during different steps of sequential annealing. The results of these calculations are illustrated in figure 5.16.

It is evident from figure 5.16 (a) that the difference in stored energy between deformed matrix and coarse recrystallized grains $\overline{KAM}_{def} - GAM_{coarse}$ is positive and increases during sequential annealing, meaning an increase in the driving pressure between coarse recrystallized grains and deformed matrix. This suggests that as they migrate, the boundaries of the coarse recrystallized grains meet deformed matrix areas with higher stored energy levels. This confirms the role played by the stored energy in the migration of the boundaries between coarse recrystallized grains and deformed matrix.

For boundaries between deformed grains and small recrystallized grains (see figure 5.16 (c)), the number fraction of boundaries having a $\overline{KAM}_{def} - GAM_{small}$ between 0.5° and 1°

increases, while the number fraction of boundaries having a $\overline{KAM}_{def} - GAM_{small}$ higher than 1° decreases. This means that the difference in stored energy across boundaries between small grains and deformed matrix decreases during sequential annealing steps, suggesting that the deformed grains surrounding small recrystallized grains are reducing their stored energy by recovery or that small recrystallized grains grow slightly by consuming the stored energy in their initial close neighborhood and then stop growing.

Figure 5.17 shows the evolution of grain boundaries during different sequential annealing steps. The boundaries between small recrystallized grains and deformed matrix are plotted in black lines, whereas the boundaries of coarse recrystallized grains are plotted in red lines. It is clear from figure 5.17 (a) that the number of recrystallized grains decreases from one annealing step to another because small recrystallized grains are consumed by coarse recrystallized grains that are growing, leading to their complete disappearance or to their transformation into island grains (represented by blue lines in figure 5.17) as indicated by the green arrow on figure 5.17 (b). The decrease in the number fraction of boundaries between small recrystallized grains and deformed ones for $\overline{KAM}_{def} - GAM_{small}$ values higher than 1° suggests that the small recrystallized grains having higher stored energy gradients across their boundaries tend to disappear, while the small recrystallized grains having lower stored energy gradients across their boundaries remain stable. Figure 5.17 (b) shows zooms onto the maps shown by figure 5.17. It is evident from figure 5.17 (b) that the size of small recrystallized grains before their disappearance does not seem to increase with annealing time. Therefore, the recovery of the deformed areas surrounding small recrystallized grains could be also behind the decrease in the driving force for the migration of these boundaries, which is consistent with their stagnation.

For boundaries between coarse recrystallized grains (see figure 5.16 (d)), most of boundaries have a $\overline{KAM}_{coarse} - GAM_{coarse}$ between 0.5° and 1°, meaning that the difference in stored energy between coarse recrystallized grains once they are in contact is very low. This result confirms that the absence of difference in stored energy between coarse recrystallized grains explains their stagnation once they are impinged on one another.

Finally, for boundaries of island grains (see figure 5.16 (b)), the number fraction of boundaries having $\overline{KAM}_{coarse} - GAM_{island}$ between 0.5° and 1° is decreasing whereas the number fraction of boundaries having $\overline{KAM}_{coarse} - GAM_{island}$ lower than 0.5° (including negative values) is increasing during sequential annealing. Figure 5.17 (b) shows clearly that the number of island grains increases with annealing time. These island grains may originate from small recrystallized grains that are formed right after deformation (see green arrow on figure 5.17 (b)) or from subgrains present in deformed grains as can be seen by figure 5.18 (a,b). The increase in the number fraction of boundaries of island grains having negative $\overline{KAM}_{coarse} - GAM_{island}$ values accompanied by a decrease in the number of boundaries of island grains having $\overline{KAM}_{coarse} - GAM_{island}$ between 0.5° and 1° could be explained by the increase in the number of island grains made of subgrains with annealing time. The stored

energy inside coarse recrystallized grains is therefore lower than the stored energy inside island grains made of subgrains. Despite this, the boundaries of these island grains remain immobile (as can be seen by figure 5.17 and figure 5.18 (a,b)), suggesting that the stored energy is not responsible for the occurrence of island grains and that another parameter must be responsible for this.

BSE images showing qualitatively the distribution of precipitates around some island grains (see figure 5.18 (c,d)) suggest that precipitates located at the boundaries of island grains cannot be held entirely responsible for their stagnation either. In fact, the amount of precipitates inside and around island grains seem to be qualitatively similar from these BSE images. Additionally, the precipitates observed around the island grain shown by a black arrow on figure 5.18 (c) suggest that boundaries of this grain were able to break away from the surrounding precipitates to reach the following position after annealing. This clearly indicates that the boundaries of stable island grains are not strongly affected by second-phase particles pinning. The formation of island grains has been attributed to the presence of low mobility or low energy boundaries in many studies [62, 67, 68]. This will be addressed in section 5.3.4.

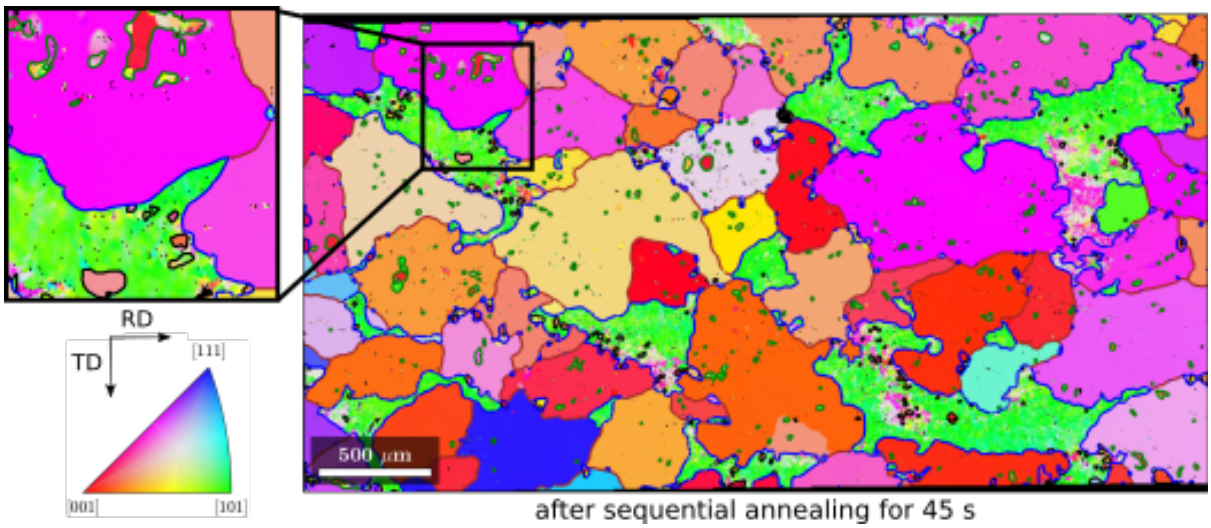

Fig. 5.15 EBSD orientation map of the final state obtained during sequential annealing showing boundaries between coarse recrystallized grains and deformed ones in blue, boundaries between impinged coarse recrystallized grains in brown, boundaries between island grains and coarse recrystallized ones in green, and boundaries between small recrystallized grains and deformed ones in black. The zoom into a randomly chosen area in the observed region shows different types of grain boundaries. The color coding as illustrated by the standard triangle is defined according to the normal direction. The EBSD measurement step is 3 µm.

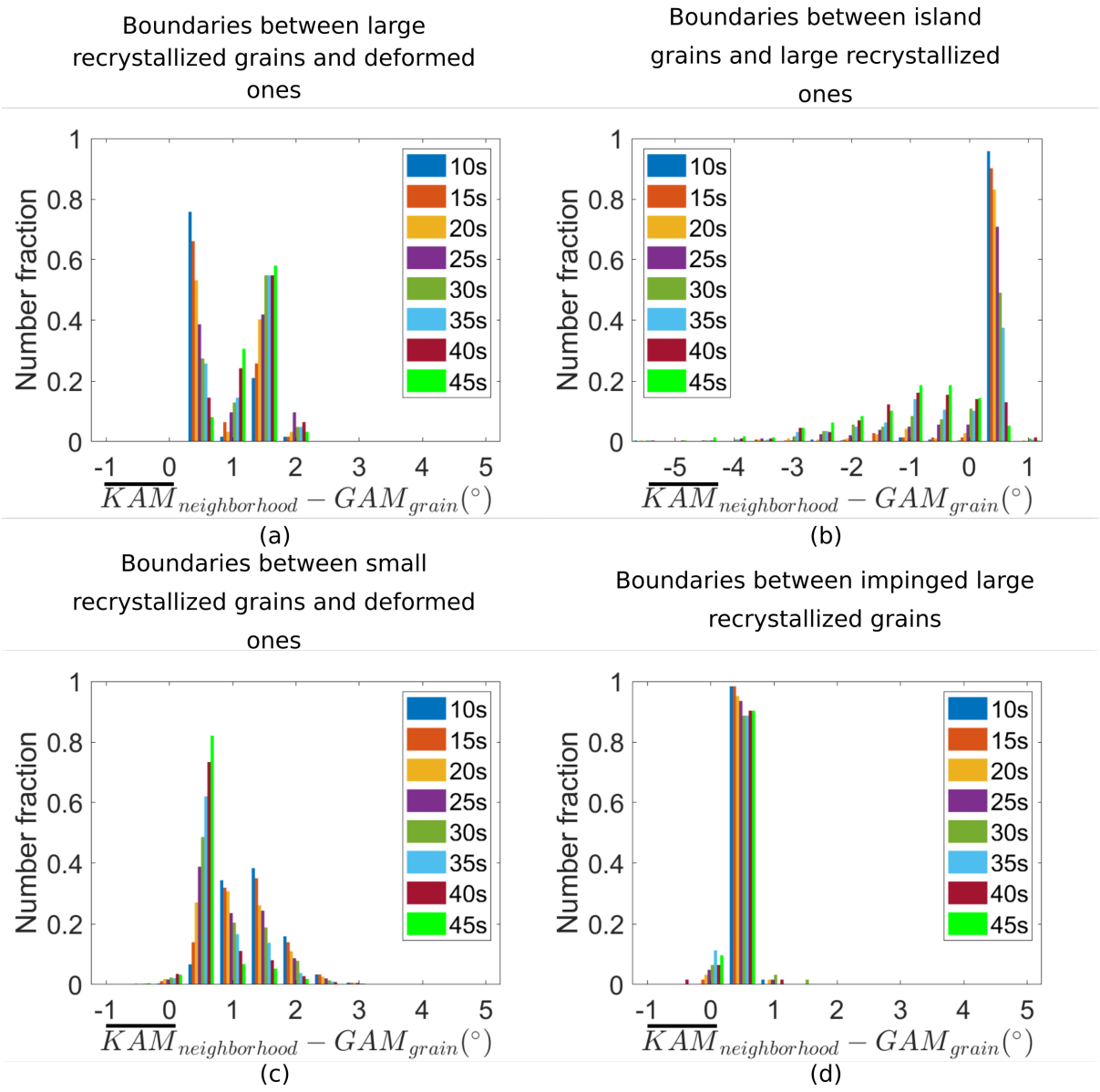

Fig. 5.16 $\overline{KAM}_{neighborhood} - GAM_{grain}$ distribution for boundaries (a) between coarse recrystallized grains and deformed matrix, (b) between island grains and coarse recrystallized ones, (c) between small recrystallized grains and deformed matrix and (d) between impinged coarse recrystallized grains.

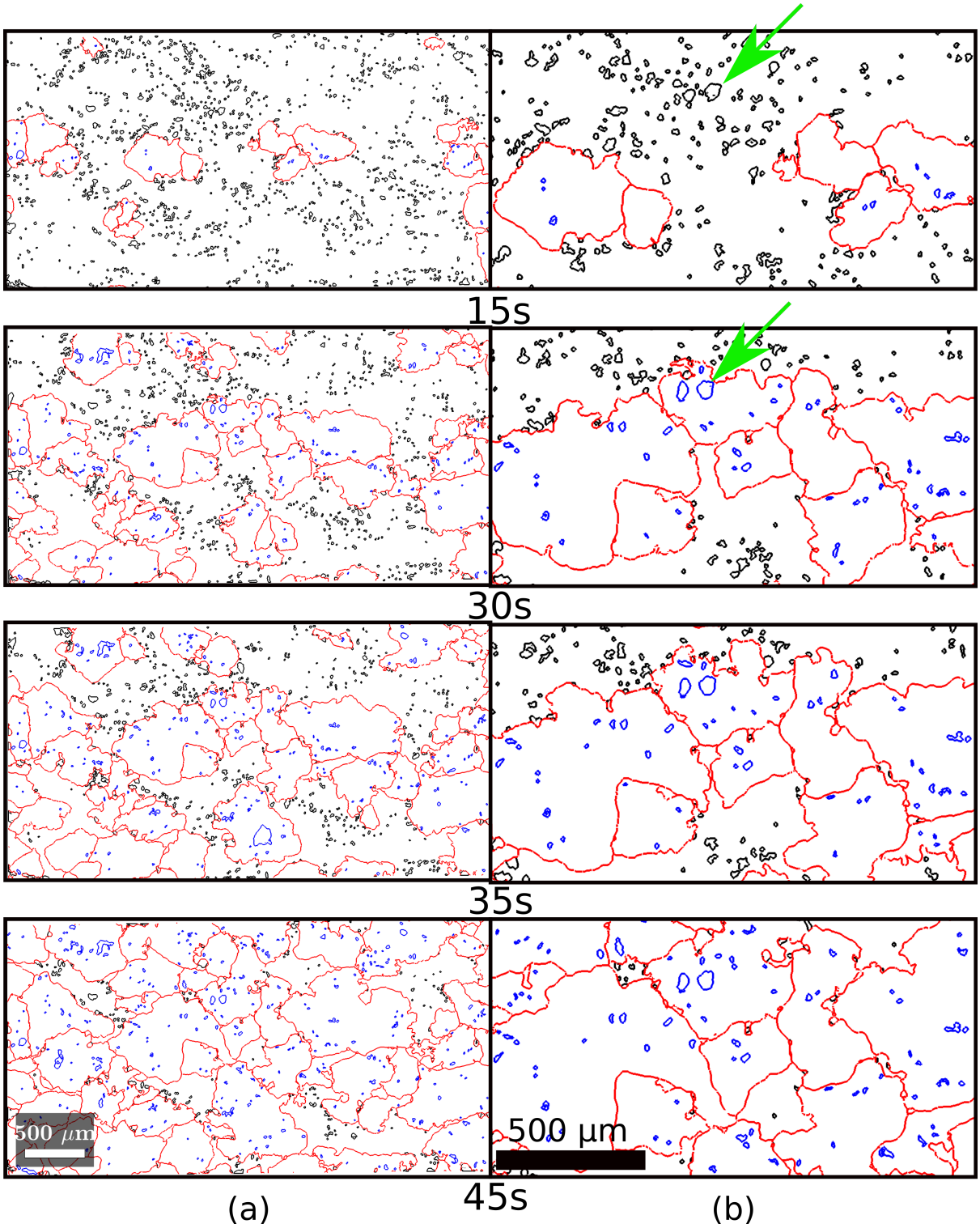

Fig. 5.17 (a) Evolution of grain boundaries during different in situ annealing steps. (b) Zoom into each grain boundary map shown in (a). Boundaries between small recrystallized grains and deformed ones are plotted by black lines. Boundaries of coarse recrystallized grains are plotted by red lines. Boundaries between island grains and coarse recrystallized ones are plotted by blue lines. The green arrow shows a small recrystallized grain that is transforming into an island grain.

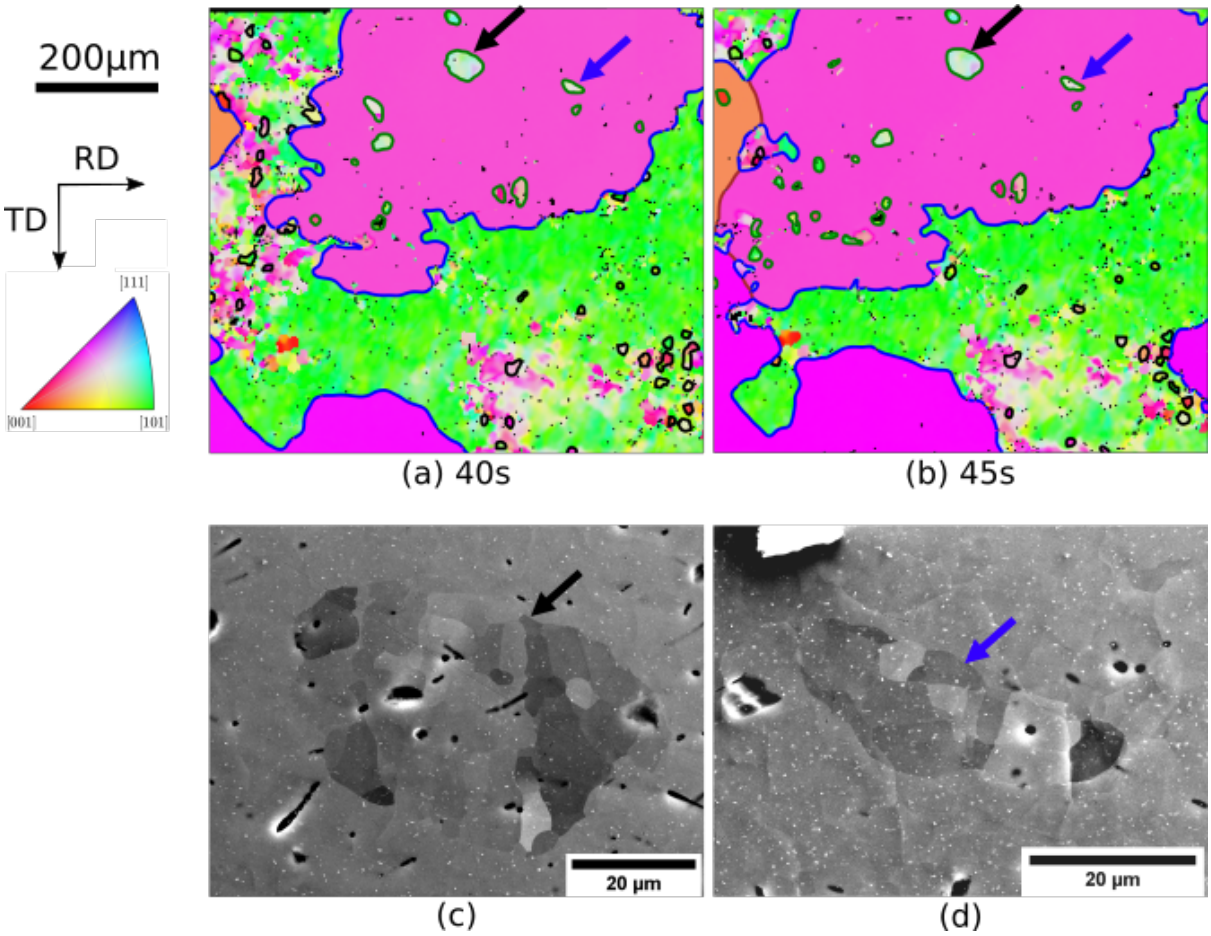

Fig. 5.18 Formation of stable island grains isolated within coarse recrystallized grains during sequential annealing: (a,b) Cropped EBSD orientation maps showing boundaries between coarse recrystallized grains and deformed ones in blue, boundaries between impinged coarse recrystallized grains in brown, boundaries between island grains and coarse recrystallized ones in green, and boundaries between small recrystallized grains and deformed ones in black. The color coding as illustrated by the standard triangle is defined according to the normal direction. The EBSD measurement step is 3 µm, (c,d) BSE images showing the distribution of precipitates around some island grains (shown by black and blue arrows in (a) and (b)).

5.3.3 Influence of second-phase particles

Despite Smith-Zener pinning, grain overgrowth occurs, suggesting that the driving pressure for the development of coarse recrystallized grains is higher than the pinning pressure. In order to verify this hypothesis, the three driving pressures controlling grain boundary migration are estimated as described in section 3.5. The numerical data used for these calculations are shown in table 5.1. f_{spp} and d_{spp} are the area fraction and mean equivalent diameter of second phase particles all types included respectively. For the estimation of f_{spp} and d_{spp}, the quantitative method described in section 3.2.2.2 has been used. R_{rex} is the mean recrystallized grain radius determined in the RD-ND plane right after deformation before holding. The Smith-Zener pinning pressure P_Z and the capillarity pressure P_C are estimated according to equations 3.6 and

3.7 (section 3.5) respectively and their estimated values are shown in table 5.2.

Parameters	2D	3D
$f_{spp}(\%)$	1.2	1.2
d_{spp}	0.19 µm	0.54 µm
R_{rex}	3.6 µm	3.9 µm

Table 5.1 Estimated values useful for driving and pinning pressures calculation.

Pressures	Estimated values (kPa)
P_Z	$\approx$ -20
P_C	$\approx$ -170
P_{SE}	$> \lvert P_Z + P_C \rvert$

Table 5.2 Estimated driving and pinning pressures for the growth of recrystallized grains observed right after deformation.

The driving pressure due to stored energy P_{SE} needs to exceed the sum $|P_Z + P_C|$ (i.e. $\approx$ 190 kPa), so that growth of recrystallized grains formed right after deformation occurs. From equation 3.5 (section 3.5) and if x is taken to be equal to the measurement step size (i.e. 1 μm in this case), it can be deduced that the quantity $\overline{KAM}_{neighborhood} - GAM_{rex}$ should be greater than 1°, which is the case if we look at the distributions of $\overline{KAM}_{neighborhood} - GAM_{rex}$ for recrystallized grains given by figure 5.14. 6% of recrystallized grains have a $\overline{KAM}_{neighborhood} - GAM_{rex}$ higher than 1°. The proportion of boundaries of recrystallized grains having a $\overline{KAM}_{neighborhood} - GAM_{rex}$ higher than 1° could be even greater if considering the contribution of SSDs in the stored energy. It can be therefore concluded that some recrystallized grains right after deformation can indeed overcome the Smith-Zener pinning pressure exerted by second phase particles and then grow at the expense of deformed matrix until mutual impingement.

5.3.4 Anisotropic grain growth behavior

The difference in stored energy between the recrystallized grains and the deformed ones observed in the as-deformed and quenched microstructure seems to be the key factor leading to grain overgrowth. Smith-Zener pinning pressure can easily be overcome in the presence of such difference in stored energy. However, these two parameters cannot explain the anisotropic grain growth behavior and the fact that specific orientations “near Cube” are more prone to overgrowth.

5.3.4.1 Role of large Fe containing particles and finer precipitates

The shape of coarse recrystallized grains could be due at least partly to the alignment of Fe containing particles. In fact, as clearly visible in the RD-ND plane (see figure 5.5), Fe con-

taining particles are aligned with the RD and located mainly on the boundaries of the original grains (see figure 4.1), which are flattened due to the high level of deformation ($\varepsilon \approx 2.4$). The pinning effect exerted by these Fe containing particles is expected to be stronger in the ND than in the RD, due to their elongated shape, as can be seen in figure 5.19. Nes et al. [109] estimated the Smith-Zener pinning force when a grain boundary meets an ellipsoidal particle. Two situations are possible in this case and are presented in figure 5.19: case 1 and case 2. The Smith-Zener pinning force exerted by the particle in case 1 is much higher than the one in case 2, leading to a growth disadvantage of coarse recrystallized grains in the ND and therefore to an elongated shape of coarse recrystallized grains in the plane RD-ND. Figure 5.5 provides a hint of the influence of these particles since it clearly shows Fe containing particles located at the horizontal boundaries of a coarse recrystallized grain.

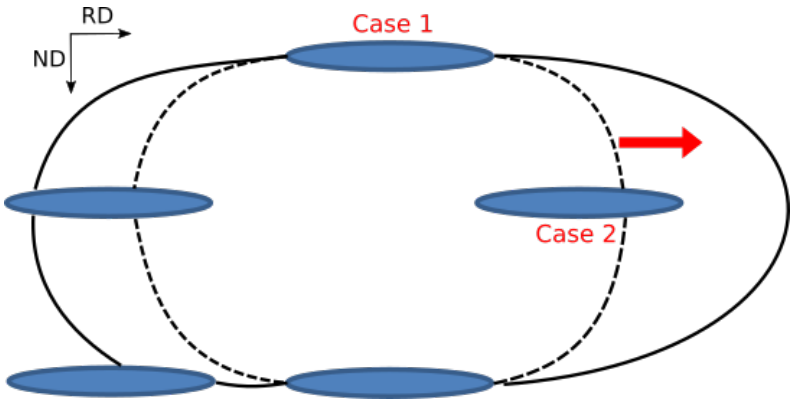

Fig. 5.19 Schematic illustration of how grain boundaries evolve in the presence of elongated and aligned Fe containing particles.

Nevertheless, some Fe containing particles are located inside the coarse recrystallized grains (see figure 5.5). This may be the result of a situation similar to case 2 shown in figure 5.19, where the vertical boundaries of a coarse recrystallized grain are able to pass through Fe containing particles. Horizontal boundaries breaking away from these Fe containing particles could also explain this observation, but it is less likely as the Smith-Zener pinning is stronger in this configuration.

The inhomogeneous distribution of finer precipitates including Mg_2Si/Si and dispersoids has been reported in the literature [28, 110, 111] as another possible reason for the elongated shape of coarse recrystallized grains.

5.3.4.2 Role of orientation pinning

Orientation pinning could also be another explanation for the obtained shape of coarse recrystallized grains. Deformed grains right after hot compression are more elongated in the RD-ND plane (see figure 5.1) than in the RD-TD plane (see figure 5.7). Recrystallized grains with orientations different than the orientations of deformed grains will preferentially grow at the expense of deformed grains [65, 111]. Due to the elongated shape of deformed grains

in the RD-ND plane, recrystallized grains have a higher probability to meet a disfavourable orientation in the ND than the RD, resulting in a growth advantage of coarse recrystallized grains in the RD than in the ND.

The comparison between the shape of coarse recrystallized grains in the RD-ND plane and RD-TD plane is therefore consistent with a combined effect of Fe containing particles, possible inhomogeneous distribution of finer precipitates and orientation pinning in the development of such grain shape, or with being controlled by either one or two of these three factors.

5.3.4.3 Role of misorientation

The anisotropic post-dynamic development of coarse recrystallized grains is very evident from their elongated shape when they are examined in the plane RD-ND (see figure 5.1 (d)). Nevertheless, it is more subtle when the RD-TD section is examined (see figure 5.15 (j)). Higher magnification EBSD maps with a smaller measurement step size showing the evolution of another region of interest during sequential annealing in the SEM chamber shed light upon the anisotropic grain growth in the RD-TD section as can be seen in figure 5.20. The recrystallized grain R1 develops more in the deformed grain D1 than in the deformed grain D2, leading to an elongated shape in the RD. However, the recrystallized grain R2 develops more in the deformed grains D2 and D4 than in the deformed grain D3 although D3 has higher KAM values and therefore stored energy than D2 and D4 (see figure 5.20 (k)). Even though those observations can be biased by 2D sectionning effect (i.e. the migration rate normal to the grain boundary plane is unknown as the grain boundary inclination itself is unkown), these suggest that the growth speed is influenced by the misorientation between the recrystallized grain and its neighboring environment.

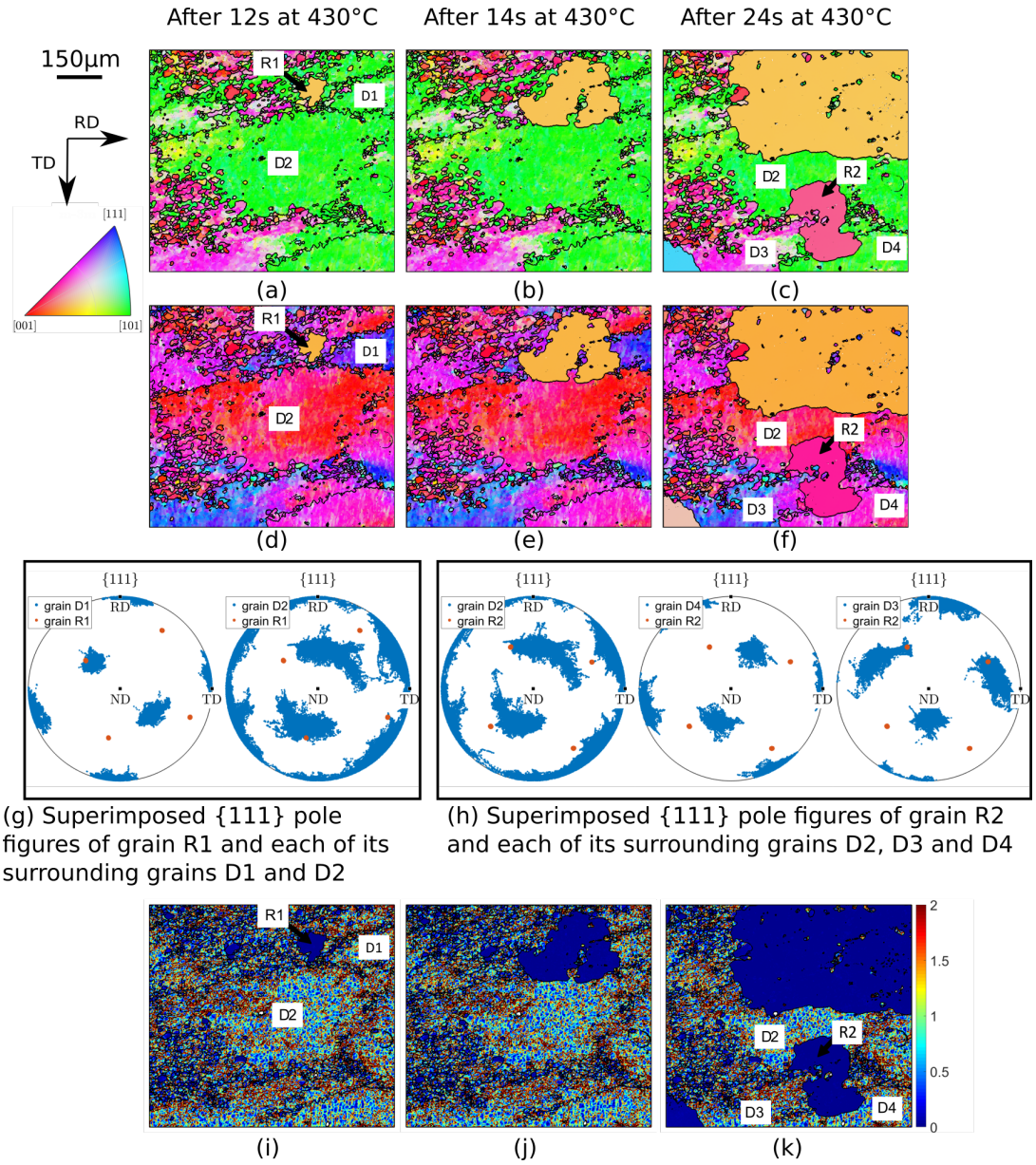

Fig. 5.20 (a-f) Higher magnification EBSD orientation maps with a smaller measurement step size (1 µm) showing the evolution of the microstructure of another region of interest on the hot deformed and quenched sample during sequential annealing in the SEM chamber. The grain boundaries are plotted in black. The color coding is defined according to the standard triangle. (a-c) ND is projected on the standard triangle). (d-f) RD is projected on the standard triangle. (g-h) Superimposed {111} pole figures of coarse recrystallized grains R1 and R2 and their surrounding grains. (i-k) Corresponding KAM maps.

The misorientations at moving and non-moving boundaries during different steps of the annealing sequence are calculated and compared to investigate the possible effect of misorientation on boundary migration. Actually, both the correlated and uncorrelated misorientations are calculated. The correlated misorientation is calculated from the orientations of neighboring pixels located on each side of the boundary. On the other hand, the uncorrelated misorientation is calculated assuming no spatial correlation between the pixels. In other words, at the

boundaries between coarse recrystallized grains and deformed ones, the uncorrelated misorientation is calculated between pairs of pixels, where the first pixel is randomly selected from the coarse recrystallized grains and the second pixel is randomly selected from the deformed grains in the whole map. At the boundaries between impinged coarse recrystallized grains, the first and second pixels are randomly selected from coarse recrystallized grains in the whole map. At the boundaries between island grains and coarse recrystallized ones, the first pixel is randomly selected inside island grains whereas the second pixel is randomly selected from coarse recrystallized grains in the whole map. At the boundaries between small recrystallized grains and deformed ones, the first pixel is randomly selected from small recrystallized grains and the second pixel is randomly selected from deformed grains in the whole map.

If the correlated and uncorrelated misorientation distributions are different, this indicates that the spatial arrangement of the grains is not random and that there are special boundaries that are favored between grains (e.g. boundaries having a low energy as discussed in [112]). However, if the correlated and uncorrelated misorientation distributions are similar, this means that there is a random spatial arrangement of the grains and that the misorientation distribution is just the result of the crystallographic texture [113].

The correlated and uncorrelated misorientation angle distributions for different types of boundaries during different annealing steps are shown in figure 5.21. It is clear that the correlated and uncorrelated misorientation angle distributions are very different for all types of boundaries except for the boundaries between coarse recrystallized grains. Provided that statistics are good enough, this means that the probability for the occurrence of a certain misorientation between two neighboring grains is not fully determined by the crystallographic texture, but, by another factor that favors specific misorientations.

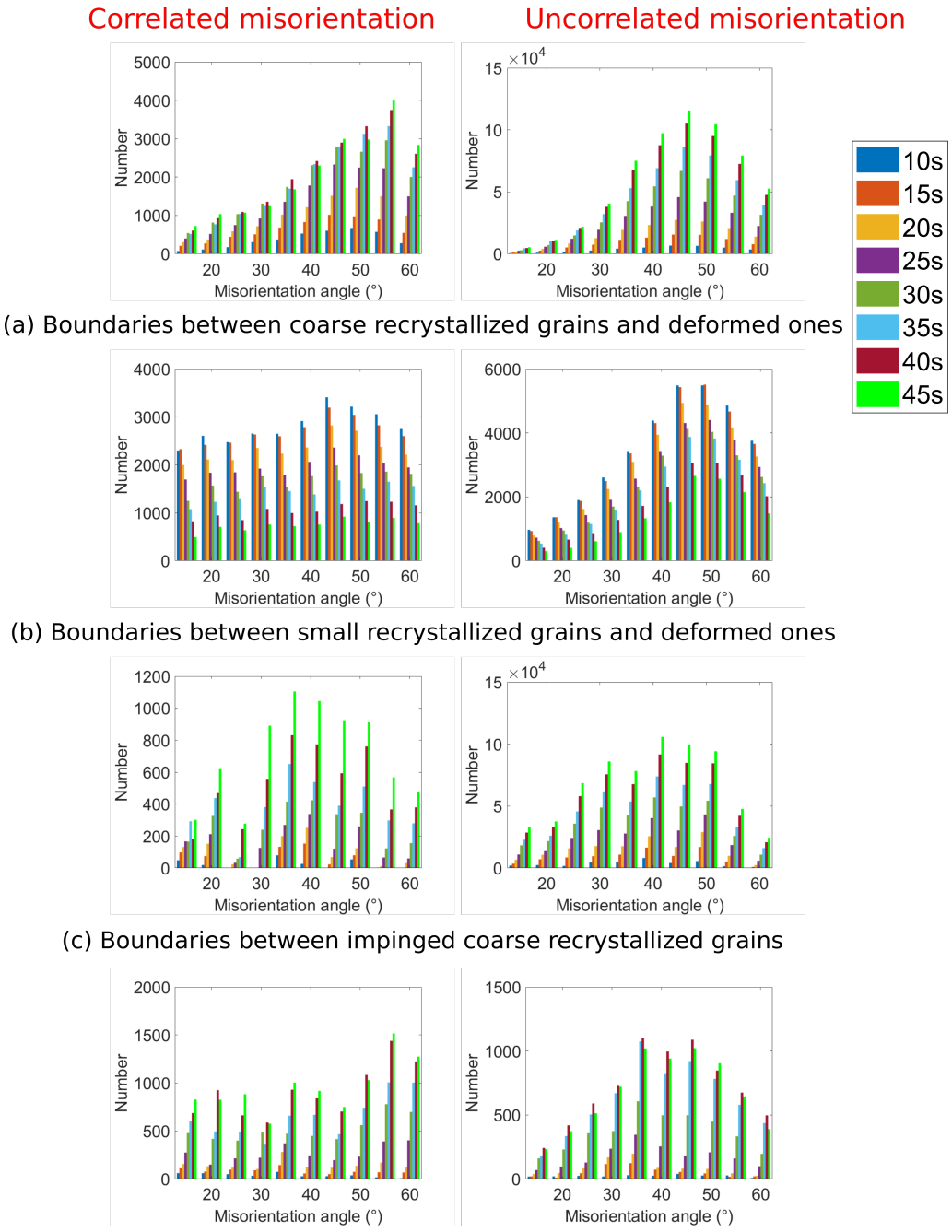

(a) Boundaries between coarse recrystallized grains and deformed ones

(b) Boundaries between small recrystallized grains and deformed ones

(c) Boundaries between impinged coarse recrystallized grains

(d) Boundaries between island grains and coarse recrystallized ones

Fig. 5.21 Correlated (left) and uncorrelated (right) misorientation angle distributions for boundaries: (a) between coarse recrystallized grains and deformed matrix, (b) between small recrystallized grains and deformed matrix, (c) between impinged coarse recrystallized grains and (d) between island grains and coarse recrystallized grains. For correlated misorientation, the number corresponds to the number of pairs of neighboring pixels along the grain boundary segments of each type in the map. For uncorrelated misorientation, the number corresponds to the number of pairs of random pixels. The number of random pairs corresponds to the number of pixels inside coarse recrystallized grains in the case of boundaries between coarse recrystallized grains and deformed ones, to the number of pixels inside coarse recrystallized grains in the case of boundaries between impinged coarse recrystallized grains, to the number of pixels inside island grains in the case of boundaries between island grains and coarse recrystallized ones, and to the number of pixels inside small recrystallized grains in the case of boundaries between small recrystallized grains and deformed ones, respectively.

More specifically, for boundaries between coarse recrystallized grains and deformed ones, the number of pairs of neighboring pixels having a misorientation angle higher than 40° increases more during annealing than the number of pairs of neighboring pixels having a misorientation angle lower than 40° (see figure 5.21 (a)). The highest increase in the number of pairs of neighboring pixels is observed for 50°-55° misorientation angles. This may lead to believe that 50°-55° boundaries have a fast migration rate as they are involved in the formation of coarse recrystallized grains. Nevertheless, this is not necessarily true since fast moving boundaries tend to disappear as recrystallization progresses. In fact, a fast moving boundary continues moving until meeting another grain with which it forms a slow moving boundary. The remaining grain boundaries are thus more likely to be low mobility boundaries. The remaining grain boundaries may also be thermo-dynamically favored (i.e. have low energy) [114].

The evolution of correlated misorientation axis distribution corresponding to the 50°-55° misorientation angles for these boundaries during different sequential annealing steps (figure 5.22 (a)) shows that the 50°-55° boundaries between coarse recrystallized grains and the deformed ones have mostly rotation axes near ⟨111⟩ and ⟨101⟩. It is interesting to note that the strength of ⟨111⟩ axis decreases from 10 s to 15 s and that the strength of ⟨101⟩ axis becomes the highest at the end of sequential annealing (i.e. after 45 s) from figure 5.22 (a). This suggests that the moving boundaries at an early annealing stage have mostly a misorientation of 50°-55° ⟨111⟩ and that at a later annealing stage, either these moving boundaries are slowly modifying their misorientation axis towards ⟨101⟩ as they migrate through orientation gradients of the neighboring deformed grain or new moving boundaries having a misorientation axis close to ⟨101⟩ form as they meet other deformed grains.

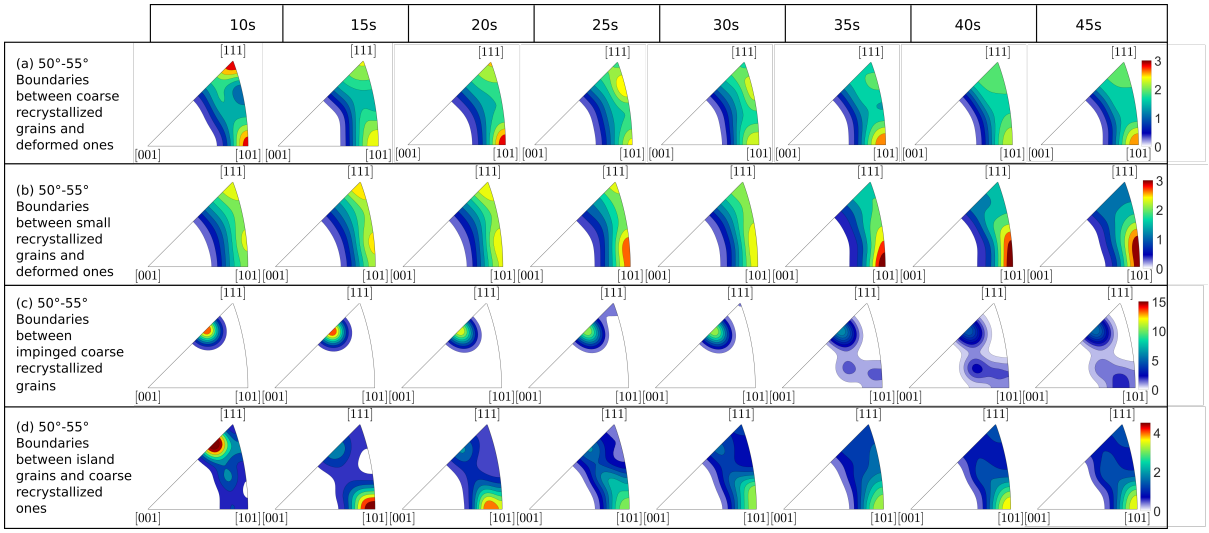

Fig. 5.22 Evolution of correlated axis distribution corresponding to 50-55° misorientation angles during different sequential annealing steps for boundaries: (a) between coarse recrystallized grains and deformed matrix, (b) between small recrystallized grains and deformed matrix, (c) between impinged coarse recrystallized grains and (d) between island grains and coarse recrystallized ones.

For boundaries between small recrystallized grains and deformed matrix (i.e. non-moving boundaries), the correlated misorientation angle distribution does not show any remarkable maximum during the different annealing steps (see figure 5.21 (b)). Additionally, the number of pairs of neighboring pixels whatever the misorientation angle between them is decreasing because small recrystallized grains are either consumed by coarse recrystallized grains or becoming themselves coarse recrystallized grains. It is important to note that some small recrystallized grains have 50°-55° misorientation angles (figure 5.21 (b)) even after 45 s of sequential annealing. The misorientation axis distributions corresponding to these 50°-55° misorientation angles during different annealing steps (see figure 5.22 (b)) show that most of the 50°-55° boundaries between small recrystallized grains and deformed matrix have rotation axes clustered around $\langle 101 \rangle$, suggesting thus that 50°-55° $\langle 101 \rangle$ boundaries are immobile. Therefore, it can be deduced that both misorientation angle and axis are not sufficient to determine the mobility of grain boundaries. 50°-55° $\langle 101 \rangle$ boundaries can be mobile in some cases (at the border of the large growing grains) and immobile in others (at the border of the small non growing grains). This is consistent with the study conducted by Zhang et al. [115] where it has been shown in pure nickel that, for a given misorientation (i.e. similar misorientation angle and axis) and similar local driving pressure, a boundary segment may move or not.

For boundaries between island grains and coarse recrystallized ones (see figure 5.21 (d)), the number of pairs of neighboring pixels is increasing regardless the misorientation angle which makes sense during sequential annealing. In fact, as coarse recrystallized grains develop, the probability of forming island grains increases. The highest increase of the number of pairs of neighboring pixels for these boundaries is again observed at 50°-55° misorientation angles. The misorientation axis distributions corresponding to these misorientation angles during different sequential annealing steps show that the remaining island grains have misorientation axes clustered around $\langle 101 \rangle$ (figure 5.22 (d)). This confirms that 50°-55° $\langle 101 \rangle$ boundaries can be mobile or immobile, depending on other factors (e.g. precipitate content around the boundary and boundary plane [116, 117]). Formation of island grains is a well-known feature for abnormal grain growth and has been reported in aluminum alloys such as in AA3102 [76] and AA5052 [118] as well as in other materials including tantalum [119], Fe-3%Si steel [120, 121] and copper [122]. It occurs when the growth front moves around the island grain, leaving it behind. This is possible when the velocity of the boundary of the island grain is much smaller than those of its neighboring grains. Since the velocity of a grain boundary (V) depends on mobility (M) and boundary energy (γ), a lower velocity suggests either a lower mobility or a lower energy or both. Koo et al. [122] found that the boundaries between island grains and surrounding coarse recrystallized grains are low misorientation angle boundaries ($\theta < 10°$) in copper. The formation of island grains was therefore attributed to the low boundary energy and mobility of low angle boundaries between island grains and their neighboring grains [122]. According to figure 5.21 (d), the boundaries between island grains and coarse recrystallized grains

are mostly high angle boundaries. Thus, low angle boundaries are not responsible here for the appearance of island grains. Coincidence site lattice (CSL) boundaries have been reported in many studies [76, 118–120] as accountable for the formation of island grains. For instance, Li et al [76] found that, in annealed AA3102, island grains tend to have special boundary relationships, such as $\Sigma 3$, $\Sigma 5$ and $\Sigma 7$, with the coarse recrystallized grains where they are entrapped. This is possible probably due to the low mobility and energy of CSL boundaries [76].

In order to inspect the role of CSL boundaries, the percentages of CSL boundaries between island grains and coarse recrystallized ones are compared to those of CSL boundaries between coarse recrystallized grains and deformed ones in figure 5.23. The percentages of CSL boundaries between island grains and coarse recrystallized ones and between coarse recrystallized grains and deformed ones are similar, which suggests that CSL boundaries do not play a role of prime importance in the stability of island grains. To conclude, the occurrence of island grains cannot be explained in terms of low angle or CSL boundaries.

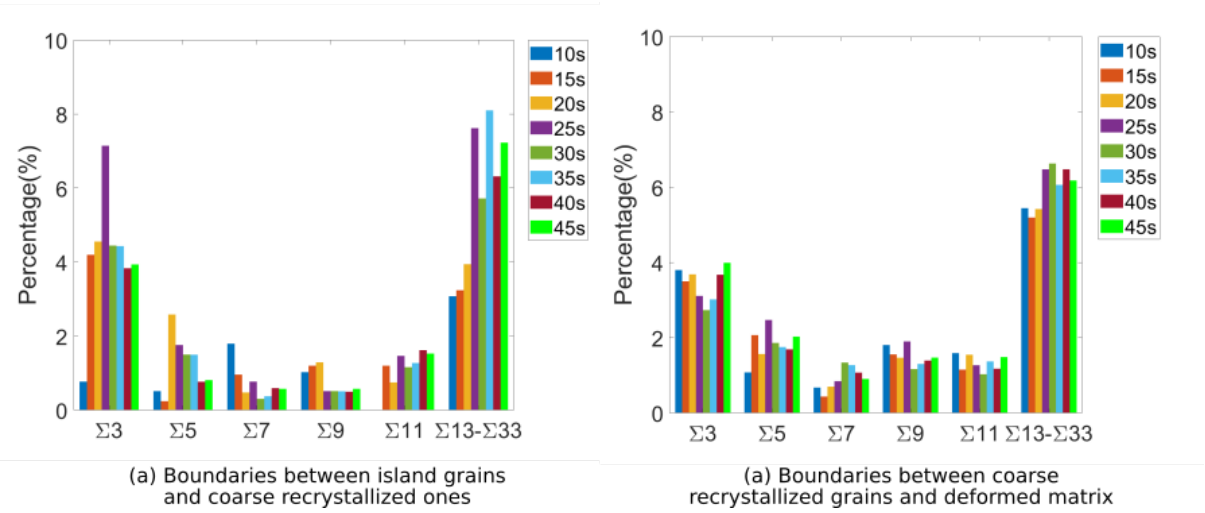

Fig. 5.23 CSL boundary distributions for (a) boundaries between island grains and coarse recrystallized ones and for (b) boundaries between coarse recrystallized grains and deformed ones. CSL boundaries are determined using Brandon's criterion [123].

This is not totally surprising since the description of boundary energy and mobility as a function of misorientation angle or CSL character is not always relevant [116, 117]. In addition to misorientation angle, both misorientation axis and boundary plane may play a role in the boundary energy and mobility [116, 117]. The effect of misorientation axis on formation of island grains is investigated by plotting the correlated misorientation axis distribution for each grain boundary type as seen in figure 5.24. It is clear from figure 5.24 that the probability that boundaries between island grains and coarse recrystallized ones have $\langle 110 \rangle$ misorientation axes is higher than that of boundaries between coarse recrystallized grains and deformed ones. Both energies and mobilities of 388 distinct grain boundaries in nickel have been calculated using atomic-scale computer simulations by Olmsted et al. [116, 117]. It has been shown that the $\langle 101 \rangle$ symmetric tilt boundaries except Σ 11 50.48° $\langle 101 \rangle$ are high in energy. However,

$\langle 101 \rangle$ symmetric tilt boundaries have a very wide range of mobilities depending on the misorientation angle and boundary plane. Therefore, the stability of island grains may be due to the low mobility of some particular $\langle 101 \rangle$ boundaries. However, this is not a sufficient reason because there as some misorientation angles/axes in common between boundaries between coarse recrystallized grains and deformed ones and those between island grains and coarse recrystallized ones (e.g. 50°-55° $\langle 101 \rangle$, figure 5.22). Second phase particles as shown in section 5.3.2 (see figure 5.18) do not seem to explain either the stability of island grains. Therefore, the remaining factors that may explain the stability of these island grains are the boundary plane, the impurity segregation effect or fine precipitation that cannot be resolved with SEM.

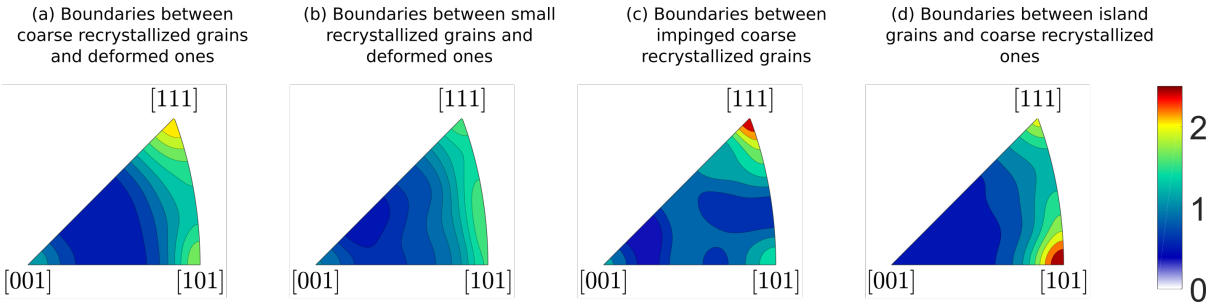

Fig. 5.24 Correlated misorientation axis distributions for boundaries after the full annealing sequence (45 s): (a) between coarse recrystallized grains and deformed matrix, (b) between small recrystallized grains and deformed matrix, (c) between impinged coarse recrystallized grains and (d) between island grains and coarse recrystallized ones.

Rohrer et al. [124] reported that, in FCC materials, the variations in the grain boundary plane orientation contribute more to the energy anisotropy than the variations in the lattice misorientation and that the grain boundary population tends to be inversely correlated to the grain boundary energy [124]. Therefore, it is important to investigate the influence of boundary plane on the evolution of the coarse recrystallized grains. The $\{111\}$ traces corresponding to coarse recrystallized grains are shown by figure 5.25. The boundaries of coarse recrystallized grains are also colored according to the minimum angle between their trace and those of $\{111\}$ planes in figure 5.25. It is clear that most of coarse recrystallized grain boundaries are colored in blue, meaning that they are close to $\{111\}$ traces. This suggests that $\{111\}$ may play a role in the favorable migration of some boundaries over some others or in the position at which the grain boundary stops or stagnates. This conclusion calls for complementary 3D characterization as a perspective of this work.

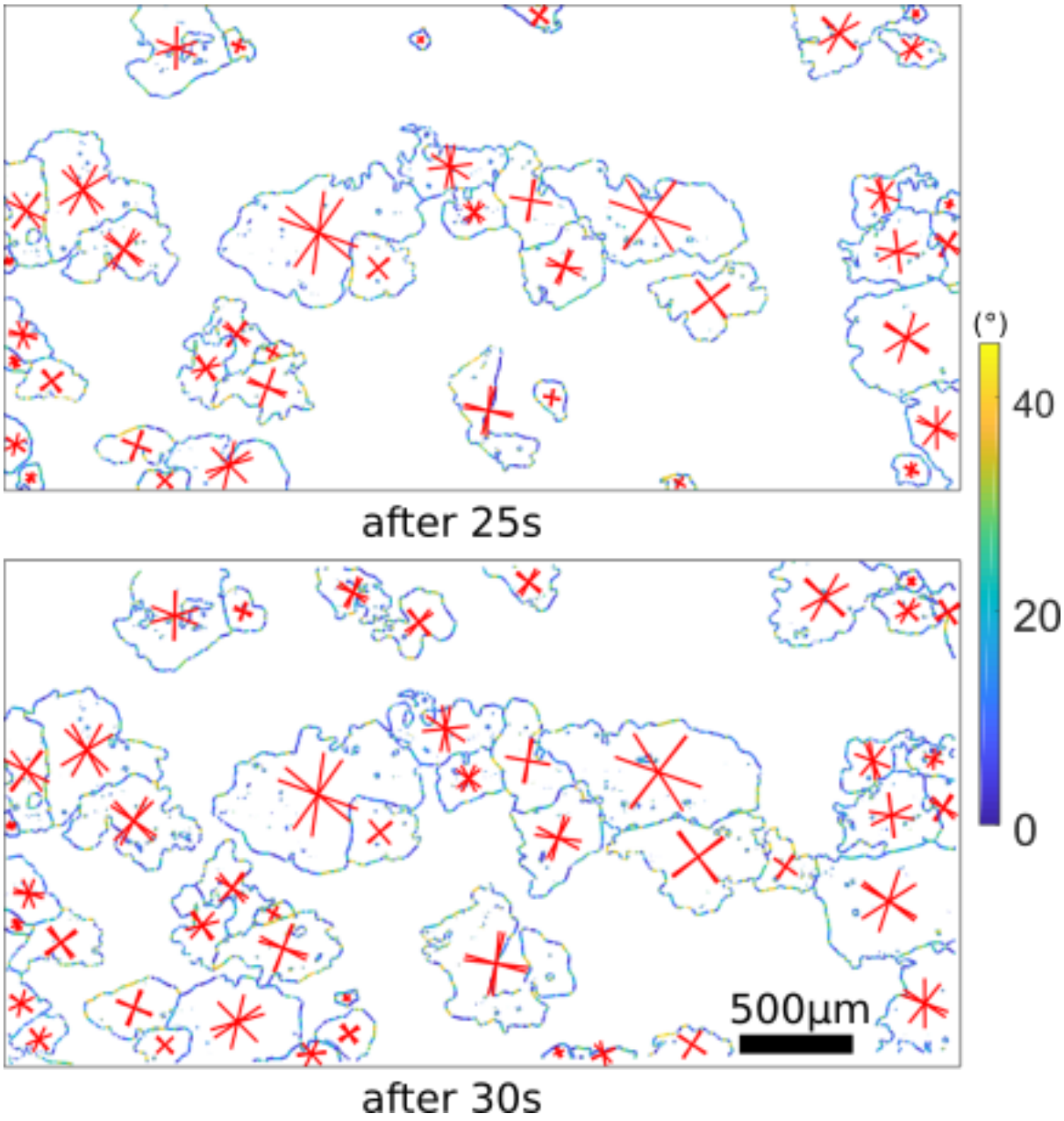

Fig. 5.25 Grain boundary maps showing the evolution of boundaries of coarse recrystallized grains from 25s to 30s of sequential annealing. The $\{111\}$ traces within coarse recrystallized grains are plotted in red. All symmetrically equivalent $\{111\}$ planes are taken into account. The boundaries of coarse recrystallized grains are colored according to the minimum angle between their trace and those of $\{111\}$ planes (scale bar on the left).

5.4 Summary

The different parameters promoting the overgrowth of recrystallized grains in 6016 aluminum alloy were investigated using hot compression tests followed by both post-deformation holding experiments and sequential annealing in the SEM chamber to follow the evolution of a given region of interest. The evolution of the microstructure was characterized in RD-ND and RD-TD sections by EBSD and the following conclusions were drawn from this work:

- Overgrowth of some recrystallized grains occurs during holding after hot deformation and is clearly visible in both RD-ND and RD-TD sections. Coarse recrystallized grains are elongated in the RD-ND and to a lower extent in the RD-TD plane, thus exhibit an anisotropic grain development. The coarse recrystallized grains have mostly "near Cube" orientations with nevertheless wide scattering;
- "Near Cube" grains have slight initial size advantage among all the small recrystallized grains found in the deformed and quenched states.
- The stored energy provides the driving force for grain overgrowth. However, it cannot explain the anisotropic development of coarse recrystallized grains alone;
- For the overgrowing grains, Smith-Zener pinning is overcome by the driving force due to stored energy, leading to overgrowth of these grains at the expense of deformed matrix and most of the other small recrystallized grains until mutual impingement;
- The combined effect of Fe containing particle, possibly inhomogeneous distribution of finer precipitates and orientation pinning is likely to contribute to the development of the anisotropic shape of coarse recrystallized grains. But, these are not the only factors. The influence of the misorientation angle and axis in the anisotropic behavior of coarse recrystallized grains has also been investigated. The analysis of misorientation angle and axis has shown that 50-55° $\langle 110 \rangle / \langle 111 \rangle$ boundaries are over-represented as compared to the misorientation distribution associated with the actual crystallographic texture. This suggests that 50-55° $\langle 110 \rangle / \langle 111 \rangle$ boundaries are somehow favored in the microstructure evolution. However, this is not a sufficient condition because other 50-55° $\langle 110 \rangle$ boundaries were found to be immobile. Many boundaries of coarse recrystallized grains are aligned with or close to $\{111\}$ plane traces, suggesting that boundary plane may play a significant role in the growth advantage of coarse recrystallized grains and their anisotropic development. This calls for complementary 3D characterizations;
- Although the stored energy provides the driving force for the formation of coarse recrystallized grains, the anisotropic behavior of these grains cannot be explained by stored energy consideration only. This leads to the conclusion that the anisotropic growth is actually due to the combination of multiple factors including alignment of Fe containing particles, heterogeneous distribution of finer precipitates, and the properties (mobility and energy) of the grain boundary types formed between coarse recrystallized grains and their neighbors.

Getting closer to the industrial process

Contents

It is evident from the industrial process that the thermomechanical conditions vary during the hot rolling step. The objective of this chapter is therefore to understand the influence of processing conditions on the microstructure evolution. The samples having a high initial precipitate content (see section 4.1) are tested in this chapter because precipitates are formed prior to deformation. This eliminates the risk of forming precipitates during deformation or holding as seen in the other sample with a low initial precipitate content. Multipass hot compression tests are performed in order to get closer to the industrial hot rolling process. The results of these multipass tests are compared with the results of the single pass tests.

6.1 Influence of strain

6.1.1 Thermomechanical parameters

In order to study the effect of strain on the evolved microstructure, the state with a high initial precipitate content that has been deformed at a temperature of 430 °C, a strain rate of 3 s^{-1} and up to a strain of 2.4 (i.e. thermomechanical path identified by TMTb in figure 4.4) has been taken as a reference because it has been extensively studied previously (in Chapters 4 and 5).

The thermomechanical tests illustrated by figure 6.1 have been thus performed on the state with a high initial precipitate content. In this context, the samples with a high initial precipitate content are heated up to the testing temperature of 430 °C in the preheat furnace (this step takes approximately 3 minutes) and are subsequently transferred to the test furnace and deformed at a nominal temperature of 430 °C (actual temperature is higher due to self-heating) and at a strain rate of 3 s^{-1}. Various strains (0.5, 1, 1.5, 2 and 2.4) were applied in a single pass during the hot compression tests. All the deformed samples are subsequenlty water quenched right after deformation in order to retain the deformed microstructure. The deformed and quenched microstructures are later characterized by EBSD.

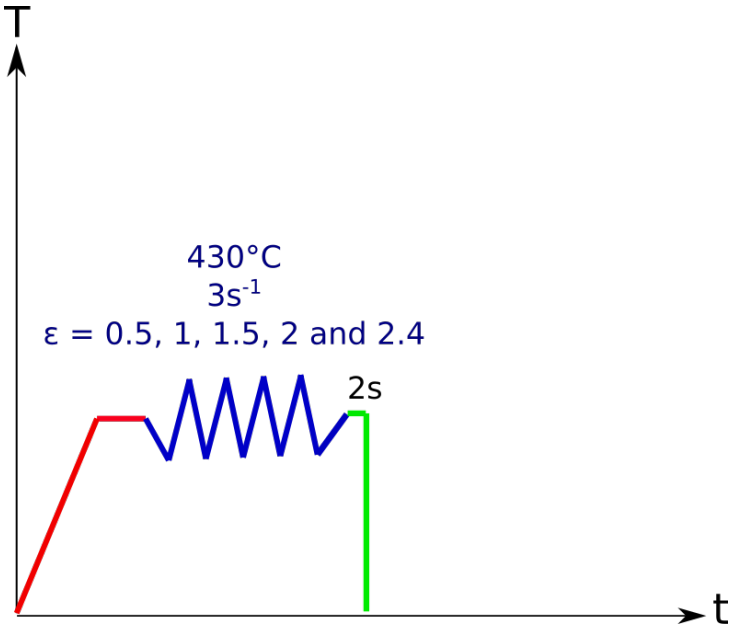

Fig. 6.1 Schematic diagram showing the applied thermomechanical paths on the high initial precipitate content samples (i.e. that are with medium $\frac{f_{spp}}{r_{spp}}$) in order to study the effect of strain ϵ on dynamic recrystallization. The testing temperature (430 °C) and strain rate (3 s^{-1}) are fixed, where as ϵ varies between 0.5 and 2.4. 2 s corresponds to the quench delay after deformation.

6.1.2 Microstructure right after deformation

The evolution of deformed and quenched microstructure with increasing strain level is shown by figure 6.2 (a). It is clear that deformed grains are gradually flattened with increasing

strain. Besides, a stronger texture develops as can be seen from the $\{111\}$ pole figures of the deformed and quenched microstructures shown by figure 6.2 (b). The evolution of microstructure, including subgrain structure, recrystallized grains and recrystallization mechanisms, with increasing strain will be studied in details below.

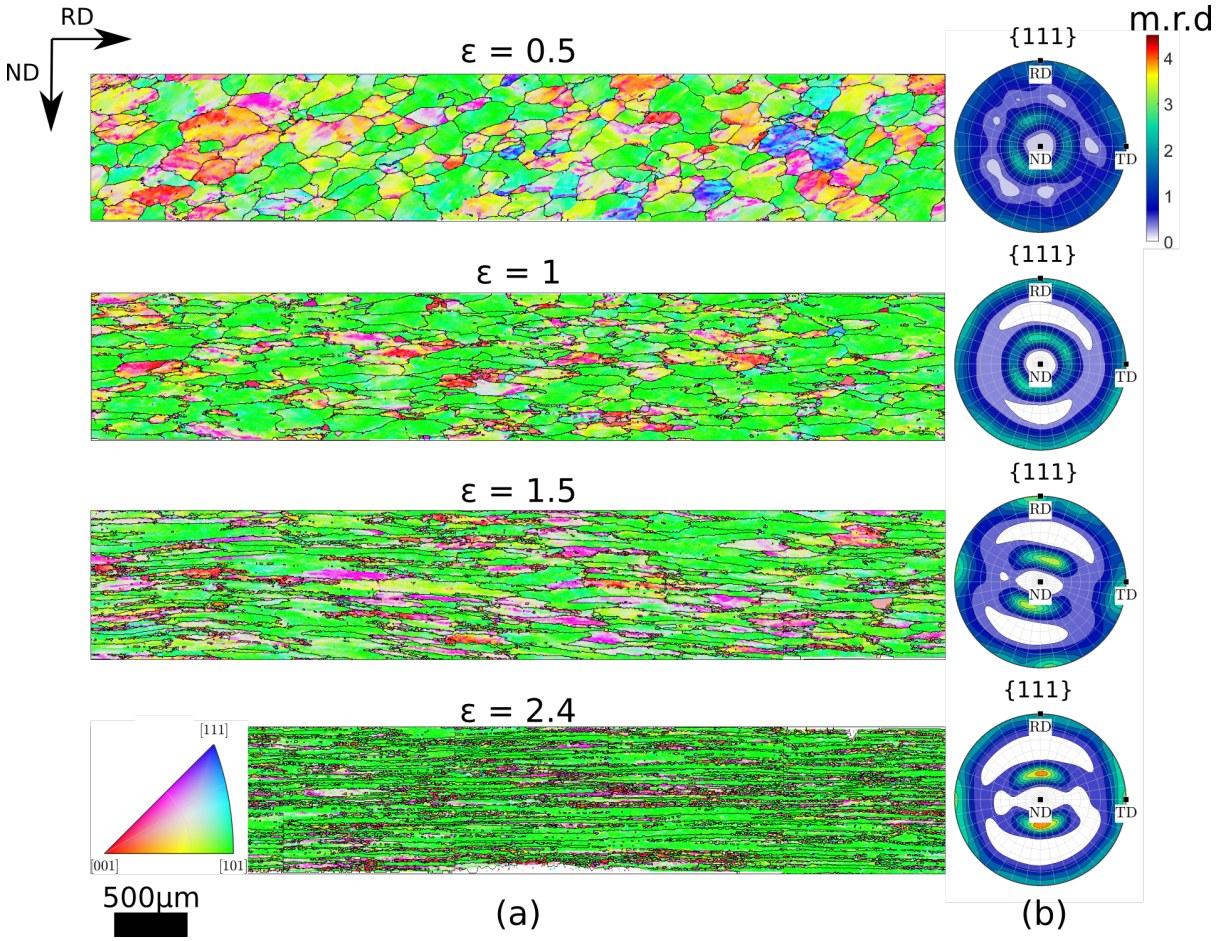

Fig. 6.2 (a) Stitched EBSD orientation maps showing the deformed and quenched microstructure at different deformation levels of 0.5, 1, 1.5, 2 and 2.4 respectively. The deforming temperature and strain rate are 430 °C and 3 s^{-1} during each test. The measurement step size is 3 µm. The color coding defined in the standard triangle refers to ND. (b) $\{111\}$ pole figures corresponding to the microstructures shown in (a). The texture intensity is expressed in multiple of random distribution (m.r.d). The initial samples have a high initial precipitate content.

Figure 6.3 shows magnified EBSD orientation maps taken at different strain levels. The high angle grain boundaries are plotted in black lines, while low angle grain boundaries are plotted in blue lines. As the strain level increases, the original grains get more elongated until reaching a thickness, which has a similar magnitude as the subgrain size at a strain level of about 2.4 (see figure 6.3 (b)). At this stage, it is difficult to distinguish the original grain boundaries. Serrations develop also on the original grain boundaries as the strain increases due to pinning and migration induced by subgrain boundaries. This suggests that geometric dynamic recrystallization may be taking place at a high strain level (2.4 in this case), which is consistent with the results described in [125, 126].

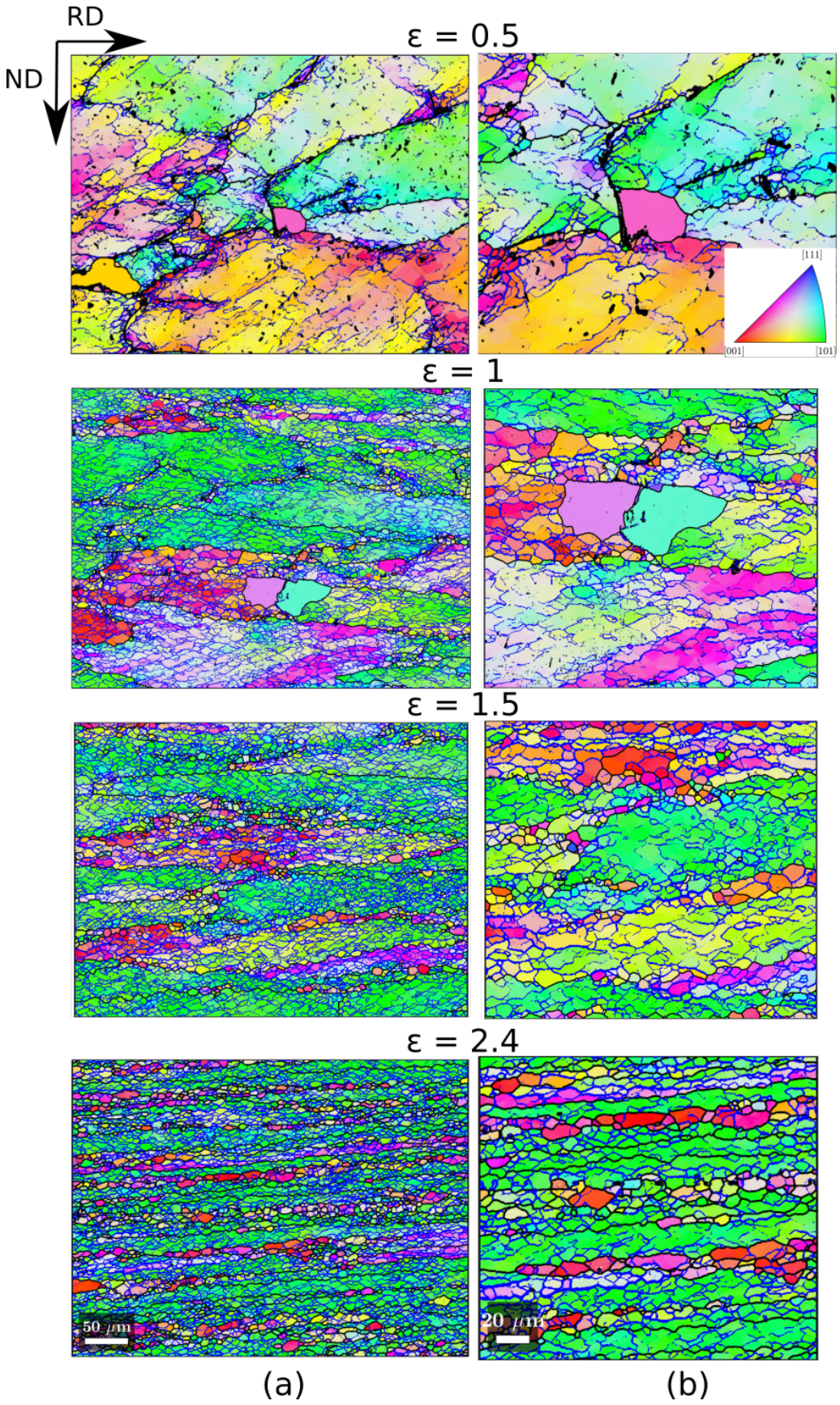

Fig. 6.3 (a) Magnified EBSD orientation map showing the deformed and quenched microstructure at different strains with smaller measurement step size (0.4 μm), (b) A zoom on the EBSD maps shown by (a). In (a) and (b), grain boundaries ($\theta > 10°$) are plotted in black lines , while subgrain boundaries ($1° \leq \theta \leq 10°$) are plotted in blue lines. The color coding defined in the standard triangle refers to ND.

It is clear from figure 6.3 (b) that the main softening mechanism during hot deformation regardless the strain level is dynamic recovery. The KAM maps shown by figure 6.4 (b) confirm this. In fact, subgrains become more equiaxed and better defined as the strain level increases from 0.5 to 2.4. Qualitatively, the mean subgrain size seems to decrease when ϵ varies from 0.5 to 1.5. However, when ϵ varies from 1.5 to 2.4, the mean subgrain size seems to stay constant. This is confirmed quantitatively by figure 6.7 (a), which illustrates the evolution of total length of subgrain boundaries per unit area with strain. The total length of subgrain boundaries per unit area increases when the strain increases from 0.5 to 1.5 and then remains almost constant when the strain increases from 1.5 to 2.4. This implies that the subgrain size does not change when the strain is above a critical value ($\epsilon \approx 1.5$) and that dislocations start to pile up at the already formed subgrain boundaries. The increase of KAM values at subgrain boundaries as can be seen by figure 6.4 (b) confirm the pile up of dislocations at these sub-boundaries. The above mentioned observations agree again with the observations made by [125, 126]. Actually, Solberg [125] reported that, for high purity aluminum deformed at 400 °C and 0.2 s^{-1}, the subgrains remained at the same size (about 7 µm) when the strain level increased from 0.5 to 60. A similar result was found by [126] in pure copper deformed at room temperature, where it was observed a decrease in the subgrain size followed by a steady state at high strains above 2 where the subgrain size approaches a constant value of about 0.2 µm.

Figure 6.5 illustrates the distribution of misorientation angles for both low ($2° \leq \theta \leq 10°$) and high angle grain boundaries ($\theta > 10°$) at different strains. The distribution of misorientation angles were determined from the EBSD orientation maps shown by figure 6.3 (a). It is clear from figure 6.5 that the numbers of both high angle boundaries and low angle grain boundaries per unit area increase as the strain increases. The average misorientation angle shifts towards higher values with increasing strain, suggesting the occurrence of CDRX by progressive increase of misorientation at subgrain boundaries.

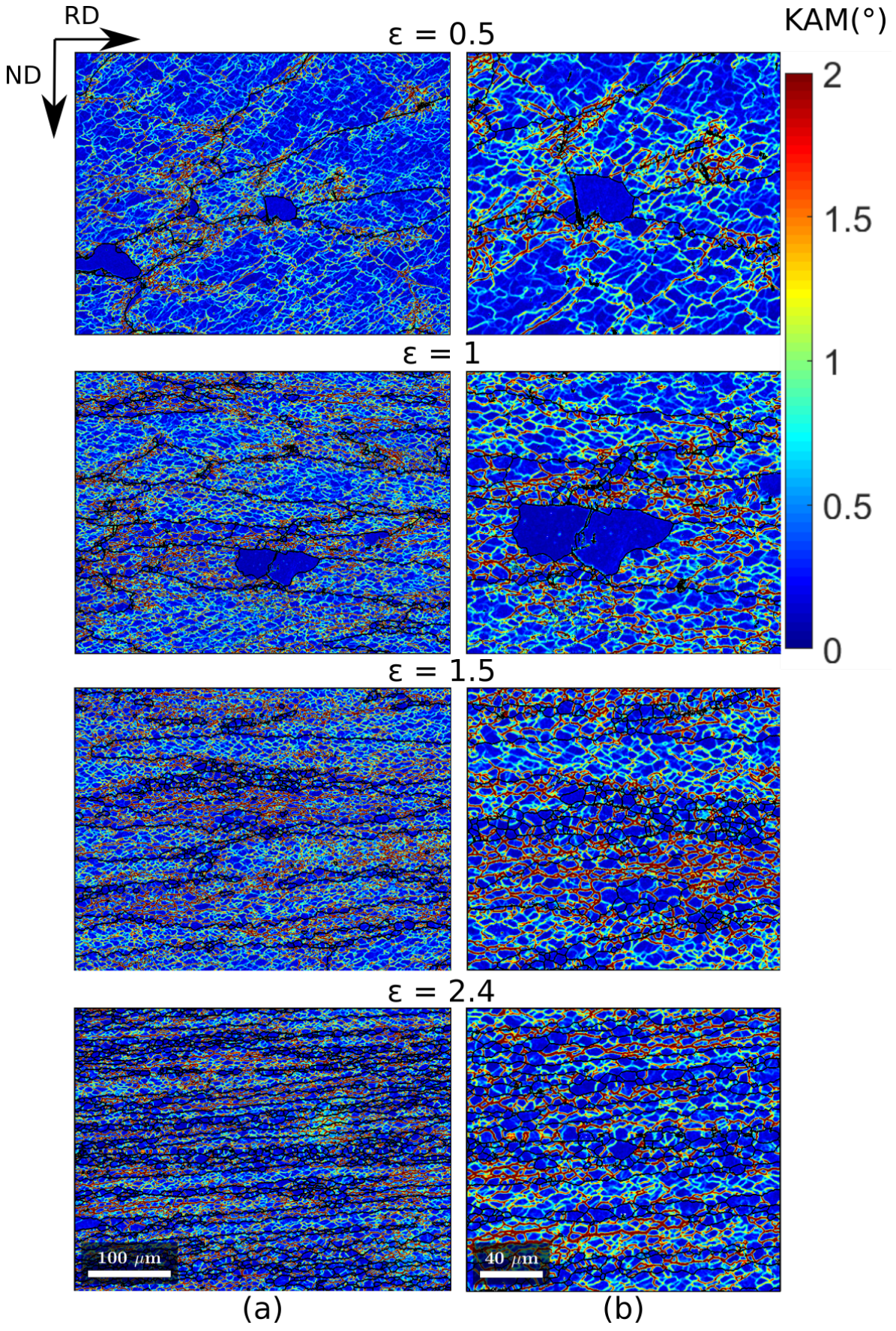

Fig. 6.4 (a) KAM maps corresponding to EBSD orientation maps shown by figure 6.3 (a), (b) Corresponding magnified KAM maps. The grain boundaries are plotted in black lines.

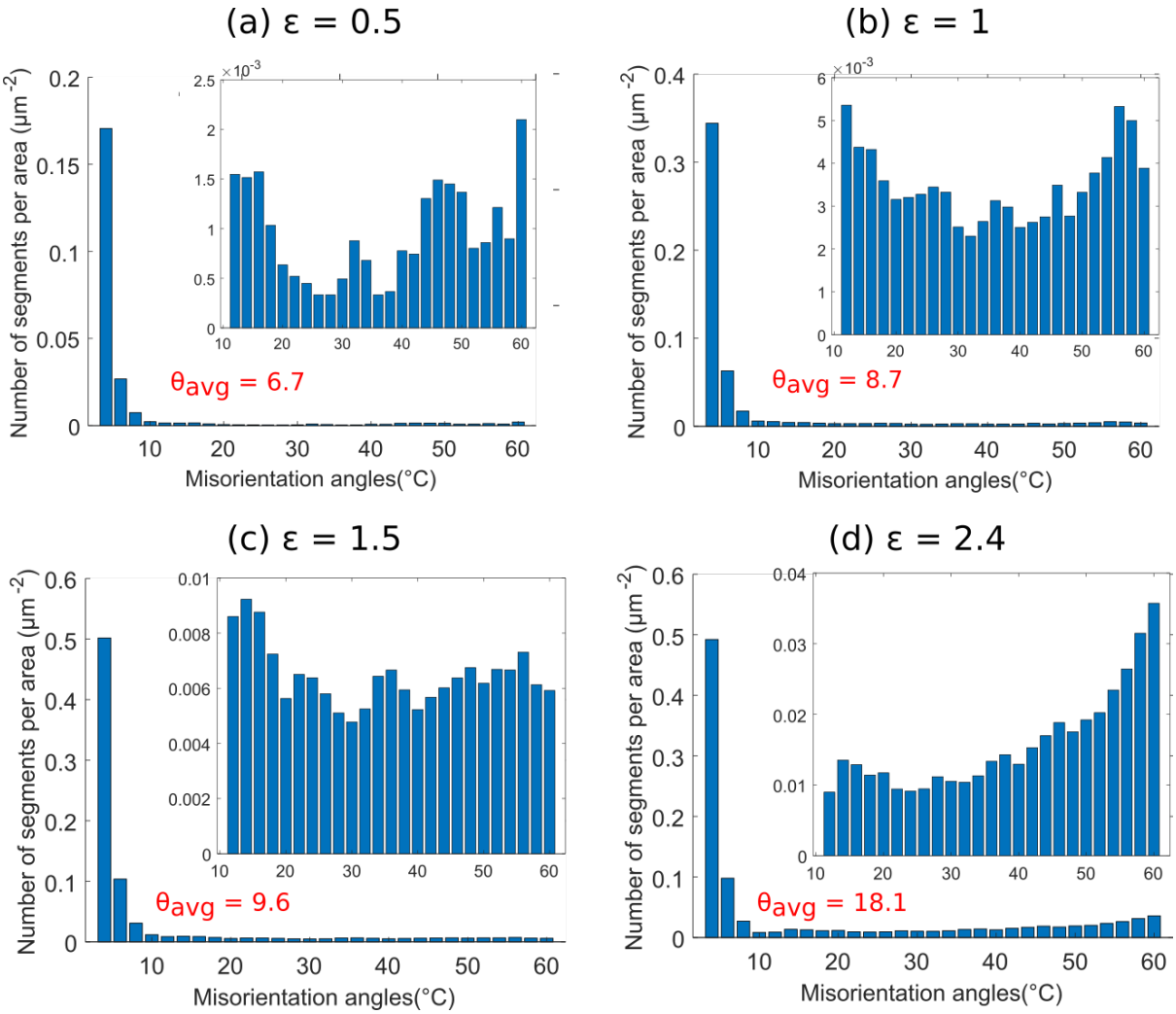

Fig. 6.5 Distributions of misorientation angles in the specimens deformed and quenched at different strains. Both low angle and high angle boundaries ($\theta > 2°$) are considered for the calculation of each distribution. The average misorientation angle is indicated in each graph.

The recrystallization mechanisms appear to be dependent on the strain level. At low strains (0.5 and 1), the recrystallized grains are large in size, do not contain any substructure (i.e. very low and uniform KAM values) and most of them are surrounded by Fe containing particles as can be seen by figures 6.6 (a,b,e,f). This suggests that the recrystallization mechanism in place at low strains can be static recrystallization by PSN. However, at high strains (1.5 and 2.4), recrystallized grains are more numerous and smaller in size. Many of them contain substructure as can be seen by figures 6.6 (c,d,g,h). This suggests that recrystallization is dynamic at high strains. The dynamically recrystallized grains may form also by PSN as seen by figure 6.6 (g), where a substructured recrystallized grain in contact with an Fe containing particle (shown by red arrow) is clearly seen.

Due to the serrations developed by original grain boundaries and the small thickness of deformed grains which approaches the subgrain size, geometric dynamic recrystallization then is likely to happen also at high strain.

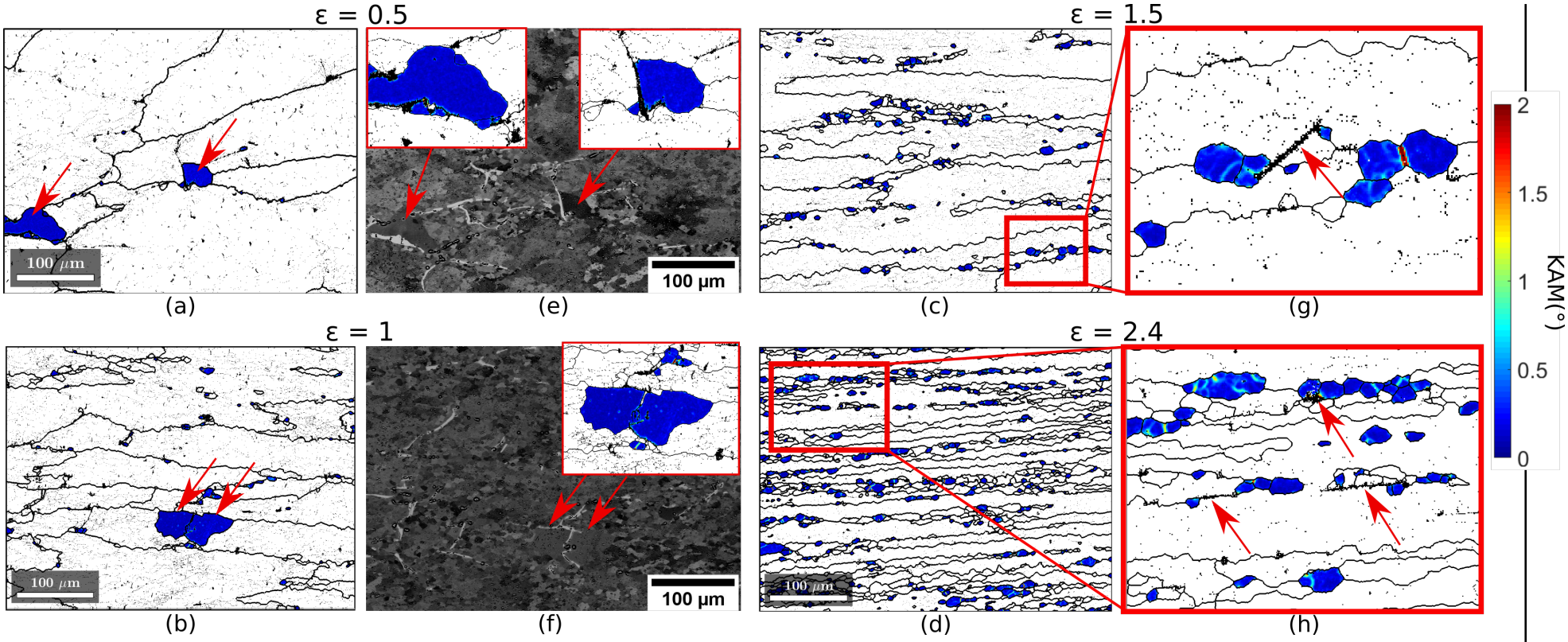

Fig. 6.6 (a,d) KAM map of recrystallized grains at different strain values. Non recrystallized grains are white. Non indexed points and high angle grain boundaries are plotted in black lines. The examined area is 454 µm x 341 µm. The pixel size is 0.4 µm. (e,f) BSE images corresponding to the KAM maps shown in (a) and (b) and zooms onto the regions shown by red arrows in (a) and (b) respectively. (g,h) Zooms onto the regions indicated by red boxes in (c) and (d) respectively, where Fe containing particles are shown by red arrows.

Figure 6.7 (a) shows also that the total length of high angle grain boundaries per unit area increases with strain. This may be simply due to the fact that original grains are increasingly flattened with increasing strain and therefore a higher total length of original grain boundaries is observed in the same cross-section. In addition to this, subdivision of flattened original grains and formation of a higher number of recrystallized grains may be responsible for the increased total length of high angle grain boundaries per unit area at high strain. Indeed, according to the literature [98, 127, 128], the high angle grain boundaries at a large strain may consist of newly formed grain boundaries by grain subdivision in addition to the original grain boundaries and recrystallized grains. By definition, grain subdivision includes the two following steps: (i) formation of cell blocks separated by microbands and/or dense dislocation walls where the misorientation increases steadily with increasing strain, (ii) the subdivision of grains into different cells leads to the presence of large orientation spread and therefore to the rotation of these different cells towards more stable orientations [98, 127, 128].

Figure 6.7 (b) shows the effect of strain on the mean size and area fraction of recrystallized grains right after deformation. The mean size of recrystallized grains decreases, while their area fraction increases with increasing strain. When strain increases, stored energy increases and therefore the driving force due to the stored energy is more likely to be sufficient to overcome the boundary curvature. The critical nucleus will be therefore reduced due to the higher stored energy, thus promoting the nucleation of recrystallized grains. The smaller mean size for recrystallized grains is probably due to the decrease in the size of subgrains with increasing strain since recrystallized grains in the deformed and quenched microstructure are originally subgrains with lower stored energy than their surroundings.

Finally, the effect of strain on the texture of recrystallized and deformed grains is shown by figure 6.7 (c). Regardless the strain level, the area fractions of recrystallized grains belonging the typical texture components are lower than 6%. The orientations of recrystallized grains are thus random whatever the applied strain. The texture of deformed grains is mostly composed of Brass and Goss components as the strain reaches 2.4.

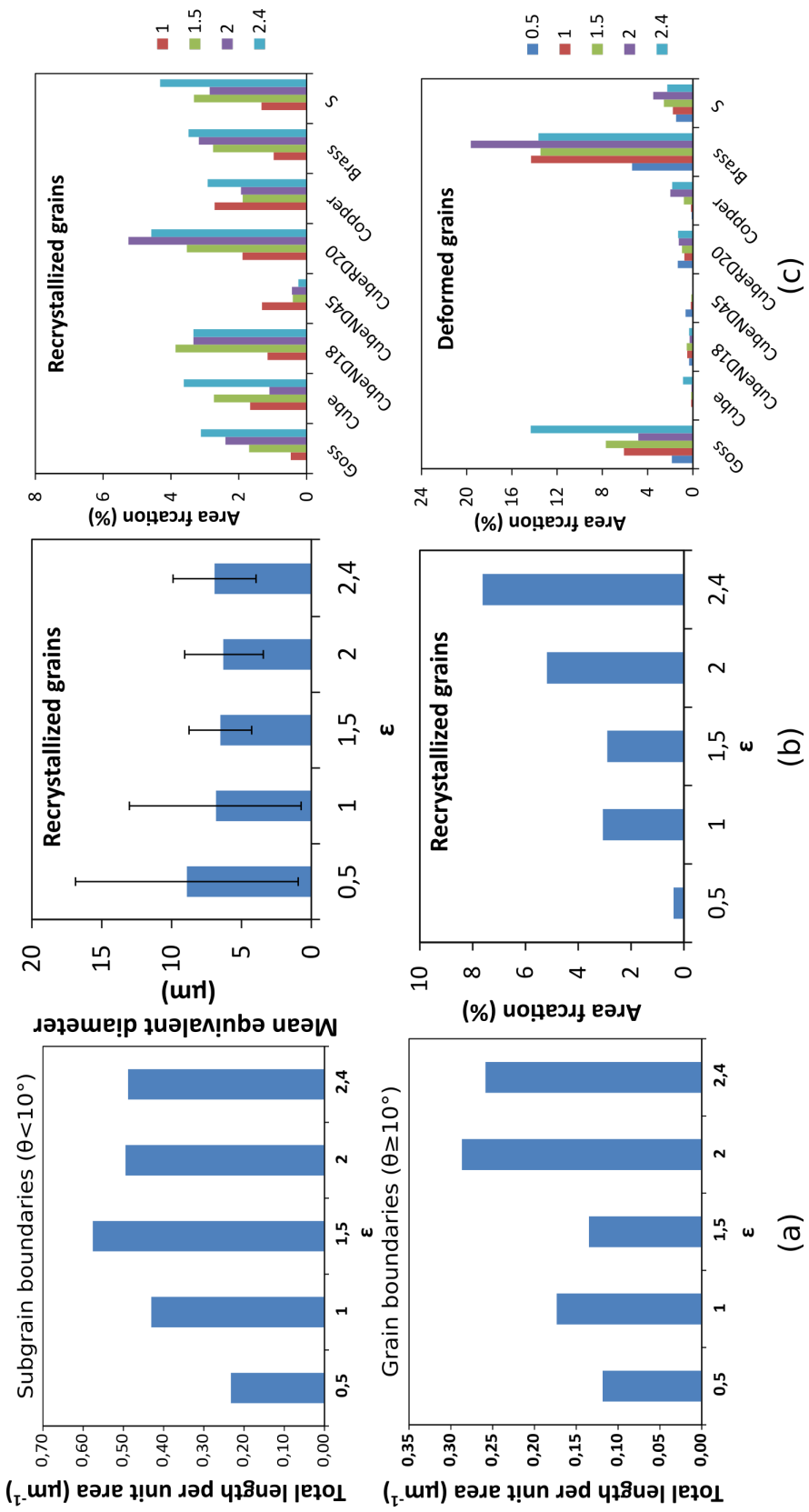

Fig. 6.7 (a) Total length of subgrain and grain boundaries as a function of strain respectively. (b) Mean size and area fraction of recrystallized grains as a function of strain. Each plotted error bar corresponds to the standard deviation. (c) Area fraction of recrystallized and deformed grains belonging to typical texture components respectively.

6.2 Comparison between single pass and multipass tests

6.2.1 Thermomechanical parameters

As mentioned in section 1.1.2, the industrial hot rolling process requires multiple passes. Two successive passes are separated by an interpass holding time, which may change the evolved microstructure after each pass. Therefore, the objective of this section is to understand the effect of multipass deformation on deformed and quenched microstructure and compare it with the result of a single pass deformation (presented in section 6.1). The parameters of performed multipass deformation tests are summarized by figure 6.8. The true strain during each applied pass is 0.5. For a total strain of 1, 2 passes of a strain of 0.5 each are conducted. The holding time between the two successive passes is chosen to be 5 s (in the range of interpass times during hot rolling). The specimen is quenched right after deformation without any holding time. However, a quench delay of 2 s is inevitable. For higher values of cumulative strain, similar approach is adopted as seen by figure 6.8.

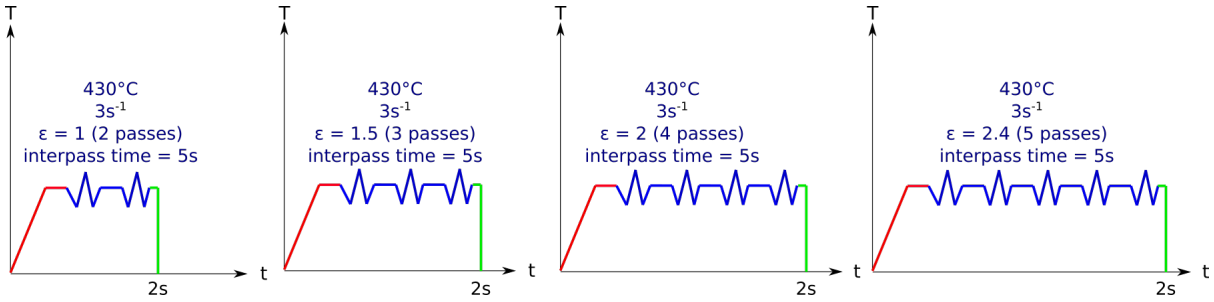

Fig. 6.8 Thermomechanical paths applied to study the effect of cumulative strain on recrystallization. These thermomechanical paths are performed on the samples with a high initial precipitate content.

The evolution of actual temperature (measured by the thermocouples located according to figure 3.5 in Chapter 3) as a function of time for each performed hot compression test is shown by figure 6.9. The temperature measured at mid-thickness of the compressed part of each sample is shown in blue, whereas the temperature measured at mid-thickness of the non-compressed part is shown in red. An increase of the temperature measured at the compressed part occurs during each single pass test. For single pass tests (figures 6.9 (e-h)), the temperature increases to about 445°C for strains of 1, 1.5 and 2 and to about 450°C for a strain of 2.4. During mutlipass tests (see figures 6.9 (a-d)), the temperature increases to about 445°C during the first passes and decreases to reach a temperature of about 440°C during the interpass time. However, at the last passes (see figures 6.9 (c,d)), the temperature measured at mid-thickness of the compressed part does not show any increase, which is inconsistent with the principle of heat generation due to plastic straining. This may be due to the fact that the thermocouple located at the compressed part of the sample does not remain in place during deformation at

the last passes or to the fact that the thermocouple is damaged at the last steps (its diameter approaching the sample's thickness at the last pass).

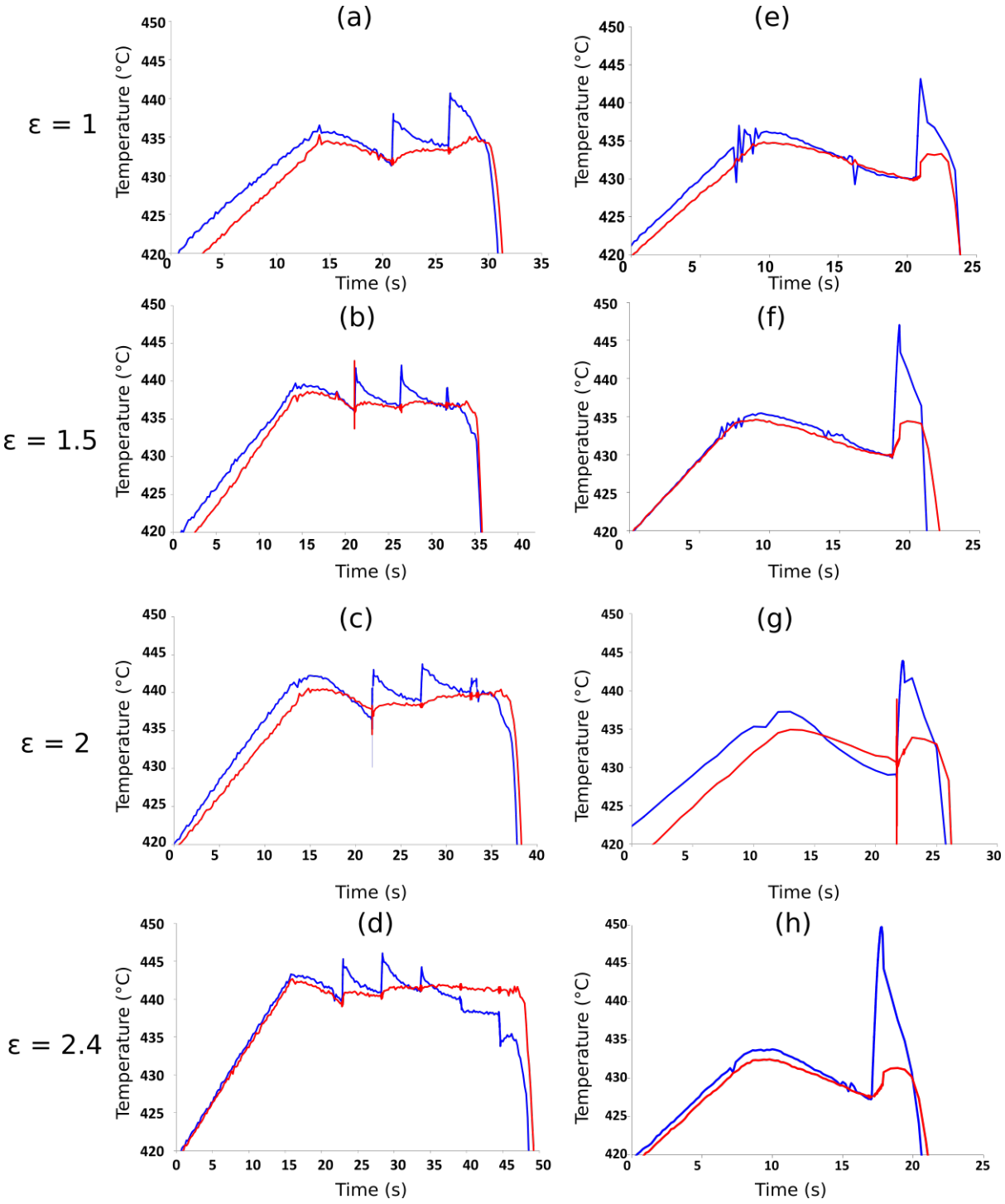

Fig. 6.9 (a-d) Evolution of actual measured temperatures during a multipass test at different strain levels: 1, 1.5, 2 and 2.4, respectively. (e-h) Evolution of actual measured temperature during a single pass test at different strain levels: 1, 1.5, 2 and 2.4, respectively. The temperature measured at mid-thickness of the compressed part is shown by a blue curve, while the temperature measured at the non-compressed part is shown by a red curve.

6.2.2 Microstructure right after multipass hot deformation

The microstructures quenched after multipass deformation are compared with the ones quenched after single pass deformation at different strains as shown by figures 6.10 (a) and (c). At this scale, no visible difference can be seen between the microstructures obtained after multipass deformation and the ones obtained after single pass deformation. This is confirmed by the $\{111\}$ pole figures corresponding to these microstructures and shown by figures 6.10 (b) and (d). For a given strain whatever it is applied in multiple passes or in a single pass, $\{111\}$ pole figures look alike. Magnified EBSD orientation maps will be analyzed in order to confirm this.

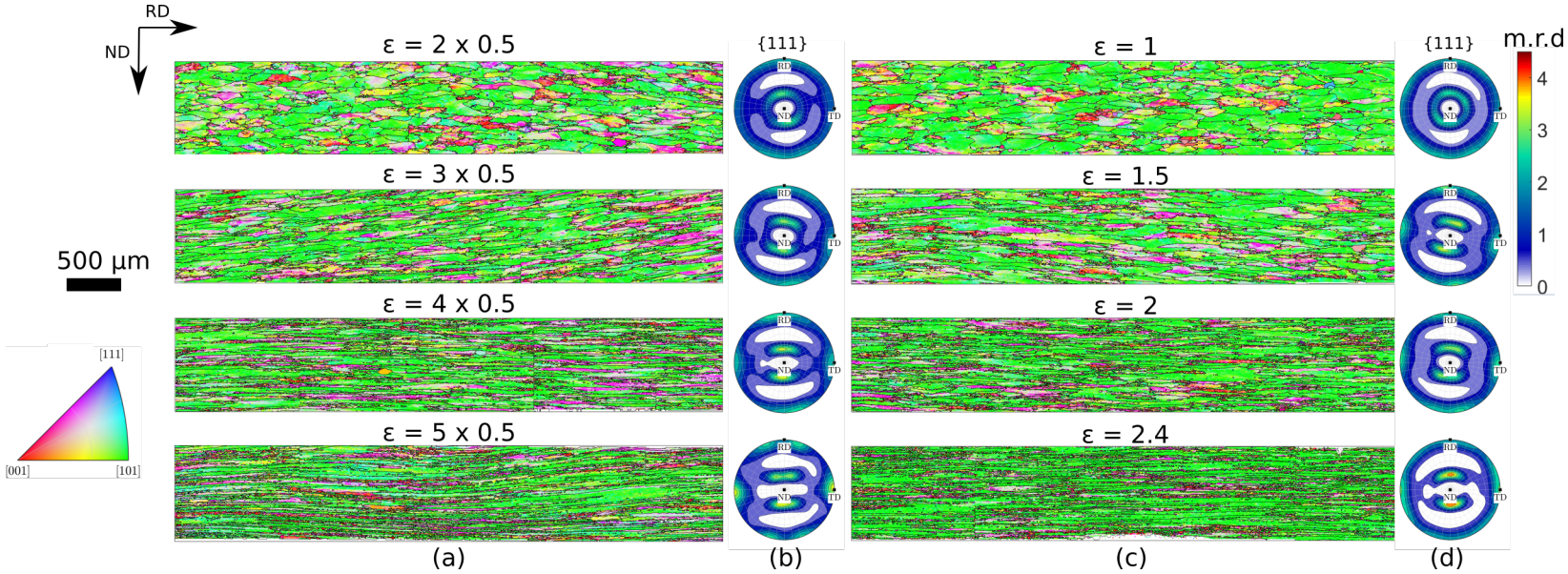

Fig. 6.10 (a) EBSD orientation maps showing the evolution of the microstructure quenched after multipass deformation at different strains, (b) $\{111\}$ pole figures corresponding to (a), (c) EBSD orientation maps showing the evolution of the microstructure quenched after single pass deformation at different strains and (d) $\{111\}$ pole figures corresponding to (c). For EBSD orientation maps, the color code defined on the standard triangle refers to the normal direction. The measurement step size is 3 µm.

Figure 6.11 shows the KAM values corresponding to magnified EBSD orientation maps on the deformed and quenched sample at different strain values (between 1 and 2.4). Figure 6.11 (a) corresponds to samples that have been deformed by multipass tests, whereas figure 6.11 (b) corresponds to samples that have been deformed by single pass tests. KAM maps corresponding to smaller regions indicated by red boxes on whole KAM maps are also shown by figure 6.11. By comparing between figures 6.11 (a) and (b), it is clear that the KAM maps of microstructures deformed to a certain cumulative strain whether by multiple passes or a single pass are similar. Regardless the strain value, dynamic recovery seems to be the main softening mechanism in all microstructures and the subgrain size seems to be similar. The only observed difference is the size of some recrystallized grains at a large strain value (i.e. $\epsilon \approx 2.4$). During a multipass hot compression test at a strain of about 2.4, one recrystallized grain (shown by a black arrow) is much larger in size than the recrystallized grains that are formed during a single pass hot compression test at the same strain. The magnified KAM map taken around this large recrystallized grain (figure 6.12) shows a subgrain boundary inside this grain. This suggests that the large recrystallized grain has been formed dynamically during one of the passes or post-dynamically during interpass and was subsequently deformed or that it has been simply formed post-dynamically at the end of deformation with a similarly oriented neighboring subgrain/grain.

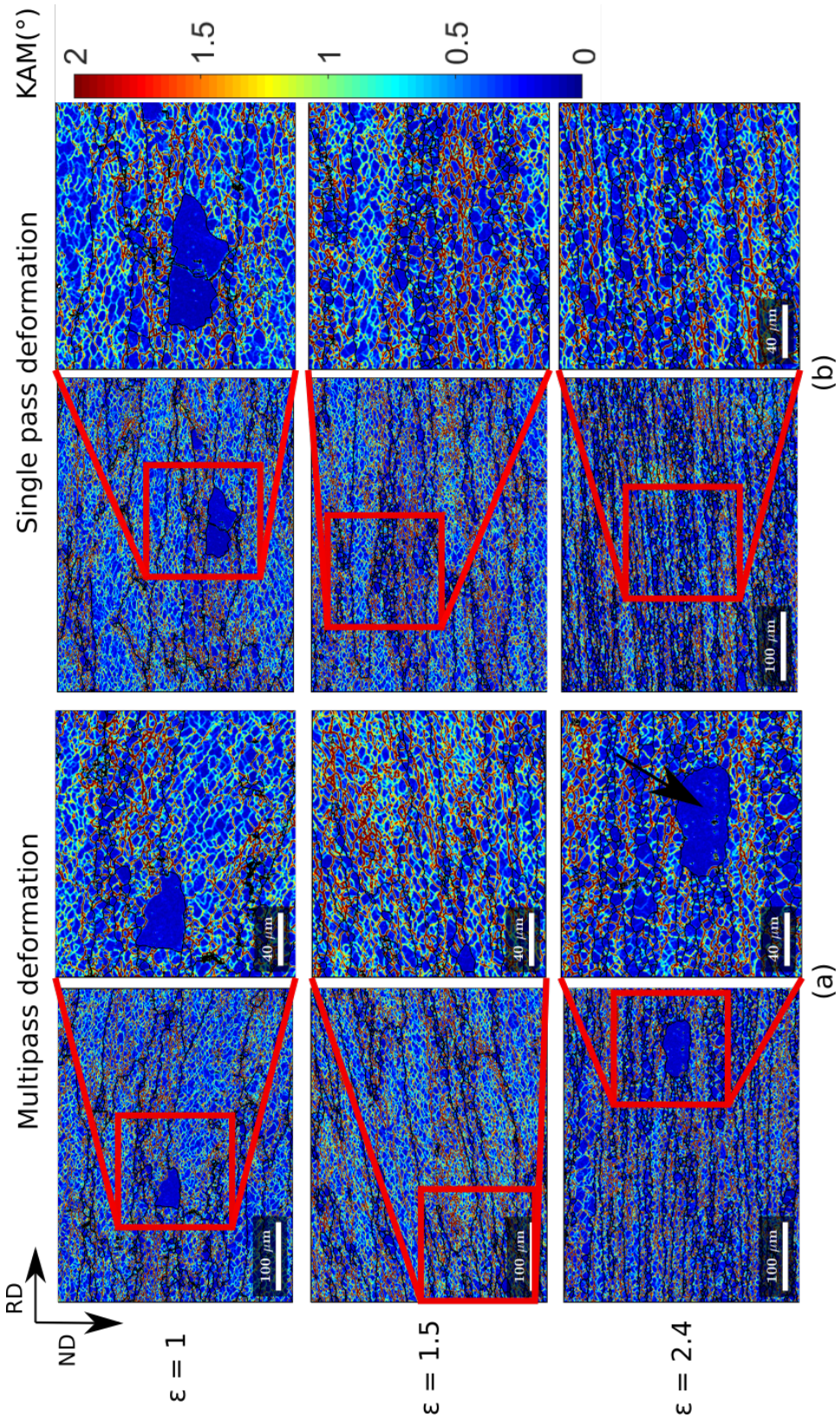

Fig. 6.11 KAM maps corresponding to magnified EBSD orientation maps taken on quenched and deformed specimens showing grain boundaries in black at different strain levels: (a) after multipass tests and (b) after single pass tests. The used EBSD pixel size is 0.4 µm.

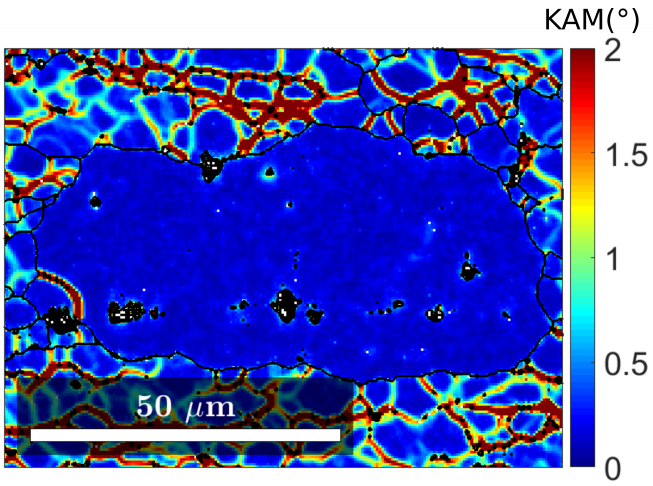

Fig. 6.12 Magnified KAM map around the large recrystallized grain shown by a black arrow on figure 6.11 (a). The EBSD measurement pixel size is 0.4 μm.

Figure 6.13 (a) shows the mean equivalent diameter of recrystallized grains examined right after deformation whether it is single pass or multipass at various strains. The mean size of recrystallized grains seems to be similar on average regardless the way the hot compression test is performed at a specific strain level. Figure 6.13 (b) shows also the evolution of area fraction of recrystallized grains with strain after both single pass and multipass hot compression tests. The area fraction of recrystallized grains is similar also between the two types of experiments. This confirms that, within the applied thermomechanical conditions, on average the size and area fraction of recrystallized grains are not dependent on the number of passes performed in order to reach a specific strain value. This may be due to short holding time between two successive passes, which does not allow additional recrystallized grains to form or already formed recrystallized grains to grow. The evolution of microstructure during post-deformation holding will be studied in the next section.

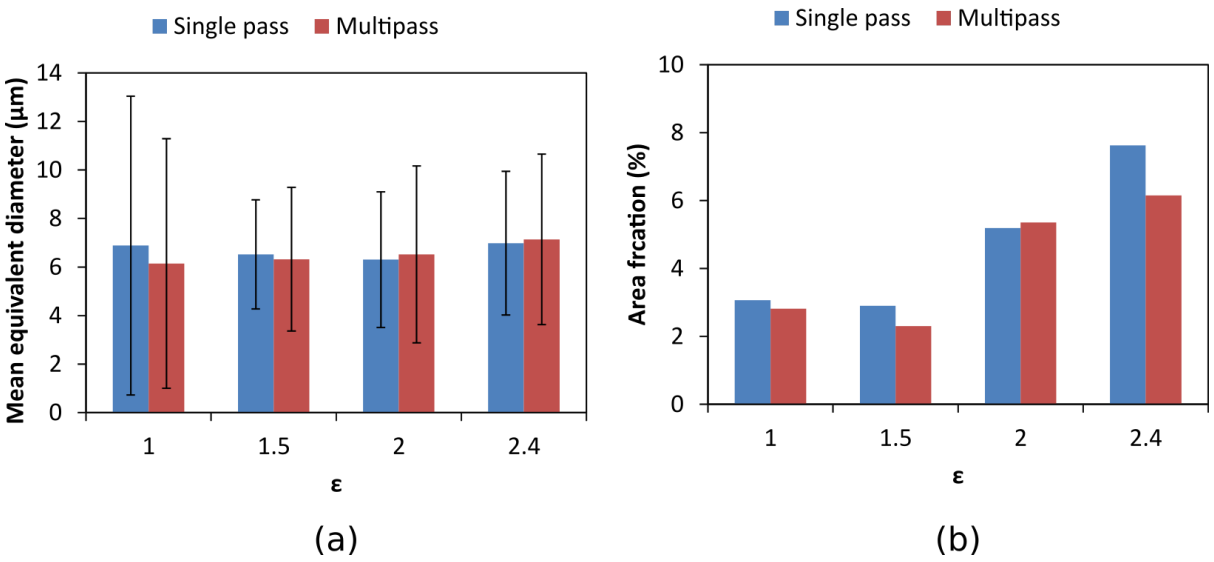

Fig. 6.13 (a) Mean equivalent diameter and (b) area fraction of recrystallized grains formed during both multipass and single hot compression tests at different strain values. Each error bar plotted in (a) corresponds to the standard deviation value.

6.2.3 Microstructure after post-deformation holding

Figure 6.14 shows the evolution of temperature with time during a single pass deformation at a strain of 2.4 followed by a holding for 20s in the test furnace before water quench. It is evident from figure 6.14 that the holding temperature is about 435°C. For the sample that is deformed in a multipass test at the same strain (i.e. 2.4) and water quenched right after deformation (whose temperature evolution is shown by figure 6.9 (d)), the holding is conducted in salt bath at 435°C for 20s. This allows to determine whether the evolved microstructures during holding after single pass or multipass deformation are different.

The evolved microstructures during holding for 20 s at 430°C after multipass hot deformation as well as after single pass hot deformation are shown by figures 6.15 (a) and (b) respectively. Larger recrystallized grains develop in the sample that has been deformed by multiple passes. Based on the SEM SE images shown by figures 6.15 (a) and (b), the precipitation state after holding for 20 s at 430°C seems to be similar between the two microstructures. This suggests that precipitates are not responsible for the differences observed in the size of large recrystallized grains. The holding temperature of 435°C is similar between the two microstructures shown by figure 6.15 and cannot thus be held responsible for the differences between these two microstructures.

As mentioned in the previous section (see figure 6.11 (a)), at a large strain ($\epsilon \approx 2.4$), one recrystallized grain in the observed area (1137 µm x 852 µm) was able to grow to a larger extent than other observed recrystallized grains. The size advantage of few recrystallized grains that have formed during the multipass deformation may be the reason behind the growth advantage of recrystallized grains in this sample. Other EBSD orientation maps with a smaller pixel size

of 1 µm would be needed to be taken on other regions in the water quenched sample right after multipass deformation in order to confirm this.

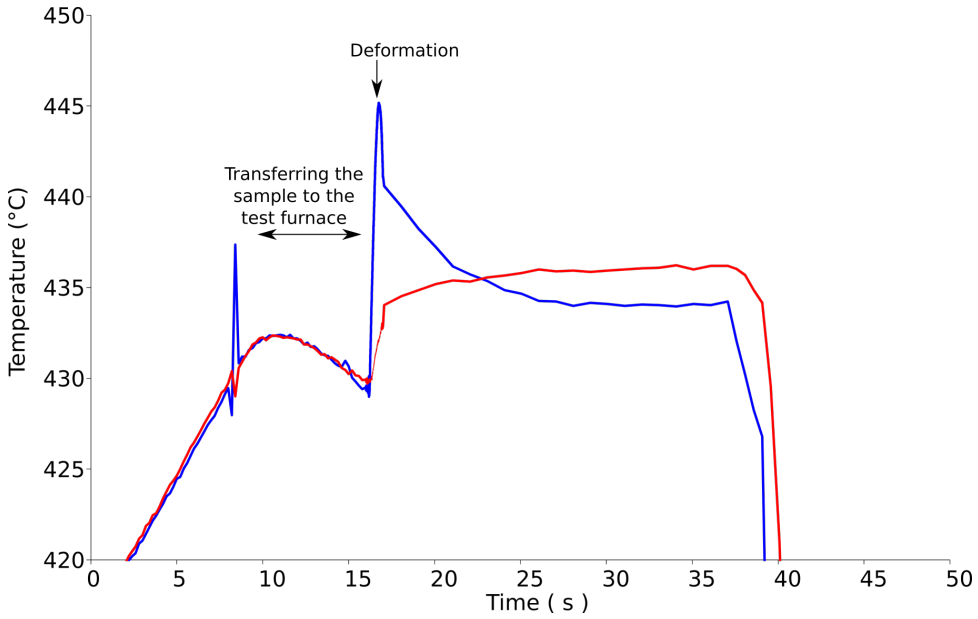

Fig. 6.14 Evolution of temperature with time during a single pass hot compression test followed by a post-deformation holding for 20s. The nominal testing conditions are 430°C, $3s^{-1}$ and ϵ = 2.4. The temperature measured at mid thickness in the deformed part of the sample is shown by the blue line, whereas the temperature measured at mid thickness in the non-compressed part is shown by the red line.

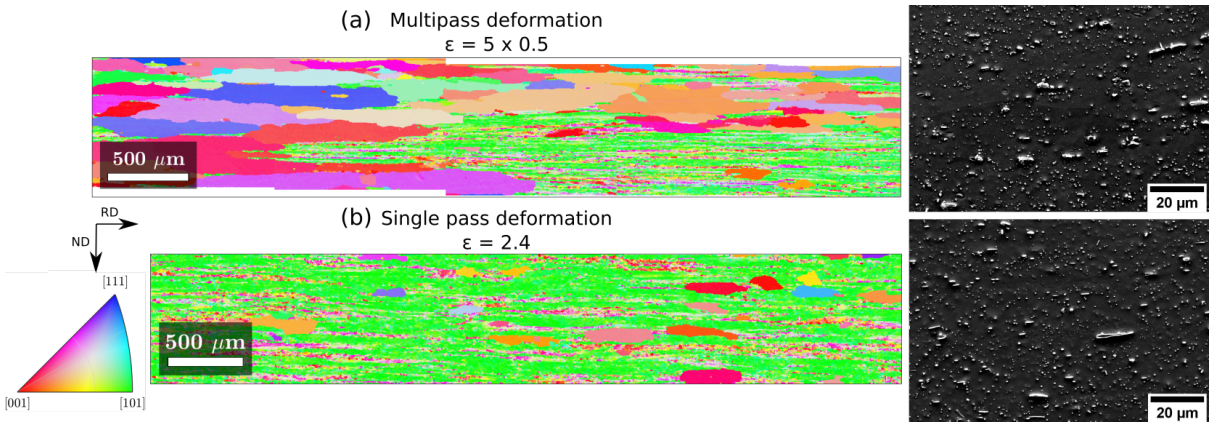

Fig. 6.15 (a) EBSD orientation map showing the microstructure after post-deformation holding for 20 s at 430°C after multipass deformation. Corresponding SEM SE image is shown on the right side. The post-deformation holding is performed on a deformed and quenched sample that has been reheated in a salt bath. (b) EBSD orientation map showing the microstructure after post-deformation holding for 20 s at 430°C after single pass deformation. Corresponding SEM SE image is shown on the right side. The post-deformation holding is performed in the test furnace of the hot compression machine right after deformation. For EBSD orientation maps, the color code defined on the standard triangle refers to the normal direction. The measurement pixel size is 3 µm.

6.3 Influence of strain rate

6.3.1 Thermomechanical schedules

Figure 6.16 illustrates the thermomechanical paths that have been applied on compression samples in order to study the effect of strain rate on recrystallization. For this purpose, the testing temperature (430 °C) and strain (2.4) were kept constant, while the strain rate was varied from 3 s^{-1} to 10 s^{-1}. For a higher strain rate value, self heating of the tested sample during deformation is expected. In order to minimize this effect, multiple passes separated by a holding time of 5 s were performed instead of a single pass. This allows to reach almost the same temperature at the end of deformation before water quench or post-deformation holding (of about 435°C as can be seen in figures 6.16 (c) and (d)). The tested specimens were held at the testing temperature for different holding times before being water quenched in order to study the evolution of microstructure during post-deformation holding. The results of these tests are presented below.

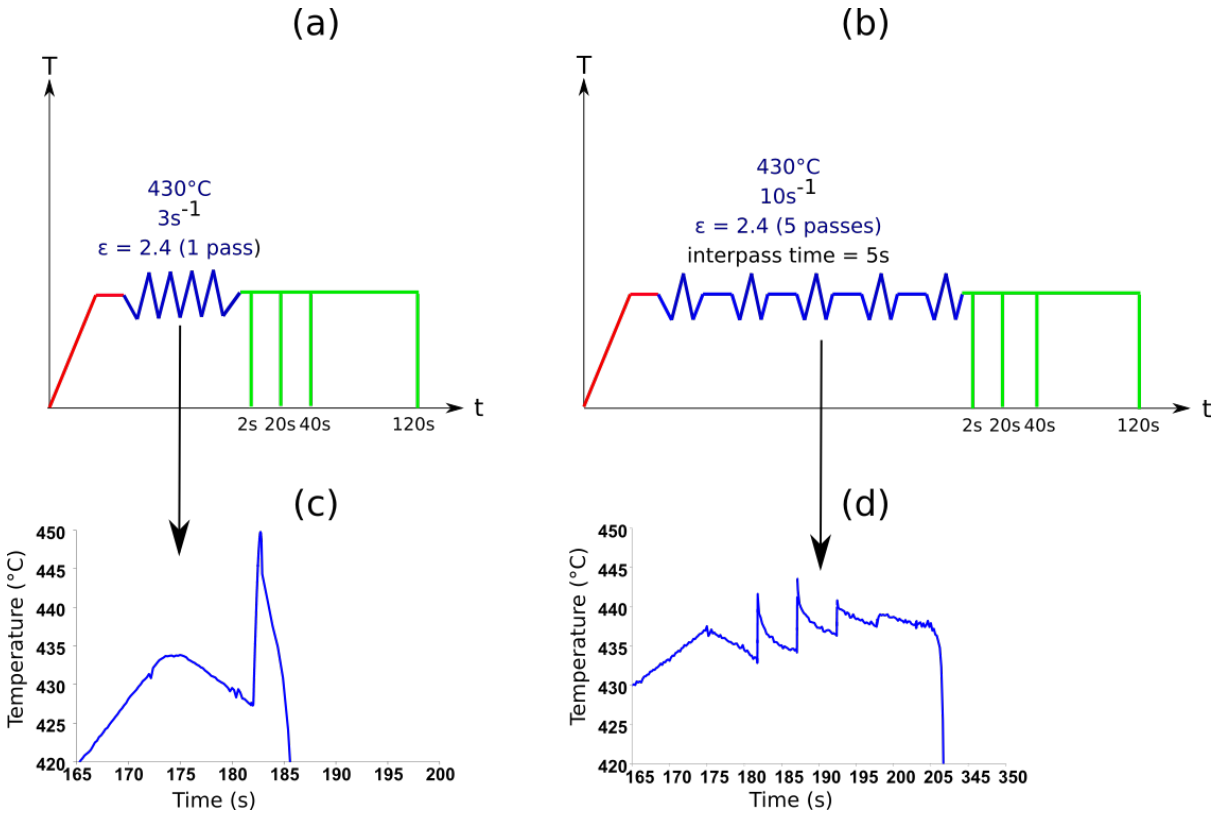

Fig. 6.16 (a,b) Schematic diagrams showing the applied thermomechanical paths in order to investigate the influence of strain rate on recrystallization. At a high strain rate, the sample has been deformed by multiple passes to minimize its self heating. (c,d) The evolution of temperature (measured at mid-thickness of the compressed part of each sample) during time during deformation in (a) and (b) respectively. The initial samples have a high initial precipitate content.

6.3.2 Evolution of microstructure during post-deformation holding

Figure 6.17 shows the evolution of microstructure during holding at 430°C after deformation at two different strain rates: 3 s^{-1} and 10 s^{-1}. It is evident that the strain rate has an influence on the post-dynamic recrystallization behavior. At a higher strain rate value (i.e. 10 s^{-1}), a larger number of large recrystallized grains is observed than at a lower strain rate (i.e. 3 s^{-1}). The final size of recrystallized grains is also smaller after deforming at a higher strain rate. This may be due to higher number of nuclei due to the higher stored energy at a higher strain rate, which is consistent with [129]. This will be verified later in this section.

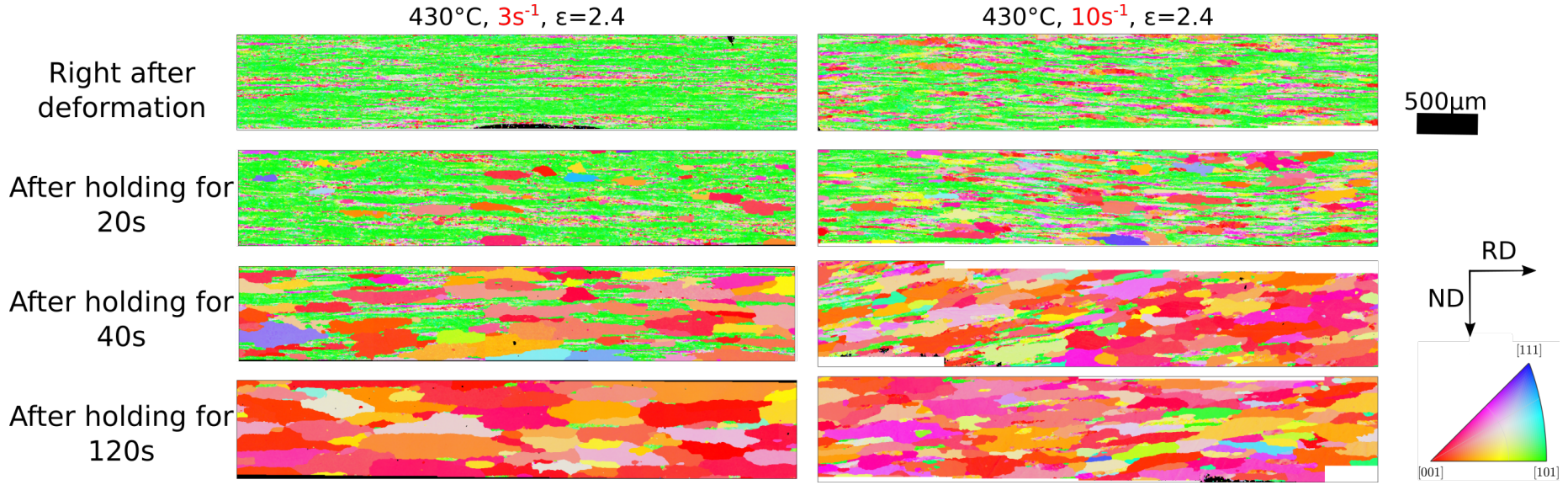

Fig. 6.17 Evolution of microstructure during holding after deformation at different strain rates. The measurement step size is 3 μm. The color code defined on the standard triangle refers to the normal direction.

Figures 6.18 (a) and (c) show magnified EBSD orientation maps of the deformed and quenched microstructures after deforming at a higher and a lower strain rates respectively. High angle boundaries ($\theta > 10°$) are plotted in black lines, while low angle boundaries ($2° \leq \theta \leq 10°$) are plotted in blue lines. The zooms onto the EBSD orientation maps show that subgrain boundaries are better defined in the case of a lower strain rate than at a higher strain rate. This makes sense since a lower strain rate gives more time for dislocation movement and therefore dynamic recovery to occur [129].

This is confirmed by figure 6.18 (d), where a higher number of smaller subgrains / grains can be observed compared to figure 6.18 (b). This is probably due to the enhanced dynamic recovery at a lower strain rate. In fact, it has been reported by [35] that at a strain higher than 0.3 and at a low strain rate (e.g. $10^{-3}\ s^{-1}$), dynamic recovery precedes CDRX. However, when strain rate increases, DDRX starts to occur instead of CDRX due to the absence of dynamic recovery [35]. Therefore, the smaller recrystallized grains observed at a lower strain rate (see figures 6.18 (c) and (d)) may originate from subgrains by CDRX. On the other hand, it is difficult to determine the origin of larger recrystallized grains formed at a higher strain rate (see figures 6.18 (a) and (b)). According to [35], they may originate by DDRX due to the inhibition of dynamic recovery and thus CDRX. The larger recrystallized grains may have formed also during the first passes, grown during the interpass time and have been deformed subsequently during the following passes since the hot compression test performed at a higher strain rate was performed in multiple passes.

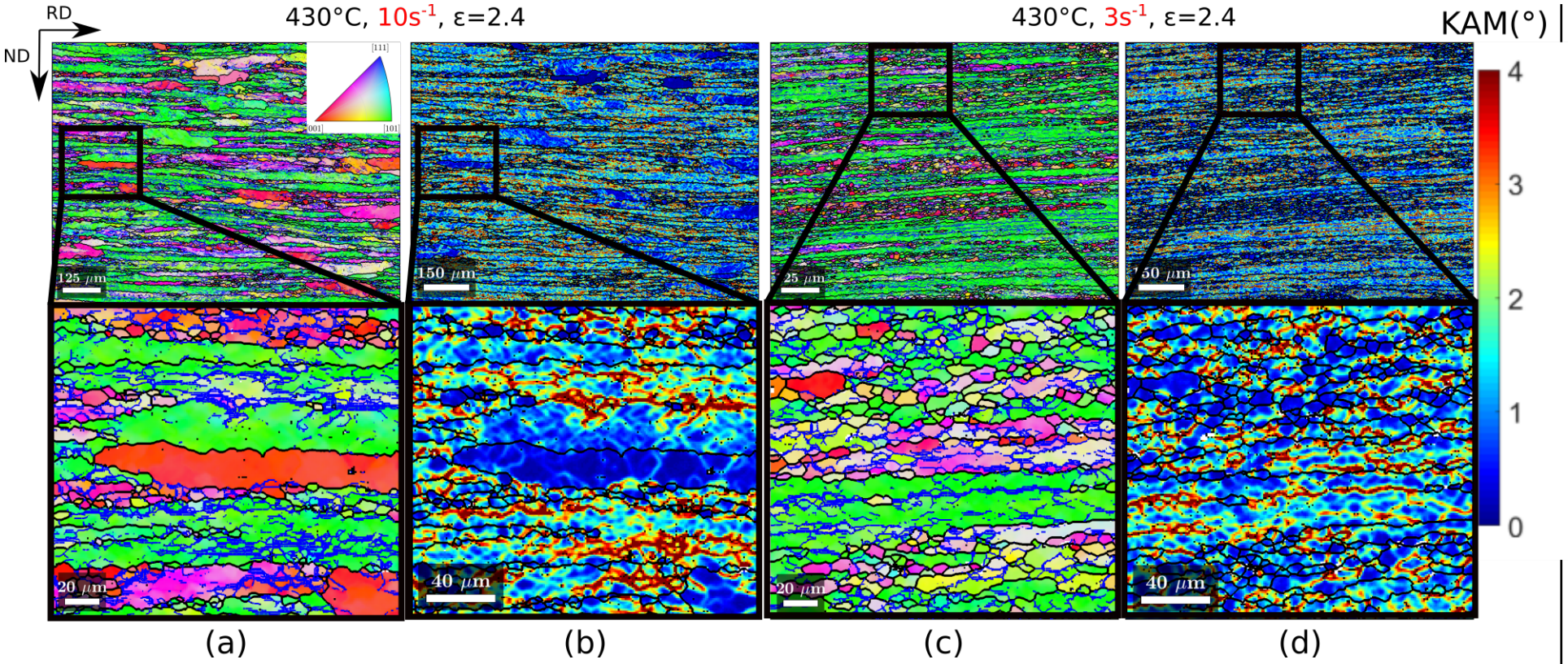

Fig. 6.18 (a) EBSD orientation map and a zoom on it showing high angle boundaries in black and low angle boundaries in blue taken on a quenched microstructure after deforming at a higher strain rate (10 s^{-1}), (b) KAM maps corresponding to images shown by (a), (c) EBSD orientation map and a zoom on it showing high angle boundaries in black and low angle boundaries in blue taken on a quenched microstructure after deforming at a higher strain rate (3 s^{-1}), (d) KAM maps corresponding to images shown by (c). The measurement pixel size is 1 μm. The color code defined on the standard triangle refers to the normal direction.

Figures 6.19 (a,b) show the recrystallized grains examined right after deformation at strain rates of 10 s^{-1} and 3 s^{-1}, respectively. Figure 6.19 (a) shows the presence of large recrystallized grains in addition to small recrystallized grains right after deforming at 10 s^{-1}, while figure 6.19 (b) shows the presence of small recrystallized grains with a more uniform size distribution after deforming at 3 s^{-1}. The larger recrystallized grains examined in the microstructure deformed at a higher strain rate in multiple passes may have been formed dynamically during one of the applied passes or post-dynamically during the interpass time as mentioned earlier, which gives time for these grains to grow to larger sizes unlike in the microstructure deformed at a lower strain rate in a single pass. In addition to that, as mentioned in the previous section, the dislocations do not have enough time to annihilate and rearrange themselves in sub-boundaries during deformation at a higher strain rate, leading thus to a higher stored energy in the microstructure deformed at a higher strain rate. This higher stored energy will promote the growth of recrystallized grains during interpass time or during the quench delay right after deformation. This could therefore explain the larger size of some recrystallized grains in the case of a microstructure deformed at a higher strain rate.

Figure 6.19 (c) shows the mean equivalent diameter of recrystallized grains in both microstructures deformed at 10 s^{-1} and 3 s^{-1} as well as the standard deviations for both recrystallized grain size distributions. The mean equivalent size is similar, but the standard deviations are different. The standard deviation in the case of a microstructure deformed at a higher strain rate is larger due to the huge scatter in the recrystallized grain size (as seen by figure 6.19 (a)). Figure 6.19 (d) shows a lower number of recrystallized grains per unit area in the case of a microstructure deformed at a higher strain rate. This could be explained by two reasons: the growth of larger recrystallized grains at the expense of smaller ones and the inhibition of the occurrence of CDRX due to the less developed subgrain structure in this case.

In order to confirm the role of stored energy in the growth of larger recrystallized grains in the case of a microstructure deformed at a higher strain rate, $\left|\overline{KAM}_{neighborhood} - GAM_{rex}\right|$ around recrystallized grains in both microstructures shown by figures 6.19 (a) and (b) are calculated and their distributions are shown by figures 6.19 (e) and (f). It has been found that 18% of recrystallized grains in the case of a microstructure deformed at 10 s^{-1} have $\left|\overline{KAM}_{neighborhood} - GAM_{rex}\right|$ values higher than 1°, while 6% of recrystallized grains in the case of a microstructure deformed at 3 s^{-1} have $\left|\overline{KAM}_{neighborhood} - GAM_{rex}\right|$ values higher than 1°. The mean value of $\left|\overline{KAM}_{neighborhood} - GAM_{rex}\right|$ in the case of a microstructure deformed at 10 s^{-1} is higher than that in the case of a microstructure deformed at 3 s^{-1}. These calculations confirm therefore that the stored energy gradients across the recrystallized grain boundaries favor the growth of recrystallized grains in the case of a microstructure deformed at a higher strain rate.

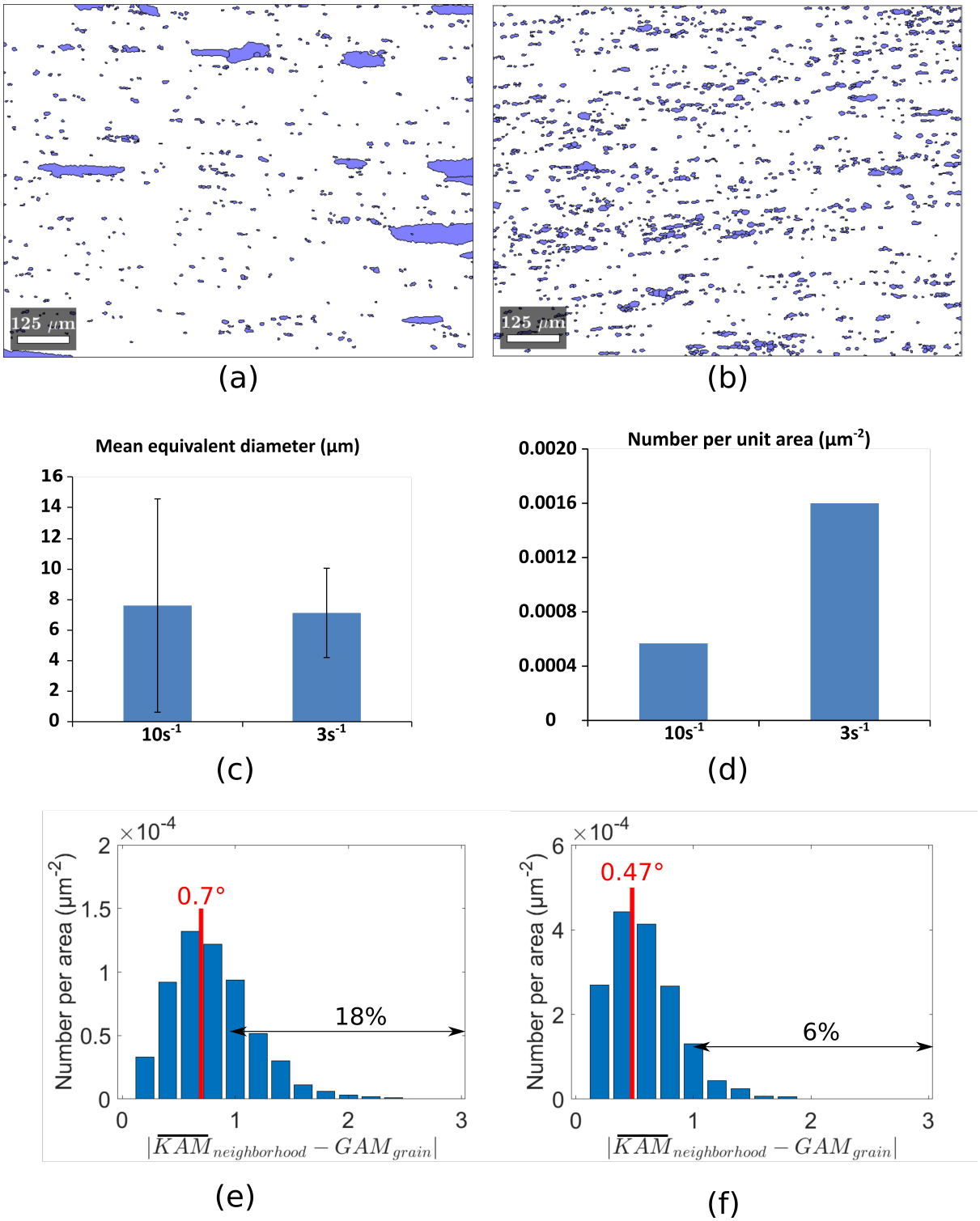

Fig. 6.19 (a,b) Maps showing only recrystallized grains in the deformed and quenched samples right after deformation at 10 s^{-1} and 3 s^{-1}, respectively. (c) Mean size and (d) density of recrystallized grains observed right after deformation at 10 s^{-1} and 3 s^{-1}, respectively. (e,f) $\left|\overline{KAM}_{neighborhood} - GAM_{rex}\right|$ distribution for recrystallized grains examined right after deformation at 10 s^{-1} and 3 s^{-1}, respectively.

Figures 6.20 (a) and (b) show the microstructures evolved during holding for 20s right after deformation at 10 s^{-1} and 3 s^{-1}. The recrystallized grains corresponding to each microstructure

are shown by figures 6.20 (c) and (d), respectively. It is evident from figure 6.20 that the number of large recrystallized grains is higher in the case of a holding of a microstructure deformed at a higher strain rate than in the case of a holding a microstructure deformed at a lower strain rate for the same amount of time. This confirms that stored energy promotes the growth of a higher number of recrystallized grains in the case of a higher strain rate, leading therefore to a higher number of large recrystallized grains. Therefore, a large recrystallized grain in the case of a microstructure deformed at a higher strain rate has less room to grow at the expense of small recrystallized grains and deformed matrix, due to the higher number of neighboring large recrystallized grains. Once large recrystallized grains impinge upon each other, grain growth is expected to stop due to the absence of a stored energy gradient between these large recrystallized grains. This is why the final recrystallized grain size after holding for 120s in the case of a microstructure deformed at a higher strain rate is smaller than that in the case of microstructure deformed at a lower strain rate (see figure 6.17).

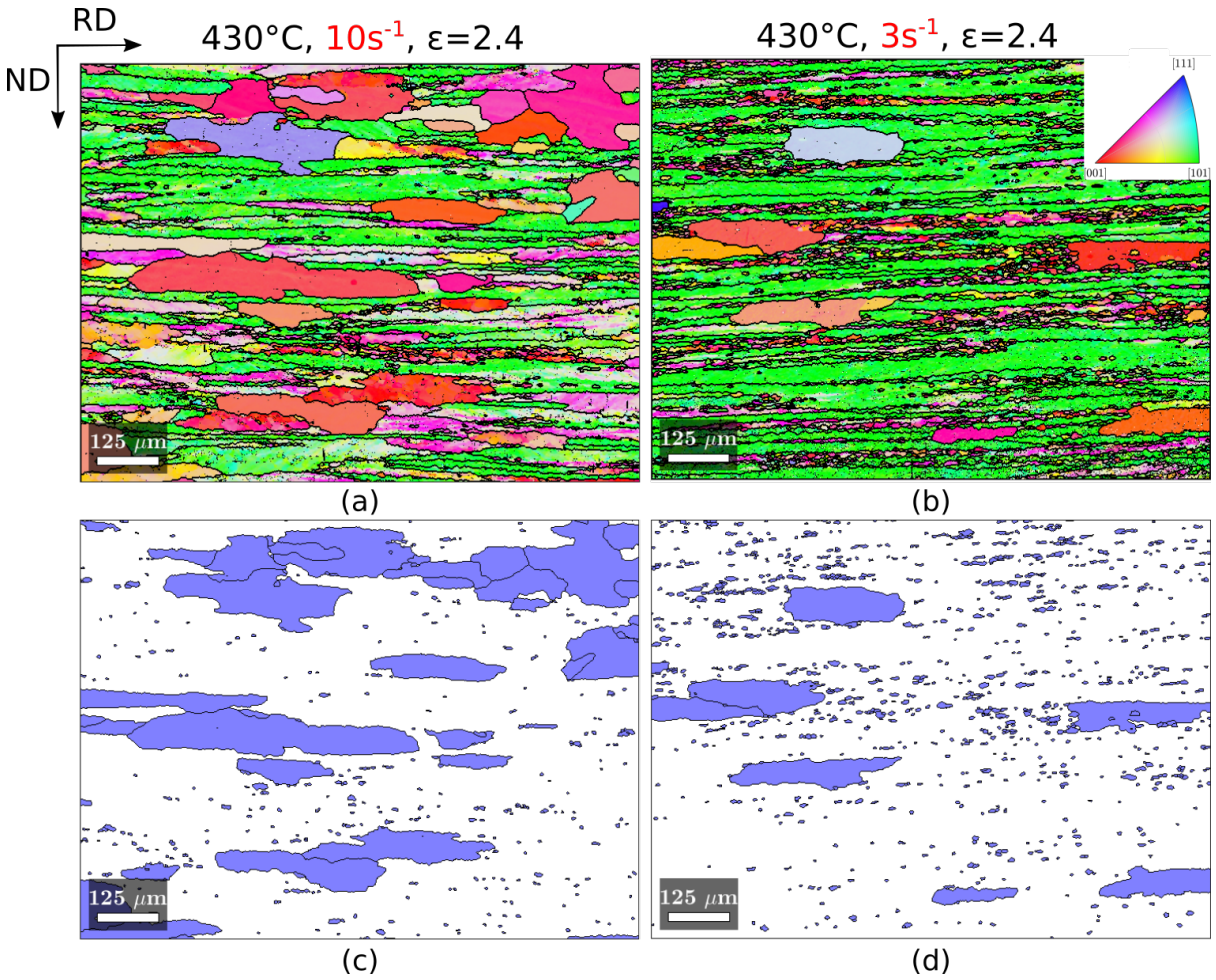

Fig. 6.20 (a) EBSD orientation map showing the microstructure quenched after deforming at 10 s^{-1} and holding for 20s. (b) EBSD orientation map showing the microstructure quenched after deforming at 3 s^{-1} and holding for 20s. (c) Map showing recrystallized grains corresponding to the EBSD orientation map in (a). (d) Map showing recrystallized grains corresponding to the EBSD orientation map in (b). The measurement step size is 1 µm. The color code defined on the standard triangle refers to the normal direction.

6.4 Influence of temperature

6.4.1 Themomechanical paths

Figure 6.21 illustrates schematically the thermomechanical paths applied to the samples in order to investigate the effect of deformation temperature on the evolved microstructure. One batch of samples was deformed at 430°C, 3 s^{-1} and a strain of 2.4. Another batch was deformed at 360°C, 3 s^{-1} and a strain of 2.4. The samples were quenched right after deformation to freeze the deformed microstructure. Other samples were held for some time after hot deformation before water quench in order to study the evolution of microstructure during post-deformation holding.

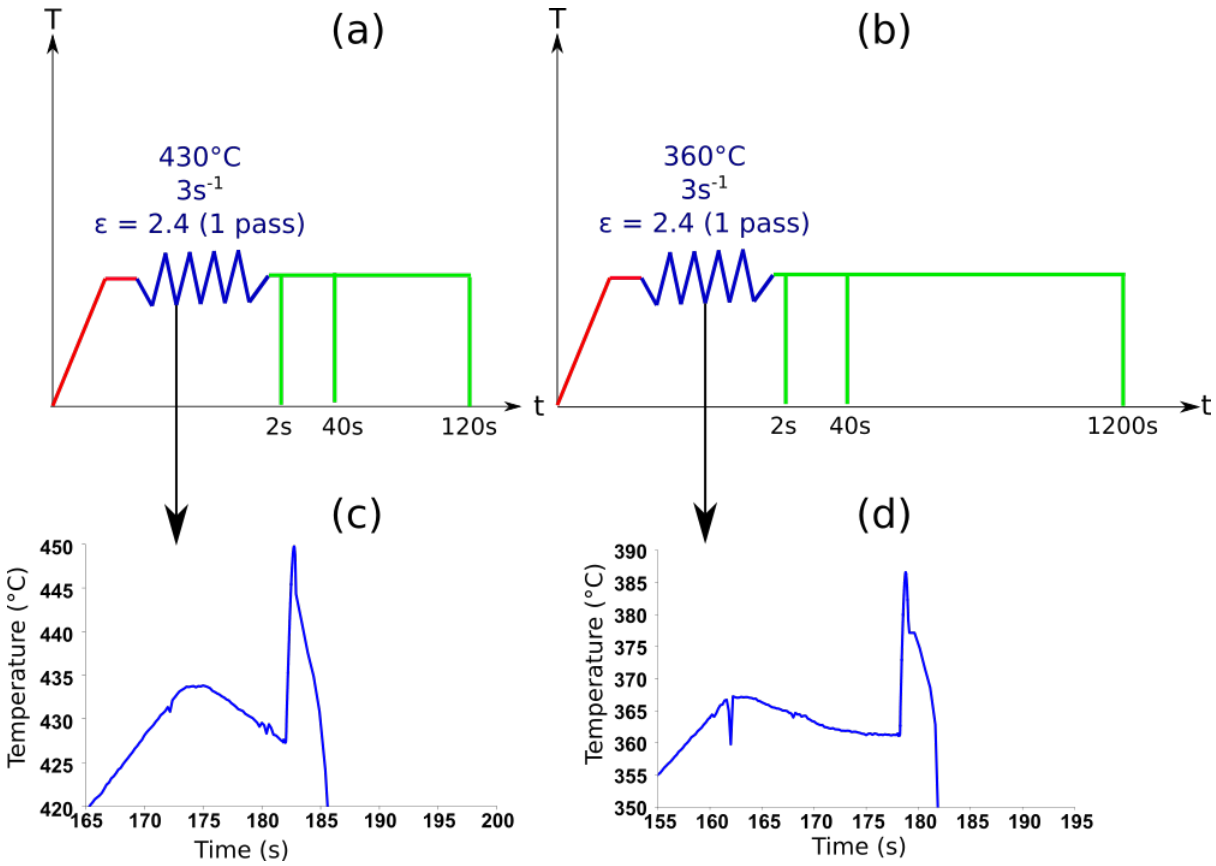

Fig. 6.21 (a,b) Themomechanical schedules applied to investigate the effect of deformation temperature on recrystallization behavior. The two tested temperature were 430°C and 360°C. The strain rate and strain are fixed. Water quenching was performed right after deformation and after each holding time. (c,d) The evolution of temperature (measured at mid-thickness of the compressed part of each sample) with time during hot compression in (a) and (b), respectively. The initial samples have a high initial precipitate content (see section 4.1).

6.4.2 Evolution of microstructure during post-deformation holding

Figures 6.22 (a) and (b) show the evolution of deformed and quenched microstructure during holding after deforming at a higher temperature (i.e. 430°C) and at a lower temperature (i.e. 360°C) respectively. Figure 6.22 (b) shows clearly that the recrystallization behavior is slower in the case of a hot deformation at 360°C. At a lower deformation temperature, it is more difficult for dislocations to move, leading to their accumulation and entanglement and therefore to the retardation of dynamic recovery. CDRX may be thus retarded, while DDRX may be promoted due to the increase of the stored energy. This will be verified in the next paragraph by analyzing higher magnification EBSD orientation maps taken on the deformed and quenched microstructures. On the other hand, during holding at a lower temperature, the mobility of grain boundaries is lower and therefore their migration does not operate easily, which may explain the slowdown of development of large grains during holding at 360°C.

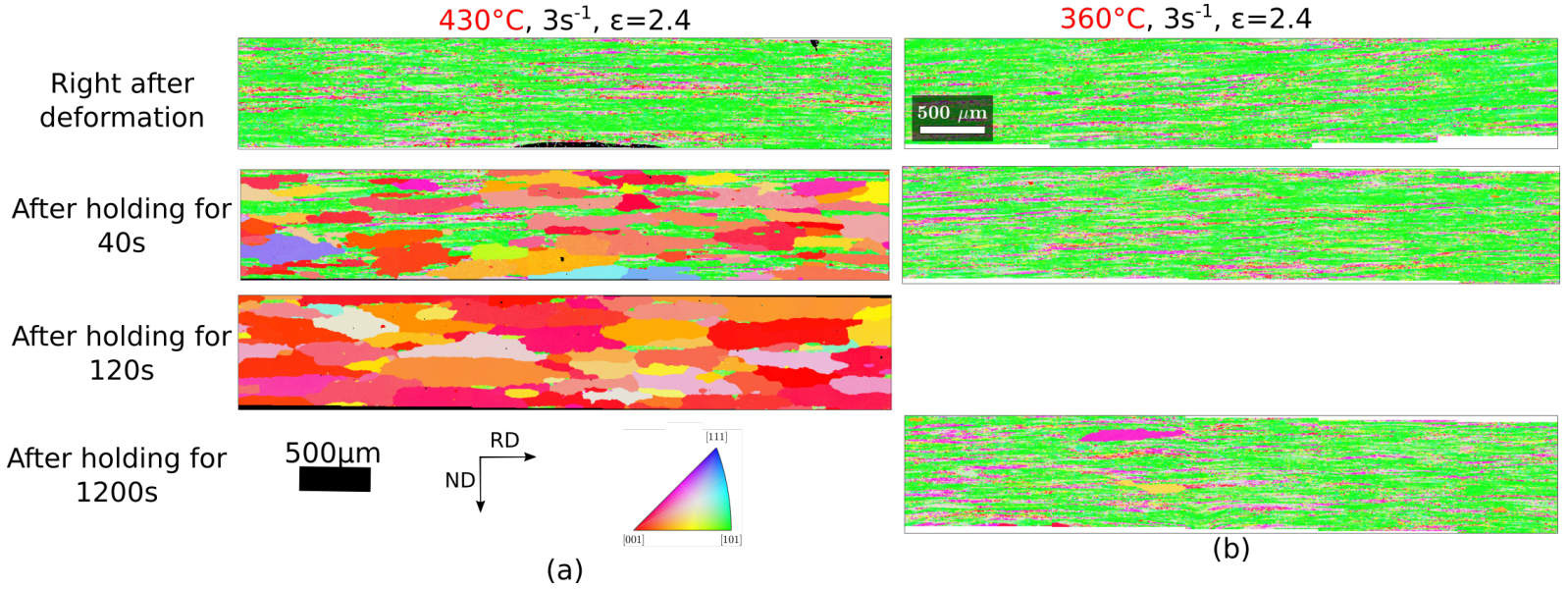

Fig. 6.22 Stitched EBSD orientation maps showing the evolution of deformed microstructure during holding after deforming at (a) a higher temperature (i.e. 430°C) and (b) at a lower temperature (i.e. 360°C) respectively. The measurement pixel size is 3 μm. The color code defined on the standard triangle refers to the normal direction.

Figures 6.23 (a) and (b) shows magnified EBSD orientation maps with a smaller measurement step size (i.e. 0.4 µm) of quenched microstructures right after deformation at 430°C and 360°C respectively. The high angle boundaries ($\theta > 10°$) are shown by black lines, whereas low angle grain boundaries ($1° \leq \theta \leq 10°$) are shown by blue lines. The zooms onto the EBSD orientation maps show clearly the difference in dynamic recrystallization behavior between the two deformed and quenched microstructures. The microstructure that was deformed at a higher deforming temperature (i.e. 430°C) shows larger subgrains as well as larger recrystallized grains. This is consistent with the literature [54, 130]. Actually, subgrain growth can occur either by low angle boundary migration or by subgrain rotation and coalescence [8, 131]. In case of subgrain boundary migration in an orientation gradient, the migration of low angle boundaries is controlled by bulk diffusion process, increasing therefore with increasing temperature [17]. During migration, the moving low angle boundary absorbs dislocations, increasing its misorientation, energy and mobility until it is transformed into a high angle boundary [8, 10, 17, 131]. In case of subgrain rotation and coalescence, subgrains rotate until adjacent subgrains have a similar orientation and will therefore coalesce into one larger subgrain. The driving force in this case arises from a reduction in involved boundary energies [8, 131]. Nevertheless, since not enough evidence of this mechanism is observed during recovery in regions of large orientation gradient, subgrain growth is assumed to occur mostly by migration of low angle grain boundaries [8].

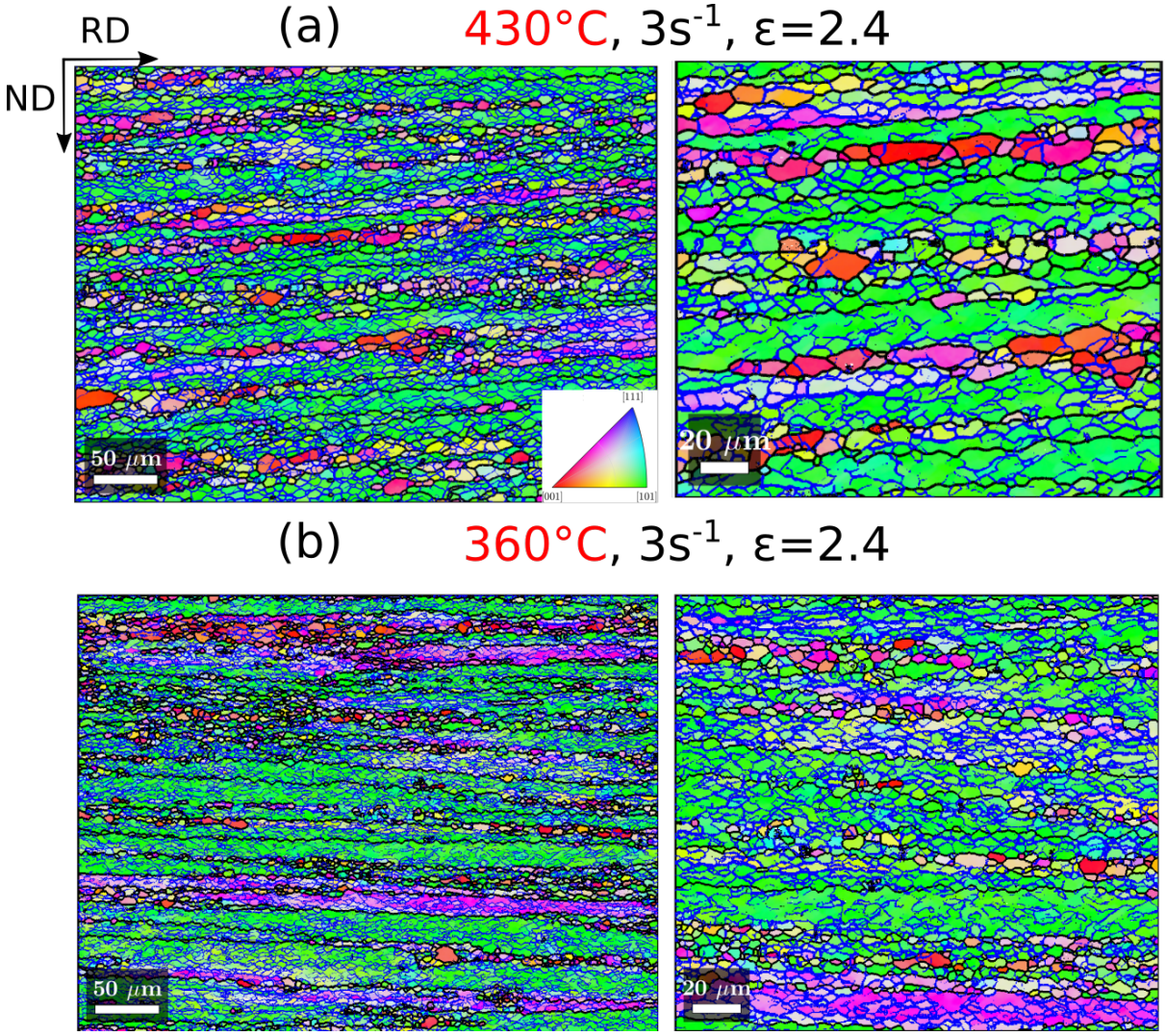

Fig. 6.23 EBSD orientation map and a zoom onto it showing the deformed and quenched microstructure after deforming at both (a) 430°C and (b) 360°C. The measurement step size is 0.4 µm. The color code defined on the standard triangle refers to the normal direction. High angle boundaries are plotted in black, while low angle boundaries are plotted in blue.

Figure 6.24 shows the area fractions and mean equivalent diameters of recrystallized grains observed right after deformation at 360°C and 430°C. Both the mean size and the area fraction of recrystallized grains are larger at a higher deformation temperature, which is consistent the observations made in the previous paragraph. In fact, due the enhanced subgrain growth observed at a higher deformation temperature, recrystallization by CDRX is more likely to occur at such temperature, leading therefore to a higher number of larger recrystallized grains.

In addition to that, at a lower deformation temperature, a higher number of finer precipitates may form and subgrain growth inhibition in the case of a deformation at low temperature (such as 360°C) could be explained by an increase in the pinning force due to these additional finer precipitates. In order to confirm this hypothesis, SEM SE images were taken on both samples quenched right after deforming at 430°C and 360°C as can be seen by figure 6.25. In this case, samples have been electropolished in order to reveal soluble phases. It is clear from figure 6.25

that the precipitation state is quite similar between the two samples regardless of the deforming temperature. This is actually expected since the studied initial sample has a high initial precipitate content (an almost completely discharged solid solution). An additional precipitation may occur during preheating the sample from room temperature to deforming temperature (as shown in Chapter 4). However, no additional precipitation occurs during deformation and holding after deformation. Only a fragmentation of precipitates is possible during deformation.

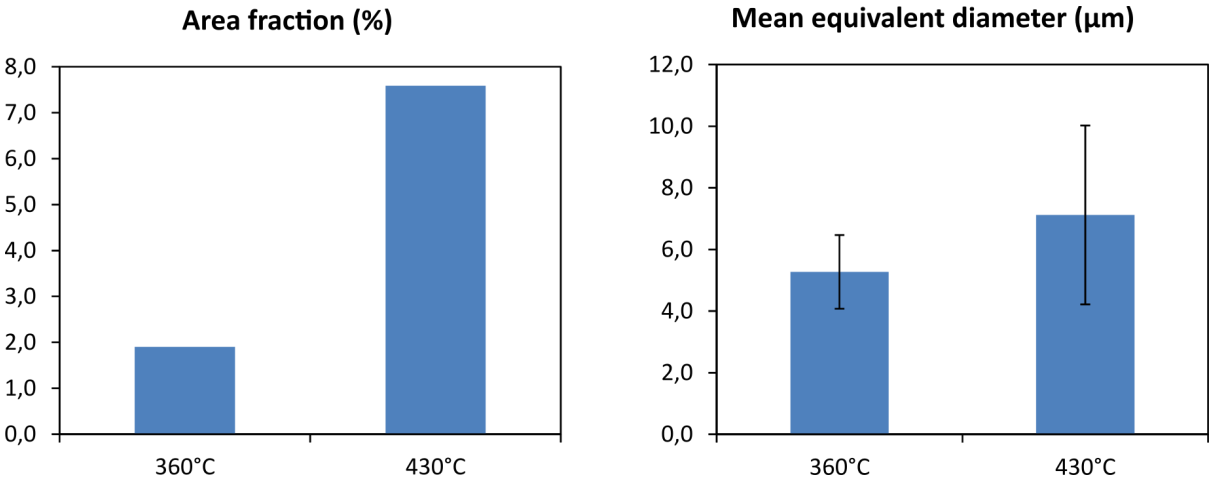

Fig. 6.24 Area fraction and mean equivalent diameter of recrystallized grains observed in the quenched and deformed microstructures after deforming at 360°C and 430°C.

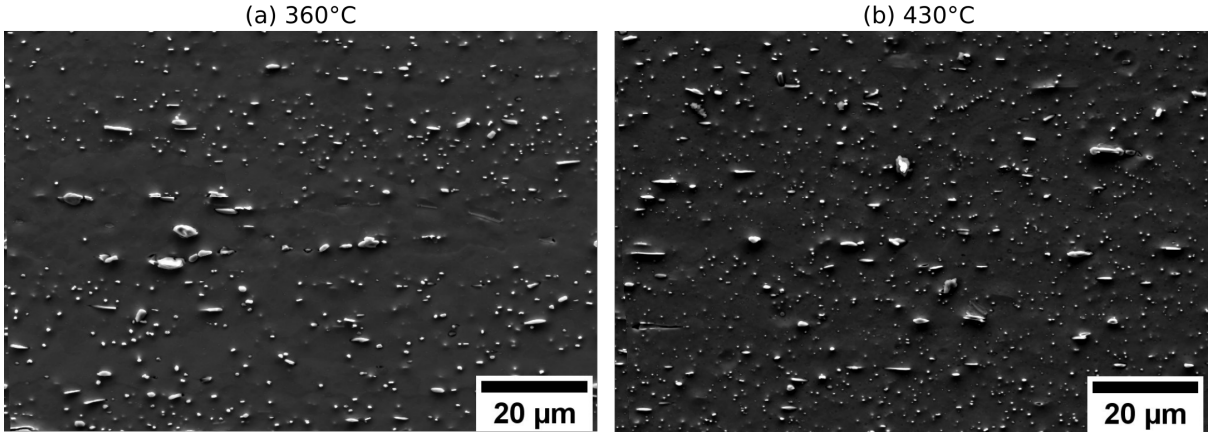

Fig. 6.25 (a,b) SEM SE images showing the distribution of precipitates on the water quenched samples right after deformation at 360°C and 430°C, respectively.

6.5 Summary

The influence of processing parameters, including strain, number of passes, strain rate and temperature, on the recrystallization behavior of 6016 aluminum alloy is studied in this chapter.

It has been shown that an increase in the strain level leads to an increase in the stored energy and therefore in the driving force for the nucleation of recrystallized grains. The formed

recrystallized grains are therefore smaller in size and higher in number. Hence, a higher strain level promotes the refinement of recrystallized grain size.

A comparison between single pass and multipass tests has been also conducted. It has been found that during multipass tests and at a higher strain ($\epsilon \approx 2.4$), few recrystallized grains are larger in size than the recrystallized grains that form during single pass tests at the same strain level. The substructure observed in one of these large recrystallized grains suggests that it may have formed during the first passes, grown during the interpass time and have deformed during subsequent passes. The interpass time allows therefore nucleation of additional grains or growth of dynamically recrystallized grains. In order to confirm the role of the interpass time, a higher interpass time (> 5 s) would be needed.

The study of the influence of strain rate has shown that a higher strain rate leads to a final microstructure with smaller grain size. This could be explained by the higher stored energy that promotes the growth of the recrystallized grains formed during and right after deformation. This leads to a higher number of recrystallized grains that are able to grow right after deformation and even during holding. Therefore, after deforming at a higher strain rate, these large recrystallized grains will have less room to grow until mutual impingement between large recrystallized grains, resulting in a finer final recrystallized grain size.

Finally, the study of the influence of temperature has shown that, at a lower deformation temperature, subgrain growth is limited during deformation. This leads to the inhibition of nucleation of recrystallized grains due to the inhibition of CDRX. Grain growth is also retarded during post-deformation holding at a lower temperature.

To conclude, industrially, a finer final grain size can be reached by increasing the applied strain level, reducing the interpass time and increasing the strain rate. Regarding the effect of temperature, longer holding times are required in order to confirm whether the final recrystallized grain size gets smaller by decreasing the deforming/holding temperature.

An attempt to simulate the anisotropic development of coarse recrystallized grains

Contents

In this chapter, 2D full-field simulations of the microstructure evolution are performed by using a level-set (LS) method within a finite element framework (LS-FE) in order to discuss the validity of certain assumptions about the anisotropic overgrowth of some recrystallized grains. In this context, the numerical framework is firstly introduced. Secondly, the factors that may influence the appearance of elongated coarse recrystallized grains in the RD-ND plane are discussed one after the other by using the experimental data and results described in the previous chapters.

7.1 Numerical framework

Numerous full-field numerical frameworks exist in the state of the art like Monte-Carlo [132], cellular automata [133], vertex [134], multi-phase field [135], LS [136], Lagrangian-FE [137] approaches and are classically classified in deterministic/stochastic and front tracking/front-capturing methodologies. The focus here will be put on the LS method. The main objective of this chapter was to use an already existing numerical method to test the different hypothesis concerning the appearance of elongated coarse grains discussed in the previous chapters.

As the CEMEF is one of the leading research centers concerning the development of the LS method dedicated to polycrystals through the DIGIMU consortium and software [138, 139], this numerical framework was adopted in this work. The LS method was initially developed by S. Osher and J.A. Sethian [136] for curvature flow problems. Later, multiple junctions in the context of grain growth problems were considered by Zhao et al. [140] and Merriman et al. [141]. A first LS method associated with adaptive anisotropic automatic remeshing dedicated to recrystallization and grain growth following large plastic deformation in polycrystalline materials has been proposed by Bernacki et al. [142–144]. The LS framework for polycrystal modeling was also developed in the context of regular grids and FFT formulations [145, 146]. Although computationally expensive, the interest for a LS-FE numerical framework, by promoting remeshing [143, 147, 148] or meshing algorithms [149], helps to consider LS modeling of grain boundary network in the case of large deformation. This capability is of prime interest for industrial applications involving complex thermomechanical paths.

The modeling of Smith-Zener pinning phenomenon has been later made possible thanks to Agnoli et al. [150] by considering in 2D the influence of second phase particles on grain growth. Second phase particles were introduced as a statistical population of spherical particles as well as from real BSE images. The particles appear as voids in the FE mesh. One of the advantages of the LS framework, comparatively to other full-field strategies, is its ability to capture easily the real interaction between second phase particles and grain boundaries. Smith-Zener pinning phenomenon in 3D through LS methodology was subsequently proposed by Scholtes et al. [151].

The numerical efficiency of the LS model has been also improved by Scholtes et al. [152–154] through the development of efficient grain recoloring, redistancing and static recrystallization algorithms. Further improvements have been implemented by Maire et al. [155] to model the dynamic and post-dynamic discontinuous recrystallization by coupling the LS method and phenomenological laws for nucleation criterion, strain hardening and recovery. More recently, an optimization of the second phase particle description in LS framework was proposed by Alvarado et al. [156] in order to consider evolutive particles.

In LS approach, the considered materials are often assumed isotropic [148], i.e. the mobility M is considered as being only temperature-dependent through an Arrhenius law and the grain boundary energy field γ as constant. However, LS can be applied to more realistic microstructures considering the heterogeneities of M and γ, by taking into consideration the misorientation angle [140, 141, 157–159], the inclination of the grain boundaries [160–162] and the influence of solute segregation [163]. In the following simulations, three LS formulations (isotropic [148, 150], heterogeneous [158] and anisotropic [162]) were used depending on the discussed mechanisms. The isotropic formulation is presented in the next section.

7.1.1 The LS description of grain boundaries

The model used in this work is based on a LS description of the grain boundaries in a finite element context. For this purpose, each grain having a grain boundary ($\mathcal{T}$) can be represented by the following level set function ϕ (defined over a domain Ω):

$$\begin{cases} \phi(x,t) &= \pm d(x,\mathcal{T}(t)), x \in \Omega \\ \mathcal{T}(t) &= \{x \in \Omega, \phi(x,t) = 0\} \end{cases}$$

where $d(x,\mathcal{T}(t))$ corresponds to the Euclidean distance from the point x to the boundary $\mathcal{T}(t)$. The function $\phi(x,t)$ is calculated at each node in the finite element mesh (P1 interpolation) and is taken, by convention, positive inside the grain and negative outside it.

The motion of grain boundaries, submitted to a velocity field $\vec{v}$, is then described by the following convective equation [136]:

$$\frac{\partial \phi(x,t)}{\partial t} + \vec{v}.\vec{\boldsymbol{\nabla}}\phi(x,t) = 0. \tag{7.1}$$

For the considered recrystallization and grain growth phenomena, the velocity acting on the grain boundary network is expressed as follows [148, 164]:

$$\vec{v} = M\,P\,\vec{n}, \tag{7.2}$$

where M, P and $\vec{n}$ are the grain boundary mobility, the net pressure and the outside unit normal to the grain boundary, respectively.

The net driving pressure P is classically defined by the sum of two terms:

$$P = p_e + p_c \tag{7.3}$$

$$= [\![e]\!] - \gamma\,\kappa, \tag{7.4}$$

where p_e is the pressure due to stored energy through dislocation density, p_c is the pressure due to the capillarity effects, κ is the local curvature (trace of the curvature tensor in 3D) of the grain boundary and $[\![e]\!]$ is the stored energy jump across the grain boundary.

Equation 7.2 becomes therefore equivalent to:

$$\begin{aligned} \vec{v} &= \vec{v}_e + \vec{v}_c \\ &= M\,[\![e]\!]\,\vec{n} - M\,\gamma\,\kappa\,\vec{n}, \end{aligned} \tag{7.5}$$

where $\vec{v}_e$ and $\vec{v}_c$ are the stored energy and capillarity kinetic contributions, respectively.

By combining equations 7.1 and 7.5, the following equation can be obtained:

$$\frac{\partial \phi(x,t)}{\partial t} + \vec{v}_e.\vec{\boldsymbol{\nabla}}\phi(x,t) - M\,\gamma\,\kappa\,\vec{n}.\vec{\boldsymbol{\nabla}}\phi(x,t) = 0. \tag{7.6}$$

Since $\vec{n} = -\frac{\vec{\nabla}\phi}{\|\vec{\nabla}\phi\|}$ and $\kappa = \vec{\nabla}.\vec{n}$ by considering that our LS functions remain distance functions (i.e. $\|\vec{\nabla}\phi\| = 1$), the previous equation (i.e. equation 7.6) can be rewritten under a convective-diffusive form:

$$\begin{aligned}
&\frac{\partial\phi(x,t)}{\partial t} + \vec{v}_e.\vec{\nabla}\phi(x,t) - M\,\gamma\,(\vec{\nabla}.\vec{n})\,\vec{n}\,.\,\vec{\nabla}\phi(x,t) = 0,\\
&\frac{\partial\phi(x,t)}{\partial t} + \vec{v}_e.\vec{\nabla}\phi(x,t) - M\,\gamma\,\vec{\nabla}.\frac{\vec{\nabla}\phi}{\|\vec{\nabla}\phi\|}\frac{\vec{\nabla}\phi}{\|\vec{\nabla}\phi\|}\,.\,\vec{\nabla}\phi(x,t) = 0,\\
&\frac{\partial\phi(x,t)}{\partial t} + \vec{v}_e.\vec{\nabla}\phi(x,t) - M\,\gamma\,\Delta\phi(x,t) = 0.
\end{aligned} \tag{7.7}$$

The grain boundary migration is therefore calculated by solving equation 7.7 for each LS function at each time step. The resolution of equation 7.7 can lead to values of $\|\vec{\nabla}\phi\| \neq 1$. Therefore, it is important to reinitialize [154] the LS functions at each time step to recover the metric property $\|\vec{\nabla}\phi\| = 1$.

The simulation time is therefore strongly dependent on the number of level set functions. Theoretically, each grain is represented by a LS function. However, this is not feasible when a large number of grains is considered in the simulation. In order to reduce the computation time, non-neighboring grains in the initial microstructure are grouped into global LS functions. A grain recoloring algorithm is introduced at each time step in order to avoid the risk of numerical coalescence. This algorithm allows to reassign the grains in other global LS functions whenever a risk of coalescence is detected (i.e. grains belonging to the same global set function are getting too close to each other) [152].

7.1.2 Interaction between grain boundaries and particles

The numerical methodology developed by Agnoli et al. [150] for the modelling of stable second phase particles will be explained in this section.

The effect of particles can be described by the following boundary condition:

$$\frac{\vec{\nabla}\phi}{\|\vec{\nabla}\phi\|}\,.\,\vec{n_p} = \vec{\nabla}\phi\,.\,\vec{n_p} = \sin\alpha = \frac{\gamma_{2p} - \gamma_{1p}}{\gamma} \tag{7.8}$$

where $\vec{n_p}$ is the outside unit normal to the particle surface and α is the angle determined from the balance of the surface tensions at the interface between the particles and the grain boundary (see figure 7.1).

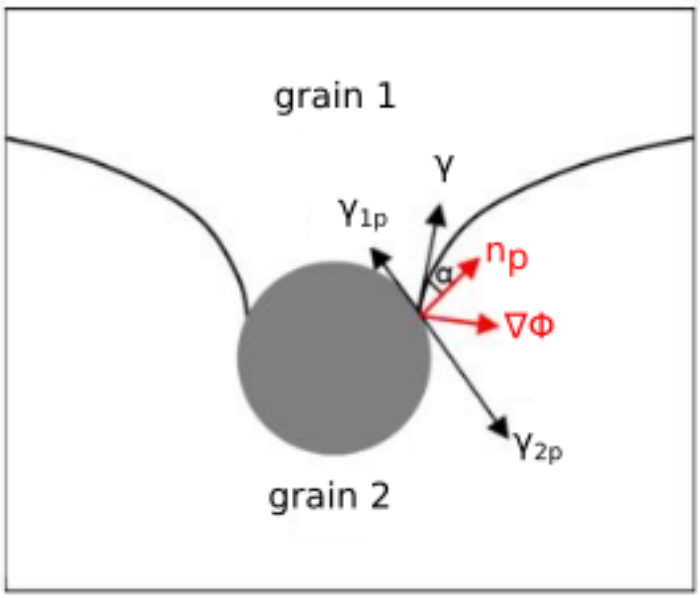

Fig. 7.1 Schematic representation showing how a moving grain boundary interacts with a second phase particle [150].

Second phase particles are represented by holes in the FE mesh and the Dirichlet boundary condition given by equation 7.8 can be included in the weak FE formulation of the equation 7.7 as follows:

$$\int_{\Omega} \frac{\partial \phi(x,t)}{\partial t}\, u\, d\Omega + \int_{\Omega} \vec{v}_e.\vec{\boldsymbol{\nabla}}\phi(x,t)\, u\, d\Omega + \int_{\Omega} \gamma\, M\, \vec{\boldsymbol{\nabla}}\phi(x,t)\,.\,\vec{\boldsymbol{\nabla}} u\, d\Omega = \int_{\delta\Omega} \gamma\, M\, \vec{\boldsymbol{\nabla}}\phi(x,t)\,.\,\vec{n}\, u\, dS \quad \forall u \in H^1(\Omega). \tag{7.9}$$

By using the condition given by equation 7.8 in the second phase particle borders $\delta\Omega_p$ and null Neumann boundary condition in the rest of the border domain, we obtain:

$$\int_{\Omega} \frac{\partial \phi(x,t)}{\partial t}\, u\, d\Omega + \int_{\Omega} \vec{v}_e.\vec{\boldsymbol{\nabla}}\phi(x,t)\, u\, d\Omega + \int_{\Omega} \gamma\, M\, \vec{\boldsymbol{\nabla}}\phi(x,t)\,.\,\vec{\boldsymbol{\nabla}} u\, d\Omega = \int_{\delta\Omega_p} \gamma\, M\, \sin\alpha\, u\, dS \quad \forall u \in H^1(\Omega). \tag{7.10}$$

This weak formulation enables to take into account naturally the local effect of each particle on the grain boundary network. Typically, the term $\sin\alpha$ could be a heterogeneous field taking into account the coherency level of each particle (for an incoherent particle, $\alpha = 0$).

Figure 7.2 illustrates an example of an initial FE mesh that contains voids. The voids represent the second phase particles present in the initial microstructure. The finite elements are highly anisotropic and refined around interfaces (i.e. particle interfaces and grain boundaries) thanks to the remeshing technique developed in [143, 153].

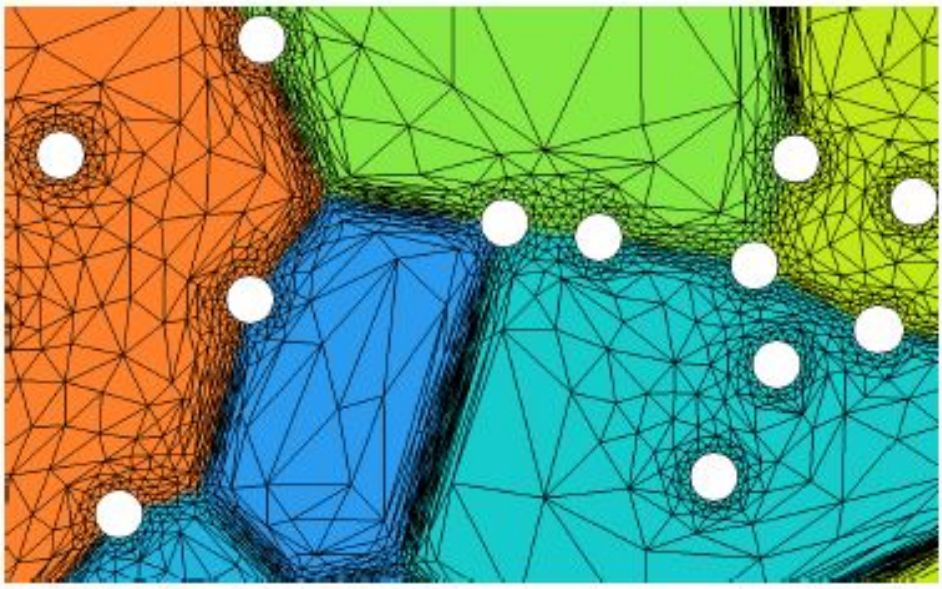

Fig. 7.2 An example of a FE mesh showing circular particles as voids. Anisotropic remeshing is employed around particles and grain boundaries [153].

7.1.3 Generation of initial microstructures

Two techniques allowing to generate initial microstructures can be considered: the generation of virtual polycrystals statistically representative of the real microstructure or the FE-immersion of real polycrystals from experimental EBSD images. The choice of one technique or another generally depends on the availability of experimental data and their quality.

When a virtual microstructure is considered in an isotropic context of M and γ, a statistical distribution of the grain size is usually used as the input. A Laguerre-Voronoï tessellation method is hence used for the generation of such microstructure as detailed in [165]. A simple Voronoï tessellation is described by N_G Voronoi sites. Each Voronoi site (marked by S_i with i $\in$ $\{1,...,N_v\}$) determines a Voronoi cell, which is composed of all points that are closer to S_i than to other Voronoï sites. According to this Voronoï tessellation method, Voronoï sites are randomly placed in the computational domain. Therefore, this approach does not respect a given statistical grain size distribution. The Laguerre-Voronoï tessellation method was therefore used and implemented in the LS framework by Hitti et al. [165] to overcome this limitation. The Laguerre-Voronoï tessellation method consists in affecting a weight to each Voronoï site. A dense sphere packing respecting the imposed weights must be generated to define the resulting Laguerre-Voronoï cells.

The second technique, which is the immersion of a real polycrystal from an experimental EBSD image, is clearly detailed in [166]. Actually, thanks to the grain recoloring algorithm (mentioned in section 7.1.1) , each grain belongs to a global level set function ϕ_i. Each grain can therefore be represented by the index i of its global level set function ϕ_i as illustrated by figure 7.3.

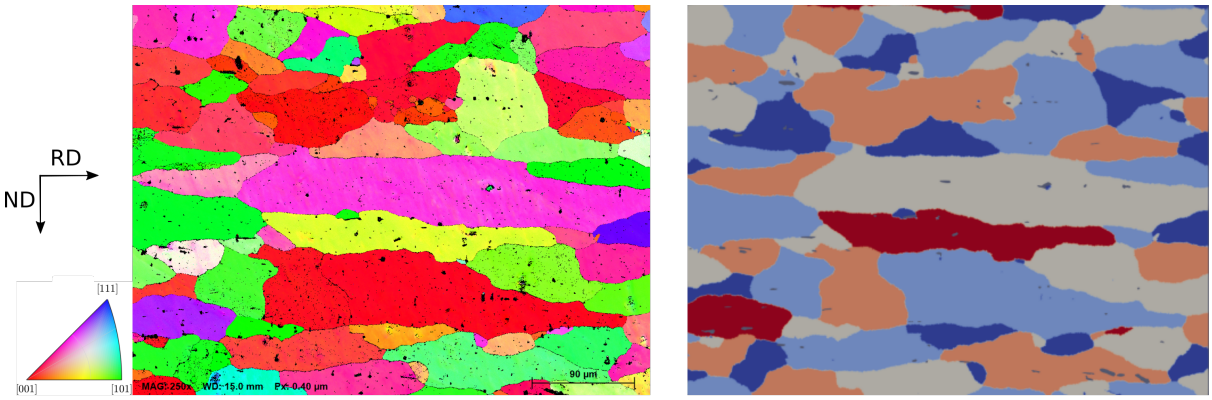

Fig. 7.3 An example showing how a real microstructure is immersed: (a) an experimental EBSD orientation map. The color code defined on the standard triangle refers to the normal direction. The measurement step size is 0.4 µm. (b) FE-immersion of the experimental image, where the color of each grain refers to the index of its representative global LS function.

As already mentioned, the LS formalism detailed from equation 7.1 to equation 7.10 is well adapted when homogeneous description of M and γ are considered. This formalism is used in the next section to discuss the effect of the stored energy (in section 7.2.1) and of the second phase particle populations (in section 7.2.2).

Finally, in the last section 7.2.3, anisotropic characteristics of γ are discussed through two more complex LS formulations. When misorientation angle dependence is discussed, the Het-Grad formalism detailed in [162] is used, whereas, when both misorientation and inclination dependence are taken into account, the Aniso-GB5DOF formalism detailed in the same reference is adopted. More details are given in the section 7.2.3.

7.2 LS discussions concerning the overgrowth of few recrystallized grains and their elongated final shape

7.2.1 Influence of stored energy

Figure 7.4 shows the effect of both temperature and strain rate on the evolution of the microstructure during holding after deformation. The effects of the strain rate ($\dot{\epsilon}$) and the deformation temperature (T) are taken into account by the Zener-Hollomon parameter ($Z = \dot{\epsilon}\exp\{\frac{Q}{RT}\}$), where Q is an activation energy. It is clear that a high temperature and a low strain rate (i.e. low Z value) leads to the formation of coarse and elongated grains in the RD-ND plane during holding after deformation (see figure 7.4(a)), whereas, a low temperature and a high strain rate (i.e. high Z value) leads to a fine-grained equiaxed microstructure (see figure 7.4(b)). These results are consistent with the observations made by Engler et al. [167]. According to [167], the decrease in the grain size with increasing Z value is due to the increase in the stored energy and thus in the total number of nucleation sites. In chapter 5, it has also been shown that the difference in stored energy between recrystallized grains and their neighborhood

is a key factor leading to the overgrowth of few recrystallized grains and that the Smith-Zener pinning pressure is easily overcome in the presence of such difference in stored energy.

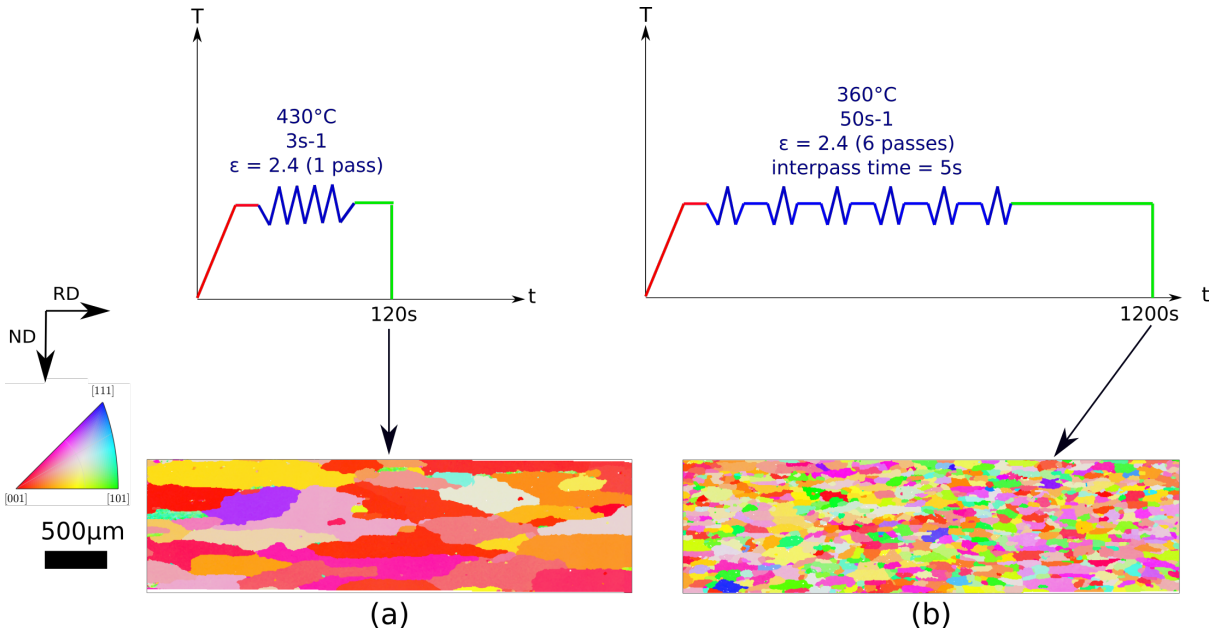

Fig. 7.4 Influence of temperature and strain rate (i.e. different values of Zener-Hollomon Z) on the evolved microstructure during holding after deformation.

In order to confirm the role of stored energy in grain overgrowth, full-field simulations of grain growth in presence of stored energy are first considered. For this purpose, two deformed and quenched microstructures are considered as shown in figure 7.5. The microstructure shown in figure 7.5 (a), and referred to as Case_430 in the following, corresponds to the microstructure obtained right after deforming at a low Z value (i.e. 430°C and 3 s^{-1}), while, the microstructure shown in figure 7.5 (b), and referred to as Case_360 in the following, corresponds to the microstructure obtained right after deforming at a high Z value (i.e. 360°C and 50 s^{-1}).

The difference in Z values leads to different stored energies right after deformation as can be seen from the KAM maps (see figure 7.5). It is evident from the KAM maps that the increase in the Z values results in higher KAM values and therefore to a higher stored energy. The GND density per pixel is estimated from the LLASS filtered EBSD data [91]. For the calculation of GND density, it is important to retrieve as accurately as possible the elastic curvature. The advantage of the LLASS filter is that it reduces the orientation noise while preserving true GND structures. The procedure to calculate the GND density from the filtered elastic curvature is explained in details by Seret et al. in [91]. The average GND density per grain is subsequently calculated and shown in figure 7.5. The experimental images corresponding to the average GND density per grain are finally used as inputs for the full-field simulations. The input temperature for the simulation is 430°C in the Case_430 (shown by figure 7.5(a)), while, it is 360°C for the Case_360 (shown by figure 7.5(b)).

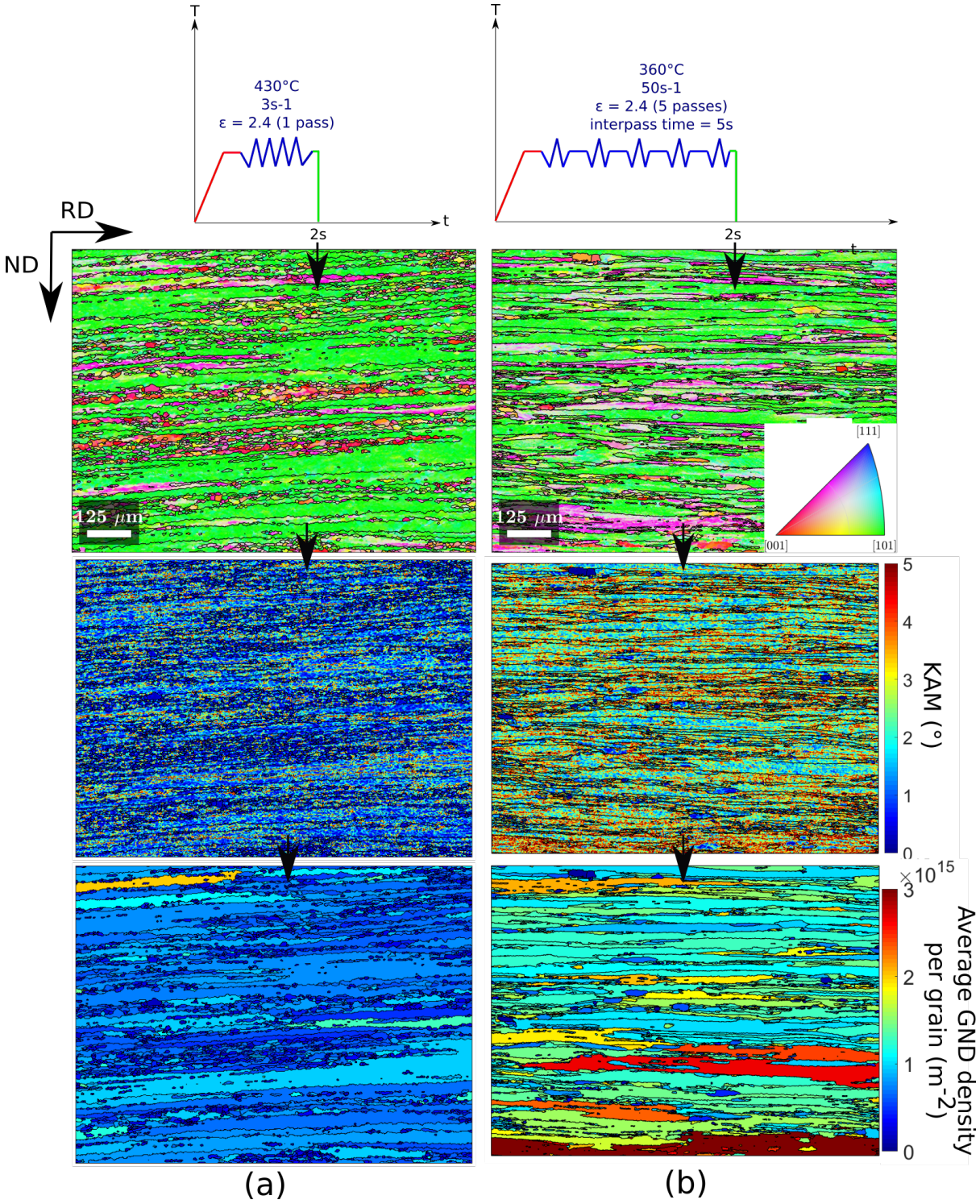

Fig. 7.5 Deformed and quenched microstructures considered as inputs for the full-field simulations. The LLASS filter (developed by Seret et al. [91]) is applied on the EBSD data sets and non indexed points have been filled before calculating the KAM values and the average GND density per grain.

By using the Burke and Turnbull methodology described in [168], the available experimental data (i.e. evolution of recrystallized grain size during post-deformation holding at 430°C obtained from EBSD orientation maps shown in figure 4.16 (b)) were used to estimate the

Arrhenius law describing $M = M_0\, exp\,(-Q_{GG}/RT)$ and the γ value. Typically, the following values were obtained and are used in the following: $M_0 = 10^{13}\, mm^4 \cdot J^{-1} \cdot s^{-1}$, $Q_{GG} = 147\, kJ \cdot mol^{-1}$ and $\gamma_{iso} = 3.24 \times 10^{-7}\, J \cdot mm^{-2}$.

In these first simulations, the second phase particle populations are not taken into account. The idea is not to be quantitatively predictive, but to discuss qualitatively these simulations. Typically, these simulations are considered to illustrate if the initial shape of the grains and the nuclei positions can explain the abnormal growth of some nuclei during the post-dynamic recrystallization step (where the Smith-Zener pinning can be a priori considered as a second order pressure).

Figure 7.6 illustrates the evolution of the stored energy and the grain size during the annealing at 430 °C (Case_430) whereas figure 7.7 corresponds to the annealing at 360°C (Case_360).

These results illustrate two main points. Firstly, the recrystallization kinetics are fast with a typical value of 20s at 360°C and 1.5s at 430°C. Secondly, it is shown that, despite the shape of deformed grains and the necklace appearance of nuclei, the post-dynamic regime leads to a classical equiaxed recrystallized microstructure without any elongated coarse recrystallized grains.

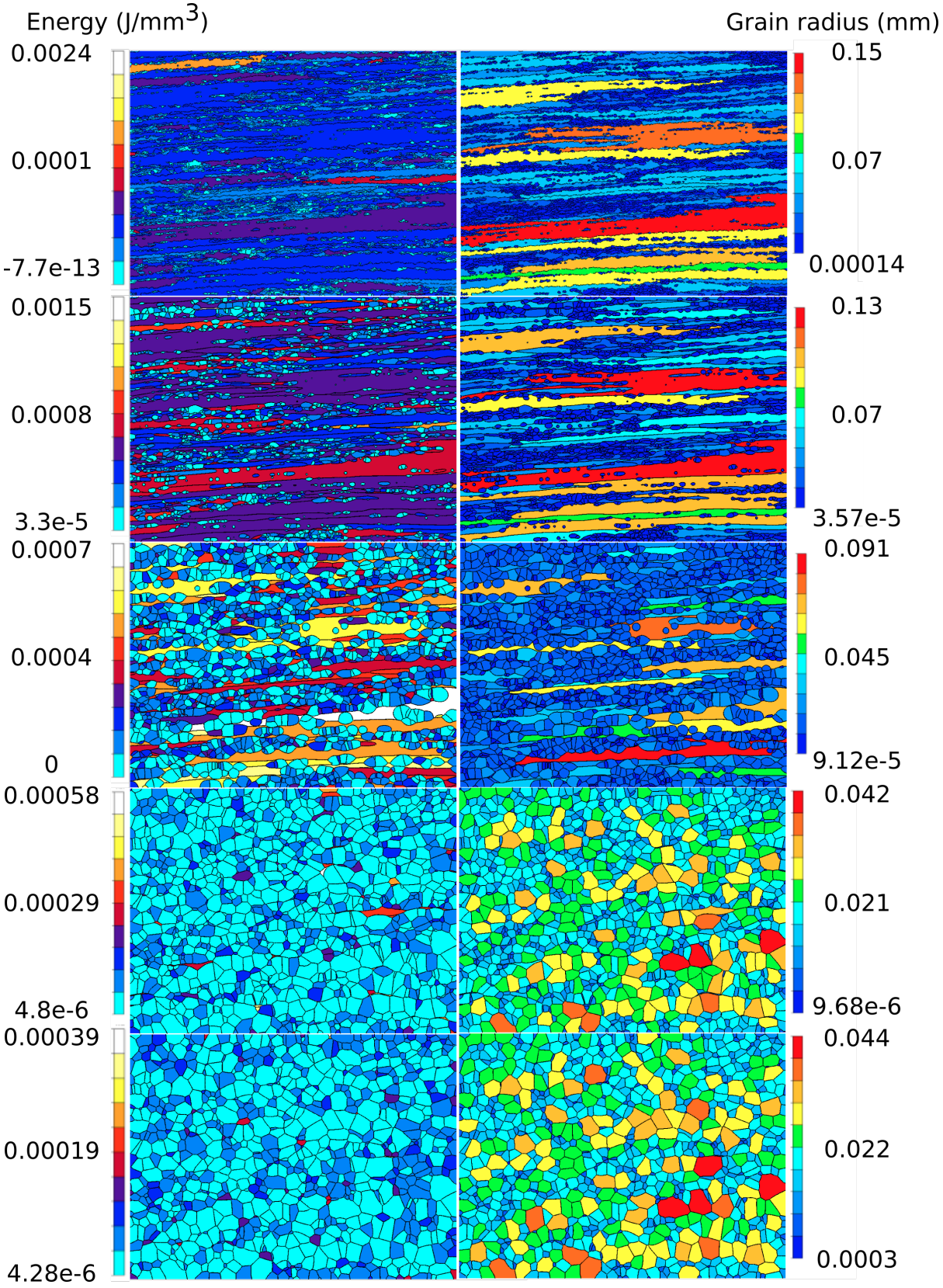

Fig. 7.6 Post-dynamic evolution of the Case_430. The domain dimensions are $1.13mm \times 0.85mm$. The left side describes the time evolution of the stored energy field and the right side corresponds to the time evolution of the equivalent radius field. From top to bottom, the considered times are $t = 0s$, $t = 0.1s$, $t = 0.4s$, $t = 1s$ and $t = 1.5s$. The microstructure can be considered fully recrystallized at $t = 1.5s$.

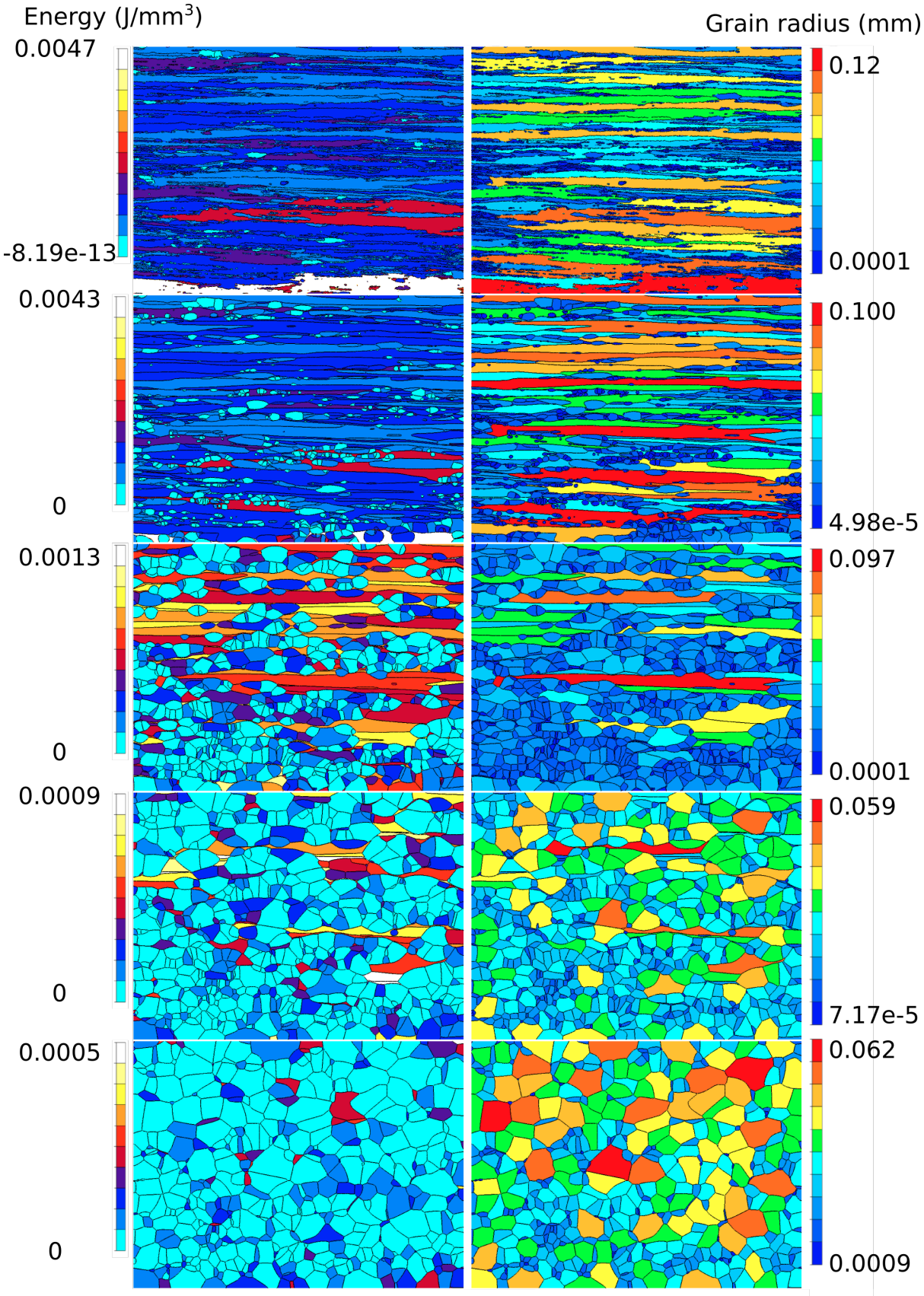

Fig. 7.7 Post-dynamic evolution of the Case_360. The domain dimensions are $1.13mm \times 0.85mm$. The left side describes the time evolution of the stored energy field and the right side corresponds to the time evolution of the equivalent radius field. From top to bottom, the considered times are $t = 0s,\ t = 1s,\ t = 5s,\ t = 10s$ and $t = 20s$. The microstructure can be considered fully recrystallized at $t = 20s$.

Finally, figures 7.8 and 7.9 illustrate the grain boundary networks when grain growth is the only remaining mechanism for Case_430 at $t = 2min$ and Case_360 at $t = 20min$, respectively. It is however important to keep in mind that these grain growth evolutions cannot be considered here as representative due to the absence of second-phase particles in the simulations (indeed the increase of the grain size leads to a decrease in the capillarity pressure. In the absence of stored energy pressure, the pinning pressure can thus become the dominant pressure and can no longer be neglected).

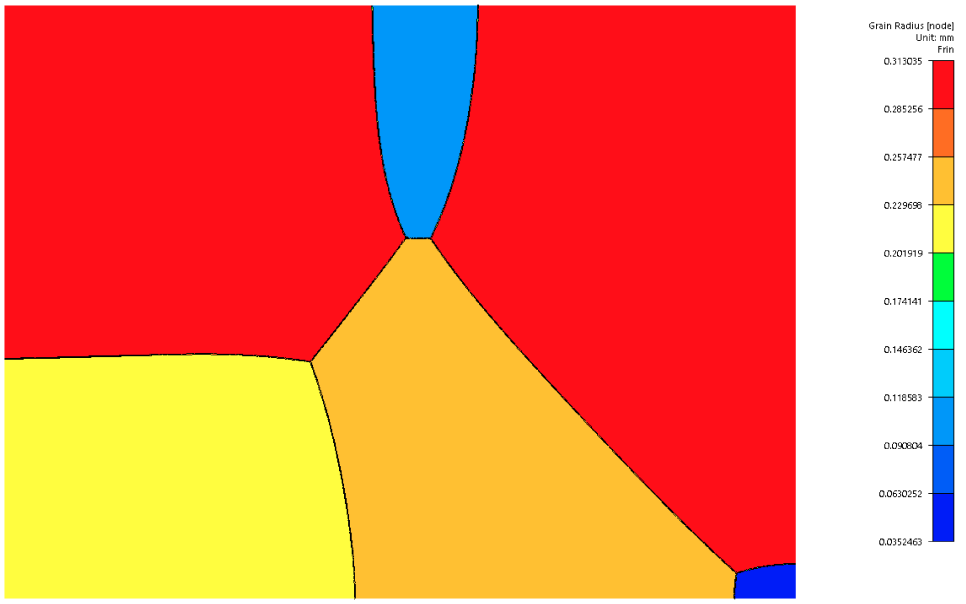

Fig. 7.8 Grain boundary network at $t = 2min$ for the Case_430.

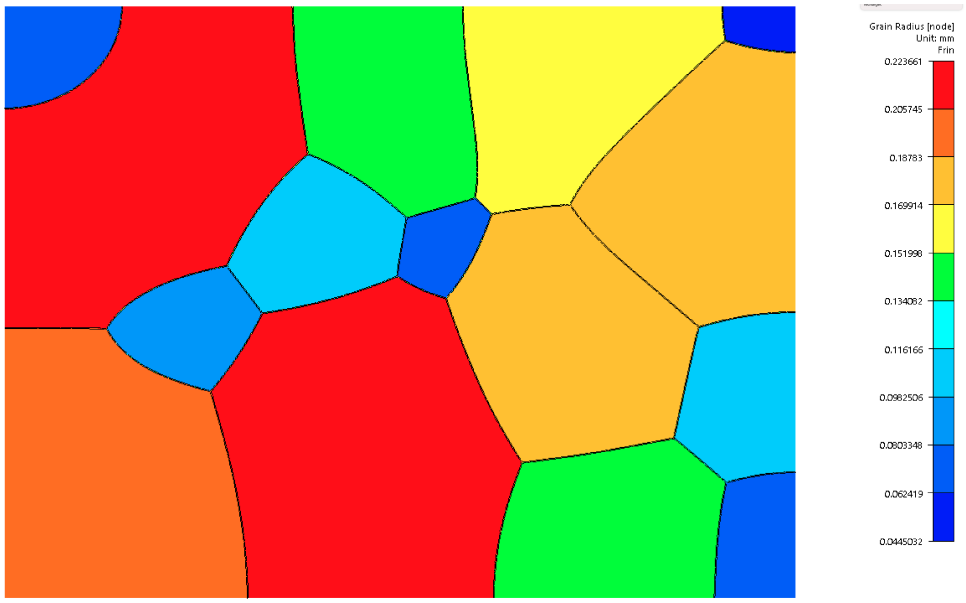

Fig. 7.9 Grain boundary network until $t = 20min$ for the Case_360.

7.2.2 Impact of second phase particle populations

In the previous simulations, the impact of stored energy on the recrystallization and grain growth evolutions was discussed and it was found that equiaxed microstructures are predicted by the isotropic LS framework. During the grain growth step, second phase particle populations have to be taken into account in order to be predictive. For this purpose, initial microstructures with representative equiaxed recrystallized grains are used as inputs to model grain growth by taking into account the different second phase particle populations existing in the considered material. Only the Case_430 is considered in the following.

7.2.2.1 Fe containing particles

The first discussion concerns Fe containing particles. Indeed, the elongated shape of the overgrown grains in the RD-ND plane could be due to the alignment of Fe containing particles as shown in chapter 5. In order to confirm the role played by Fe containing particles in controlling the shape of overgrown grains, LS simulations in the presence of elongated Fe containing particles are performed. The Fe containing particles are introduced statistically. For this purpose, the BSE stitched images were analyzed as explained in section 3.2.2.2 and the Fe containing particles were quantified. The estimated values for Fe containing particles (i.e. mean equivalent radius, aspect ratio and area fraction) are summarized in table 7.1. These values are used as inputs for the generation of holes that represent these Fe containing particles.

Mean equivalent radius	1.4 µm
Mean aspect ratio	5.9
Area fraction	0.0045

Table 7.1 Properties of Fe containing particles used in the simulations.

Regarding the initial microstructure generation, a statistical grain size distribution equivalent to the microstucture obtained in figure 7.6 at $t = 1.5s$ is taken as an input for the simulation. Figure 7.10 describes the initial state of the microstructure with a zoom on some Fe containing particles and figure 7.11 illustrates the microstructure evolution at 430°C. The comparison between figures 7.11 and 7.8 shows that the second phase particles have a clear impact on the grain boundary evolution. It is also clear that the alignment of the Fe containing particles in the RD does not seem to promote the development of elongated grains in the same direction.

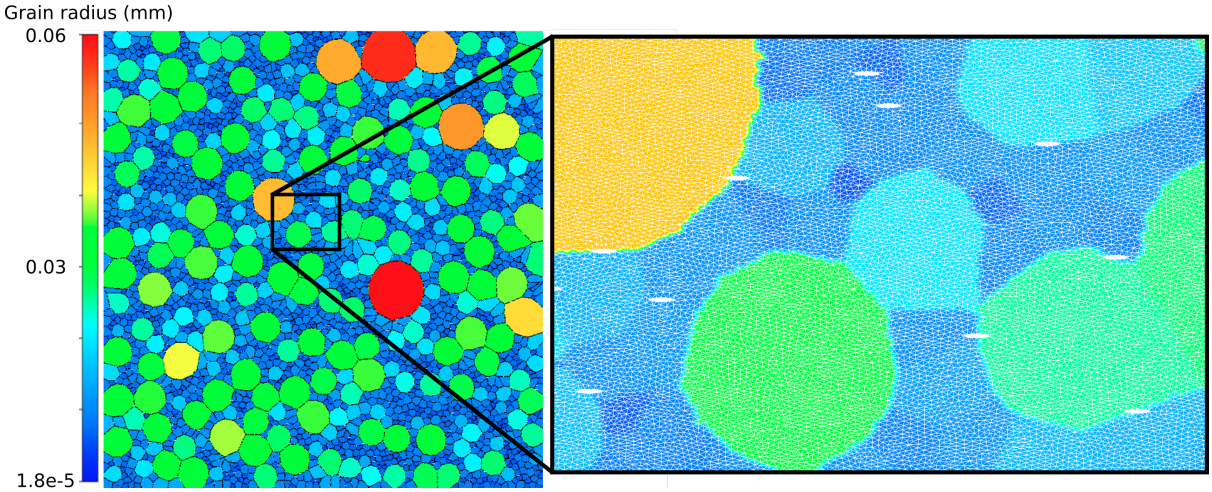

Fig. 7.10 Initial state of the grain growth evolution of the Case_430 after recrystallization by considering Fe containing particles and a representative Laguerre-Voronoï initial microstructure. The domain dimensions are $1mm \times 1mm$. (Left) initial state and (right) zoom on some Fe containing particles.

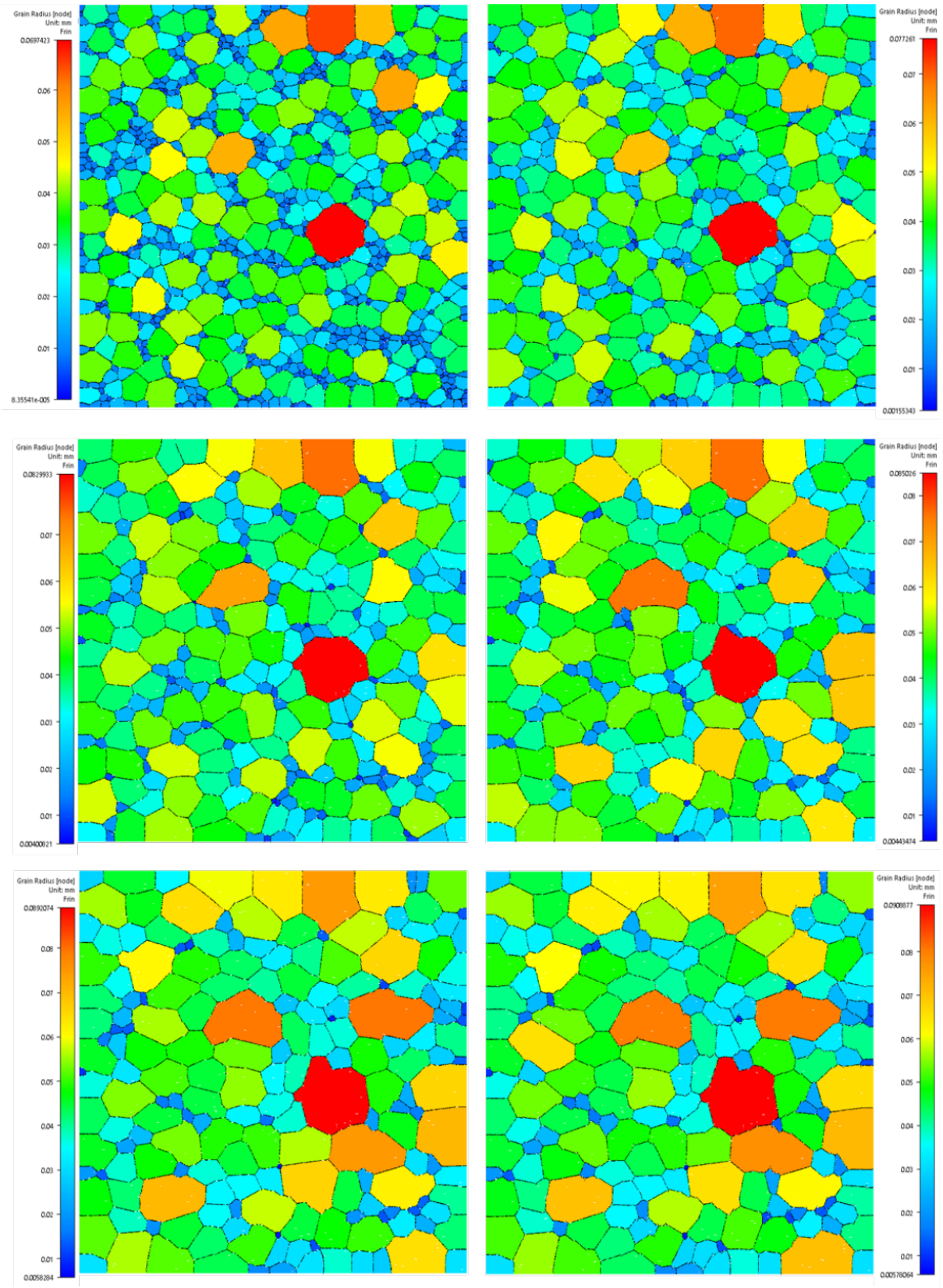

Fig. 7.11 Grain growth evolution of the Case_430 after recrystallization by considering Fe containing particles. From left to right and top to bottom: $t = 10s$, $t = 20s$, $t = 50s$, $t = 100s$, $t = 250$ and $t = 450s$.

7.2.2.2 Finer particles

Second, the effect of finer particles including Mg_2Si, Si and Mn dispersoids is included in the simulation. In this context, the size distribution of these finer particles that is used as an input is estimated according to section 3.2.2.2 in chapter 3 and is shown by figure 7.12. The initial state for the simulation is described in figure 7.13. Figure 7.14 shows that, in the presence of finer particles and in the absence of stored energy, a quasi-static microstructure is reached. These results illustrate that the observed elongated grains cannot be explained by a pure isotropic grain growth evolution.

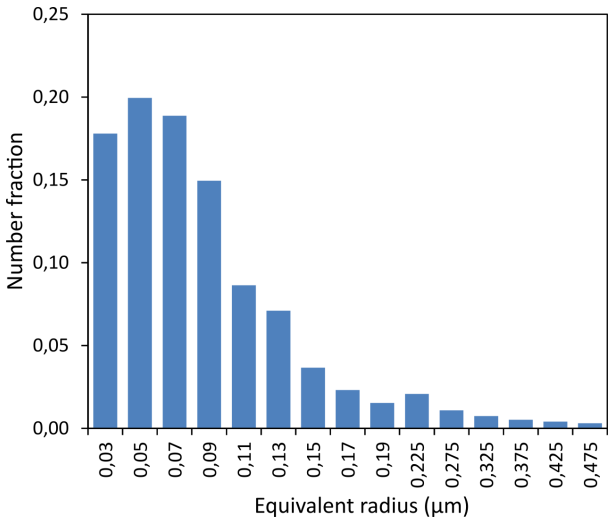

Fig. 7.12 Experimental size distribution for smaller particles including Mg_2Si, Si and Mn dispersoids. The mean aspect ratio used in simulation is equal to 1.9 and the area fraction is fixed to 0.0355.

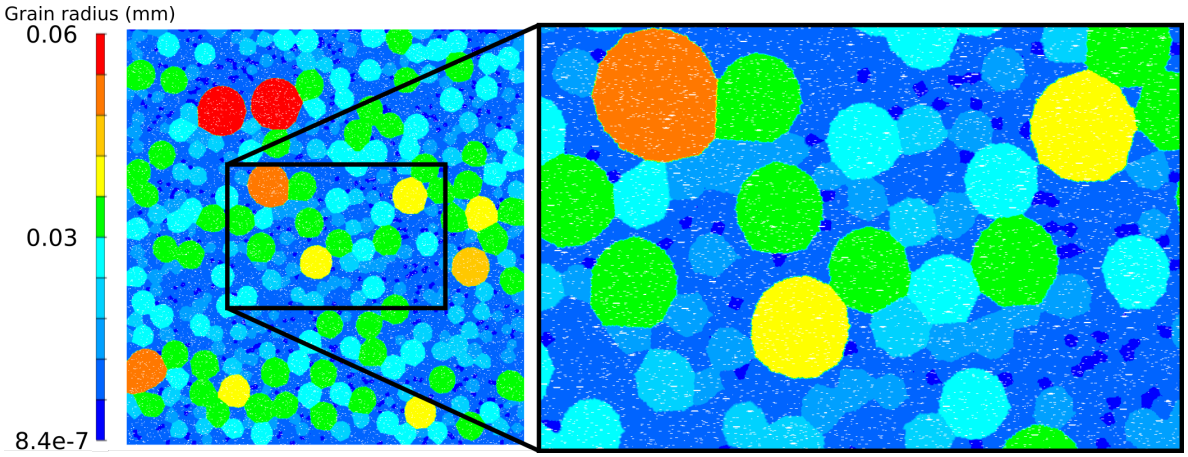

Fig. 7.13 Initial state of the grain growth evolution of the Case_430 after recrystallization by considering Fe containing particles and finer particles including Mg_2Si, Si and Mn dispersoids. The domain dimensions are $1mm \times 1mm$. (Left) initial state and (right) zoom on some particles.

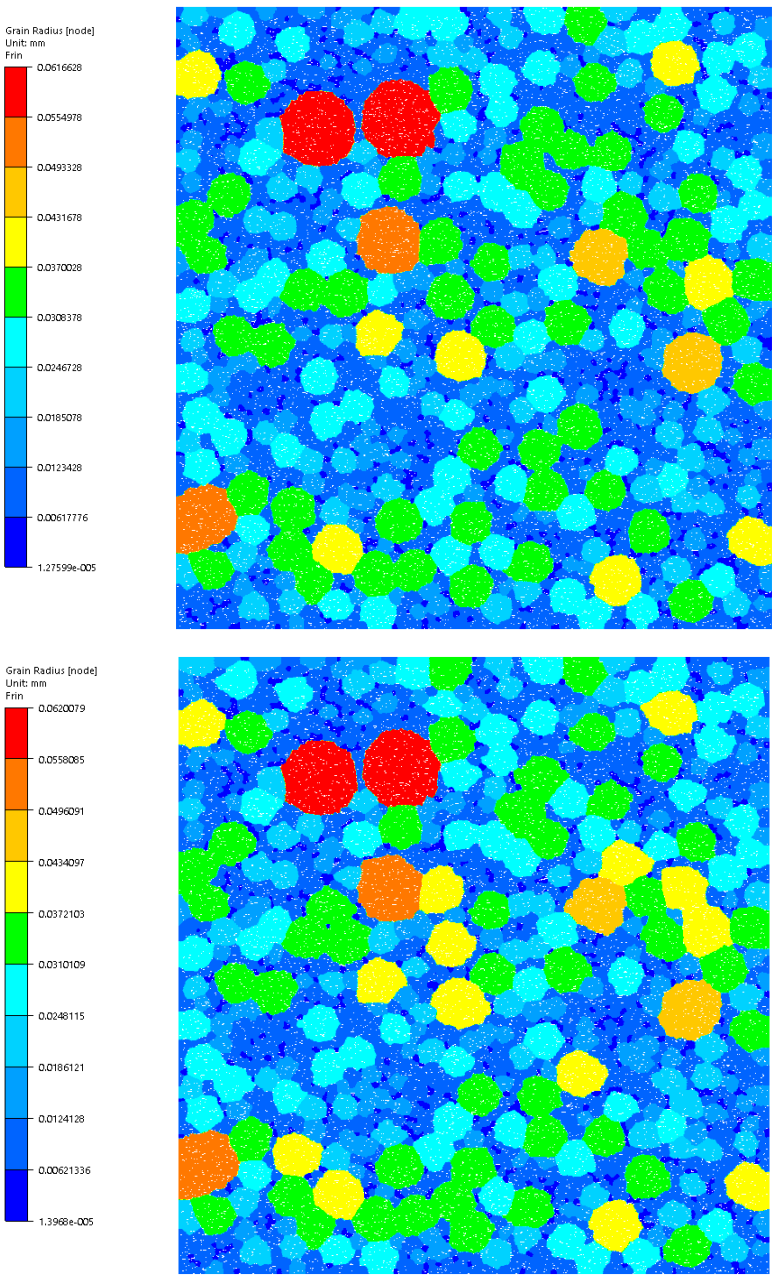

Fig. 7.14 Grain growth evolution of the Case_430 after recrystallization by considering Fe containing particles, finer particles including Mg_2Si, Si and Mn dispersoids and a representative Laguerre-Voronoï initial microstructure: (top) after 7s and (bottom) after 13s.

7.2.3 Influence of grain boundary misorientation and inclination

In order to evaluate the role of misorientation and/or inclination on the shape of coarse recrystallized grains during the recrystallization process, the used full-field formulation as well as the grain boundary energy γ description must be improved. If the previous simulations were performed in an isotropic context thanks to the DIGIMU software, the following ones were

performed thanks to the recent developments realized in the cimlib library [143] and which are not yet integrated in the DIGIMU software. This also explains some differences in the way the results are represented. At the mesoscopic scale, a grain boundary, $\mathcal{T}$, is characterized by its morphology and its crystallographic properties, which may be mathematically summarized by a tuple $\mathcal{B} = (\Theta, n)$ with two shape properties describing the interfaces through the unitary-outward normal direction n, and three crystallographic properties related to the orientation relationship between the two adjacent grains known as the misorientation tensor Θ. The two quantities of interest, (M, γ) must then be seen as functions from the grain boundary space $\mathcal{B}$ to $\mathbb{R}^+$. Since ten years, the LS framework was drastically improved in order to take into this complex description of (M, γ) [157, 158, 162, 169]. In the works of Murgas et al. [162], a global formulation, that takes into account the $\mathcal{B}$ 5D-space, was proposed through the following kinetic equations:

$$\vec{v} = M\left(\Theta, T\right)\left(\left[\!\left[e\right]\!\right] + \mathbb{P}\vec{\nabla}\gamma(\Theta, n)\cdot\vec{\nabla}\phi - \left(\vec{\nabla}_{\vec{n}}\vec{\nabla}_{\vec{n}}\gamma(\Theta, n) + \gamma(\Theta, n)\mathbb{I}\right) : \mathbb{K}\right)\vec{\nabla}\phi \tag{7.11}$$

where $\mathbb{I}$ is the unitary matrix, $\mathbb{P} = \mathbb{I} - \vec{n}\otimes\vec{n}$ is the tangential projection tensor, $\vec{\nabla}_{\vec{n}}$ the surface gradient, and $\mathbb{K} = \vec{\nabla}\vec{n} = \vec{\nabla}\vec{\nabla}\phi$ is the curvature tensor. The term $\Gamma(\Theta, n) = \vec{\nabla}_{\vec{n}}\vec{\nabla}_{\vec{n}}\gamma + \gamma\mathbb{I}$ corresponds to the GB stiffness tensor [170].

In the following simulations, the mobility is assumed to be only temperature dependent, the torque term $\vec{\nabla}_{\vec{n}}\vec{\nabla}_{\vec{n}}\gamma$ is neglected and the grain boundary energy γ is dependent on the GB misorientation and/or inclination. Thus, the kinetics equation can be simplified as:

$$\vec{v} = M\left(T\right)\left(\left[\!\left[e\right]\!\right] + \mathbb{P}\vec{\nabla}\gamma(\Theta, n)\cdot\vec{\nabla}\phi - \gamma(\Theta, n)\Delta\phi)\vec{\nabla}\phi. \tag{7.12}$$

For this purpose, the mean orientation of each grain is introduced as an input in addition to the mean GND density per grain. This allows to simulate the evolution of the deformed and quenched microstructure shown by figure 7.5(a) during holding at 430°C in the presence of stored energy and anisotropic grain boundary energies. Two simulations are considered: a first one which is based on a Read-Shockley [171] description of $\gamma(\Theta)$ (i.e. where only the misorientation angle is considered) and a second description of $\gamma\left(\Theta, n\right)$ which is more complex, based on a model of GB energy proposed for FCC metals by Bulatov et al. [172] and available in the GB5DOF code. In the GB5DOF code, both the effects of the misorientation and of inclination are taken into account by using the crystallographic orientations of the two adjacent grains and the local coordinate system of the grain boundary between them. In these two first simulations, the second-phase particles are not taken into account.

When a Read-Shockley (RS) description of the γ field is used, the following equation is

considered [171]:

$$\begin{cases} \gamma(\Theta) = \gamma_{max} \frac{\theta}{\theta_0} \left(1 - ln\left(\frac{\theta}{\theta_0}\right)\right), \ \theta < \theta_0 \\ \gamma_{max}, \ \theta \geq \theta_0 \end{cases} \tag{7.13}$$

where θ is the disorientation, and γ_{max} is the maximal GB energy. $\theta_0 = 10$ is the disorientation defining the transition from a low angle grain boundary (LAGB) to a high angle grain boundary (HAGB). The maximal value for γ corresponds to the isotropic value already used in the previous sections.

Finally, when a full anisotropic description of γ is preferred, the GB5DOF code [172] is adopted to evaluate the γ field. The main advantage of the GB5DOF code is that it is possible, for FCC metals, to describe the γ dependence on the disorientation, the misorientation axis and the inclination. Nevertheless, two main limitations of the proposed full anisotropic simulation must be highlighted. First of all, torque terms are not taken into account (although they can have a significant impact on the global GB network migration [173]). Secondly, the 2D context limits the actual use of the grain boundary inclination described here with one degree of freedom and not in a 3D framework with 3D experimental data.

The results of these two first simulations are shown by figure 7.15, where the post-dynamic evolution of the Case_430 in this new numerical framework is illustrated. The left sided and middle columns describe the time evolution of the stored energy field and the equivalent radius field when the RS description of γ is considered, respectively. The right sided column corresponds to the time evolution of the equivalent radius field when the GB5DOF code is used to interpolate γ and when the grain boundary inclination is considered to be perpendicular to the observed section.

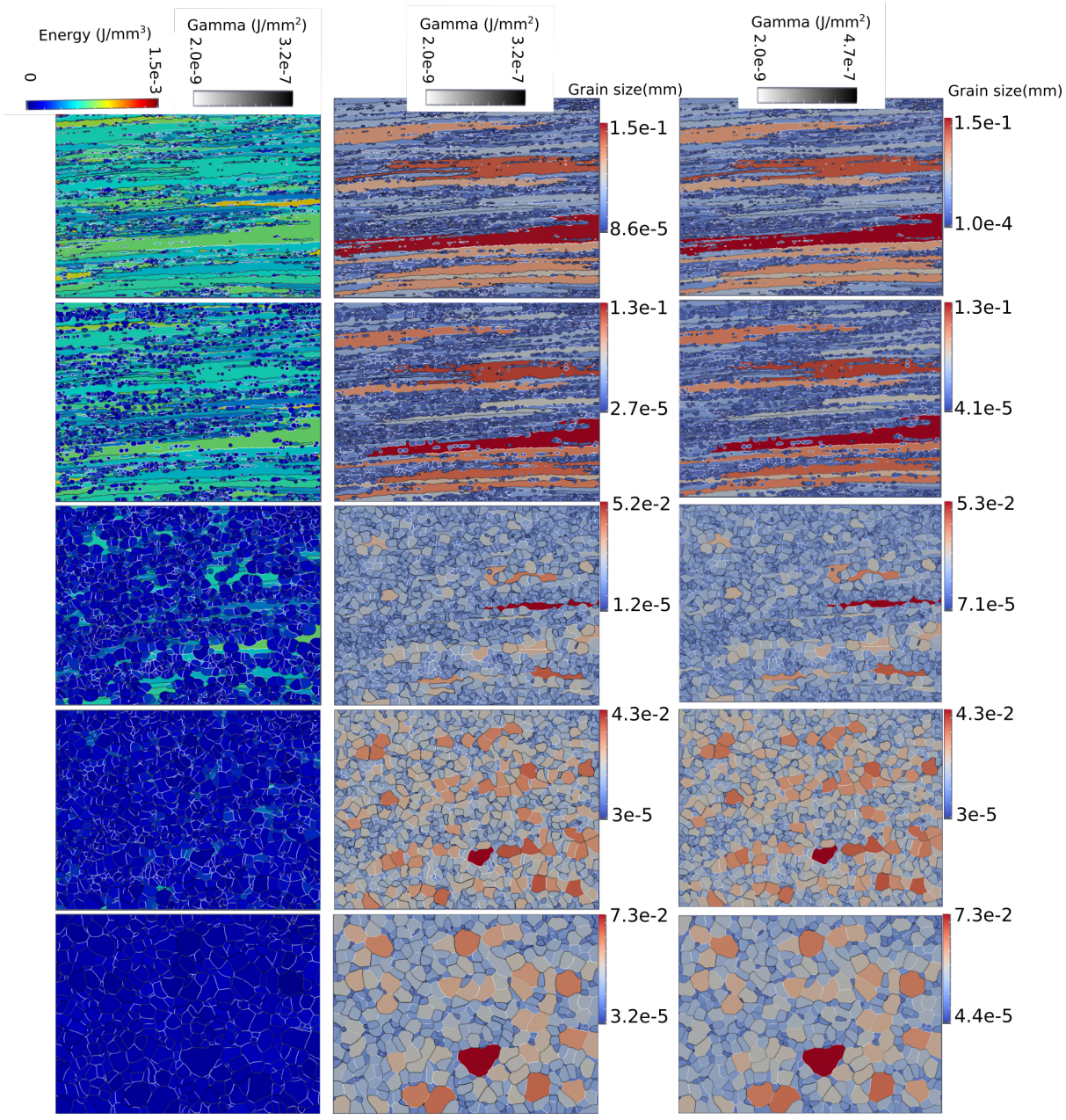

Fig. 7.15 Post-dynamic evolution of the Case_430. The domain dimensions are $1.13mm \times 0.85mm$. The left sided and middle columns describe, in the RS formalism, the time evolution of the stored energy field and equivalent radius field, respectively. The right sided column corresponds to the time evolution of the equivalent radius field when the GB5DOF code is used to interpolate γ. Moreover, in all views, the γ field is superimposed to the GB network. From top to bottom, the considered times are $t = 0s,\ t = 0.1s,\ t = 0.5s,\ t = 1s$ and $t = 3.5s$. The microstructure can be considered fully recrystallized at $t = 1.5s$.

Besides, in all views, the γ field is superimposed to the GB network. It is clear that there is no noticeable difference between the RS description results (middle side column) and the full anisotropic description ones (right side column). This may be due to the description mode used for the grain boundary energy (where the inclination is considered perpendicular to the observed section and the torque terms are neglected). In the following discussions, only the RS

description will be considered.

Figure 7.16 shows at $t = 1s$ the differences between the isotropic and RS predictions concerning the post-dynamic evolution of the Case_430 through their equivalent radius field. Although the enrichment in the description of the γ field has a clear impact on the grain morphology, it does not seem to influence notably the global kinetics of the postdynamic evolution, nor, to promote an elongated shape for recrystallized grains.

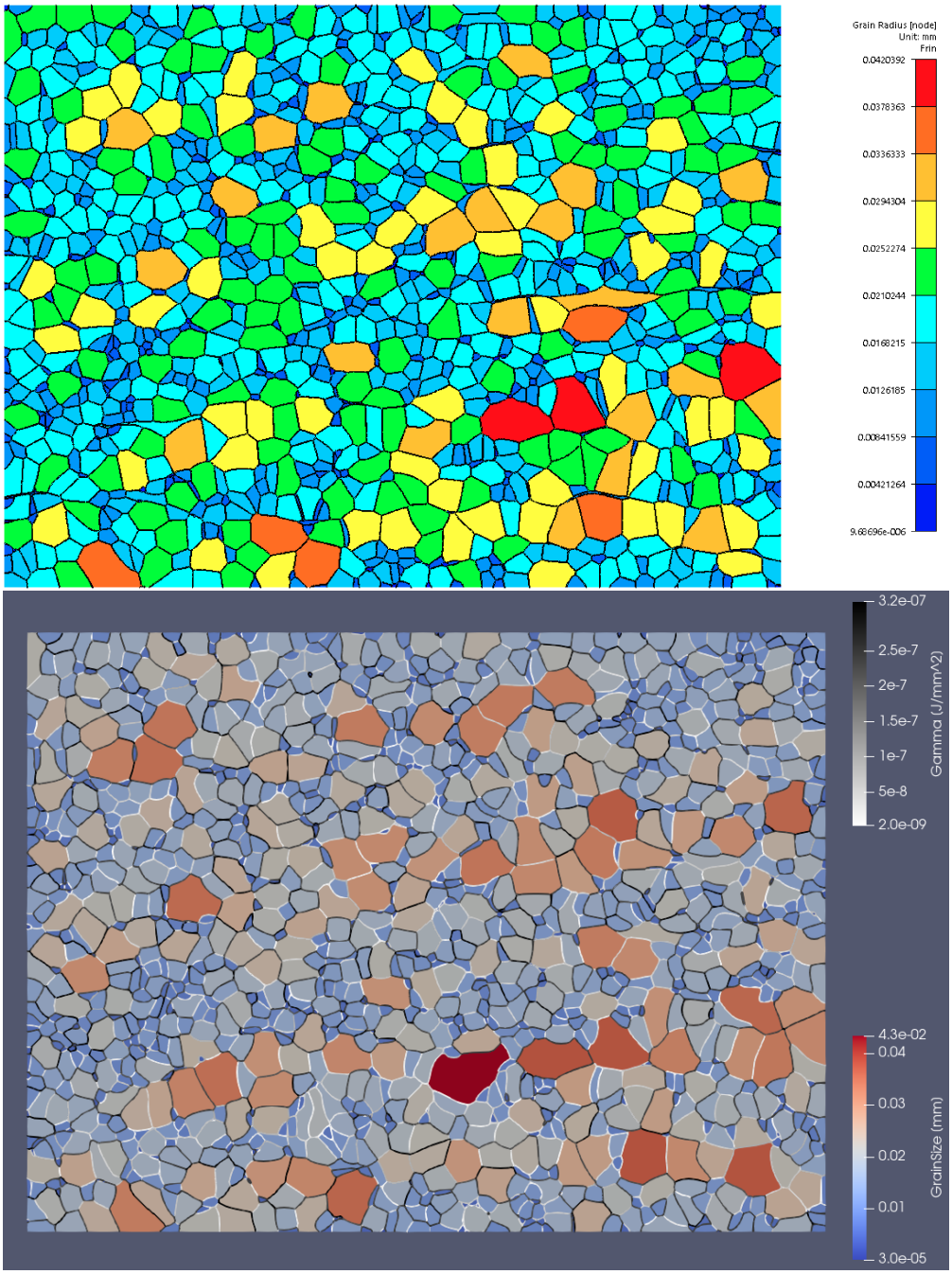

Fig. 7.16 Post-dynamic evolution of the Case_430. Comparison, at $t = 1s$, of the isotropic (top - DIGIMU sofware computation) and RS (bottom - cimlib library computation) simulations. The γ field is superimposed to the GB network.

The philosophy of this chapter aimed at providing a numerical understanding of the shape of the coarse recrystallized grains observed experimentally in the RD-ND plane (Chapter 5) by progressively, and not unnecessarily, complexifying the considered simulations .

In view of the obtained results, this strategy has finally led us to consider all the microstructural ingredients present experimentally and possibly responsible for the anisotropic development of coarse recrystallized grains. Thus, in the next and final simulation, second phase particles will be considered even during the recrystallization stage (i.e. in the presence of a stored energy). It should be noted that such a level of complexity in a full-field simulation of a post-dynamic mechanism has never been proposed in the literature. Indeed, this simulation combines an immersion of experimental data (grains, orientations, stored energy field), heterogeneity of the interface energy and complex submicrometric and micrometric populations of second phase particles described explicitly.

Figure 7.17 shows the evolution of the Case_430 (equivalent radius field) during holding at 430°C at different times: $t = 0.5s$, $t = 1s$, $t = 3.5s$, and $t = 4.5s$, by considering Fe containing particles, Mg_2Si, Si and Mn dispersoids, the stored energy field, and the RS description of the GB energy field. The complex particle populations are clearly visible in figure 7.18, where a zoom on few grains for the $t = 4.5s$-state is shown. It is evident from figure 7.17 that, at the beginning until 1s, the grain boundary network follows a similar evolution comparatively to the results described in figure 7.15 (middle or right column). However, it is not the case after 1s with the clear appearance of few abnormally large recrystallized grains. Such evolution was not present in the results described by figure 7.15 (where the second phase particles were not taken into account), in figure 7.11 (where only Fe containing particles were taken into account), nor in figure 7.14 (where all second phase particles are taken into account, but, the real morphology of recrystallized grains and RS γ field were not considered). Therefore, these results demonstrate the necessity to consider, in simulations, the different characteristics of the microstructure to converge towards representative evolutions even though the shape of these coarse recrystallized grains seems to still remain equiaxed. This can be interpreted as another indication that the anisotropy of the grain boundary properties (i.e. their dependence on inclination), which is not considered in this last simulation, matters in the mrophological development of coarse recrystallized grains.

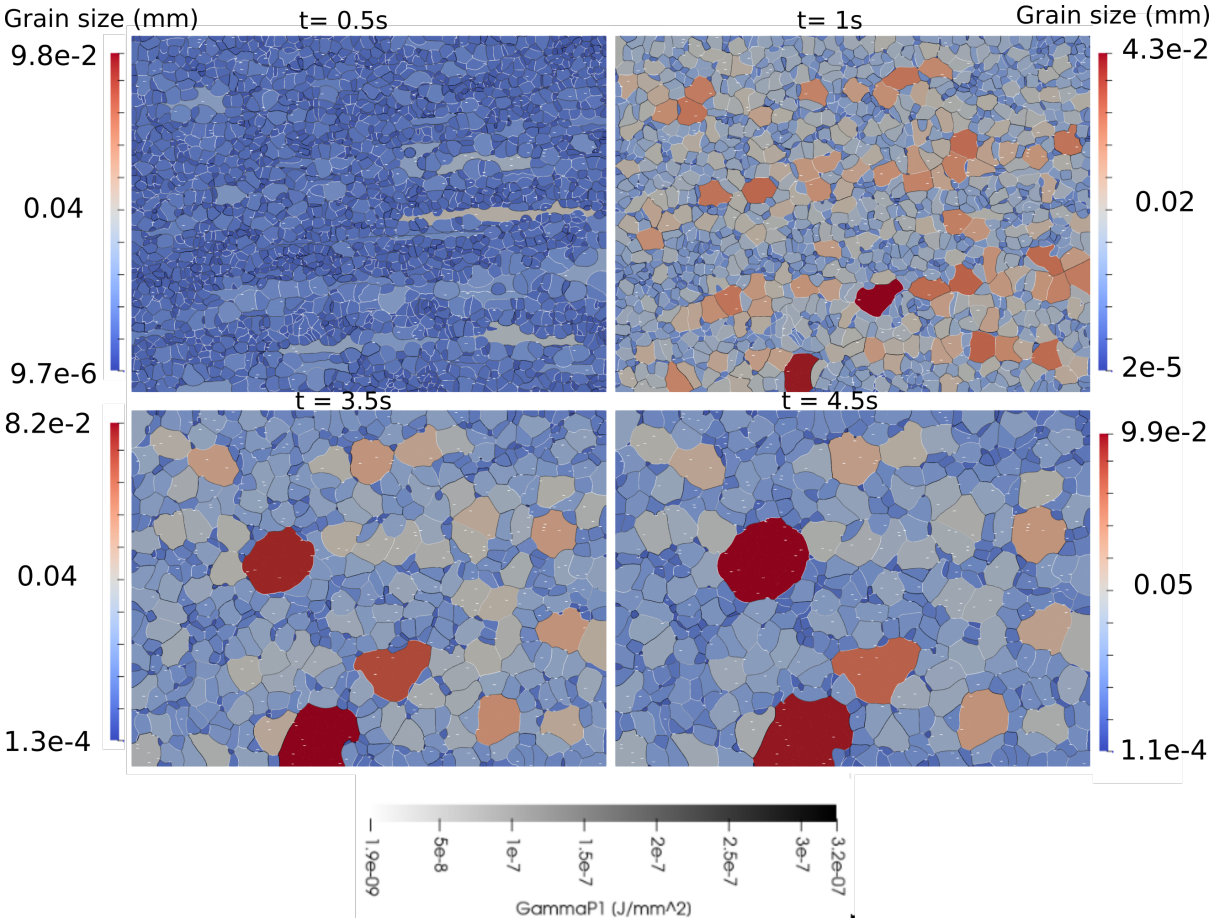

Fig. 7.17 Post-dynamic evolution of the Case_430 with a RS description of the γ field, and by considering Fe containing particles, Mg_2Si, Si and Mn dispersoids. From top to bottom and from left to right: $t = 0.5s$, $t = 1s$, $t = 3.5s$ and $t = 4.5s$. The γ field is superimposed to the GB network.

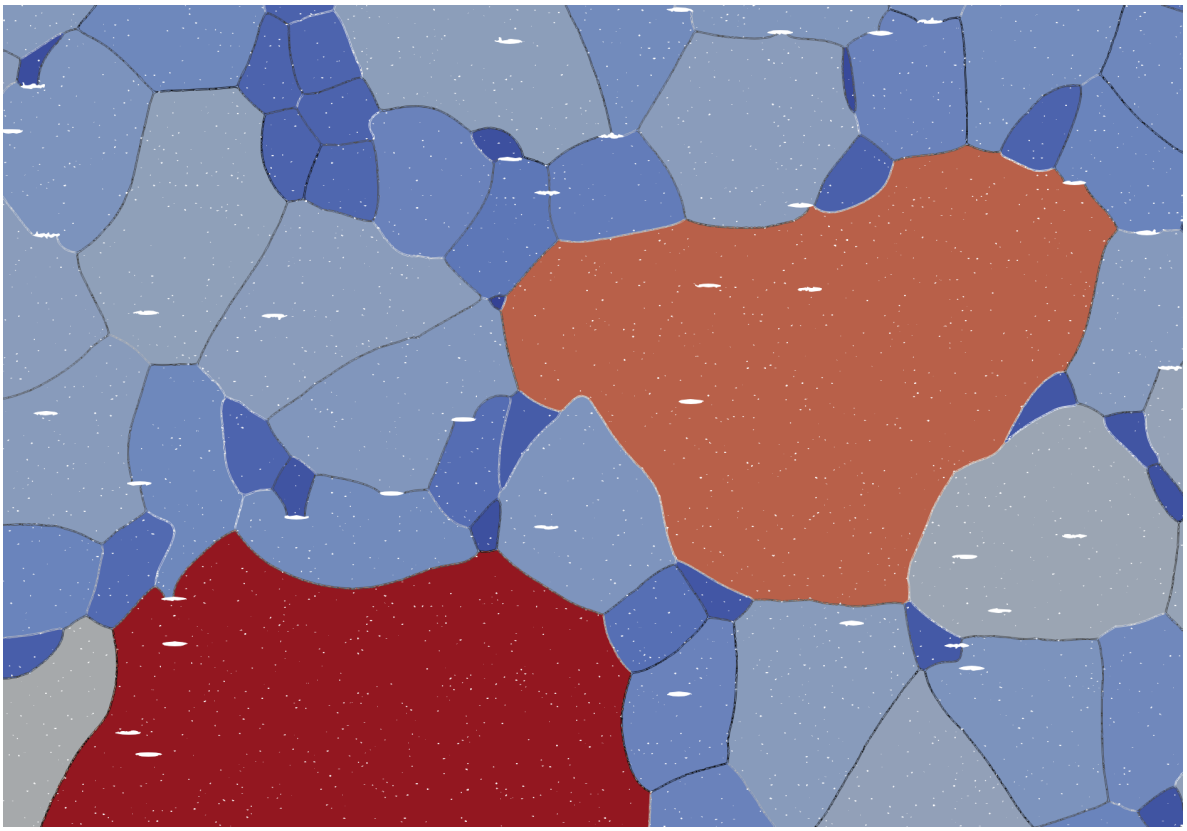

Fig. 7.18 A zoom into figure 7.17 at $t = 4.5s$. Large elongated white holes correspond to Fe containing particles, whereas very small white holes correspond to Mg_2Si, Si and Mn particles. The γ field is superimposed to the GB network.

7.3 Conclusion and perspectives

Full-field simulations have been used in order to predict the anisotropic development of coarse recrystallized grains (described in Chapter 5). Factors possibly leading to the development of these coarse grains and determined in Chapter 5 have been included in the simulations in order to evaluate their importance.

Thanks to the use of a more advanced LS framework where the GND density, a heterogeneous description of the γ field, and the different populations of the second phase particles are taken into account, it was possible to predict the development of coarse recrystallized grains. However, the elongated morphology of coarse recrystallized grains examined in the RD-ND plane could not be predicted.

Some choices made in this chapter can be criticized and seen as possible future ways of improvement of the current numerical campaign. First of all, 3D simulations should be considered. Of course, this aspect is not only important to improve the representativity of the considered polycrystals, but also to describe correctly the γ dependence to the inclination. Based on the conclusion of chapter 5 where it has been reported that the boundary plane may play a role in the anisotropic shape of coarse recrystallized grains, the γ dependence to the

inclination seems to be of prime importance. Furthermore, the possible heterogeneity of the mobility parameter was here not discussed and its possible dependence to the disorientation was not investigated.

Finally, despite the reasonable number of grains considered, the computational cost of the proposed final simulation was quite huge (few days in 48 cores calculations) due to the complexity of the second phase particle populations. To be able to perform larger simulations for longer annealing times remains therefore a crucial perspective.

Conclusions and perspectives

Contents

8.1 Conclusions

The general objective of this thesis was to understand the microstructural evolution occurring in 6016 aluminum alloy during and after hot deformation. For this purpose, hot plane compression tests were performed and resultant microstructures were interpreted in terms of interactions between precipitates/solutes and grain boundaries. The possible factors leading to the development of coarse grains during holding after hot deformation were investigated. The influence of thermomechanical parameters on the evolution of the microstructure was finally studied for a better industrial control of the evolved microstructure. The main findings are summarized below.

8.1.1 Interactions between precipitates/solutes and grain boundaries

- Three different precipitation states have been generated right before hot deformation in order to investigate the influence of precipitates/solutes on the evolution of microstructure during deformation and during holding after deformation. The estimation of both $\frac{f_{spp}}{r_{spp}}$ and f_{spp} has allowed the evaluation of the Smith-Zener pinning force and solute drag in the three states right before, right after deformation and after holding for 40 s.

- It has been found that, in the state with a low value of $\frac{f_{spp}}{r_{spp}}$ and a high value of f_{spp} right before deformation, precipitation occurs during both hot deformation and holding. However, in the states with medium and high values of $\frac{f_{spp}}{r_{spp}}$ right before deformation, evolution of precipitates occurs only during deformation. More specifically, in the state with medium value of $\frac{f_{spp}}{r_{spp}}$, the breakage of precipitates during deformation seems to occur. In the state with high value of $\frac{f_{spp}}{r_{spp}}$, the exact process by which the refinement of precipitates takes place seems to be more complex, most likely including dissolution/re-precipitation of finer precipitates.
- The above mentioned evolutions of precipitates have demonstrated to highly affect the deformed and quenched microstructure. It has been shown that the deformed and quenched state with a medium $\frac{f_{spp}}{r_{spp}}$ has the lowest work hardening and the highest dynamic recovery, leading therefore to a well-developed substructure. However, in the case of low $\frac{f_{spp}}{r_{spp}}$, substructure development is inhibited due to the higher amount of solutes. In the case of high $\frac{f_{spp}}{r_{spp}}$, the slowdown of substructure development is due to the higher number of fine precipitates.
- These differences in the substructure development between the three deformed states will have an effect on the initiation of dynamic and post-dynamic recrystallization. Due to the delay in the substructure development, the number of subgrains that can be transformed into viable nuclei is smaller in both cases of deformed and quenched states with low and high $\frac{f_{spp}}{r_{spp}}$ than in the case of deformed and quenched state with medium $\frac{f_{spp}}{r_{spp}}$. The growth of these nuclei in the case of low $\frac{f_{spp}}{r_{spp}}$ occurs subsequently rapidly compared to the other two states due to the lower Smith-Zener effect and to the higher dislocation density. However, in the case of high $\frac{f_{spp}}{r_{spp}}$, growth of these nuclei does not occur due to the higher Smith-Zener pinning effect (due to a very fine and dense precipitation state) despite the presence of a high dislocation density.
- The evolution of microstructure during post-deformation holding is studied. The slowest growth kinetics are observed in the state with a high $\frac{f_{spp}}{r_{spp}}$, while, the highest growth kinetics are observed in the state with a medium $\frac{f_{spp}}{r_{spp}}$, leading to the development of coarse recrystallized grains. In the case of initially low $\frac{f_{spp}}{r_{spp}}$, the growth kinetics decrease with holding time. This may be due to the precipitation that occurs during post-deformation holding in this sample.

8.1.2 Development of coarse recrystallized grains during post-deformation holding

- The possible reasons behind the development of coarse recrystallized grains in the case of medium $\frac{f_{spp}}{r_{spp}}$ are investigated. For this purpose, hot compression tests followed by both post-deformation holding experiments and sequential annealing in the SEM chamber to

follow the evolution of a given region of interest are performed.

- The overgrowth of some recrystallized grains is visible in both RD-ND and RD-TD sections during holding after deformation. The coarse recrystallized grains grow anisotropically leading to their elongated shape in the RD-ND section. In the RD-TD plane, the anisotropic grain growth behavior is more subtle.
- It has been shown that the stored energy is behind the development of coarse recrystallized grains. Indeed, the driving force due to the stored energy is higher than the Smith-Zener pinning force, resulting thus in the growth of these grains until their mutual impingement. However, stored energy cannot explain the anisotropic grain development behavior.
- The combined effect of Fe rich intermetallic particles, inhomogeneous distribution of finer precipitates and orientation pinning seems to contribute the anisotropic grain development. The influence of the misorientation angle and axis is also investigated. No clear evidence of any special misorientation angles or axes being associated with the boundaries of coarse recrystallized grains is found. Nevertheless, it has been found that many boundaries of coarse recrystallized grains are aligned with or close to $\{111\}$ plane traces, suggesting that boundary plane may also play a role in the anisotropic development of coarse recrystallized grains.
- It is concluded therefore that the anisotropic development of coarse recrystallized grains can be explained by a combination of multiple factors including alignment of Fe rich intermetallic particles, heterogeneous distribution of finer precipitates and the properties of the grain boundaries between coarse recrystallized grains and their neighbors.
- Full-field simulations have been used in order to predict the anisotropic development of coarse recrystallized grains. By taking into account the influence of stored energy, of a heterogeneous description of the grain boundary energy (i.e. γ) and of second phase particles (including Fe containing particles, Mg_2Si, Si and dispersoids), the development of coarse recrystallized grains was possible to predict. Nevertheless, the elongated shape of coarse recrystallized grains examined in the RD-ND plane could not be predicted. This may be due to the incomplete description of the inclination (i.e. perpendicular to the examined section) and/or to the fact that the torque terms are neglected.

8.1.3 Influence of thermomechanical processing parameters on microstructure evolution

- The sample having a high initial precipitate content has been studied in details in this section because precipitates are formed prior to deformation. This allows to avoid the occurrence of additional precipitation during hot deformation or holding and thus the

possible interactions between these additional precipitates and the evolution of the microstructure.

- The comparison between single pass and multipass tests shows that the interpass time allows more time for recrystallized grains to grow. Therefore, recrystallized grains obtained after multipass tests seem to be larger in size than the ones obtained after single pass tests.
- The effects of temperature, strain and strain rate on the developed microstructure have been also investigated. It has been found that subgrain growth is inhibited during deformation in the case of a low deformation temperature, leading therefore to the inhibition of nucleation of recrystallized grains by CDRX. An increase in the strain level or in the strain rate is found to increase the stored energy and therefore the driving force for nucleation and growth of recrystallized grains.
- It can be therefore concluded from these findings that a finer recrystallized grain size can be reached by reducing the interpass time and increasing the strain and the strain rate. Regarding the effect of temperature, longer holding times are required in order to confirm whether the final recrystallized grain size gets smaller by decreasing the deforming/holding temperature.

8.2 Perspectives

- Further quantitative analyses of the evolution of precipitates in both states with low and high $\frac{f_{spp}}{r_{spp}}$ are required. In fact, it is still unclear how precipitates are evolving in the case of high $\frac{f_{spp}}{r_{spp}}$ during deformation. A hypothesis of dissolution and re-precipitation of finer precipitates is made in this work. Therefore, in order to validate this hypothesis, it is important to characterize accurately the precipitation process occurring in this state during deformation, which could be done by using in-situ Synchrotron X-ray diffraction [82]. In the case of low $\frac{f_{spp}}{r_{spp}}$, precipitates formed during holding seem to be responsible for the inhibition of growth of recrystallized grains. In addition to that, the BSE images taken on electropolished samples did not show any evidence of preferential nucleation and growth of precipitates at boundaries of large grains. Therefore, it is important to perform TEM analysis on the boundaries of large grains in the case of low $\frac{f_{spp}}{r_{spp}}$ in order to verify if there are smaller precipitates (i.e. unresolved by SEM) that are pinning the movement of these large grains.
- The grain boundary plane seems to be responsible for the anisotropic development of coarse recrystallized grains. It is therefore recommended to characterize the boundary planes of coarse recrystallized grains by using 3D-EBSD and/or to perform 3D simulations with proper description of the grain boundary properties anisotropy.
- It has been demonstrated that a multipass hot compression test with an interpass time of

5 s and a higher strain of 2.4 leads to the appearance of larger recrystallized grains right after deformation. It has been also found that the largest recrystallized grain observed after a multipass test contains some substructure, suggesting therefore its enhanced growth during the interpass time. In order to confirm the effect of interpass time on the evolution of these large grains, it is important to increase the interpass time.

- Regarding the full-field numerical simulations, the focus was put in this work on the understanding of the factors promoting the anisotropic development of coarse recrystallized grains. Therefore, in this context, full-field simulations of grain growth in presence of stored energy, precipitates and/or heterogeneous GB properties have been performed. It will be interesting in the future to continue these simulations with 3D anisotropic data and to investigate the dynamic recrystallization occurring in 6016 aluminum alloy. Notably, the evolution of precipitates during deformation can be also taken into account in the future thanks to the recent developments proposed by Alvarado et al. [156].

Bibliography

[1] O Engler and E Brünger. "Microstructure and texture of aluminium alloys for autobody applications". *Matériaux and Techniques* 90.5-6 (2002), pp. 71–78. ISSN: 0032-6895. DOI: 10.1051/mattech/200290050071.

[2] O Engler and J Hirsch. "Texture control by thermomechanical processing of AA6xxx Al-Mg-Si sheet alloys for automotive applications-a review". *Materials Science and Engineering: A* 336.1-2 (2002), pp. 249–262. ISSN: 0921-5093. DOI: 10.1016/S0921-5093(01)01968-2.

[3] G. Baczynski et al. "Development of roping in an aluminum automotive alloy AA6111". *Acta Materialia* 48.13 (2000), pp. 3361–3376. ISSN: 13596454. DOI: 10.1016/S1359-6454(00)00141-5.

[4] T. Bennett, R. Petrov, and L. Kestens. "Texture-induced surface roping in an automotive aluminium sheet". *Scripta Materialia* 61.7 (2009), pp. 733–736. ISSN: 13596462. DOI: 10.1016/j.scriptamat.2009.06.016.

[5] L Qin, M Seefeldt, and P Van Houtte. "Analysis of roping of aluminum sheet materials based on the meso-scale moving window approach". *Acta Materialia* 84 (2015), pp. 215–228. ISSN: 1359-6454. DOI: 10.1016/J.ACTAMAT.2014.10.054.

[6] L. Qin, M. Seefeldt, and P. Van Houtte. "Meso-scale modelling on ridging or roping of aluminium alloys". *Materials Science and Technology Conference and Exhibition 2013, MS and T 2013* 2 (2013), pp. 1274–1283.

[7] O Engler, L Löchte, and J Hirsch. "Through-process simulation of texture and properties during the thermomechanical processing of aluminium sheets". *Acta Materialia* 55.16 (2007), pp. 5449–5463. ISSN: 1359-6454. DOI: 10.1016/J.ACTAMAT.2007.06.010.

[8] F. Humphreys and M Hatherly. *Recrystallization and Related Annealing Phenomena*. 2nd. Pergamon, 2004, p. 658. ISBN: 978-0-08-044164-1. DOI: https://doi.org/10.1016/B978-0-08-044164-1.X5000-2.

[9] F. Humphreys et al. "Developing stable fine-grain microstructures by large strain deformation". *Philosophical Transactions of the Royal Society A: Mathematical, Physical and Engineering Sciences* 357.1756 (1999), pp. 1663–1681. ISSN: 1364503X. DOI: 10.1098/rsta.1999.0395.

[10] K Huang et al. “The double-edge effect of second-phase particles on the recrystallization behaviour and associated mechanical properties of metallic materials”. *Progress in Materials Science* 92 (2018), pp. 284–359. ISSN: 00796425. DOI: 10.1016/j.pmatsci.2017.10.004.

[11] J. Hatch. *Aluminum: Properties and Physical Metallurgy*. Ed. by A. S. for Metals. 1984th ed. 1984, pp. 25–57.

[12] S. Lillywhite, P. Prangnell, and F. Humphreys. “Interactions between precipitation and recrystallisation in an Al-Mg-Si alloy”. *Materials Science and Technology* 16.10 (2000), pp. 1112–1120. ISSN: 02670836. DOI: 10.1179/026708300101507037.

[13] S. Pogatscher et al. “Influence of the thermal route on the peak-aged microstructures in an Al–Mg–Si aluminum alloy”. *Scripta Materialia* 68.2 (2013), pp. 158–161. ISSN: 13596462. DOI: 10.1016/j.scriptamat.2012.10.006.

[14] L. Ding et al. “The natural aging and precipitation hardening behaviour of Al-Mg-Si-Cu alloys with different Mg/Si ratios and Cu additions”. *Materials Science and Engineering: A* 627 (2015), pp. 119–126. ISSN: 09215093. DOI: 10.1016/j.msea.2014.12.086.

[15] M. Winning and A. D. Rollett. “Transition between low and high angle grain boundaries”. *Acta Materialia* 53.10 (2005), pp. 2901–2907. ISSN: 13596454. DOI: 10.1016/j.actamat.2005.03.005.

[16] Y Huang and F. Humphreys. “Measurements of grain boundary mobility during recrystallization of a single-phase aluminium alloy”. *Acta Materialia* 47.7 (1999), pp. 2259–2268. ISSN: 13596454. DOI: 10.1016/S1359-6454(99)00062-2.

[17] Y Huang and F. Humphreys. “Subgrain growth and low angle boundary mobility in aluminium crystals of orientation {110}001”. *Acta Materialia* 48.8 (2000), pp. 2017–2030. ISSN: 1359-6454. DOI: 10.1016/S1359-6454(99)00418-8.

[18] E Nes, K Marthinsen, and Y Brechet. “On the mechanisms of dynamic recovery”. *Scripta Materialia* 47.9 (2002), pp. 607–611. ISSN: 13596462. DOI: 10.1016/S1359-6462(02)00235-X.

[19] S. Ahl et al. “Subgrain dynamics during recovery of partly recrystallized aluminum”. *Acta Materialia* 185 (2020), pp. 142–148. ISSN: 13596454. DOI: 10.1016/j.actamat.2019.10.042.

[20] K. Huang and R. Logé. “A review of dynamic recrystallization phenomena in metallic materials”. *Materials and Design* 111 (2016), pp. 548–574. ISSN: 0264-1275. DOI: 10.1016/J.MATDES.2016.09.012.

[21] Y. V. Prasad and N. Ravichandran. “Effect of stacking fault energy on the dynamic recrystallization during hot working of FCC metals: A study using processing maps”. *Bulletin of Materials Science* 14.5 (1991), pp. 1241–1248. ISSN: 02504707. DOI: 10.1007/BF02744618.

[22] T Sakai et al. “Dynamic and post-dynamic recrystallization under hot, cold and severe plastic deformation conditions”. *Progress in Materials Science* 60 (2014), pp. 130–207. ISSN: 0079-6425. DOI: 10.1016/J.PMATSCI.2013.09.002.

[23] H. Yamagata. “Dynamic recrystallization of single-crystalline aluminum during compression tests”. *Scripta Metallurgica et Materialia* 27.6 (1992), pp. 727–732. ISSN: 0956716X. DOI: 10.1016/0956-716X(92)90496-2.

[24] H. Yamagata. “Dynamic recrystallization and dynamic recovery in pure aluminum at 583K”. *Acta Metallurgica Et Materialia* 43.2 (1995), pp. 723–729. ISSN: 09567151. DOI: 10.1016/0956-7151(94)00267-L.

[25] D Ponge, M Bredehöft, and G Gottstein. “Dynamic recrystallization in high purity aluminum”. *Scripta Materialia* 37.11 (1997), pp. 1769–1775. ISSN: 1359-6462. DOI: 10.1016/S1359-6462(97)00346-1.

[26] S Gourdet and F Montheillet. “An experimental study of the recrystallization mechanism during hot deformation of aluminium”. *Materials Science and Engineering A* 283.1 (2000), pp. 274–288. ISSN: 09215093. DOI: 10.1016/S0921-5093(00)00733-4.

[27] F. Castro-Fernández and C. Sellars. “Static recrystallisation and recrystallisation during hot deformation of Al–1Mg–1Mn alloy”. *Materials Science and Technology (United Kingdom)* 4.7 (1988), pp. 621–627. ISSN: 17432847. DOI: 10.1179/mst.1988.4.7.621.

[28] S Tangen et al. “Effect of concurrent precipitation on recrystallization and evolution of the P-texture component in a commercial Al-Mn alloy”. *Metallurgical and Materials Transactions A: Physical Metallurgy and Materials Science* 41.11 (2010), pp. 2970–2983. ISSN: 10735623. DOI: 10.1007/s11661-010-0265-8.

[29] A Chamanfar et al. “Analysis of flow stress and microstructure during hot compression of 6099 aluminum alloy (AA6099)”. *Materials Science and Engineering: A* 743 (2019), pp. 684–696. ISSN: 0921-5093. DOI: 10.1016/J.MSEA.2018.11.076.

[30] K.-F. Adam, Z Long, and D.-P. Field. “Analysis of Particle-Stimulated Nucleation (PSN)-Dominated Recrystallization for Hot-Rolled 7050 Aluminum Alloy”. *Metallurgical and Materials Transactions A: Physical Metallurgy and Materials Science* 48.4 (2017), pp. 2062–2076. ISSN: 10735623. DOI: 10.1007/s11661-017-3967-3.

[31] F.-J. Zhu et al. “Dynamic behavior of a 6069 Al alloy under hot compression”. *Materials Science and Engineering: A* 640 (2015), pp. 385–393. ISSN: 0921-5093. DOI: 10.1016/J.MSEA.2015.06.026.

[32] F. Humphreys and P. Kalu. “Dislocation-particle interactions during high temperature deformation of two-phase aluminium alloys”. *Acta Metallurgica* 35.12 (1987), pp. 2815–2829. ISSN: 00016160. DOI: 10.1016/0001-6160(87)90281-1.

[33] C Shi, J Lai, and X. Chen. “Microstructural evolution and dynamic softening mechanisms of Al-Zn-Mg-Cu alloy during hot compressive deformation”. *Materials* 7.1 (2014), pp. 244–264. ISSN: 19961944. DOI: 10.3390/ma7010244.

[34] D.-F. Li et al. “Dynamic recrystallization behavior of 7085 aluminum alloy during hot deformation”. *Transactions of Nonferrous Metals Society of China* 26.6 (2016), pp. 1491–1497. ISSN: 1003-6326. DOI: 10.1016/S1003-6326(16)64254-1.

[35] Q Yang et al. “Effects of strain rate on flow stress behavior and dynamic recrystallization mechanism of Al-Zn-Mg-Cu aluminum alloy during hot deformation”. *Materials Science and Engineering: A* 662 (2016), pp. 204–213. ISSN: 0921-5093. DOI: 10.1016/J.MSEA.2016.03.027.

[36] I Samajdar and R. Doherty. “Cube recrystallization texture in warm deformed aluminum: Understanding and prediction”. *Acta Materialia* 46.9 (1998), pp. 3145–3158. ISSN: 13596454. DOI: 10.1016/S1359-6454(97)00492-8.

[37] H. Vatne, T Furu, and E Nes. “Nucleation of recrystallised grains from cube bands in hot deformed commercial purity aluminium”. *Materials Science and Technology* 12.3 (1996), pp. 201–210. ISSN: 02670836. DOI: 10.1179/mst.1996.12.3.201.

[38] H. Vatne, R Shahani, and E Nes. “Deformation of cube-oriented grains and formation of recrystallized cube grains in a hot deformed commercial AlMgMn aluminium alloy”. *Acta Materialia* 44.11 (1996), pp. 4447–4462. ISSN: 13596454. DOI: 10.1016/1359-6454(96)00077-8.

[39] O Daaland and E Nes. “Origin of cube texture during hot rolling of commercial Al-Mn-Mg alloys”. *Acta Materialia* 44.4 (1996), pp. 1389–1411. ISSN: 13596454. DOI: 10.1016/1359-6454(95)00289-8.

[40] S De La Chapelle. “Cube recrystallization textures in a hot deformed Al–Mg–Si alloy”. *Scripta Materialia* 45.12 (2001), pp. 1387–1391. ISSN: 1359-6462. DOI: 10.1016/S1359-6462(01)01174-5.

[41] M. Alvi et al. “Cube texture in hot-rolled aluminum alloy 1050 (AA1050)—nucleation and growth behavior”. *Acta Materialia* 56.13 (2008), pp. 3098–3108. ISSN: 1359-6454. DOI: 10.1016/J.ACTAMAT.2008.02.037.

[42] R Kaibyshev et al. “Continuous dynamic recrystallization in an Al–Li–Mg–Sc alloy during equal-channel angular extrusion”. *Materials Science and Engineering: A* 396.1-2 (2005), pp. 341–351. ISSN: 0921-5093. DOI: 10.1016/J.MSEA.2005.01.053.

[43] Q Yang et al. “Hot deformation behavior and microstructure of AA2195 alloy under plane strain compression”. *Materials Characterization* 131 (2017), pp. 500–507. ISSN: 1044-5803. DOI: 10.1016/J.MATCHAR.2017.06.001.

[44] Q Zang et al. “Hot deformation behavior and microstructure evolution of annealed Al-7.9Zn-2.7Mg-2.0Cu (wt%) alloy”. *Journal of Alloys and Compounds* 763 (2018), pp. 25–33. ISSN: 09258388. DOI: 10.1016/j.jallcom.2018.05.307.

[45] J Zhao et al. “Effect of strain rate on the recrystallization mechanism during isothermal compression in 7050 aluminum alloy”. *Materials Science and Engineering A* (2018). ISSN: 09215093. DOI: 10.1016/j.msea.2018.07.068.

[46] C Zhang et al. “Investigation of dynamic recrystallization and modeling of microstructure evolution of an Al-Mg-Si aluminum alloy during high-temperature deformation”. *Journal of Alloys and Compounds* 773 (2019), pp. 59–70. ISSN: 0925-8388. DOI: 10.1016/J.JALLCOM.2018.09.263.

[47] Y. Y. Wang et al. “Effect of deformation temperature on the microstructure developed in commercial purity aluminum processed by equal channel angular extrusion”. *Scripta Materialia* 50.5 (2004), pp. 613–617. ISSN: 13596462. DOI: 10.1016/j.scriptamat.2003.11.027.

[48] Y. Deng, Z. Yin, and J. Huang. “Hot deformation behavior and microstructural evolution of homogenized 7050 aluminum alloy during compression at elevated temperature”. *Materials Science and Engineering A* 528.3 (2011), pp. 1780–1786. ISSN: 09215093. DOI: 10.1016/j.msea.2010.11.016.

[49] H. McQueen et al. “Microstructural evolution in Al deformed to strains of 60 at 400°C”. *Scripta Metallurgica* 19.1 (1985), pp. 73–78. ISSN: 00369748. DOI: 10.1016/0036-9748(85)90268-6.

[50] H. McQueen et al. “Evolution of flow stress in aluminium during ultra-high straining at elevated temperatures. Part II”. *Philosophical Magazine A* 60.4 (1989), pp. 473–485. ISSN: 0141-8610. DOI: 10.1080/01418618908213873.

[51] W Blum et al. “Geometric dynamic recrystallization in hot torsion of Al-5Mg-0.6Mn (AA5083)”. *Materials Science and Engineering: A* 205.1-2 (1996), pp. 23–30. ISSN: 0921-5093. DOI: 10.1016/0921-5093(95)09990-5.

[52] A Gholinia, F. Humphreys, and P. Prangnell. “Production of ultra-fine grain microstructures in Al–Mg alloys by coventional rolling”. *Acta Materialia* 50.18 (2002), pp. 4461–4476. ISSN: 13596454. DOI: 10.1016/S1359-6454(02)00253-7.

[53] C Poletti et al. “Microstructure development in hot deformed AA6082”. *Materials Science and Engineering: A* 528.6 (2011), pp. 2423–2430. ISSN: 0921-5093. DOI: 10.1016/J.MSEA.2010.11.048.

[54] X. Fan et al. “Dynamic recrystallisation and dynamic precipitation in AA6061 aluminium alloy during hot deformation”. *Materials Science and Technology* 30.11 (2014), pp. 1263–1272. ISSN: 0267-0836. DOI: 10.1179/1743284714Y.0000000538.

[55] X Zeng et al. “Grain morphology related microstructural developments in bulk deformation of 2219 aluminum alloy sheet at elevated temperature”. *Materials Science and Engineering A* 760.February (2019), pp. 328–338. ISSN: 09215093. DOI: 10.1016/j.msea.2019.06.022.

[56] R Kaibyshev, I Mazurina, and O Sitdikov. “Geometric dynamic recrystallization in an AA2219 alloy deformed to large strains at an elevated temperature”. *Materials Science Forum* 467-470.II (2004), pp. 1199–1204. ISSN: 16629752. DOI: 10.4028/www.scientific.net/msf.467-470.1199.

[57] H. McQueen. “Development of dynamic recrystallization theory”. *Materials Science and Engineering: A* 387-389 (2004), pp. 203–208. ISSN: 0921-5093. DOI: 10.1016/J.MSEA.2004.01.064.

[58] M. Kassner and S. Barrabes. “New developments in geometric dynamic recrystallization”. *Materials Science and Engineering: A* 410-411 (2005), pp. 152–155. ISSN: 0921-5093. DOI: 10.1016/J.MSEA.2005.08.052.

[59] M. Charpagne, J. Franchet, and N Bozzolo. “Overgrown grains appearing during subsolvus heat treatment in a polycrystalline γ-γ’ Nickel-based superalloy”. *Materials and Design* 144 (2018), pp. 353–360. ISSN: 02641275. DOI: 10.1016/j.matdes.2018.02.048.

[60] D. Srolovitz, G. Grest, and M. Anderson. “Computer simulation of grain growth-V. Abnormal grain growth”. *Acta Metallurgica* 33.12 (1985), pp. 2233–2247. ISSN: 00016160. DOI: 10.1016/0001-6160(85)90185-3.

[61] C. Thompson, H. Frost, and F Spaepen. “The relative rates of secondary and normal grain growth”. *Acta Metallurgica* 35.4 (1987), pp. 887–890. ISSN: 00016160. DOI: 10.1016/0001-6160(87)90166-0.

[62] B. DeCost and E. Holm. “Phenomenology of Abnormal Grain Growth in Systems with Nonuniform Grain Boundary Mobility”. *Metallurgical and Materials Transactions A: Physical Metallurgy and Materials Science* 48.6 (2017), pp. 2771–2780. ISSN: 10735623. DOI: 10.1007/s11661-016-3673-6.

[63] E. Holm, G. Hassold, and M. Miodownik. “On misorientation distribution evolution during anisotropic grain growth”. *Acta Materialia* 49.15 (2001), pp. 2981–2991. ISSN: 13596454. DOI: 10.1016/S1359-6454(01)00207-5.

[64] E. Holm, M. Miodownik, and A. Rollett. “On abnormal subgrain growth and the origin of recrystallization nuclei”. *Acta Materialia* 51.9 (2003), pp. 2701–2716. ISSN: 13596454. DOI: 10.1016/S1359-6454(03)00079-X.

[65] O Engler. “On the influence of orientation pinning on growth selection of recrystallisation”. *Acta Materialia* 46.5 (1998), pp. 1555–1568. ISSN: 13596454. DOI: 10.1016/S1359-6454(97)00354-6.

[66] H. Kim et al. “Effect of primary recrystallization texture on abnormal grain growth in an aluminum alloy”. *Scripta Materialia* (2007). ISSN: 13596462. DOI: 10.1016/j.scriptamat.2007.04.023.

[67] D.-K. Lee et al. “Comparison of the advantages conferred by mobility and energy of the grain boundary in inducing abnormal grain growth using Monte Carlo simu-

lations". *Materials Transactions* 50.11 (2009), pp. 2521–2525. ISSN: 13459678. DOI: 10.2320/matertrans.M2009209.

[68] K.-J. Ko et al. "Abnormal grain growth induced by sub-boundary-enhanced solid-state wetting: Analysis by phase-field model simulations". *Acta Materialia* 57.3 (2009), pp. 838–845. ISSN: 13596454. DOI: 10.1016/j.actamat.2008.10.030.

[69] E Fjeldberg et al. "Mobility driven abnormal grain growth in the presence of particles". *Materials Science Forum* 715-716 (2012), pp. 930–935. ISSN: 16629752. DOI: 10.4028/www.scientific.net/MSF.715-716.930.

[70] E. Holm et al. "Particle-assisted abnormal grain growth". *IOP Conference Series: Materials Science and Engineering* 89.1 (2015), p. 012005. ISSN: 1757-8981. DOI: 10.1088/1757-899X/89/1/012005.

[71] N Lu et al. "Dynamics of particle-assisted abnormal grain growth revealed through integrated three-dimensional microanalysis". *Acta Materialia* 195 (2020), pp. 1–12. ISSN: 13596454. DOI: 10.1016/j.actamat.2020.04.049.

[72] C. Thompson. "Grain growth in thin films". *Annual Review of Materials Science* 20.1 (1990), pp. 245–268. ISSN: 00846600. DOI: 10.1146/annurev.ms.20.080190.001333.

[73] S.-G. Kim and Y.-B. Park. "Grain boundary segregation , solute drag and abnormal grain growth". 56 (2008), pp. 3739–3753. DOI: 10.1016/j.actamat.2008.04.007.

[74] J Dennis, P. Bate, and F. Humphreys. "Abnormal grain growth in Al–3.5Cu". *Acta Materialia* 57.15 (2009), pp. 4539–4547. ISSN: 13596454. DOI: 10.1016/j.actamat.2009.06.018.

[75] J. Chang et al. "Abnormal Grain Growth and Recrystallization in Al-Mg Alloy AA5182 Following Hot Deformation". *Metallurgical and Materials Transactions A* 41.8 (2010), pp. 1942–1953. ISSN: 1073-5623. DOI: 10.1007/s11661-010-0213-7.

[76] K Li et al. "On Formation of Abnormally Large Grains in Annealing Prestrained Aluminum Alloy Multiport Extrusion Tubes". *Metallurgical and Materials Transactions A* 50.12 (2019), pp. 5734–5749. ISSN: 1073-5623. DOI: 10.1007/s11661-019-05453-0.

[77] H.-K. Park et al. "Ex Situ Observation of Microstructure Evolution During Abnormal Grain Growth in Aluminum Alloy". *Metallurgical and Materials Transactions A* 43.13 (2012), pp. 5218–5223. ISSN: 1073-5623. DOI: 10.1007/s11661-012-1334-y.

[78] W. C. Liu et al. "Effect of hot and cold deformation on the recrystallization texture of continuous cast AA 5052 aluminum alloy". *Scripta Materialia* 53.11 (2005), pp. 1273–1277. ISSN: 13596462. DOI: 10.1016/j.scriptamat.2005.07.040.

[79] W Liu, M Ma, and F Yang. “Effect of the Heat Treatment on the Cube Recrystallization Texture of Al-Mn-Mg Aluminum Alloy”. 44.June (2013), pp. 2857–2868. DOI: 10.1007/s11661-012-1601-y.

[80] W. C. Liu et al. “Effect of precipitation on rolling texture evolution in continuous cast AA 3105 aluminum alloy”. *Materials Science and Engineering A* 434.1-2 (2006), pp. 105–113. ISSN: 09215093. DOI: 10.1016/j.msea.2006.06.102.

[81] O. Engler and K. Lücke. “Influence of the precipitation state on the cold rolling texture in 8090 Al-Li material”. *Materials Science and Engineering: A* 148.1 (1991), pp. 15–23. ISSN: 09215093. DOI: 10.1016/0921-5093(91)90861-G.

[82] A Deschamps et al. “In situ evaluation of dynamic precipitation during plastic straining of an Al-Zn-Mg-Cu alloy”. *Acta Materialia* 60.5 (2012), pp. 1905–1916. ISSN: 13596454. DOI: 10.1016/j.actamat.2012.01.002.

[83] I Gutierrez-Urrutia, M. Munoz-Morris, and D. Morris. “The effect of coarse second-phase particles and fine precipitates on microstructure refinement and mechanical properties of severely deformed Al alloy”. 394 (2005), pp. 399–410. DOI: 10.1016/j.msea.2004.11.025.

[84] Q. Zhao et al. “Orientation Preference of Recrystallization in Supersaturated Aluminum Alloys Influenced by Concurrent Precipitation”. *Metallurgical and Materials Transactions A* 47.3 (2016), pp. 1378–1388. ISSN: 1073-5623. DOI: 10.1007/s11661-015-3314-5.

[85] X Qian, N Parson, and X. Chen. “Effects of Mn content on recrystallization resistance of AA6082 aluminum alloys during post-deformation annealing”. *Journal of Materials Science and Technology* 52 (2020), pp. 189–197. ISSN: 10050302. DOI: 10.1016/j.jmst.2020.04.015.

[86] S Gourdet and F Montheillet. “A model of continuous dynamic recrystallization”. *Acta Materialia* 51.9 (2003), pp. 2685–2699. ISSN: 1359-6454. DOI: 10.1016/S1359-6454(03)00078-8.

[87] F Bachmann, R Hielscher, and H Schaeben. “Texture analysis with MTEX- Free and open source software toolbox”. *Solid State Phenomena* 160 (2010), pp. 63–68. ISSN: 10120394. DOI: 10.4028/www.scientific.net/SSP.160.63.

[88] N Bozzolo, S Jacomet, and R. Logé. “Fast in-situ annealing stage coupled with EBSD: A suitable tool to observe quick recrystallization mechanisms”. *Materials Characterization* 70 (2012), pp. 28–32. ISSN: 10445803. DOI: 10.1016/j.matchar.2012.04.020.

[89] C. Kerisit et al. “EBSD coupled to SEM in situ annealing for assessing recrystallization and grain growth mechanisms in pure tantalum”. *Journal of Microscopy* 250.3 (2013), pp. 189–199. ISSN: 00222720. DOI: 10.1111/jmi.12034.

[90] H. Nakamichi, F. J. Humphreys, and I. Brough. “Recrystallization phenomena in an IF steel observed by in situ EBSD experiments”. *Journal of Microscopy* 230.3 (2008), pp. 464–471. ISSN: 00222720. DOI: 10.1111/j.1365-2818.2008.02006.x.

[91] A Seret et al. “Estimation of geometrically necessary dislocation density from filtered EBSD data by a local linear adaptation of smoothing splines”. *Journal of Applied Crystallography* 52.3 (2019), pp. 548–563. ISSN: 16005767. DOI: 10.1107/S1600576719004035.

[92] A Nicolaÿ et al. “Discrimination of dynamically and post-dynamically recrystallized grains based on EBSD data: application to Inconel 718”. *Journal of Microscopy* 273.2 (2019), pp. 135–147. ISSN: 13652818. DOI: 10.1111/jmi.12769.

[93] S. Saltikov. “The Determination of the Size Distribution of Particles in an Opaque Material from a Measurement of the Size Distribution of Their Sections”. *Stereology*. Berlin, Heidelberg: Springer Berlin Heidelberg, 1967, pp. 163–173. DOI: 10.1007/978-3-642-88260-9_31.

[94] P. Konijnenberg, S Zaefferer, and D Raabe. “Assessment of geometrically necessary dislocation levels derived by 3D EBSD”. *Acta Materialia* 99 (2015), pp. 402–414. ISSN: 13596454. DOI: 10.1016/j.actamat.2015.06.051.

[95] Y Huang and F. Humphreys. “The effect of solutes on grain boundary mobility during recrystallization and grain growth in some single-phase aluminium alloys”. *Materials Chemistry and Physics* 132.1 (2012), pp. 166–174. ISSN: 0254-0584. DOI: 10.1016/J.MATCHEMPHYS.2011.11.018.

[96] A. Biswas, D. J. Siegel, and D. N. Seidman. “Compositional evolution of Q-phase precipitates in an aluminum alloy”. *Acta Materialia* 75 (2014), pp. 322–336. ISSN: 13596454. DOI: 10.1016/j.actamat.2014.05.001.

[97] M. Muñoz-Morris et al. “Refinement of precipitates and deformation substructure in an Al – Cu – Li alloy during heavy rolling at elevated temperatures”. 492 (2008), pp. 268–275. DOI: 10.1016/j.msea.2008.03.036.

[98] D. A. Hughes and N. Hansen. “High angle boundaries formed by grain subdivision mechanisms”. *Acta Materialia* 45.9 (1997), pp. 3871–3886. ISSN: 13596454. DOI: 10.1016/S1359-6454(97)00027-X.

[99] Y. J. Bréchet, H. S. Zurob, and C. R. Hutchinson. “On the effect of pre-recovery on subsequent recrystallization”. *International Journal of Materials Research* 100.10 (2009), pp. 1446–1448. ISSN: 18625282. DOI: 10.3139/146.110194.

[100] S. Liang, F. Fazeli, and H. S. Zurob. “Effects of solutes and temperature on high-temperature deformation and subsequent recovery in hot-rolled low alloy steels”. *Materials Science and Engineering A* 765.June (2019), p. 138324. ISSN: 09215093. DOI: 10.1016/j.msea.2019.138324.

[101] P. Trivedi, D. P. Field, and H. Weiland. “Alloying effects on dislocation substructure evolution of aluminum alloys”. *International Journal of Plasticity* 20.3 (2004), pp. 459–476. ISSN: 07496419. DOI: 10.1016/S0749-6419(03)00097-4.

[102] H. J. McQueen. “The production and utility of recovered dislocation substructures”. *Metallurgical Transactions A* 8.6 (1977), pp. 807–824. ISSN: 03602133. DOI: 10.1007/BF02661562.

[103] T Radetic et al. “The effect of ECAP and Cu addition on the aging response and grain substructure evolution in an Al – 4 . 4 wt .% Mg alloy”. 527 (2010), pp. 634–644. DOI: 10.1016/j.msea.2009.08.037.

[104] C Shi and X Chen. “Effect of vanadium on hot deformation and microstructural evolution of 7150 aluminum alloy”. *Materials Science and Engineering A* 613 (2014), pp. 91–102. ISSN: 0921-5093. DOI: 10.1016/j.msea.2014.06.082.

[105] A Agnoli et al. “Selective Growth of Low Stored Energy Grains During δ Sub-solvus Annealing in the Inconel 718 Nickel-Based Superalloy”. *Metallurgical and Materials Transactions A* 46.9 (2015), pp. 4405–4421. ISSN: 1073-5623. DOI: 10.1007/s11661-015-3035-9.

[106] M. Moghaddam et al. “Characterization of the microstructure, texture and mechanical properties of 7075 aluminum alloy in early stage of severe plastic deformation”. *Materials Characterization* 119 (2016), pp. 137–147. ISSN: 10445803. DOI: 10.1016/j.matchar.2016.07.026.

[107] A. Ridha and W. Hutchinson. “Recrystallisation mechanisms and the origin of cube texture in copper”. *Acta Metallurgica* (1982). ISSN: 00016160. DOI: 10.1016/0001-6160(82)90033-5.

[108] B Hutchinson. “The cube texture revisited”. *Materials Science Forum* 702-703.December (2012), pp. 3–10. ISSN: 02555476. DOI: 10.4028/www.scientific.net/MSF.702-703.3.

[109] E Nes, N Ryum, and O Hunderi. “On the Zener drag”. *Acta Metallurgica* 33.1 (1985), pp. 11–22. ISSN: 00016160. DOI: 10.1016/0001-6160(85)90214-7.

[110] C. Sinclair et al. “Recrystallization and Texture in a Ferritic Stainless Steel: An EBSD Study”. *Advanced Engineering Materials* 5.8 (2003), pp. 570–574. ISSN: 14381656. DOI: 10.1002/adem.200300377.

[111] X. Fang et al. “Tailoring microstructure and texture of annealed Al-Mn alloy through the variation of homogenization and prior cold deformation strain”. *Materials Characterization* 166.May (2020). ISSN: 10445803. DOI: 10.1016/j.matchar.2020.110438.

[112] N Bozzolo et al. “Grain boundary character evolution during grain growth in a Zr alloy”. *Materials Science Forum* 558-559.PART 2 (2007), pp. 863–868. ISSN: 16629752. DOI: 10.4028/0-87849-443-x.863.

[113] S. Wright. “Random thoughts on non-random misorientation distributions”. 22.11 (2006), pp. 1287–1297. DOI: 10.1179/174328406X130876.

[114] N. Bozzolo et al. “Texture evolution during grain growth in recrystallized commercially pure titanium”. *Materials Science and Engineering A* 397.1-2 (2005), pp. 346–355. ISSN: 09215093. DOI: 10.1016/j.msea.2005.02.049.

[115] Y. Zhang et al. “Analysis of the growth of individual grains during recrystallization in pure nickel”. *Acta Materialia* 57.9 (2009), pp. 2631–2639. ISSN: 13596454. DOI: 10.1016/j.actamat.2009.01.039.

[116] D. Olmsted, S. Foiles, and E. Holm. “Survey of computed grain boundary properties in face-centered cubic metals: I. Grain boundary energy”. *Acta Materialia* 57.13 (2009), pp. 3694–3703. ISSN: 13596454. DOI: 10.1016/j.actamat.2009.04.007.

[117] D. Olmsted, E. Holm, and S. Foiles. “Survey of computed grain boundary properties in face-centered cubic metals-II: Grain boundary mobility”. *Acta Materialia* 57.13 (2009), pp. 3704–3713. ISSN: 13596454. DOI: 10.1016/j.actamat.2009.04.015.

[118] C.-S. Park et al. “New understanding of the role of coincidence site lattice boundaries in abnormal grain growth of aluminium alloy”. *Philosophical Magazine Letters* 95.4 (2015), pp. 220–228. ISSN: 13623036. DOI: 10.1080/09500839.2015.1033027.

[119] N. Pedrazas et al. “Dynamic abnormal grain growth in tantalum”. *Materials Science and Engineering A* 610 (2014), pp. 76–84. ISSN: 09215093. DOI: 10.1016/j.msea.2014.05.031.

[120] H Park et al. “Microstructural evidence of abnormal grain growth by solid-state wetting in Fe-3%Si steel”. *Journal of Applied Physics* 95.10 (2004), pp. 5515–5521. ISSN: 00218979. DOI: 10.1063/1.1712012.

[121] K.-J. Ko et al. “Morphological evidence that Goss abnormally growing grains grow by triple junction wetting during secondary recrystallization of Fe-3% Si steel”. *Scripta Materialia* 59.7 (2008), pp. 764–767. ISSN: 13596462. DOI: 10.1016/j.scriptamat.2008.06.021.

[122] J. Koo, D. Yoon, and M. Henry. “Island grains of low misorientation angles formed during abnormal grain growth in Cu”. *Metallurgical and Materials Transactions A: Physical Metallurgy and Materials Science* 31.5 (2000), pp. 1489–1491. ISSN: 10735623. DOI: 10.1007/s11661-000-0267-z.

[123] D. Brandon. “The structure of high-angle grain boundaries”. *Acta Metallurgica* 14.11 (1966), pp. 1479–1484. ISSN: 00016160. DOI: 10.1016/0001-6160(66)90168-4.

[124] G. Rohrer. “Grain boundary energy anisotropy: A review”. *Journal of Materials Science* 46.18 (2011), pp. 5881–5895. ISSN: 00222461. DOI: 10.1007/s10853-011-5677-3.

[125] J. K. Solberg et al. “Influence of ultra-high strains at elevated temperatures on the microstructure of aluminium. Part I”. *Philosophical Magazine A* 60.4 (1989), pp. 447–471. ISSN: 0141-8610. DOI: 10.1080/01418618908213872.

[126] A. Belyakov et al. “Grain refinement in copper under large strain deformation”. *Philosophical Magazine A: Physics of Condensed Matter, Structure, Defects and Mechanical Properties* 81.11 (2001), pp. 2629–2643. ISSN: 01418610. DOI: 10.1080/01418610108216659.

[127] W. Liu, D Juul Jensen, and J. Morris. “Effect of grain orientation on microstructures during hot deformation of AA 3104 aluminium alloy by plane strain compression”. *Acta Materialia* 49.16 (2001), pp. 3347–3367. ISSN: 1359-6454. DOI: 10.1016/S1359-6454(01)00009-X.

[128] R. Gholizadeh et al. “Strain-dependence of deformation microstructures in ultra-low-C IF steel deformed to high strains by torsion at elevated temperatures”. *Nano Materials Science* 2.1 (2020), pp. 83–95. ISSN: 25899651. DOI: 10.1016/j.nanoms.2020.03.005.

[129] L. Liu, W. Yunxin, and G. Hai. “Effects of Deformation Parameters on Microstructural Evolution of 2219 Aluminum Alloy during Intermediate Thermo-Mechanical Treatment Process”. *Materials* (2018). DOI: https://doi.org/10.3390/ma11091496.

[130] H Jazaeri and F. Humphreys. “The transition from discontinuous to continuous recrystallization in some aluminium alloys: I – the deformed state”. *Acta Materialia* 52.11 (2004), pp. 3239–3250. ISSN: 13596454. DOI: 10.1016/j.actamat.2004.03.030.

[131] P. R. Rios et al. “Nucleation and growth during recrystallization”. *Materials Research* 8.3 (2005), pp. 225–238. ISSN: 15161439. DOI: 10.1590/S1516-14392005000300002.

[132] A. Rollett et al. “Computer simulation of recrystallization in non-uniformly deformed metals”. *Acta Metallurgica* 37.2 (1989), pp. 627–639. ISSN: 0001-6160. DOI: https://doi.org/10.1016/0001-6160(89)90247-2.

[133] D. Raabe. “Cellular Automata in Materials Science with Particular Reference to Recrystallization Simulation”. *Annual Review of Materials Research* 32.1 (2002), pp. 53–76. DOI: 10.1146/annurev.matsci.32.090601.152855.

[134] A. Harun et al. “On computer simulation methods to model Zener pinning”. *Acta Materialia* 54.12 (2006), pp. 3261–3273. ISSN: 1359-6454. DOI: https://doi.org/10.1016/j.actamat.2006.03.012.

[135] N. Moelans, B. Blanpain, and P. Wollants. “A phase field model for the simulation of grain growth in materials containing finely dispersed incoherent second-phase particles”. *Acta Materialia* 53.6 (2005), pp. 1771–1781. ISSN: 1359-6454. DOI: https://doi.org/10.1016/j.actamat.2004.12.026.

[136] S. Osher and J. A. Sethian. “Fronts propagating with curvature-dependent speed: Algorithms based on Hamilton-Jacobi formulations”. *Journal of Computational Physics*

79.1 (1988), pp. 12–49. ISSN: 0021-9991. DOI: https://doi.org/10.1016/0021-9991(88)90002-2.

[137] S. Florez et al. "A novel highly efficient Lagrangian model for massively multidomain simulation applied to microstructural evolutions". *Computer Methods in Applied Mechanics and Engineering* 367 (2020), p. 113107. ISSN: 0045-7825. DOI: https://doi.org/10.1016/j.cma.2020.113107.

[138] P. De Micheli et al. "DIGIMU®: Full field recrystallization simulations for optimization of multi-pass processes". *AIP Conference Proceedings*. Vol. 2113. 1. AIP Publishing LLC. 2019, p. 040014.

[139] P. De Micheli et al. "DIGIMU®: 2D and 3D Full Field Recrystallization Simulations with coupled Micro-Macro approaches". *NEMU 2019*. 2019.

[140] H.-K. Zhao et al. "A Variational Level Set Approach to Multiphase Motion". *Journal of Computational Physics* 127.1 (1996), pp. 179–195. ISSN: 0021-9991. DOI: https://doi.org/10.1006/jcph.1996.0167.

[141] B. Merriman, J. K. Bence, and S. J. Osher. "Motion of Multiple Junctions: A Level Set Approach". *Journal of Computational Physics* 112.2 (1994), pp. 334–363. ISSN: 0021-9991. DOI: https://doi.org/10.1006/jcph.1994.1105.

[142] M. Bernacki et al. "Level set framework for the numerical modelling of primary recrystallization in polycrystalline materials". *Scripta Materialia* 58.12 (2008), pp. 1129–1132. ISSN: 13596462. DOI: 10.1016/j.scriptamat.2008.02.016.

[143] M. Bernacki et al. "Finite element model of primary recrystallization in polycrystalline aggregates using a level set framework". *Modelling and Simulation in Materials Science and Engineering* 17.6 (2009). ISSN: 09650393. DOI: 10.1088/0965-0393/17/6/064006.

[144] M. Bernacki, R. E. Logé, and T. Coupez. "Level set framework for the finite-element modelling of recrystallization and grain growth in polycrystalline materials". *Scripta Materialia* 64.6 (2011), pp. 525–528. ISSN: 13596462. DOI: 10.1016/j.scriptamat.2010.11.032.

[145] M. Elsey, S. Esedog¯lu, and P. Smereka. "Diffusion generated motion for grain growth in two and three dimensions". *Journal of Computational Physics* 228.21 (2009), pp. 8015–8033. ISSN: 0021-9991. DOI: https://doi.org/10.1016/j.jcp.2009.07.020.

[146] C. Miessen et al. "An advanced level set approach to grain growth@ Accounting for grain boundary anisotropy and finite triple junction mobility". *Acta Materialia* 99 (2015), pp. 39–48.

[147] H Resk et al. "Adaptive mesh refinement and automatic remeshing in crystal plasticity finite element simulations". *Modelling and Simulation in Materials Science and Engineering* 17.7 (2009), p. 075012. DOI: 10.1088/0965-0393/17/7/075012.

[148] M Bernacki, R. E Logé, and T Coupez. “Level set framework for the finite-element modelling of recrystallization and grain growth in polycrystalline materials”. *Scripta Materialia* 64.6 (2011), pp. 525–528. ISSN: 13596462. DOI: 10.1016/j.scriptamat.2010.11.032.

[149] H. Hallberg. “A modified level set approach to 2D modeling of dynamic recrystallization”. *Modelling and Simulation in Materials Science and Engineering* 21 (2013), p. 085012.

[150] A. Agnoli et al. “Development of a level set methodology to simulate grain growth in the presence of real secondary phase particles and stored energy – Application to a nickel-base superalloy”. *Computational Materials Science* 89 (2014), pp. 233–241. ISSN: 09270256. DOI: 10.1016/j.commatsci.2014.03.054.

[151] B. Scholtes et al. “Full field modeling of the Zener pinning phenomenon in a level set framework- discussion of classical limiting mean grain size equation”. *Superalloys* (2016), pp. 497–503.

[152] B. Scholtes et al. “New finite element developments for the full field modeling of microstructural evolutions using the level-set method”. *Computational Materials Science* 109 (2015), pp. 388–398. ISSN: 09270256. DOI: 10.1016/j.commatsci.2015.07.042.

[153] B. Scholtes et al. “Full Field Modeling of the Zener Pinning Phenomenon in a Level Set Framework - Discussion of Classical Limiting Mean Grain Size Equation”. *Superalloys 2016*. Ed. by M. Hardy et al. Hoboken, NJ, USA: John Wiley and Sons, Inc., 2016, pp. 497–503. ISBN: 9781119075646. DOI: 10.1002/9781119075646.ch53.

[154] M. Shakoor et al. “An efficient and parallel level set reinitialization method – Application to micromechanics and microstructural evolutions”. *Applied Mathematical Modelling* 39.23 (2015), pp. 7291–7302. ISSN: 0307-904X. DOI: https://doi.org/10.1016/j.apm.2015.03.014.

[155] L Maire et al. “Modeling of dynamic and post-dynamic recrystallization by coupling a full field approach to phenomenological laws”. *Materials and Design* 133 (2017), pp. 498–519. ISSN: 0264-1275. DOI: 10.1016/J.MATDES.2017.08.015.

[156] K. Alvarado et al. “A level set approach to simulate grain growth with an evolving population of second phase particles”. *Modelling and Simulation in Materials Science and Engineering* 29.3 (2021). ISSN: 1361651X. DOI: 10.1088/1361-651X/abe0a7.

[157] J. Fausty et al. “A novel Level-Set Finite Element formulation for grain growth with heterogeneous grain boundary energies”. *Materials and Design* 160 (2018), pp. 578–590.

[158] J Fausty, N Bozzolo, and M Bernacki. “A 2D level set finite element grain coarsening study with heterogeneous grain boundary energies”. *Applied Mathematical Modelling* 78 (2020), pp. 505–518. ISSN: 0307904X. DOI: 10.1016/j.apm.2019.10.008.

[159] J. Furstoss et al. “Full Field and Mean Field Modeling of Grain Growth in a Multiphase Material Under Dry Conditions: Application to Peridotites”. *Journal of Geophysical Research* 125 (2020), p. 18138.

[160] J. Fausty et al. “A new analytical test case for anisotropic grain growth problems”. *Applied Mathematical Modelling* 93 (2021), pp. 28–52. ISSN: 0307-904X. DOI: https://doi.org/10.1016/j.apm.2020.11.035.

[161] H. Hallberg and V. V. Bulatov. “Modeling of grain growth under fully anisotropic grain boundary energy”. *Modelling and Simulation in Materials Science and Engineering* 27.4 (2019), p. 045002.

[162] B. Murgas et al. “Comparative Study and Limits of Different Level-Set Formulations for the Modeling of Anisotropic Grain Growth”. *Materials* 14 (2021).

[163] J. Furstoss et al. “On the role of solute drag in reconciling laboratory and natural constraints on olivine grain growth kinetics”. *Geophysical Journal International* 224.2 (2021), pp. 1360–1370.

[164] F. Humphreys. “The nucleation of recrystallization at second phase particles in deformed aluminium”. *Acta Metallurgica* 25.11 (1977), pp. 1323–1344. ISSN: 00016160. DOI: 10.1016/0001-6160(77)90109-2.

[165] K. Hitti et al. “Precise generation of complex statistical Representative Volume Elements (RVEs) in a finite element context”. *Computational Materials Science* 61 (2012), pp. 224–238. ISSN: 09270256. DOI: 10.1016/j.commatsci.2012.04.011.

[166] B. Scholtes. “Development of an efficient level set framework for the full field modeling recrystallization in 3D”. PhD thesis. MINES ParisTech, 2016.

[167] O. Engler and H. E. Vatne. “Modeling the recrystallization textures of aluminum alloys after hot deformation”. *Jom* 50.6 (1998), pp. 23–27. ISSN: 10474838. DOI: 10.1007/s11837-998-0123-y.

[168] K. Alvarado et al. “Dissolution of the γ' particles during solution treatment of three Nickel base superalloys: mean field and full field simulations”. *Metals* Submitted (2022).

[169] Y. Jin et al. “2D finite element modeling of misorientation dependent anisotropic grain growth in polycrystalline materials: Level set versus multi-phase-field method”. *Computational Materials Science* 104 (2015), pp. 108–123. ISSN: 0927-0256. DOI: https://doi.org/10.1016/j.commatsci.2015.03.012.

[170] F. Abdeljawad et al. “The role of the interface stiffness tensor on grain boundary dynamics”. *Acta Materialia* 158 (2018), pp. 440–453. ISSN: 1359-6454. DOI: https://doi.org/10.1016/j.actamat.2018.06.025.

[171] W. T. Read and W. Shockley. “Dislocation models of crystal grain boundaries”. English. *Physical Review* 78.3 (1950), pp. 275–289.

[172] V. V. Bulatov, B. W. Reed, and M. Kumar. “Grain boundary energy function for fcc metals”. *Acta Materialia* 65 (2014), pp. 161–175.

[173] S. Florez et al. “Statistical behaviour of interfaces subjected to curvature flow and torque effects applied to microstructural evolutions”. *Acta Materialia* 222 (2022), p. 117459. ISSN: 1359-6454. DOI: https://doi.org/10.1016/j.actamat.2021.117459.

RÉSUMÉ

Le besoin croissant de véhicules automobiles plus légers pousse à s'intéresser de plus en plus aux alliages d'aluminium, en particulier aux alliages 6xxx (Al-Mg-Si) à durcissement structural. Bien que ces alliages soient connus pour leur bonne formabilité, leur bonne résistance à la corrosion et leur potentiel de renforcement suffisant, ils sont sujets à l'apparition de défauts de surface. Cette thèse porte sur la nuance 6016. Une meilleure compréhension des évolutions microstructurales se produisant au cours du processus de laminage à chaud est requise pour optimiser les propriétés finales. En particulier, l'interaction entre les précipités et les solutés avec les processus de restauration dynamique et de recristallisation dynamique et post-dynamique est étudiée. Dans ce contexte, différents états de précipitation initiaux sont générés puis soumis à essais de compression à chaud. Des analyses microstructurales sont effectuées par microscopie électronique à balayage (MEB) et cartographie des orientations cristallines par EBSD. Les facteurs favorisants le développement anisotrope de gros grains recristallisés lors du maintien après déformation sont également étudiés par recuit séquentiel à l'aide d'une platine chauffante couplée au MEB/EBSD. Cette étude est complétée par des simulations 2D en champ complet basées sur la méthode Level Set afin de discuter de la validité des hypothèses émises concernant le développement anisotrope de certains grains recristallisés. Enfin, l'influence de divers paramètres thermomécaniques sur l'évolution de la microstructure est étudiée, permettant ainsi de déterminer les conditions favorables à la formation de grains recristallisés plus fins.

MOTS CLÉS

Alliages d'aluminium, laminage à chaud, recristallisation, gros grains recristallisés, effet des précipités/solutés

ABSTRACT

The increasing need for weight reduction in automotive applications has led to paying increasing attention to aluminum alloys, especially to age-hardenable 6xxx (Al-Mg-Si) alloys. Although these alloys are known for their good formability, good corrosion resistance and sufficient strengthening potential, they are prone to the appearance of sheet surface defects. This PhD work focusses on the grade 6016. A better understanding of the microstructural evolutions occurring during the hot rolling process is needed to optimize the final properties of the material. Particularly, the interaction between precipitates and solutes with dynamic recovery, dynamic and post-dynamic recrystallization processes is studied. In this context, different initial precipitation states are generated prior to deformation and are subsequently submitted to hot compression tests. Microstructural analyses are performed using Scanning Electron Microscopy and crystal orientation mapping by EBSD. The factors possibly leading to the anisotropic development of coarse recrystallized grains during holding after deformation are also investigated through sequential annealing using a fast heating stage coupled to SEM. This is followed by 2D full field simulations based on the Level Set method in order to discuss the validity of specific assumptions regarding the anisotropic overgrowth of some recrystallized grains. Finally, the influence of different thermomechanical parameters on microstructure evolution is studied, determining thus the thermomechanical parameters promoting the formation of a finer final recrystallized grain size.

KEYWORDS

Aluminum alloys, hot rolling, recrystallization, coarse recrystallized grains, effect of precipitates/solutes